Hybridising electrohydrodynamic and aerosol jet printing for the manufacture of functional soft structures

Nathan James Wilkinson

Submitted in accordance with the requirements for the degree of
Doctor of Philosophy in Mechanical Engineering

The University of Leeds
The School of Mechanical Engineering

September 2020

The candidate confirms that the work submitted is their own, except where work which has formed part of jointly authored publications has been included. The contribution of the candidate and the other authors to this work has been explicitly indicated below. The candidate confirms that appropriate credit has been given within the thesis where reference has been made to the work of others.

Chapters three, four, five, and six of this thesis contains work published in the journal article "*Electrohydrodynamic and Aerosol Jet printing for the co-patterning of polydimethylsiloxane and graphene platelet inks"*. The work of N.J. Wilkinson includes the design and construction of all apparatus; design and completion of empirical work; design and validation of functional demonstrators; and writing of the manuscript. R. W. Kay and R. A. Harris provided guidance throughout and suggestions for the practical work, manuscript production, and review.

Chapter five of this thesis includes work from the journal article *"A review of aerosol jet printing – a non-traditional hybrid process for micro-manufacturing"*. N. J. Wilkinson and M. A. A. Smith jointly compiled the literature and wrote the manuscript. R. W. Kay and R. A. Harris provide guidance and made suggestions on presentation.

Chapters five and six include work from *"Aerosol Jet Printing for the Manufacture of Soft Robotic Devices"* from the 2019 IEEE International Conference on Soft Robotics (RoboSoft 2019, South Korea). N. J. Wilkinson conducted all practical work; designed and analysed the experiments; and wrote the manuscript. M. Lukic-Mann completed early stage material formulation. M. P. Shuttleworth built the linear strain test equipment. R. W. Kay and R. A. Harris provided guidance throughout and made suggestions on presentation. In the same sections, aerosol jet printing on to conformal surfaces was completed alongside N. Fry.

Full details of manuscripts the author contributed to as part of this doctoral work can be found in the **Academic Publications** section.

Abstract

Soft robotics can bridge the gap between the built and natural environment to deliver impact in many areas, including healthcare, biosciences, and haptics. Research, to improve the resolution, power density, and efficiency of soft actuation and sensing systems, will be essential for delivering their potential. Device performance is dependent on their design, the electro-mechanical response of materials, and the ability to co-pattern structural and function features. For film based soft structures, such as wearable sensors and artificial muscles, manufacturing challenges persist that prevent the translation of technology from laboratory to practical application.

This thesis presents a hybrid manufacturing technique that integrates electro-hydrodynamic (EHD) deposition with aerosol jet printing for the production of soft, functional films. The combined approach overcomes the respective rheological constraints of the individual process and provides a pathway for high resolution computer-controlled patterning. An experimental apparatus for broad investigation of EHD deposition is developed and validated, before a focussed study on e-jet printing of polydimethylsiloxane is presented. Axial resolution and surface roughness of 5µm and 0.26µm (Sa), respectively, demonstrates the potential for the technology in emerging thin film technologies, such as dielectric elastomer actuators. Aerosol jet printing of a graphene nano-platelet is used as a more robust method for producing conductive features. Characterisation and refinement enabled the production of 50µm traces with a minimum height of ~200nm.

Finally, the aforementioned processes are used to produce functional demonstrators that highlight the potential of the manufacturing technology. Combining the two materials required a complimentary oxygen plasma surface treatment to improve material wetting. Elastomer actuators, resistive strain, and capacitive sensors are all produced to demonstrate the efficacy of the techniques.

Acknowledgements

Throughout this research I have received tremendous support from my academic supervisors, Dr Robert Kay and Prof. Russell Harris. They have expertly guided my research, helped me understand how to deliver meaningful impact, and provided endless opportunities for my development. My experience would have been less worthwhile without their persistent encouragement and commitment to my growth. I am grateful for the opportunity to work under their guidance and I look forward to our future professional collaborations and on-going friendships.

I have been fortunate to share a research lab with all the members of the Future Manufacturing Processes Research Group. I would like to thank Lee Wetherill for his technical input, tales of his glory days, and (mainly) moans about his golf handicap. I am delighted to have worked with a number of brilliant post-docs who have provided insight, advice, and entertainment in equal measure, specifically Nicholas Fry and Mohammadreza Eshfahani.

A particular acknowledgement to my fellow students; Matthew Smith, Jack Hinton, Matthew Shuttleworth, and Luke Tinsley. Between us, it often felt like the blind leading the blind; but, without their collective input, discussions, and willingness to spend all night in The Library, I am sure the completion of my studies would have been a lot more difficult and certainly a lot less fun.

I would like to thank my family, especially my parents, who have been an unwavering source of support throughout my PhD and beyond. I owe my interests and passions to the opportunities and experiences they have provided and will always be grateful for everything they have done, and continue to do.

Finally, the most special thank you to Charlotte Bray. Since before I considered studying for a PhD, Charlotte has been my greatest supporter and the biggest source of encouragement. Her kindness, drive, and passion is a constant source of inspiration, for which I am eternally grateful and endlessly lucky.

Table of Contents

List of Figures

List of Tables

Abbreviations

AC – Alternating current

AJ – Aerosol jet

CNT – Carbon nano-tubes

DC – Direct current

DEA – Dielectric elastomer actuators

DIW – Direct ink write

DoD – Drop-on-demand

DTI – Dial test indicator

E-Jet – Electro-hydrodynamic jet

EAP – Electroactive polymer

EHD – Electro-hydrodynamic

EPFL - École Polytechnique Fédérale de Lausanne

ESI-MS – Electrospray ionizing mass spectrometry

FWHM – Full width at half maximum

IJ - Inkjet

IPN – Interpenetrating polymer networks

MBD – Molecular beam epitaxy

MICE – Mesoscale integrated conformal electronics

MWCNT – Multi-walled carbon nanotubes

Oh – Ohnesorge's number

PDMS - Polydimethylsiloxane

PET – Poly ethyl terephthalate

PoD – Pulse-on-demand

PVD – Physical vapour deposition

PVP – Poly vinyl pyrrolidone

Re – Reynold's number

SEBS - Styrene-ethylene-butadiene-styrene

SMU – Source meter unit

SWCNT – Single walled carbon nanotubes

TRL – Technology readiness level

We – Weber's number

Academic Publications

Journal Articles

Wilkinson, N.J.; Kay, R.W.; and Harris, R.A. 'Electrohydrodynamic and Aerosol Jet printing for the co-patterning of polydimethylsiloxane and graphene platelet inks'. Adv. Mater. Technol, (2020). DOI: 10.1002/admt.202000148

Wilkinson, N.J.; Smith, M.A.A.; Kay, R.W.; and Harris, R.A. 'A review of aerosol jet printing—a non-traditional hybrid process for micro-manufacturing.' *Int J Adv Manuf Technol* **105,** 4599–4619 (2019). DOI: 10.1007/s00170-019-03438-2.

Eshfahani, R.N.; Shuttleworth, M.P.; Doychinov, V.; **Wilkinson, N.J.**; Hinton, J.; Jones, T.D.A.; Ryspayeva, A.; Robertson, I.D.; Marques-Hueso, J.; Desmulliez, M.P.Y.; Harris, R.A.; and Kay, R.W. 'Light based synthesis of metallic nanoparticles on surface-modified 3D printed substrates for high performance electronic systems'. Additive Manufacturing. DOI: 10.1016/j.addma.2020.101367

da Veiga, T.; Chandler, J.; Lloyd, P.; Pittiglio, G.; **Wilkinson, N.J.**; Hoshiar, A.; Harris, R.A.; Valdastri, P. 'Challenges of continuum robots in clinical context: a review.' Progress in Biomedical Engineering. DOI: 10.1088/2516-1091/ab9f41

Conference Proceedings

N. J. Wilkinson, M. Lukic-Mann, M. P. Shuttleworth, R. W. Kay and R. A. Harris, "Aerosol Jet Printing for the Manufacture of Soft Robotic Devices," 2019 2nd IEEE International Conference on Soft Robotics (RoboSoft), Seoul, Korea (South), 2019, pp. 496-501. DOI: 10.1109/ROBOSOFT.2019.8722766

1 Introduction

Soft robotics is a field that focusses on the construction, control, and application of compliant mechanisms to overcome the constraints of traditional rigid-link robotics. Pioneering work has demonstrated how improved outcomes in rehabilitation [1, 2], surgery [3, 4], grasping [5, 6], and human-robot collaboration [7, 8] can be achieved; however, intrusion caused by bulky design, tethered devices, and limited control strategies have prevented adoption beyond research environments. Improving the integration of soft technologies and removing the tether requires the development of devices with greater efficiency and power density than existing designs.

Early work focused on fluidic inflation of cavities within soft bodies to induce actuation [9]. Strain limiting layers were introduced for directional motion [10] while multi-cavity designs were created to form agnostic pairs. Fluid driven actuation systems continue to be the most popular in soft robotics due to their ease of manufacture, high speed, and high power. The main developments in the field have been driven by innovative design and an expansion of applications, while the fundamental operating principles have largely remained the same.

With the exception of aquatic soft robotics [11, 12], which use the buoyancy of water to overcome the limits of power density (10-1000kWm^{-3} [13]), most soft robotics remain tethered to a gas or hydraulic supply. While suitable for industrial settings, these devices cannot effectively be translated to fields, such as wearables and rehabilitation robotics, where they hold most promise. Furthermore, deformation as an actuation mechanism makes soft systems significantly harder to model than traditional rigid body robotics [14]; a challenge that is compounded as the structures also distort and deflect as they interact with their environment. This has implications for the control of soft devices and requires significant developments in proprioceptive sensing that can reliably feedback the state of the system [15].

Alternative methods of actuation and sensing have been investigated and their operating principles are increasingly well understood [16–18]. Perhaps the most attractive of these are electrically stimulated devices (electroactive polymers) that are capable of large strains (>100% [19]), high-speed actuation (>10kHz [20]),

and high power density (10^3-10^5kWm^{-3} [13]). In recent years, a small number of studies have shown how the performance gains of these actuators can enable tether-free operation in air [21]. Electroactive polymers hold further value as they can also be used for positional sensing [22] and energy harvesting [23]. Effective implementation of these technologies has been limited by the quality and performance of the materials and manufacturing processes used in their creation; as recently highlighted in *"The Grand Challenges of Science Robotics"* [24].

Many emerging electroactive polymer technologies are film-based devices that are either assembled into or manufactured directly within the bodies of soft devices. Manufacturing research in the field is centred around techniques borrowed from the micro-electronics industry [25], such as spin coating [26, 27] or transfer printing [28], that face challenges due to fundamental differences in the required size scales, production volumes, and material properties. Although successful in demonstrating the fundamental principles, there is a growing appreciation within the soft robotics community that bespoke manufacturing strategies need to be developed to advance the field from laboratory to practical application.

Producing soft structures with integrated function requires controlled co-patterning of structural elastomers and functional materials. The disparate mechanical, rheological, and processing requirements of the two material types has hindered progress of electrically driven soft robotics.

1.1 Research Objectives

The aim of this work was to develop a new manufacturing approach that helps overcome the limitations of soft film fabrication while also increasing the range of materials that can be processed. More specifically, the work targets techniques that can enable emerging forms of actuation and sensing, with a focus on film-based electrically stimulated devices. The primary objectives of this work were:

- A critical review of the current state-of-the-art in manufacturing for film-based soft robotics
- Identification of manufacturing process requirements for the creation of multi-material elastomer films

- Design of specific manufacturing process(es) for the co-patterning of elastomeric and functional materials
- The engineering and development of experimental apparatus to investigate the manufacturing process(es)
- Identification of elastomeric and functional inks with the appropriate characteristics for processing and application development
- Characterisation of the process(es) used for fabrication and presentation of a methodology for producing a reliable deposit
- Production of demonstrators that showcase the capabilities of the manufacturing process(es)

1.2 Thesis Outline

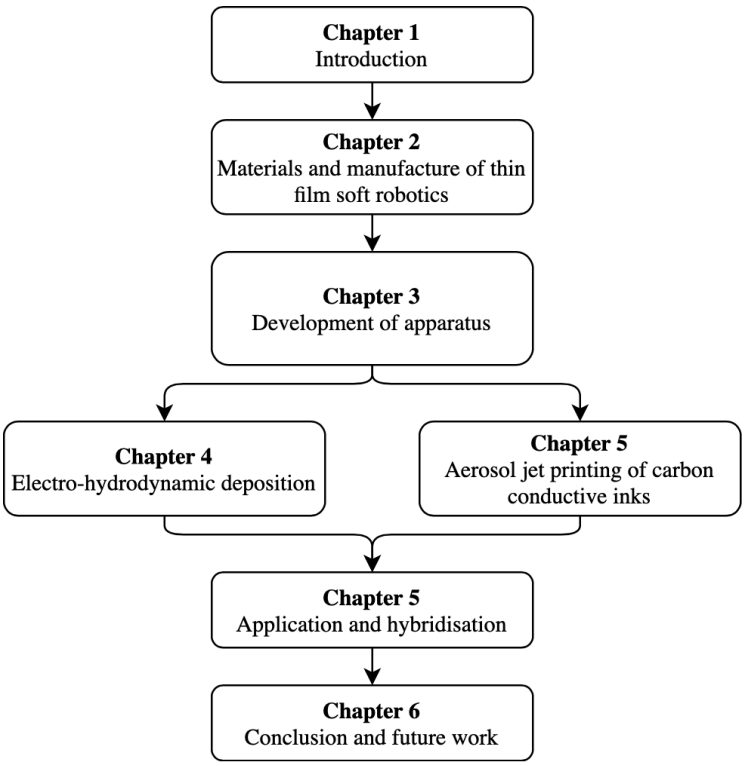

Figure 1 - Thesis structure summary

Chapter 2 provides a review of current manufacturing techniques for the production of soft films. It first introduces the operating principles of soft sensors and actuators before exploring the materials used in their construction. A critical review of existing manufacturing techniques is then presented and used to develop an ideal machine specification for the production of multi-layer films.

Chapter 3 builds on the previous chapter by documenting the development of an experimental apparatus. This includes a brief review of the core technology (electro-hydrodynamic deposition (EHD)) and a discussion of the design and tool path planning techniques. Finally, this chapter concludes by presenting initial deposition results from the apparatus using a model ink.

Chapter 4 explores the use of the apparatus developed in Chapter 3 for the deposition of materials relevant to thin film soft robotics. This begins with an exploration of the different EHD modes using a number of elastomeric inks before focusing on the deposition of a Sylgard elastomer using electro-hydrodynamic jet (e-jet) printing. The deposition of a low-viscosity aqueous conductive inks using the EHD is also presented.

In Chapter 5, Aerosol Jet (AJ) is presented as it overcomes many of the challenges of using EHD for low viscosity inks compared to more established technologies. The higher technology readiness of AJ is shown to produce robust, high resolution, and selective patterning of a graphene nano-platelet ink. The process is extended to demonstrate patterning on to complex 3D geometries to highlight its potential to the wider field of soft robotics.

Chapter six presents a number of demonstrators produced using the manufacturing techniques presented in the preceding chapters. Oxygen plasma surface treatment and spin-coated sacrificial supports are presented to overcome challenges in material wetting and substrate removal, respectively. The development of working dielectric elastomer actuators, resistive strain sensors, and capacitive touch sensors are all presented. Finally, conclusions from this work are included alongside recommendations for further work.

2 Materials and manufacture of thin film soft robotics

Common thin film manufacturing techniques have been explored by the soft robotics community to improve the performance of film-based actuation and sensing devices [26–29]. However, challenges persist that require significant innovation in material science and processing to realise commercial translation [25, 30]. This chapter explores these ideas by introducing the operating principles behind common soft film sensing and actuation technologies; highlighting the hurdles to successful adoption; and, finally, by reviewing materials and manufacturing processes that have been used in their development. The chapter concludes by suggesting a list of requirements for an idealised manufacturing process.

2.1 Construction and operating principles

The performance of soft sensing and actuation devices is dependent on their design, the electro-mechanical response of materials, and the ability to co-pattern structural and functional features. Specifically, the ability to alternately form thin layers of elastomers with micro-patterned, stretchable circuitry can improve sensor density and fidelity; while the automated and repeatable manufacture of low-roughness elastomeric films has importance in soft electroactive polymers, such as dielectric elastomer actuators.

2.1.1 Soft Sensing

Effective strategies for proprioceptive and exteroceptive sensing are essential for producing soft structures with the required dexterity and to transition the field away from open-loop control [15]. The most common approaches have introduced sensing through the incorporation of conventional rigid sensors [31, 32] or strain tolerant conductors; such as liquid metals [33, 34], ionic liquids [35–37], or nanoparticle-filled polymers [38–40]. More recently, optical waveguides [41, 42] are being explored as they overcome many of the challenges associated with hysteresis and resolution often found in conductive networks.

These techniques all rely on deformation of the polymer body to induce changes to the characteristic response of the sensor. For conductive approaches, changes in resistance or capacitance are used to estimate position, whilst optical methods

examine time of flight or transmission losses. Since soft devices have infinite degrees of freedom (continuum mechanics), determining the direction or magnitude of deflection presents a challenge for all sensors when devices operate without constraint [43]. Increasing the number of sensors, collating their relative outputs, and using machine learning to build complex models are currently the most promising methods for improving their efficacy [14]; however, this approach will be dependent on the development manufacturing processes that can pattern emerging elastomer and functional materials with the required electro-mechanical properties at the required resolution.

2.1.2 Electroactive polymers

Electroactive polymers (EAP) is a term used to describe number of soft technologies (Table 1) that achieve mechanical work from electrical energy [18, 44]. These can be split into devices that rely on ion mobility (ionic EAP) or the build-up of Maxwell stresses (electronic EAP) (Table 1).

Table 1 - Common types of electroactive polymer [28]

Electronic EAP	*Ionic EAP*
Liquid crystal elastomers	*Ionic polymer gels*
Electro-viscoelastic elastomers	*Electro-rheological fluids*
Electro-strictive paper	*Conductive polymers*
Electro-strictive graft elastomers	*Ionic polymer metal composites*
Ferro-electric polymers	-
Dielectric elastomers	-

Ionic EAPs typically exhibit low forces, response times, and require the encapsulation of liquids or gels that are vulnerable to evaporation and device deterioration. Electronic EAPs, more specifically Dielectric Elastomer Actuators (DEAs), overcome many of these constraints and offer high-speed and force operation, efficiency, simple construction, and have sufficient power density for tether-free operation [21]. The key challenges for the technology are the requirements for driving fields on the order of 100-150V/μm and the development of electrodes that are strain tolerant over a high number of cycles.

DEAs are comprised of a soft dielectric layer sandwiched between two compliant electrodes (Figure 2) [45]. Actuation is achieved through electrostatic attraction upon the application of a voltage [46]. The resultant pressure produces axial strain through compression of the soft dielectric and radial strain as the soft dielectric expands to conserve mass. Through radial expansion, researchers have presented strains of 1692% [47].

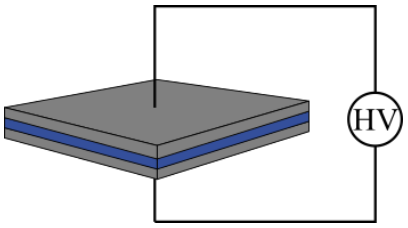

$$P = \varepsilon_0 \varepsilon_r (\frac{U}{Z})^2$$

Figure 2 - Dielectric Elastomer Actuator Schematic

Although the viscoelastic response of the actuator can be difficult to model, the interaction of charges on parallel plates is well understood and borrows much of the theory from the electronics industry's modelling of capacitors. In their seminal paper, Pelrine et al. [19] derived Equation 1 for predicting the pressure output of a DEA. Where *P* is the actuation pressure, ε_0 is the permittivity of free space, ε_r is the relative permittivity (dielectric constant) of the dielectric material, U is the applied voltage and z is the thickness of the dielectric material.

Using Pelrine's model, the pressure produced by an actuator is proportional to the magnitude of the electric field. Therefore, any moderate decrease in electrode separation or applied voltage will have a significant impact on the achievable pressure. Improving an actuator's performance (pressure at a given voltage) requires improvement in the relative permittivity of the dielectric materials or a decrease in the separation of the electrodes. Innovation in manufacturing to enable a reduction in dielectric layer height and, therefore, a reduction in the required driving voltage will be essential to the effective commercialisation of the technology [25].

2.2 Materials: Elastomers

Soft robotic technologies are usually developed from materials (Figure 3) with an elastic (Young's) modulus in the range of 10^2 - 10^7 Pa [48, 49], with silicone

elastomers, PDMS, and polyurethanes being widely used. Designs often use a range of elastic moduli materials or geometrically vary the stiffness to constrain the devices and trigger directional motion. Compared to conventional robotics, which use materials with moduli ranging from 10^9 – 10^{12}, this has allowed the development of devices that can more easily operate in delicate environments, improve human-robot interaction, and allow more robust operation. The diversity of materials, and Young's modulus available, means that their selection is driven by the force and strain requirements of the application. In this section, materials for DEA applications are reviewed as it is one of the technologies will gain the most from the development of effective manufacturing techniques for soft films. Furthermore, any technology that realises effective implementation of DEAs will have direct applications in soft sensing and power generation.

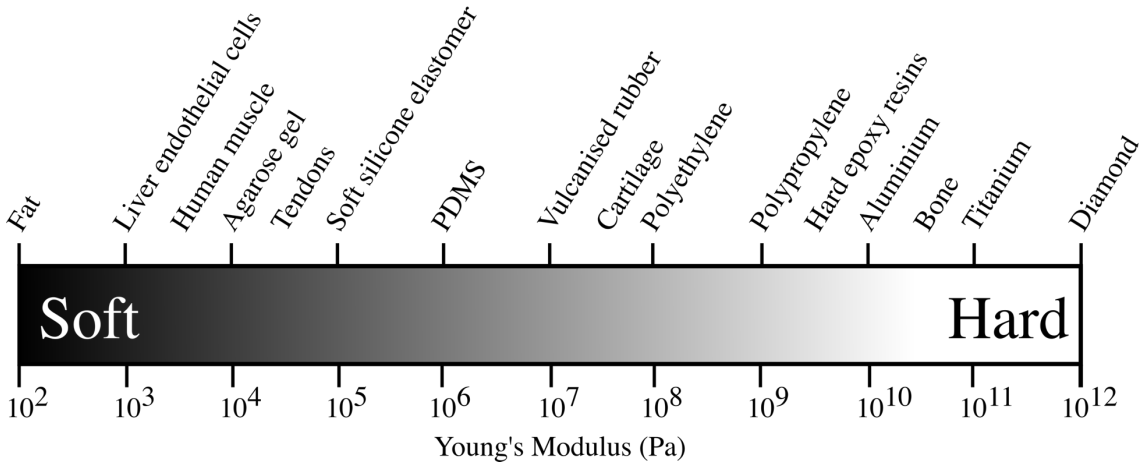

Figure 3 - Young's modulus of materials found soft robotics, conventional robotics, and the natural environment (Adapted from [50])

2.2.1 *Dielectric elastomers*

Typical dielectric elastomer actuators use silicone rubbers, thermoplastic polyurethanes, acrylic elastomers, and rubbers [16] due to their availability; low cost; and relatively high performance. In their influential paper, Pelrine et al. [50] demonstrated DEAs constructed from six common materials and reported their peak strain and actuation pressure (Table 2).

Table 2 - Performance of dielectrics in Pelrine's initial experiments in 1997 (adapted from [50]*)*

Polymer	*Energy Density (Jcm^{-3})*	*Strain (%)*	*Pressure (MPa)*	*Young's Modulus (MPa)*
Polyurethane	*0.10*	*11*	*1.9*	*17*
Silicone	*0.034*	*32*	*0.21*	*0.7*
Fluoro-silicone	*0.019*	*28*	*0.14*	*0.5*
Ethylene propylene	*0.013*	*12*	*0.022*	*1.8*
Polybutadiene	*0.011*	*12*	*0.19*	*1.7*
Isoprene	*0.0052*	*11*	*0.094*	*0.85*

These seminal results demonstrated that electrostatic attraction could be an effective soft actuation mechanism. DEAs based on silicone elastomers were able to achieve strains of 32% and polyurethane devices could achieve pressures as high as 1.9MPa. The materials each demonstrated a unique strain and pressure response, therefore highlighting an opportunity to tailor actuator performance by modifying the elastic modulus or by combining materials. Research continued to investigate common laboratory materials; with Brochu and Pei providing an updated list in their 2010 review [45].

Pre-strain of Elastomer Films

Pre-strain of elastomer films has been shown to suppress the electromechanical instability of DEAs [51], which is caused by the positive feedback loop established during actuation: the dielectric is compressed under the application of a voltage and the distance between electrodes is decreased; therefore, the magnitude of the electric field increases and further actuation is induced. While proving a theoretical basis for the instability, Zhao and Suo showed that pre-strain

overcame the instability by increasing the dielectric breakdown strength of elastomers [52].

a) b)

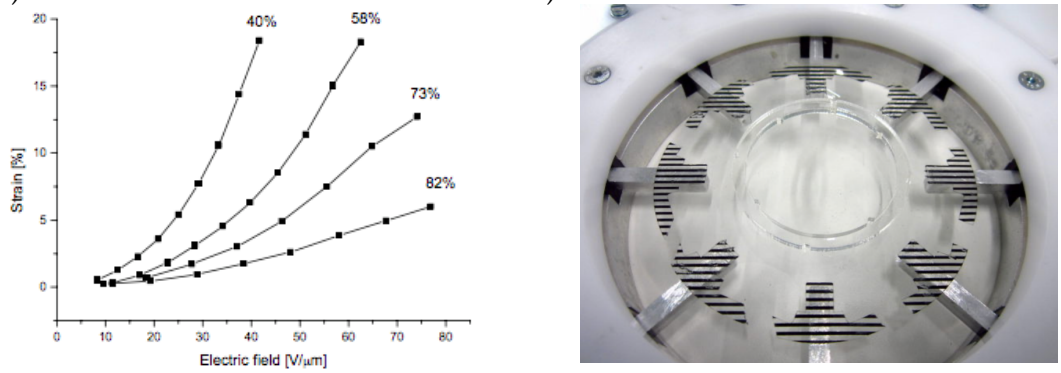

Figure 4 – a) Effect of pre-strain on Actuator Performance (Percentages Show Amount of Pre-strain) [53]. Pre-straining of elastomer film [29]

In practice, this allows the application of higher magnitude electric fields and a higher peak strain. However, the strain achieved from a given voltage is diminished (Figure 4). Zhang et al. [53] showed that increasing elastomer pre-strain from 40% to 82% led to a 15% reduction in actuation strain during exposure to a 40V/μm electric field. This effect has been attributed to an increased Young's modulus in pre-strained films for acrylic [54] and silicone films.

A challenge for pre-strained elastomers is the requirement for a stiff support structure, which removes the benefits of compliance and conformity that have been key motivations for the field. Work has been completed to investigate interpenetrating polymer networks (IPNs) to achieve a compromise between actuator stiffness and performance [55, 56]. In this approach, a secondary polymer network is crosslinked to a pre-strained base polymer. When the base polymer is released, the secondary network is placed in a state of compression that retains a degree of pre-strain. Although inhibiting the most conformal applications, such as wearables, pre-strained elastomers are being readily applied to emerging applications, with impressive results in tuneable lenses [57, 58] and active cell culture platforms [59, 60].

2.2.2 *Improving the properties of the dielectric layer*

Beyond 'off-the-shelf' materials, researchers are developing bespoke material formulations for DEAs. The focus has been on materials with a high relative permittivity (dielectric constant) that also maintain a sufficiently low elastic modulus. Approaches to increasing the relative permittivity broadly fit within three categories: creating composite elastomers using high dielectric constant fillers; developing polymer blends; and modifying the backbone of elastomeric materials. An overview of these approaches can be found below and a more comprehensive study has been completed by Romasanta, Lopez-Manchado, and Verdejo [61].

Filled elastomer composites

High permittivity fillers distributed within a polymer matrix can raise the overall permittivity to increase the response of a dielectric elastomer actuator. Disrupting the crosslinked polymer network with particles can lead to a decrease in the elastic modulus of the material and high volume fractions can lead to a complete loss of elasticity and even brittle properties.

The inclusion of conductive fillers (carbon black [62], carbon nano-tubes [63, 64], graphene platelets [65]) below the percolation threshold has been shown to increase the permittivity. Micro-scale particles should be avoided as agglomeration can lead to localised conductivity and device failure. Evenly distributed nano-scale conductive particles have achieved greater success as the material properties become increasingly dependent on the interface between the filler and the bulk material [66]. By encapsulating multi-walled carbon nano-tubes (MWCNTs) within polyacrylonitrile and diurethane polyacrylate shells within a polyurethane matrix, Galantini et al. [67] demonstrated a 100% increase in actuation strain.

An alternative approach is to introduce high permittivity, insulating ceramic fillers (barium titanate [68–70], calcium copper titanate [71], titanium dioxide[72]) in to the polymer matrix. In principal, these fillers increase the relative permittivity of the composite and, unlike conductive fillers, they should provide minimal change in conductivity. Ceramic fillers still interfere with the crosslinking of the elastomer; therefore, they suffer from a reduction in elastic

modulus at low loading and an increase at high fractions. Yang et al. [70] demonstrated that an optimum loading, which strikes a compromise between increased permittivity and decreased elastic modulus, can be found to maximise actuation strain for a composite. Using a 6wt% loading, the electric field needed for ~12% strain reduced from 15.6V/μm to 9.8V/μm [73]. Coating ceramic particles in PDMS oil [74] or dopamine [68] has also been shown to increase actuation performance by up to 30%.

Elastomer Blends

Elastomer blends are a specific type of composite that combine two or more polymers to produce a material with properties more suitable for dielectric elastomer actuators. Zhang et al. [75] initiated this work by evaluating the performance of a copper-phthalocyanine (CuPc) oligomer in poly(vinylidene fluoride-trifluoroethylene) (P(VDF-TrFE)) matrix. A sample with 40wt.% CuPC showed significant increases in strain. Although the peak strain value was only 2%, this could be achieved at a low electric field (13V/μm).

This early work was improved by incorporating polyaniline alongside CuPC in a polyurethane matrix. This three-polymer blend show significantly improved strain (9.3%) compared to the previous two-polymer material (1.92%) and plain polyurethane (0.82%) from the same applied electric field (20V/μm) [76]. Gallone, Galantini, and Carpi [77] used a similar approach to investigate a PDMS-polyurethane polymer blend that was found to have a significantly higher relative permittivity than either of the constituent polymers. At a ratio of 60:40 (PDMS:Polyurethane), strains of ~3% were achieved from electric fields as low as 5-6V/μm. Like many of the approaches discussed, a side effect of this approach is decreased dielectric breakdown strength, which limits strain through a restriction on the applied electric field. Similar results have been demonstrated through the addition of polyethylene glycol to thermoplastic polyurethane [78].

Chemical Modification

Rather than combining complimentary materials, this approach aims to improve the properties of the dielectric elastomers through the synthesis of molecular structures or by modifying the backbone of existing elastomers. Stoyanov et al. [79] demonstrated this by grafting a PANI macromolecules to a flexible poly-

styrene-co-ethylene-co-butylene-co-styrene-g-maleic anhydride (SEBS-g-MA). Their work increased the relative permittivity of the elastomer by 470% while decreasing the dielectric breakdown strength from 140V/μm to 120V/μm (~14.3.%). This improved actuation strain from 0.7% to 2.9% from an applied field of 90V/μm. The maximum achievable strain was also greater for the modified elastomer (4% at 107V/μm) compared to the unmodified elastomer (1.5% at 136V/μm) [80]. The performance increase was driven by the increase a decrease in elastic modulus combine with the increase in permittivity.

More recently, Dunki et al. [81] have made steps to produce self-repairing dielectric materials based on PDMS. Their material has the advantage of being able to heal itself following dielectric breakdown, which is a significant step for devices that are required to operate near their electrical limit [82]. By modifying PDMS with polar nitrile groups and controlling the cross-linking reaction, they demonstrated that the permittivity and mechanical properties could be controlled. Through their work, they developed a DEA that could achieve 20.8% strain at 10V/μm).

2.3 Materials: Conductors

The role of the conductive layer is to supply a potential difference through the delivery of charge to the surface of the dielectric. Any conductive material needs to achieve this without restricting the movement of the actuator and, as the conductive material is not compressed during actuation, the conductive layer should be as thin as possible to maximise the total strain [83]. This section of the literature reviews common materials and patterning approaches that have been used to achieve stretchable electrodes and electronics.

2.3.1 Conductive powders, greases, and elastomer matrices

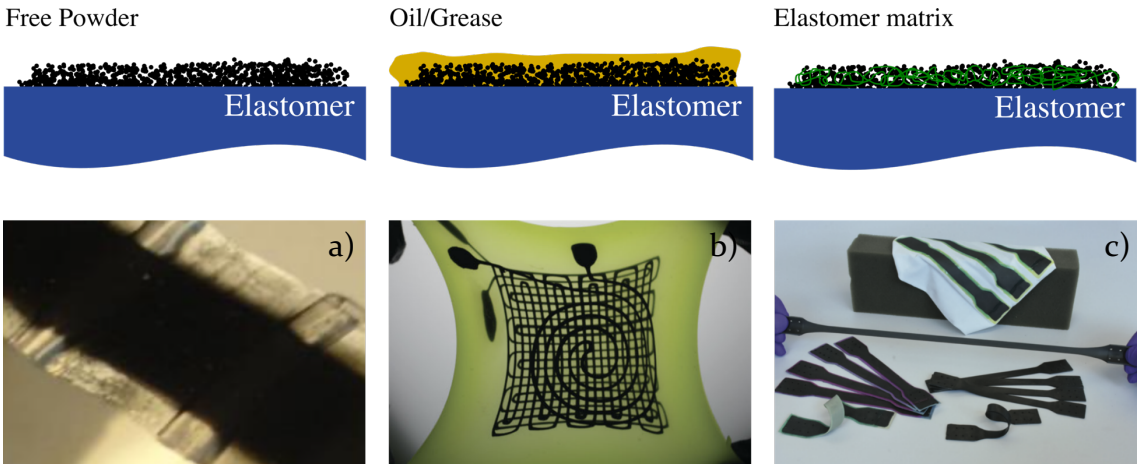

Figure 5 - (a) Free powder electrode[100], (b) Embedded 3D Printing of Strain Sensors within Highly Stretchable Elastomers [152] , and (c) Low-Cost, Facile, and Scalable Manufacturing of Capacitive Sensors for Soft Systems [130]

Powders

Common powders are based on graphite or carbon black due to their low cost and ease of processing. A limited number of studies have been completed with high conductivity metallic powders but the formation of a non-conductive oxide layer often reduces the overall conductivity [84] and they do not sufficiently interact with the dielectric due to large particle sizes [85]. Combined with their added cost, metallic powders offer little benefit over comparable carbon materials. Increased conductivity can increase the actuator response rates as it enables charge to be transferred to the dielectric at a greater rate. In most practical applications, the electrical charge/discharge rate is faster than the mechanical bandwidth of actuation. Rosset and Shea [83] showed that a 1cm^2

silicone DEA with a thickness of 40μm, a capacitance of 65pF, and an electrode resistance in the megaohm range would still be able to actuate at frequencies above 1kHz.

Powders are attractive as they are not strictly bonded to the surface of the dielectric material, which provides low resistance to actuation. However, the freedom of the particles to move relative to one another can lead to problems during operation: the powder acts as an abrasive that degrades the elastomer layer; powders struggle to maintain a continuous conductive network at moderate strains [86]; particles are shed during actuation; and particles do not promote interlayer adhesion in stacked actuator configurations. Furthermore, powders can cause processing challenges, particularly in cleanroom environments that are often used in the production of DEAs.

Powders have been most successful when used in combination with adhesive dielectric films, such as VHB 4905 and 4910, as the inherent stickiness bounds the particles the dielectric. A notable exception to the short-life powder electrode DEAs are the devices created by Lotz et al. [27, 87, 88] (Section 2.4.1), where layers of graphite powder where encapsulated between silicone layers by combining spin coating with aerosolised graphite deposition. However, since layers of PDMS are cast over graphite powder this perhaps does not fit the definition of loose powder electrodes.

Greases

Conductive greases were the type of electrode used in Pelrine's seminal papers on dielectric elastomer actuators [19]. They entrap conductive particles (Carbon black, graphite, CNTs etc.) within a highly viscous matrix material. Greases negate some of the issues of conductive powders as they are easier to process and handle; the matrix allows the conductive particles to be better distributed at high strains; and particles are prevented from simply falling from the surface of the dielectric film. The use of a viscous matrix causes durability issues for an assembled actuator as it has a tendency to creep under gravitational forces, diffuse in to the dielectric film, and dry out over time [83]. On top of this, they do little to improve interlayer adhesion over conductive powders and, as Bingham plastics, they are prone to ratcheting under cyclic loading [89].

Conductive elastomer matrices

Conductive polymer matrices are an electrode class that combine the durability of polymer composites with the conductivity of particles based on carbon or metallic elements [90, 91]. Fundamentally, conductive polymer matrices are similar in nature to the filled elastomers discussed in Section 2.2.2, but with conductive filler contents above the percolation threshold. The similarities are partly why this type of electrode is so appealing: it is conceivable that a dielectric elastomer actuator could be constructed from a single matrix material with selective introduction of the filler material. This approach could allow for highly tailorable, multifunctional designs in terms of both mechanical and electrical properties while alleviating problems regarding inter-layer adhesion. This effect has already been demonstrated in a non-DEA context through the Aerosol Jet Printing process discussed in Section 2.4.4 (Figure 6) [92].

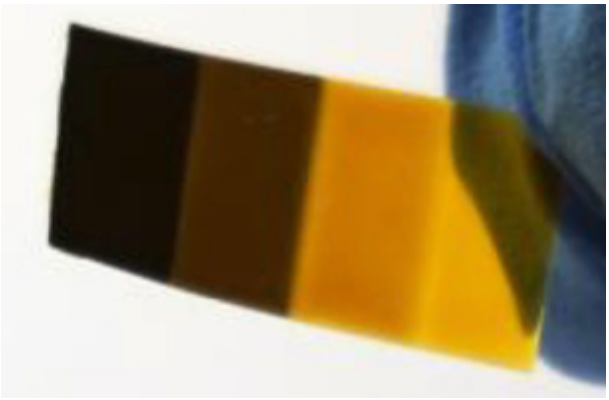

Figure 6 - Conductive-on-Demand: Selective Introduction of Carbon Nano-tubes in to Polyimide [93]

Most investigations regarding conductive polymer matrices have focused around the introduction of carbon based conductive particles in to elastomer membranes [93]. High surface area fillers allow a conductive network (percolation) to be achieved at lower volume fractions [94]. For example, percolation thresholds for multi-walled carbon nanotubes are as low as 0.0025% [95] compared with 0.1% [96] for carbon black compounds. A low percolation threshold has the benefit of minimising the impact on the mechanical properties of the elastomer matrix.

Conductive fillers carry current through physical connection or via tunnelling between proximate particles [97]. When tunnelling occurs, the resistance increases exponentially as the distance between particles increases. Therefore, to

ensure conductivity, it is paramount that fillers are evenly distributed within the polymer matrix and that all efforts have been made to avoid the agglomeration of the filler. This can increase the complexity and duration of the manufacturing process.

2.3.1 Conductive polymers

Table 3 - Common Properties of Common Inherently Conducting Polymers (Adapted from a Review by Kaur et al.[98]*)*

Polymer	Conductivity ($S.cm^{1)}$	Properties	Limitations
Polypyrrole	$10 - 7.5*10^3$	High electrical conductivity, Ease of preparation and surface modification	Rigid, brittle and insoluble
Polyaniline	30 - 200	Diverse structural forms, Environmentally stable, Low cost	Hard to process, Non-biodegradable, Limited solubility
Polythiphene	$10 – 10^3$	High electrical conductivity Ease of preparation Good optical properties	Hard to process
Poly-(3,4-ethylene dioxythiophene)	0.4 - 400	Transparent conductor, Environmentally and electrochemically stable	Limited solubility

DEA studies using conducting polymers as the electrode material are relatively sparse with those available focusing on the self-clearing ability of the conductive polymer electrodes. This is perhaps a side effect of the relatively high stiffness of inherently conducting polymers when compared to elastomers, such as PDMS [98] (Table 3).

A study conducted by Yuan et al. [99] focussed on the self-clearing ability of PANI, P3DOT and CNTs; where self-clearing is the ability of the electrode to cause a localised, rather than global, failure of the actuator when the elastomer undergoes dielectric breakdown. This ability is useful for the life of DEAs as it allows some leeway in the manufacturing process for imperfections such as dust

or air bubbles than can occur on multi-layered structures. The device produced had comparable strain to other DEAs fabricated using similar elastomers, suggesting conductive polymers could be a viable electrode material [99, 100]. Later work highlighted a potential problem for conducting polymers: the conductivity of the PANI electrodes were found to deteriorate under high electrical fields [101]. This may be curable using alternative conducting polymer materials; however, the lack of published data for conducting polymer electrodes in DEA applications, despite being relatively established technology, may be suggestive that there are significant pitfalls with this approach.

2.3.1 Nanowire and platelet meshes

Conductive nanowire meshes are a relatively new solution to flexible electrodes. As they are based on metallic elements, their conductivity is higher than many of the other flexible, non-metallic electrodes discussed here. Therefore, nanowire meshes are increasingly used in applications that are current (Organic Light Emitting Diodes and Solar Cells) rather than voltage driven (Capacitive Sensors, Liquid Crystal Displays or DEAs) [102]. A nanowire mesh is typically comprised of interconnected metallic wires embedded within or on the surface of a flexible substrate (Figure 7).

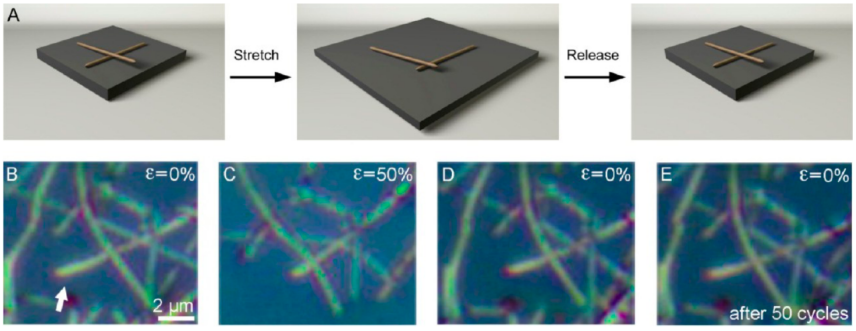

Figure 7 - Schematic and Optical Microscopy Images of Nanowire Sliding at 0 and 50% Strain [105]

The bulk of the work in this area uses silver nanowire meshes owing to its higher conductivity and increased time before oxidation compared to other metallic elements. There is significant interest in developing electrodes based on copper nanowire meshes due to its greater natural abundance, comparable conductivity, and significantly lower cost [102, 103]. Within the field of DEAs, Wu et al. [104] evaluated sliding nanowire meshes on an acrylic VHB 4905 films. Optical

microscopy allowed the sliding-expansion mechanism to be identified by looking the nanowire configuration at different strains (Figure 7).

The performance of the DEA with this type of electrode are comparable to the original devices developed by Pelrine et al. [54], with values of 200% and 32%s^{-1} reported for the strain and strain rates, respectively [104]. The device had an optical transmittance that ranged from 13 to 58% depending on the degree of actuation, which opens the device for use as an optical gate. A primary issue with the device developed by Wu is that the electrodes were not bonded to the surface of the elastomer, meaning it faces many of the same issues as conductive powders in a multi-layered DEA arrangement. A feasible, long-term solution would require the nanowires to be embedded within a membrane's surface [105]. However, this would have the undesirable effect of stiffening the electrode and potentially stifling the DEA's performance. Further to this, the use of metallic elements presents issues regarding oxidation that lead to a loss in conductivity. The relative novelty and limited commercial availability of these types of materials means steep challenges need to be overcome if they are to be more widely applied to DEAs.

2.3.2 Geometrically stretchable electrodes

Metal coatings have greater conductivity and allow soft devices to interface with traditional electronic technolgies, such as solder surface mount [106]. However, bulk metallic coatings have been shown to crack at relatively low strains (<5%) [107] and, while continuous plastic deformation can be encouraged by improving adhesion, this limits their use for soft robotics. Furthermore, the inclusion of metallic electodes, even at low thicknesses, can lead to high increases in the elastic modulus. Rosset et al. [108] demonstrated that a 8nm sputter coated gold layer on a 30.6µm PDMS substrate can lead to a 400% increase in Young's modulus. High-magnitude, reversible elastic strain requires structures that can maintain conductivity while minimising local stresses to prevent cracking [109].

In plane patterning of electrodes

Pelrine et al. [86] were amongst the first to demonstrate geometrically stretchable electrodes for soft robotics when they increased the achievable strain of gold from 4% to 80% by switching from bulk patterning to planar 'zig-zag' electrodes (Figure 8a). Verplancke et al. [110] improved on this by depositing a 200nm thick gold electrodes on to a silicone membrane in a horseshoe configuration (Figure 8c). These electrodes could undergo strains approaching 100% and, at 10% strain, were able to withstand over 500,000 cycles. A large number of studies have been completed using this technique with a variety of metals in a plethora of applications. A full review of all demonstrations of this approach is beyond the scope of this report and a number of groups have published comprehensive reviews [111–113].

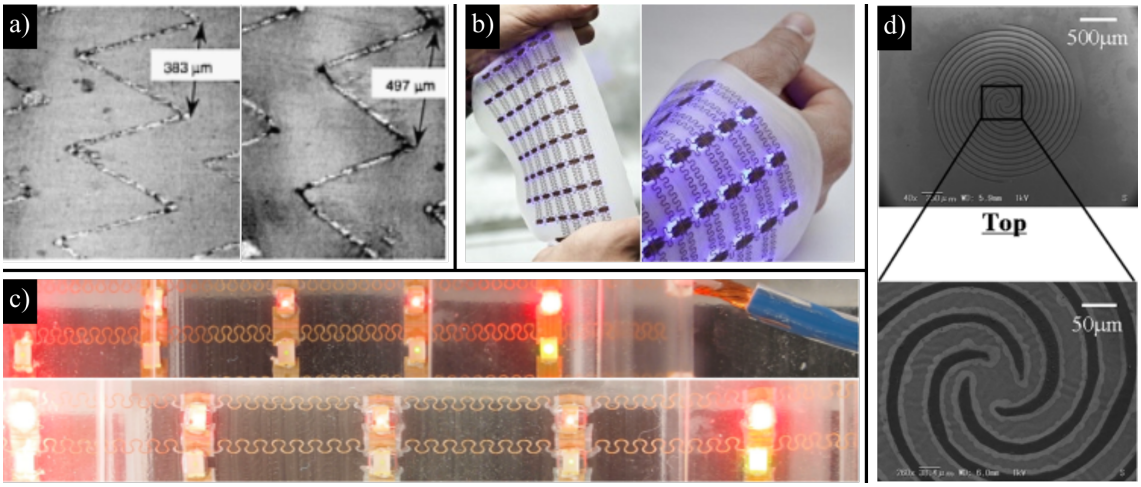

Figure 8 - Zig-Zag Patterned Gold Electrodes [87] at (a) 0% strain and 30% strain (b) Flexible and stretchable electronics for wearable health devices , (c) Microelectrostrictive Actuator With Large Out-of-Plane Deformation for Flow-Control Application [114], (d) Stretchable Circuits with Horseshoe Shaped Conductors Embedded in Elastic Polymers [115]

These electrodes introduce anisotropy into devices since electrodes exhibit lower stiffness along their length when compared to their width. Depending on the specific design and application, this constraint may be an advantage or disadvantage of the technology. Fractal, or self-similar, designs [112, 116] have been used to minimise the anisotropy but these still face challenges with electrode density. For sensing applications, this presents less of an issue and has been one of the driving forces behind '*e-skin*' technologies [109, 117]. However, for actuation devices, these designs limit the active area of the electrode layers and restricts device performance. Through a combination of empirical and numerical

studies, Pimpin et al. [114] showed that the electrode gap to width ratio should be 0.3 for their design to achieve maximum actuation in a DEA for a given electrode height (Figure 8d). Pelrine's [19] initial study examined challenges in electrode spacing and used a secondary, lower-conductivity material to bridge the gap. They also showed that the humidity of ambient air may be sufficiently conductive for actuation provided that low actuation speed is not an issue.

Corrugated metallic electrodes

Corrugated electrodes use similar shapes to planar patterned devices; however, the metallic features are patterned perpendicular to the plane of the film Figure 9. This is achieved by depositing metal on to a designed micro-patterned surface. This alleviates challenges with electrode density while maintaining the conductivity and strain performance of planar patterning. Benslimane et al. [118] first introduced the approach for DEAs by coating a 110nm silver film on an elastomer film patterned with a quasi-sine wave optimised to achieve 30% strain before loss of conductivity through cracking. A device, consisting of two opposing actuators, was shown to achieve over 3 million cycles with minimum change in strain or actuation performance in this initial study.

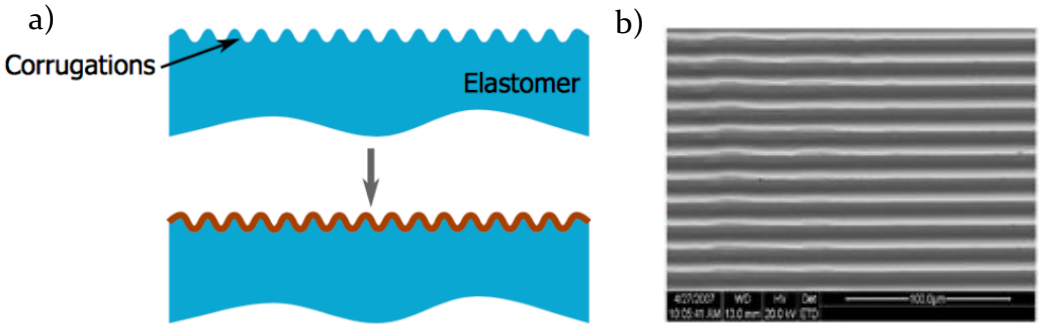

Figure 9 – a) Corrugated Membrane Actuator and (b) Factors affecting the surface and release properties of thin polydimethylsiloxane films [119]

The manufacturing technique has since been refined and scaled by Danfoss PolyPower, where the corrugation profile was further optimised to achieve a 4.5x reduction stiffness and an increase in maximum strain to 80% [120]. Numerical modelling has shown that corrugated electrodes are 810ox less stiff than planar counter parts. Push actuators capable of 3% linear strain, 6N/cm^2, and sub-10ms response times were produced by rolling films to produce push actuators [121]. Corrugated electrodes retain many of the anisotropic characteristics of planar

patterned electrodes but overcome the challenges with electrode density. The compromise is in manufacturing complexity and expense due to the requirements for micro-structured moulds and back-to-back lamination (Section 2.4.3).

Out-of-plane buckled electrodes

Out-of-plane buckled electrodes are conceptually and visually similar to corrugated electrodes as they achieve improved elasticity by patterning the conductive layer on a plane perpendicular to the film (Figure 10). Buckled electrodes, however, reduce the anisotropy by randomly orientating the corrugations. Creating a micro-mould to produce randomly orientated features would likely be prohibitively expensive at medium to large scales, therefore stretchable electrodes are produced by inducing buckled features in metallic coatings. To date, this has been achieved by pre-straining the elastomer and then depositing a metallic layer or by leveraging differences in the coefficients of thermal expansion for elastomer and metallic materials.

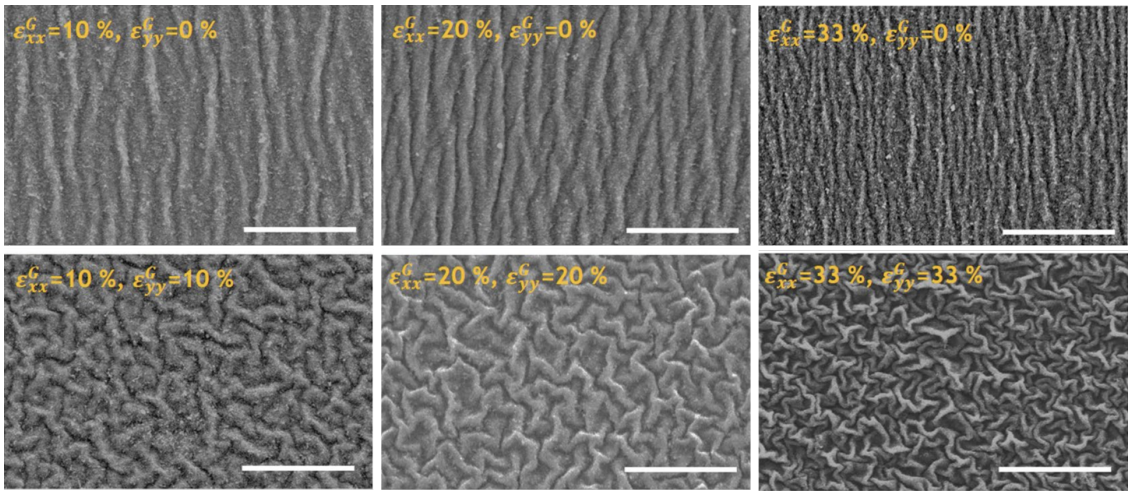

Figure 10 - Out-of-Plane Buckled Electrode (Surface Modification of Anisotropic Dielectric Elastomer Actuators with Uni- and Bi-axially Wrinkled Carbon Electrodes for Wettability Control) [122]

When relying on the thermal expansion of elastomer substrates, precise and uniform control of the amplitude of the patterned features is difficult to achieve as it is dependent local thermal stresses. The application of a 10-20% pre-strain before deposition of a 25nm gold layer produced electrodes with an 8.4µm wavelength and 1.2µm magnitude. The electrodes could withstand strains up to 28% and maintain a stable resistance over 100 cycles.

Jun et al. [122] built on this work produce functional DEA devices. In their work, uniaxial and biaxial pre-strain was used to produce anisotropic and isotropic devices, respectively. The DEAs were able to produce areal actuation strains of 30%. In this work, they actuated the DEA to dynamically change the wettability of liquids on the surface of the actuator as it altered the structure of the surface. There has been a relatively small body of work investigating this technique since it is largely incompatible with conventional microfabrication technologies as it requires removal from a common substrate [83].

2.3.3 Ion gels

All of the above work relies on conventional electronic conductivity using metallic or carbon elements, which has led to challenges in resistance, hysteresis, increased stiffness, or limited electrode durability. Furthermore, metallic elements present application specific hurdles due to a lack of biocompatibility. Ion-gels – ionically conductive liquids that are immobilised within a polymer matrix [123] – have gained popularity as they provide more stable resistance response while providing opportunities for novel behaviour, such as self-healing, extreme softness, and transparency .

In soft robotics, Keplinger et al. [124] demonstrated that an ion gel can maintain lower resistivity per unit stretch when compared to SWCNT or graphene coatings and, in a uniaxial strain test, an acrylamide-sodium chloride ionic skin developed by Sun et al. [37] could withstand strains up to 600%. While doing so, the capacitance was found to increase linearly with strain and a number of sensing applications were presented. The culmination of these works led to the development of an acrylic elastomer ion gel DEA that could actuate at frequencies of 20kHz and achieve strains >150%. As a demonstration of the technology, the researchers created an optically transparent loud speaker that recreated Edvard Grieg's Morgenstimmung [124]. A number of other publications using the more stable response of ionically conductive liquids have been demonstrated for sensing in soft robotics [15, 36].

In a recent paper, a self-heling elastomer actuator using ion gel electrodes was presented [125]. This effect is of great benefit for any device, but for technologies that are aimed at wearable, assistive devices this could be a significant

development in ensuring their longevity. In the figure below, it can be that the self-healing ionic conductor is able to repair a cut and actuate following a 24-hour healing time at room temperature.

Problems with this type of actuator are typically related to the thicknesses of the electrodes themselves: in Keplinger's initial work, the hydrogel electrodes were 100μm. This is significantly thicker than elastomer actuators produced by many other groups and means a single unit DEA has a total thickness of 1.2mm: 100μm for each electrode and then 1mm from the dielectric layer. To achieve the reported area strain (>150%), the applied voltage was ~18kV. If this technology was to be scaled for larger actuators, the electrodes would likely be on the same size scale as the dielectric. The passive nature of the electrode means the total device strain would significantly lower than currently reported. Although promising in terms of flexibility, transparency, sensing capabilities, and self-healing; this technology currently faces serious challenges for application in film based soft robotics. Improvements in processing to allow fabrication at smaller scales, could be a significant step forward for the technology.

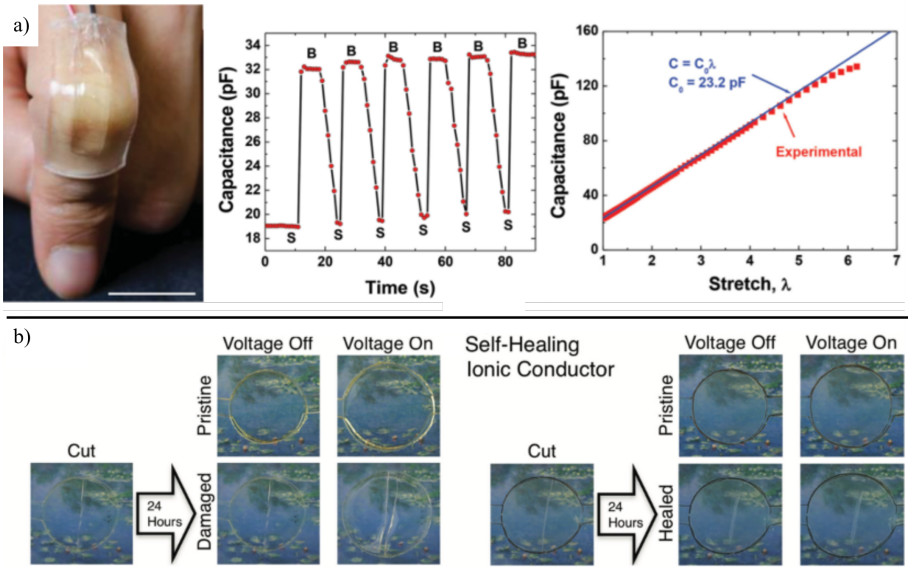

Figure 11 - Self-repair of Ionic Conducting Electrodes [125]

2.4 Manufacturing of thin film soft robotics

Soft films have widely been produced using techniques borrowed from the thin film electronics industry, with screen printing and spin coating being the predominant technologies. Although useful for initial proof of concepts, they have been shown to be limited in their scalability, manufacturing throughput, and ability to produce multilayer devices. Furthermore, most processes are bulk film coating techniques that significantly design freedom. Vacuum based processing shares similar challenges, while also introducing hurdles with processing speed. Thin film techniques that rely on transfer printing showed some early promise, but limitations on layer thickness and capital expenditure have proven restrictive for exploratory, low technology readiness research. The following section reviews manufacturing processes for film based soft robotics.

2.4.1 Spin Coating

In spin coating, a volume of material is placed at the centre of a substrate that is spun around its vertical axis. Centrifugal forces cause radial flow and gradual thinning of the material on the substrate [126]. If centrifugal forces overcome the opposing viscous and surface tension forces, material is ejected from the substrate. The ubiquity, simplicity and short turnaround time of spin coating have made it an attractive batch manufacturing technique for soft films.

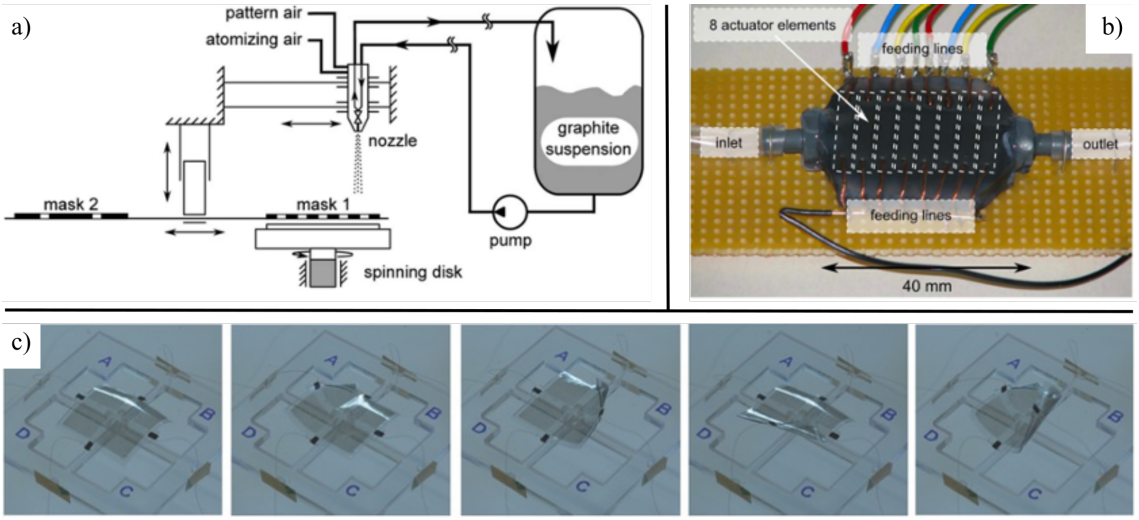

Figure 12 – a) Spin coated multi-layers DEAs, b) Peristaltic Pump based on Spin Coated DEAs [88], & c) Multilayer Dielectric Elastomers for Fast, Programmable Actuation without Prestretch [127]

Elastomer precursor solutions are often viscoelastic materials that exhibit shear thinning behaviour and spin coating procedures are less well refined than commercially available, Newtonian photoresists. Most soft robotics research labs have developed their own spin profiles with minimal reporting of film characterisation, experimental procedure, and repeatability. As a rule of thumb, spin coating PDMS, or other viscoelastic materials, requires lower spin speeds but increased spin duration when compared to Newtonian fluids. The lack of volatile solvents in PDMS compared to photoresists means reliable models can be built that can lead to reliable micro-scale PDMS films when combined with in process metrology [128].

PDMS surface coatings with thicknesses as low as 30nm have been produced using precursors heavily diluted in toluene [129]; however, these approaches have primarily focussed on biocompatible coatings and limited investigation in to the mechanical properties of films, multi-layer devices, or the effect of solvent have been conducted. The elastic modulus has been shown to be highly dependent on the thickness of the films when the layer height is less than 200μm. Liu et al. [130] demonstrated a nearly 5-fold increase in elastic modulus as the thickness of film decreased from 250μm to 30μm. In their work, they attribute the sharp increase in modulus to the shear stresses induced during spin coating.

Lotz et al. [27] first presented spin coating as an effective technique for producing thin film soft robotics. By combining spin coated silicone elastomer (Elastosil P7670) layers with masked aerosol deposition of graphite electrodes, they developed a technique that could reliably produce DEAs. They ultimately showcased their approach by producing a soft, DEA driven peristaltic pump and a capacitive touch sensor mounted on a coin [88]. Although elastomer films with thicknesses a low as 3μm were produced, functional actuators required films thicknesses of 20μm.

More recently, work from David R. Clarke's and Robert J. Wood's laboratories at Harvard have used spin coating to underpin their work on modular and rolled dielectric elastomer actuators. Spin coating of PDMS (Sylgard 184, 1:40), silicone elastomers (Ecoflex 0030), or a blend of the two in combination with pad printing/stamping of carbon nanotubes [131] (Section 2.4.2) has led to a number

of novel demonstrators. Their first work created a free-standing, 'multi-morph' film that can bend, twist, and distort. Subsequent publications have demonstrated muscle like actuation [132] and flight of a microrobot powered by soft elastomer actuators [131]. The thickness of their spin coated elastomer layers were reported to be ~30μm [127].

Spin coating is attractive for stacked devices as it removes the requirement for handling thin, delicate films as many layers can be produced before removal from a substrate. Lotz et al. [88] claim that the spin coating approach allowed the production of devices with up to 100 layers. Although no explanation is provided, this limit is likely imposed polymer becoming unstable on the spin coating platform and reduced manufacturing yields for devices with a high number of layers. In a stacked arrangement, breakdown or insufficient coverage of an elastomer layer will cause they entire stack to fail. Therefore, increasing the number of layers significantly reduces manufacturing yields. Commonly, reduced sized stacks (25-50 layers) are produced and then assembled to produce larger actuators. Such a method is used by CTSytems, a spin out from the Swiss Federal Laboratories for Materials Science and Technology, to commercialise DEAs [25, 133].

A key challenge for widespread commercialisation of DEAs using spin coating is the speed of manufacture. Existing approaches take anywhere from 20 seconds to a couple of minutes to produce an individual silicone layer of ~30μm. Building devices with sufficient stroke length will be time prohibitive especially as spin coating only covers substrates of a limited size. In addition, if the low voltage operation (<24V) is to be achieved, an order of magnitude decrease in film thickness needs to be realised [134]. Existing work suggests that a two-fold decrease in thickness requires a 4-fold increase in spin time [128]. As an increased number of layers will be required for an equivalent stroke length in ultra-thin film DEAs, manufacturing timescales will become prohibitive beyond low-volume laboratory scales.

2.4.1 *Blade casting of Elastomers*

Blade casting (tape casting or doctor blading) uses a blade set at a well-defined height to drag layers of material across a substrate (Figure 13). Its application to silicone elastomers has been pioneered by Prof. Herbert Shea's group at École Polytechnique Fédérale de Lausanne (EPFL), where it has been used to produce elastomer films for sensing, power generation, and actuation devices. Their process first deposits a sacrificial layer of polyacrylic acid dissolved in isopropanol (5wt%) on to a polyethylene terephthalate (PET) substrate before casting a layer of silicone elastomer (Sylgard 186, Dow Corning). Application of polyacrylic acid results in a 20µm wet layer that evaporates to 1µm. Using the same universal applicator, a layer of PDMS can be applied and left to cure for 30 minutes at 80°C.

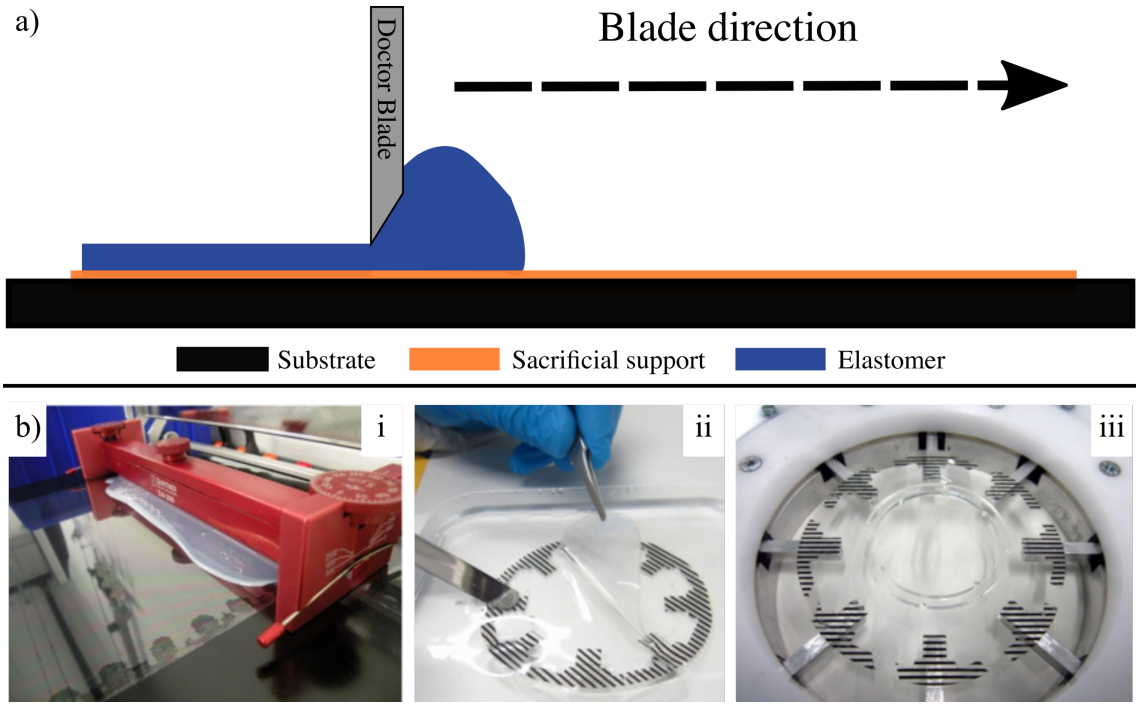

Figure 13 - Universal Applicator used in the Screen Printing Technique [135]

The thickness and uniformity of silicone films is dependent on the distance between the blade and substrate (blade gap) and the speed of the applicator. At a 50µm effective blade gap and 1mm/s blade speed, 20µm layers have been demonstrated; however, the films exhibited a large variance across their width due to manual setting of the blade height. Increasing the blade gap to 100µm led to increased thickness (~40µm) but reduced variation to approximately ±1µm.

Further increase to the blade gap led to 'wavy' films due to solvent evaporation [29].

To produce DEAs, the silicone films were attached to acrylic frames using a pressure sensitive adhesive. The PET film was then removed by submerging the assembly in to boiling water. A 30% pre-stretch is applied, which reduces the thickness to ~34.5µm, before electrodes are pad printed on to the film. The final devices have been shown to achieve ~10% actuation strain from voltages of 3.6kV [59]. This approach has been used to make biological cell stretchers [59, 136], rotary motors [137], grippers [5], and tuneable lenses [138].

Current blade casting techniques are unable to produce multi-layer stacked structures, have limited manufacturing throughput, and cannot fabricate layers thinner than 20µm. Furthermore, device demonstrations using this method have all required pre-strain to achieve practical application. Screen printing – a related process that introduces a mask to selectively apply material to a substrate – has been more widely investigated for the application of conductive features [139, 140]. However, since the process still struggles to produce sub-micron layers, its primary application is likely to be in sensing networks, rather than actuation or energy harvesting.

2.4.2 Pad Printing

Pad printing (tampography) is used for the transfer of two-dimensional patterns from flat templates (cliché) to more complex three-dimensional substrates. A soft pad collects ink from the cliché and then deforms around the target substrate to create the desired pattern. The soft pad makes it viable for interacting with soft films, which can be prone to tearing when transferring ink using rigid transfer pads. The Soft Transducer's lab at EPFL have been the primary proponents of the technique for the production of electrodes [135] and silicone films [141, 142]. Manual versions have been applied more widely for electrode production [127].

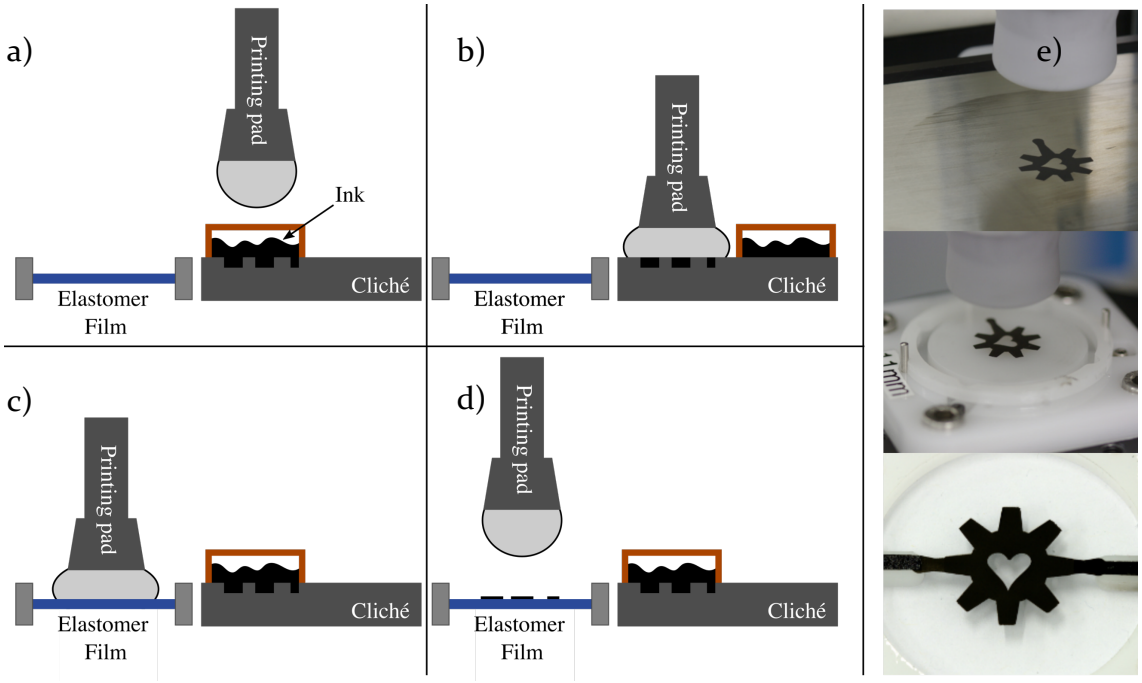

Figure 14 – a) Loading ink in to cliché, b) transfer of ink to pad, c) print material on substrate, d) remove pad from substate, & e)Fully Pad Printed Dielectric Elastomer Actuators [135]

When applying electrodes to pre-strained elastomer films pad printing has been shown to tear films with thicknesses below 20µm. Application of the electrodes to the elastomer films before removal from the rigid substrate provides mechanical support and can stop the films from tearing. Using a PET support, Poulin, Rosset, & Shea [142] printed electrodes on to elastomer layers with thicknesses as low as 1µm. This approach only allows patterning on one side of the elastomer and prevents the patterning of pre-stretched films; therefore, two films need to be assembled back to back to create viable actuators or capacitive sensors and limited pre-strain can be applied as it reduces the conductivity of the electrodes.

Pad printing elastomers is achieved by carefully controlling the rheology of the elastomer precursors as well as the contact pressure of the silicone transfer pad [143]. Achieving uniform layers required dilution (OS-2, Dow Corning) of the elastomers (Sylgard 186 & 184, Dow Corning; Silbione LSR4305, Bluestar Silicones) combined with a resting time of 30 minutes post deposition to allow elastomers to 'self-level'. Using pad printing to produce the elastomer and conductive features enabled the production of 3µm actuator that achieved 7.5% strain from an actuation voltage of 245V. The main challenge for this fabrication strategy is the inability to pattern multi-layer films and the secondary assembly processes reduces manufacturing yield by introducing opportunities for

imperfections such as dust and air ingress. Furthermore, the requirement of extended materials settling times (30 minutes) currently makes the process unfeasible for scale up.

2.4.3 Roll-to-roll transfer Printing

Gravure printing is a transfer printing technique that is used to produce low-cost, high volume products such as food packaging or wallpaper [144]. With manufacturing throughput at rates of up to 500m/min, the process is increasingly applied as an alternative method to produce high volumes of thin film electronic components [145]. A Danish company, Danfoss PolyPower, aimed to commercialise DEA technology by using the gravure technique to pattern large areas of thin elastomer films.

Gravure printing is a well understood transfer printing process. The complexity in Danfoss' system is caused by the rheology of the ink and the secondary elements required to produce a working actuator, particularly: the design of the carrier web, or mould; peeling the elastomer films from the carrier web; and laminating the sheets into multiple layers.

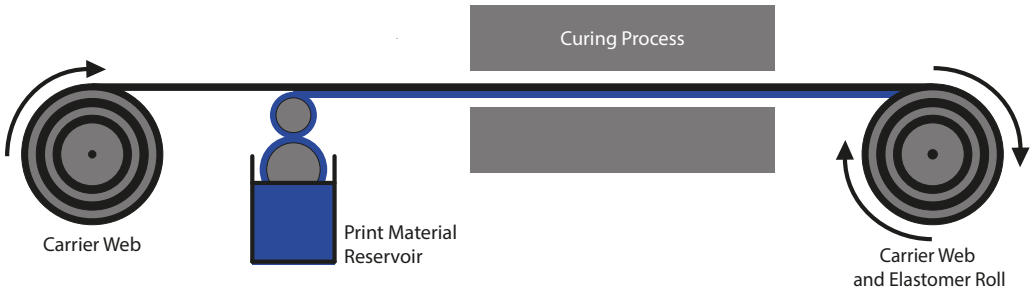

Figure 15 - Schematic of a Roll-to-Roll Gravure Printing Process

Production of Elastomer Films and the Carrier Web

The gravure process uses a series of rollers to transfer a liquid elastomer, Polydimethylsiloxane (PDMS), from a reservoir to a carrier web (Figure 15). The carrier web featured a corrugated surface profile allow stretchable electrodes. The elastomer then goes through a curing process, changing the elastomer from a liquid to a solid state [28]. The reported process used thermally (100°C) crosslinking PDMS elastomers; but it would be relatively trivial to use another curing process (e.g. Ultraviolet light) [146].

Once cured, the elastomer is peeled from the carrier web [146] to expose the corrugated geometry ahead of the electrode deposition [28]. The electrode deposition is a three-stage process: a plasma treatment to promote adhesion followed by a low and high seed rate Physical Vapour Deposition (PVD) (Vacuum Sputtering) [146]. Being a commercial attempt, specific details were hard to establish but in Vudayagiri's thesis on the process it is stated that 'silver, gold, nickel and alloys' can be deposited at thicknesses of approximately 100nm at a rate of ~36m/hour[28].

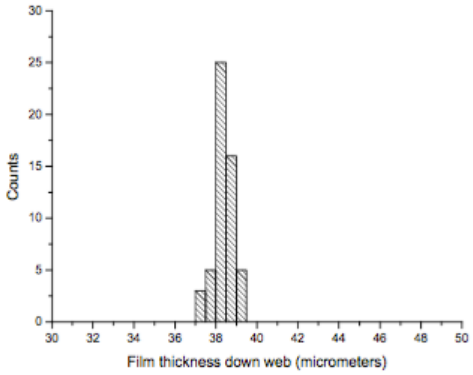

Figure 16 - Film Thickness of a Gravure Printed Elastomer [28]

The major criticism of this technique is that the corrugation pattern (electrodes) can only be manufactured on to one side of the elastomer film. Therefore, to create a functioning actuator two of these films need to be manufactured and then laminated back to back. A single layer of the elastomer is 39μm (Figure 16))[146], therefore the thickness of the assembled device will be 78μm. This drives the required actuation voltage up to the region of 2.5kV for relatively small stroke length device (Figure 17) (~1.2mm) [147].

A further implication of the secondary lamination step is that it provides an opportunity for the ingress if imperfections such as air bubbles or dust. The dielectric breakdown of air is in the region of 3V/μm, which is substantially lower than the PDMS films. These imperfections create sites in which dielectric breakdown, and therefore failure of the elastomer can occur.

The final point regarding the carrier web is its expense: the roll actuators produced using this technique require 7m of continuous dielectric laminate to produce a single actuator [147]. The carrier web must at least match this size while having micro-scale corrugation on its surface. No other roll-to-roll processes uses a similar carrier, therefore at this stage in the processes development each must be bespoke. This makes replacing, iterating, or experimenting with mould design prohibitively expensive for low TRL research [28].

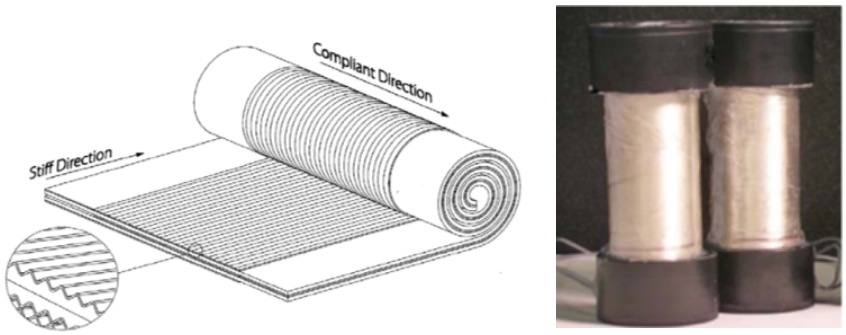

Figure 17 - Elastomers Produced using Roll-to-Roll Gravure Printing [28]

The bulk of the published work for this manufacturing process relates to the peeling, or release, of the PDMS elastomer films from the surface of the carrier web [28, 119]. The release of the elastomer from the carrier web is not a smooth process, despite the application of consistent pressure levels. When this is combined with the delicacy of the 39µm films, it leads to defects or splits in the elastomer[119]. Even when the films remain intact, variation in release force leads to spatially varying mechanical properties in the film due to the Mullins effect.

Vudayagiri [28] showed it is possible to decrease the required separation force by using additives or release agents. Experiments using additives were shown to negatively affect the properties of the dielectric layer by reducing the Young's Modulus of the material or by decreasing the voltage at which dielectric breakdown occurs. The use of a non-ionic release agent was shown to significantly lower the adhesive force from 118N/m to 2.8N/m without any apparent effect on the dielectric material itself. Despite this though, the production of a dielectric elastomer with an average thickness lower than 39µm has not been reported.

2.4.4 Additive manufacture

Additive techniques, those that selectively build three-dimensional structures in a layer-wise process, have driven recent advances in soft robotics [148, 149] and film-based structures are poised to be revolutionised through the same methodology. Work completed at EPFL's Soft Transducers Lab has shown the value of inkjet printing for soft devices and demonstrated an initial application in printed electrodes for DEAs. Their initial study on the deposition for seven elastomeric materials shows promise, but also highlights the limitation of the process when working with higher viscosity elastomeric inks. Similarly, commercial additive techniques have all faced similar issues when working with elastomeric inks: they either lack the spatial resolution or struggle to reliably process the materials.

Direct Ink Write

Direct ink write (DIW) (robocasting) is a material extrusion process that uses back pressure and controlled ink rheology to selectively extrude material (Figure 18a). Along with stereolithography [150], it has been a key driver in the advancements of printed soft robotics. Primarily, it has been used to produce pneumatically actuating structures with comparable performance to devices produced using soft lithography [151]. Multi-material DIW has recently enabled embedded sensing in soft robotics [15, 36, 152] and the first fully soft, autonomous robot [153].

Successful DIW requires the development of inks with the correct rheological response to printing. Inks are required to easily flow from the nozzle but then retain their shape once deposited on to a substrate. This response can be achieved by a sharp stress reduction, rapid solvent evaporation, polymerisation, phase change, or combination thereof [154]. For the shear-thinning viscoelastic polymers used in soft robotics, a sharp reduction in stress as the material exits the nozzle is most commonly used to transition the shear stress fluid below the yield point of the elastomer. Although the response from off-the-shelf materials may not be sufficient to limit material spreading, the inclusion of thixotropic additives can be used to increase the shape retention [148]. Furthermore, full curing of the deposited material can be used to increase the stiffness of printed

features through external heating (thermal cure) or increased humidity (moisture cure).

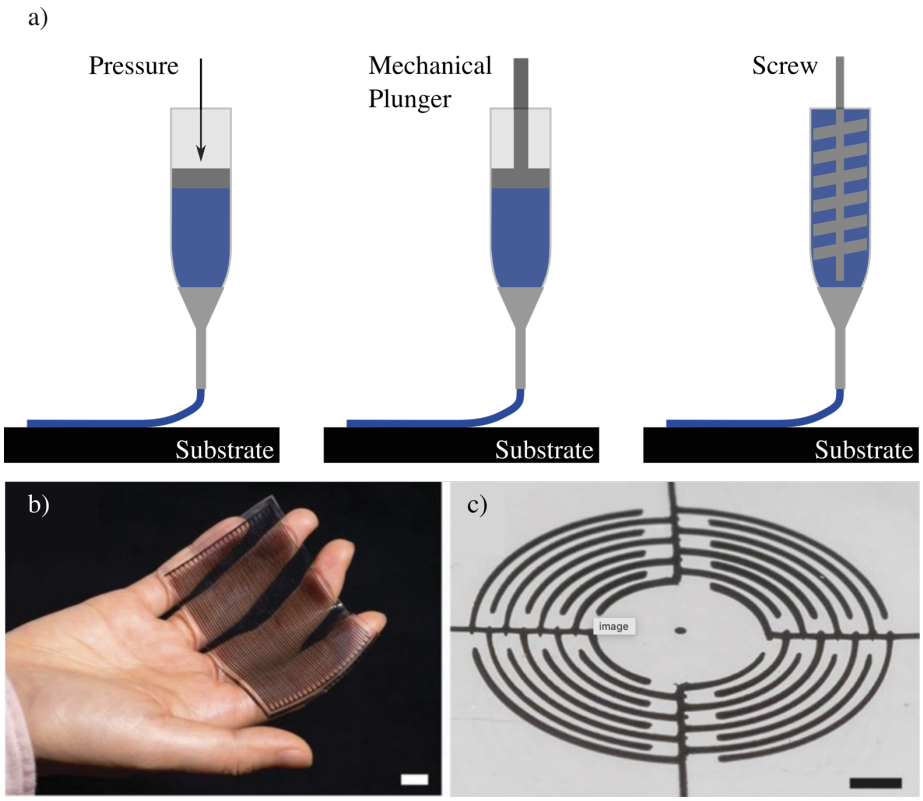

Figure 18 - 3D Printing of Interdigitated Dielectric Elastomer Actuators [157]

The resolution of DIW processing is limited by the size of the nozzles with most examples demonstrating minimum features of 10-250μm. Further reductions in nozzle orifices combined with rheology optimisation has driven smaller feature sizes; however, the additional empirical work and the inverse proportionality of nozzle diameter and print speed rarely justify the research time or expense. Multi-nozzle systems have been developed to increase throughput through voxelated printing [155] but fundamental limitations in nozzle density continue to plague the process. For functionally loaded materials, such as conductive elastomers, there are further challenges for the minimum feature size as they increase the likelihood of nozzle clogging. As a rule of thumb, Lewis [156] suggests that the nozzle orifice should be at least 100x the size of the building blocks of the ink.

For film based soft robotics, equivalent resolution but extended print times means there has been little motivation to explore application of the technology. Recently, however, the Lewis Group at Harvard have demonstrated how DIW can

allow DEA to be fabricated directly within 3D structures (Figure 18b-c) [157]. Using their approach, they can selectively orientate electrodes to introduce novel actuation modalities. The filament size (minimum feature) in this work was approximately 80µm from a 100µm nozzle. The demonstrated device could achieve actuations strains of 9% from an 25V/µm electric field. This work shows the first example how selective patterning of both the electrode and elastomer materials can be used to create novel actuation modalities.

Inkjet

Inkjet (IJ) printing selectively deposits droplets of build material to produce 3D structures (Figure 19). Commercial systems can be split into continuous jetting and drop-on-demand (DoD). Continuous IJ ejects a pressurised stream from a nozzle that breaks in to a series of droplets through surface tension effects (Plateau-Rayleigh instability) [158]. Acoustic vibrations are introduced into the fluid to provide consistent jet disturbances (perturbations) that lead to uniform droplet size and distribution. Droplets are electrically charged and deflected out of the print head towards the substrate using an electric field. Continuous IJ is best suited to higher volume manufacture as it can achieve high droplet ejection frequencies. Continuous jetting is vulnerable to ink contamination and requires greater material volumes, which can be prohibitive for high value inks [159].

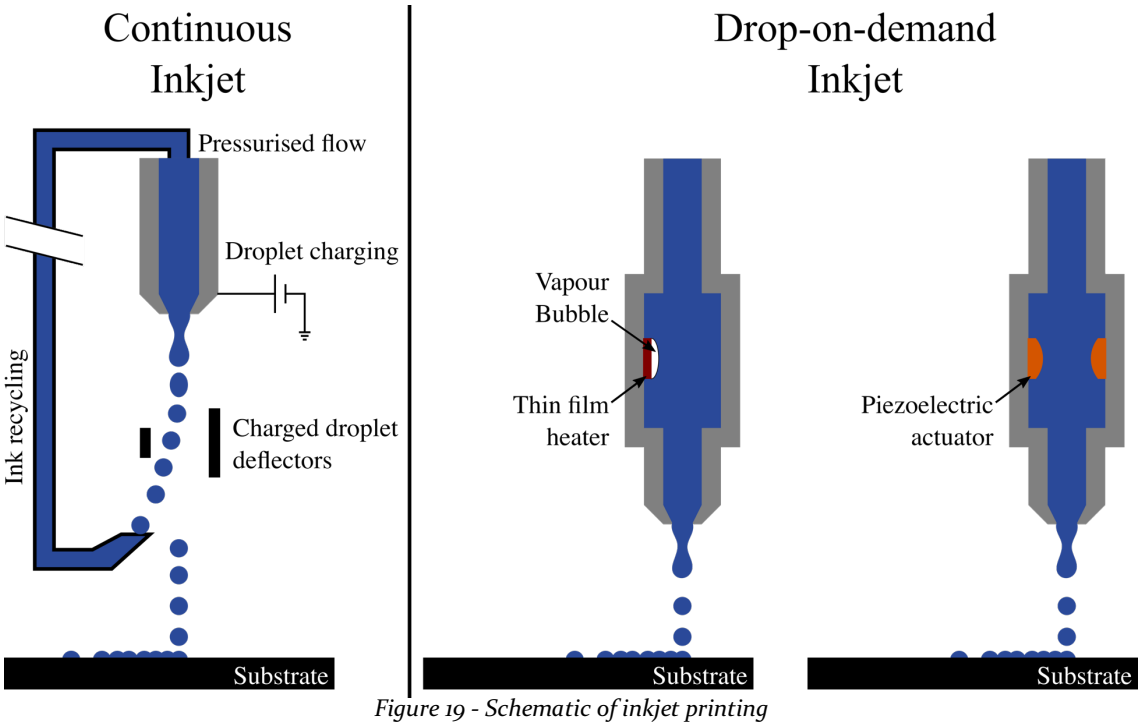

Figure 19 - Schematic of inkjet printing

In contrast DoD IJ, generates individual droplets, or droplet streams, as required using either piezoelectric or thermal print heads. Both techniques generate pressure waves within a reservoir to force the ejection of a droplet from a nozzle. Piezo print heads achieve this by mechanical actuation within the chamber [160], while thermal print heads rapidly heat the ink to produce vapour bubbles that increase nozzle pressure [161]. Thermal print heads are simpler and less expensive to produce; however, the ink must include low-volatility solvents that can be easily vaporised. Furthermore, heating of the ink can leave residue inside the nozzles that increases instances of nozzle blocking. Piezo print heads are more expensive to produce but have less restrictive solvent requirements. DoD typically produces smaller droplets and has greater spatial resolution when compared to continuous IJ [162] and is the technology most widely targeted for IJ of soft robotics.

As with all types of additive manufacturing, the greatest challenge for IJ-printed soft robotics is the development of suitable inks. For consistent patterning, droplets should be generated with no satellite droplets or significant tail. The maturity of IJ means that ink requirements are well understood and are characterised by the ratio of inertial to viscous forces (Reynold's number, Re); the inertial forces to surface tension (Weber number, We); and viscous forces to surface tension (Ohnesorge, Oh) [163]. For IJ, these are combined into the Z-number (Z) for printability:

$$Re = \frac{v\rho\alpha}{\eta}$$

$$We = \frac{v^2\rho\alpha}{\eta}$$

$$Z = \frac{1}{Oh} = \frac{Re}{\sqrt{We}} = \frac{\gamma\rho\alpha}{\eta}$$

Where, v, γ, ρ, η, and α are the velocity, surface tension, density, viscosity, and characteristic length (droplet diameter) of the ink, respectively. Inks with print numbers between 1-10 are typically found to be printable [164]. Low Z leads to viscous dissipation of pressure waves and high Z leads to a high number of satellite deposits. For functionally loaded inks, the rate of solvent evaporation

and particle-nozzle size ratio also need to be considered to prevent nozzle clogging [165].

Early application of IJ to soft robotics used commercial systems and materials that have a higher hardness than silicone rubbers or polyurethanes. Objet's (Stratasys) polyjet process, which uses IJ to deposit photocurable polymers, provided the Tango-range of materials that was used to develop simple fluidic [166, 167], combustion [168], and DEA [169] driven soft devices. Eventually, the carbon black filler in the Tango-black ink was found to exhibit sufficient conductivity for soft resistive sensing [170].

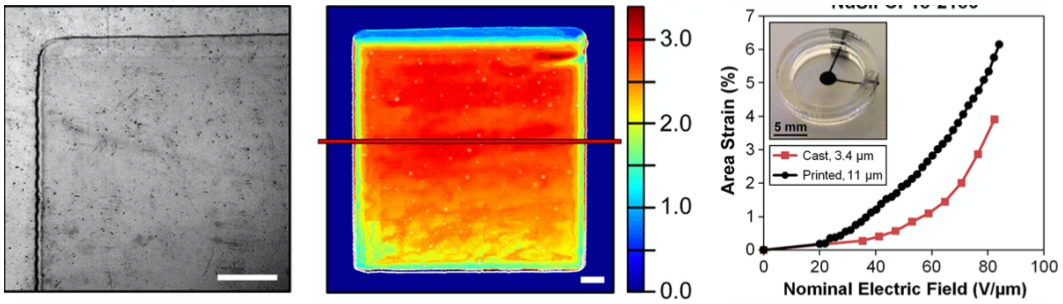

Figure 20 - Inkjet printed silicone film, and b) inkjet printed DEA and strain response [171]

Subsequent work targeted IJ printing of materials with hardness comparable to conventional soft robotics (Figure 20). A detailed study by McCoul et al. [171] investigated seven commercially available, UV-cure silicones for deposition through inkjet printing. All materials were diluted using OS-2 solvent (Dow Corning) so that the Z number fell within the calculated range for ink jet printing. Materials with low pre-dilution viscosity were found to achieve the best results and, through careful control of the ejection waveform, stable satellite-free drops could be deposited. Since the printed layers were sufficiently thin, diffusion mixing allowed the production of films using two-part materials. Nusil CF18-2186 IJ printed films were found to have increased performance (6.1% strain at 84V/μm) when compared to screen printed films (3.9% strain at 82.4V/μm).

The high viscosity of silicone elastomer materials presents a challenge for IJ and, even in McCoul's successful study, nozzle blocking and process inconsistency presents a challenge. Despite filtering the materials using a 1μm pore filter, the authors still report frequent nozzle blocking as a challenge for the process. Inkjet

printing has been most successful in the production of stretchable electrodes and its application in this area has been covered by a number of reviews [164, 172, 173].

Aerosol Based Direct Write

The first attempt at using aerosols as a technique to produce dielectric elastomer actuators was completed by Araromi et al. [174] at the University of Bristol (Figure 21). Their approach used an artist's airbrush to deposit aerosolised silicone (Dow Corning Silastic 3481) and conductive powders (Graphite) on to a rotating drum. Deposition from a static nozzle led to a Gaussian material distribution, which led to an uneven electric field distribution for completed films. Empirical investigation showed the material distribution could be improved by increasing the nozzle-substrate distance; decreasing the ink concentration; or by offsetting the nozzle between passes. Ultimately, the process produced an actuator with a strain of 3.4% from an actuation voltage of 4kV. Although the performance is limited compared to other work presented in this thesis, the use of a non-standard deposition arrangement and deposition mechanism has contributed towards more innovative approaches to soft film manufacture.

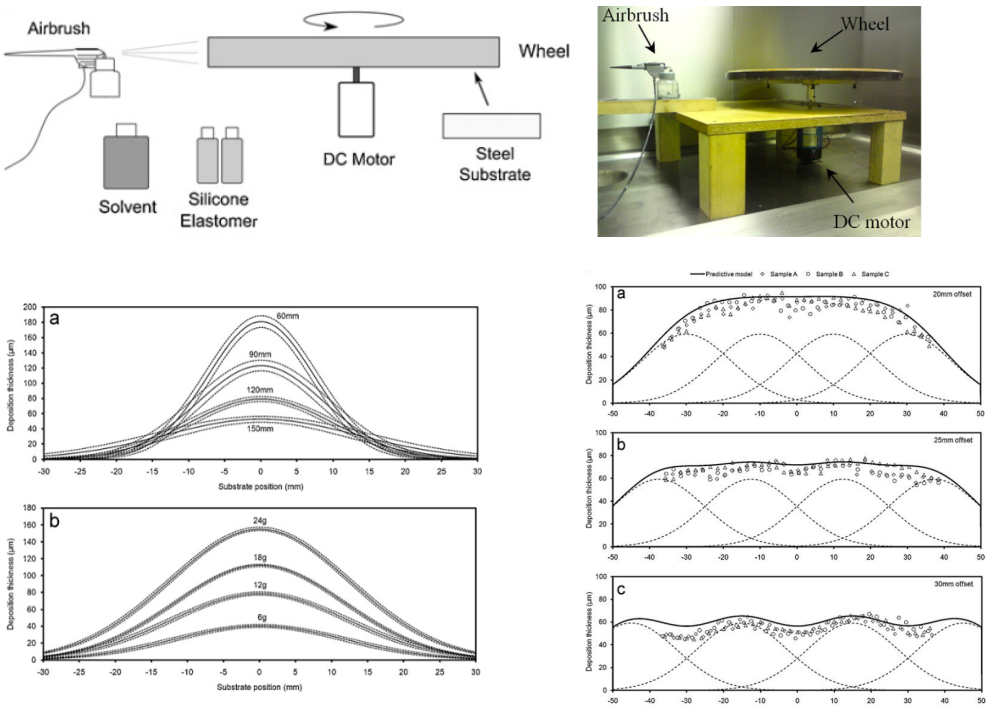

Figure 21 - Low-Cost Aerosolisation Equipment for the Manufacture of DEAs at the University of Bristol [174

Aerosol Jet Printing

Aerosol Jet (AJ) printing is a commercial aerosol based direct write technology sold and developed by Optomec Inc. that couples aerosol production with an innovative focussing mechanism to increase the resolution and uniformity of the deposit (Figure 22). The process can atomise materials with viscosities ranging from 1-1000cp and produce features with lateral resolution approaching 10µm and sub-micron layer thicknesses. A more comprehensive review of the technology is provided in Section 5 and a review paper, which was authored and published as a part of this body of work, can be found in Appendix A.

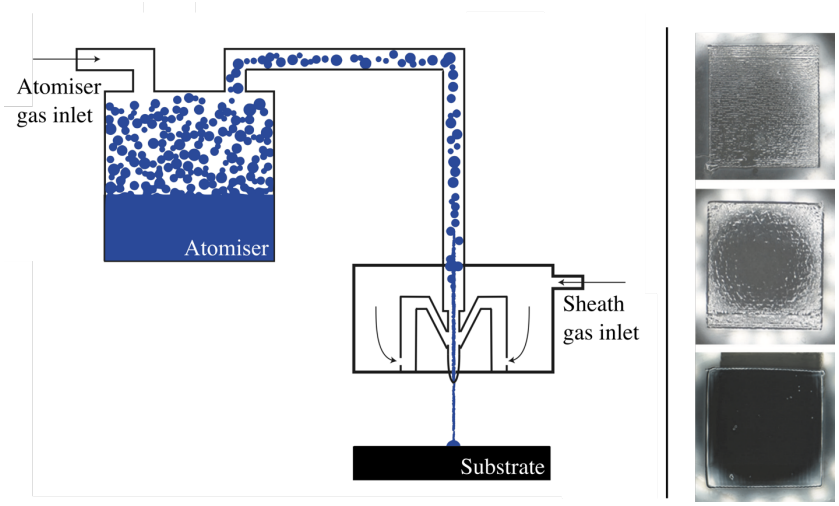

Figure 22 - Schematic of the AJP, and b) Aerosol-Jet-Printing silicone layers and electrodes for stacked dielectric elastomer actuators in one processing device [175]

The Factory Automation and Production Systems Research Group is currently leading the way for the Aerosol Jet Printing of DEAs [175]. They have shown the deposition of a two-part silicone material (Elastosil P760) using Aerosol Jet deposition. Their approach atomises the two parts separately and then combines them in a static mixer prior to ejection from the nozzle. This approach increases the print window by preventing material curing and allows elastomer layers to be printed in a single pass. This mixing method also introduces the option to control the relative flow to dynamically alter the composition of a printed composite. For two-part silicone elastomers, this could enable the production of components with spatially varying mechanical response. More interestingly, by selectively controlling the ratio of elastomer to functional filer content, monolithic devices

with variable conductivity can be produced. Outside of a soft robotics context, this has already been demonstrated for a CNT-filled polyimide structure.

2.4.1 Molecular beam epitaxy/vacuum processing

Molecular Beam Deposition (MBD) is a technique commonly used to produce high purity, structurally precise, ultra-thin films in the optoelectronics industry [176]. The process works by holding a purified powder, or liquid melt, in a crucible and heating the material between its sublimation temperature and chemical decomposition temperature. The chamber is held at an ultra-high vacuum which causes evaporation of the material. As the evaporated material moves through the chamber towards the substrate it is collimated by a series of small orifices. Eventually the material is deposited and grows as a continuous film[176].

This approach was the first to demonstrate that sub-micron DEAs could be successfully manufactured and maintain performance when compared to micron scale actuators. Topper et al. [177] produced, and actuated, a 200nm cantilever device that produce an almost identical bend radius to a 4µm, spin-coated actuator. Furthermore, the 200nm actuator achieved this from a driving voltage of just 12V compared to 800V for the more conventional DEA [177] (Figure 23).

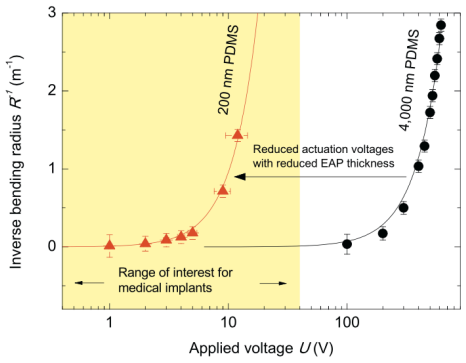

Figure 23 - Inverse Bending Radius of Cantilever DEAs Produced using MBD and Spin Coating [177]

The price for high purity, ultra-thin films is the time taken to complete a deposition and the limited patterning capabilities. The 200nm layer produced for this study took upwards of two hours to produce (Figure 24). The requirement for high vacuum conditions also makes this an expensive process to maintain. If a multi-layer actuator is ever to be produced using this manufacturing technology,

then it could take upwards of 10,000 hours to produce am actuator no larger than a couple of millimeters [178]. Realistically, if dielectric elastomer actuators are ever going to become a more widely adopted technology then a manufacturing process that can match the performance of MBD at a lower cost and at higher deposition rate will be required.

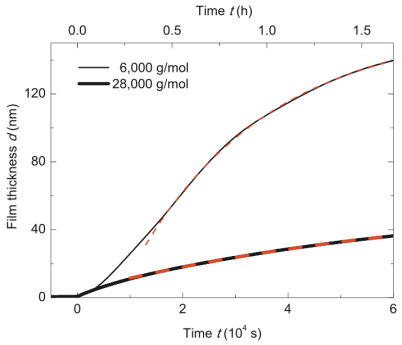

Figure 24 - MBD Layer Growth Times for Different Molecular Weight PDMS Films [178]

2.5 Summary and Process Specification

The literature review introduced thin film soft robotics, the materials used in their construction, and common manufacturing methods. It is clear that the translation of these robotic technologies from research laboratories to widespread practical applications still requires significant innovation in materials and processing. Spin coating, blade casting, and pad printing have all been used as effective batch manufacturing techniques for low-volume research; however, fundamental constraints in throughput mean they are unlikely to deliver products for widespread societal impact. Additive manufacturing faces similar challenges for high volume production although it provides novelties in design, actuator response, and mass customisation. Higher volume, roll-to-roll processes have been explored but are resolution limited and have a high fiscal barrier for entry that limits their development. In recent years, novel approaches, such as molecular beam epitaxy and electrohydrodynamic deposition, have begun to present possible pathways for improved performance and throughput.

2.5.1 Process Specification

This process specification outlines the ideals of a process that would improve the capabilities and viability of film-based soft robotics. Many of the targets within this section have been derived from, arguably, the most challenging aspect of soft

robotics manufacturing research: the development of low-voltage dielectric elastomer actuators. Other film-based technologies, such as e-skins, do not have the same requirements, particularly in terms of resolution and roughness of the printed films.

Material Compatibility

Current work in soft robotics is dominated by silicone elastomers, with options from Wacker, Dow-Corning, and Smooth-on regularly being used. These materials are purchased as two-part elastomer kits that are mixed and then cured through the application of ultraviolet light or heat. Processing two-part materials can be achieved through premixing followed by processing or by the sequential application of each part. If the two parts are applied separately, the layers must be sufficiently fine to allow mixing through diffusion. A viscosity compatibility of 0-1500cp should provide enough scope for these types of materials, as most of their viscosities can be modified to this range through the dilution or the addition of solvents. Therefore, any proposed fabrication strategy should be capable of processing these types of materials.

The significant interest in printed electronics means a number of techniques have already been developed that could be used for soft structures. Nevertheless, the technique proposed in this work should aim to be compatible with both particulate and solution-based inks, while also having a wide enough material compatibility to not limit material choice. Commercially available functional inks are typically aqueous or have low viscosity to ensure compatibility with IJ printing (1-15cp)

Solution Processing

Since soft robotics are built using polymeric materials, plastic processing techniques, such as casting and moulding, have the greatest prevalence within the research community. The relatively low-cost and barrier to entry of these techniques have been instrumental in the increased interest of the technique[179]. Furthermore, low-cost and immediate suitability for scale-up also help feed into the potential commercial interest for soft robotics. Solution based processes that still enable bench top manufacture with relatively low investment is important for a technology that promises to make robotics ubiquitous.

Transition to high-value manufacturing techniques will likely remove many of the advantages introduced through the application of soft structures.

The development of a technique that is obviously transferable to mass-manufacturing approaches, such as roll-to-roll or injection moulding, are perhaps most immediately appealing. It is also worth noting that previous work at Technical University of Denmark has shown that large scale template-based methods face severe fiscal limitations during the research and development stage. As such, they should also be avoided in this type of project.

Resolution

For the proposed impact areas, the critical resolution of the process is dependent on the function of the material. For the elastomeric structures the lateral resolution is of secondary importance to the axial resolution of the process. That is, control over the thickness of the elastomer layers is much more important than the ability to pattern the elastomer structures on a 2D plane. Particularly for dielectric elastomer actuators, a sub-1µm resolution is paramount for low voltage operation [134]. For this work, a target of 10µm, which is comparable to DIW and inkjet resolutions, is set. For lateral resolution, a 500µm has been set. This value is comparable to the state of elastomeric direct write and provides more design capabilities than film-based methods, such as spin coating.

For patterning functional inks, high lateral resolution is required to provide scope for increased sensor density. Also, since functional inks have a tendency to increase stiffness and are not active in artificial muscle applications, the thickness of the layers should be as fine as possible. The proposed targets in this work is 150µm and 1µm for the width and thickness, respectively. Both techniques should be able to maintain the aforementioned resolutions while enabling multilayer, patterned structures. The transition to multilayer structures will be essentials as the complexity of soft devices continues to increase.

Roughness

Low roughness films are important for the production of DEAs. A high roughness can create regions of greater electric field strength that can lead to premature

actuator failure. Determining an appropriate roughness target has been set by using the current capabilities of inkjet printing as a target.

Manufacturing Time

A key challenge for film based soft robotics is the time for manufacture. Again, this has been particularly evident in for DEA devices. Films produced using molecular beam epitaxy had a growth rate of 200nm/day, which makes commercial adoption unfeasible. A developed process should present a substantial increase on this while offering further opportunities for reduced production speeds. Printing based manufacture should aim to at least meet the current state-of-the-art printing techniques.

Cleanliness

Any developed process must be able to be locally contained to prevent the requirement for full cleanroom conditions. This will be paramount to reducing cost and ensuring commercial viability. Ensuring this can be achieved by minimising the requirement for the manufactured device to move between workstations.

2.5.2 *Table of manufacturing requirements*

Title		Requirement	Measurable
Material compatibility		Wide range of viscosities and ink types w/minimal nozzle clogging	1-1500cp with instances of nozzle clogging less than 1/hour of printing
		Multi-part materials	Must be capable of depositing and curing Sylgard elastomers (Y/N)
Solution Processing		Must not require special environmental conditions (e.g. Vacuum)	Y/N
Resolution	X-Y	Comparable resolution to state-of-the-art	500µm elastomer ink 150µm functional ink
	Z	Thin features	Sub-10µm features
Roughness		Comparable to state-of-the-art	Thickness std. dev <0.32µm
Manufacturing Time	Direct-write	Comparable to state-of-the-art	>=Inkjet print speeds
	Bulk Coatings	Comparable to state-of-the-art	Sub-1µm: >200nm/day
Cleanliness	Non-clean room process	Process must be able to operate without requirement of clean room	Y/N

3 Development of Apparatus

The literature review introduced film-based soft robotics, examined the materials used in their creation, and discussed common manufacturing techniques. Translation of the core actuation and sensing technologies requires innovation in process engineering as current methods are limited in their reliability, resolution, and/or speed of manufacture. The research presented in this chapter builds the fundamental work completed by Weiss et al. [178] at University of Basel who demonstrated the electrospraying technique for the production of thin elastomer films. Here, an automated experimental apparatus for investigating multi-modal electro-hydrodynamic deposition is developed. The chapter first introduces the three primary electrohydrodynamic deposition modes (electrospray, electrospinning, and electrohydrodynamic jetting) before discussing the challenges for the process and the apparatus design. The chapter will conclude by presenting initial results from the apparatus using aqueous polyvinylpyrrolidone (PVP).

3.1 Electro-hydrodynamic deposition for soft films

Electrohydrodynamic (EHD) deposition is a term for processes that use an electric field to charge, direct and deposit a material on to a substrate. This method has been recognised for over a century [180]; however, it has only begun to have direct industrial applications in the last couple of decades. EHD deposition encompasses three primary deposition regimes: electrospinning [181], electrospraying [182], and electro-hydrodynamic jet (e-jet) printing [183]. Most practical applications of EHD deposition have used electrospinning, which provides a low-cost method of producing fibres in the micro and nanoscale. The fibrous nature of the technique has made it invaluable in the production of high performance filtration systems [184], drug delivery [185], and tissue scaffolds [186].

The primary application of electrospray techniques has been in electrospray ionization mass spectrometry (ESI-MS) [187], where it is used as a method for converting ions in the liquid phase to the gas phase. Since its discovery, the technique has become a standard technique in analytical chemistry and its

creation won John B. Fenn and Koichi Tonaka the Noble Prize for chemistry in 2002. In manufacturing, electrospray deposition is increasingly being investigated for film based devices, such as photovoltaics [188], that are geometrically and fiscally limited by vacuum-based manufacturing.

E-Jet printing is the most recent technology and has been described as the convergence of electrospinning and additive manufacture [189]. In electrospinning, fibres are randomly orientated due to inflight instabilities that cause whipping effects. Although techniques have emerged to increase fibre alignment, true spatial control for more complex patterning remains a challenge. E-Jet overcomes this by depositing material before the whipping or spraying instabilities can arise. Coupling this with computer controlled articulation of a collection plate allows feature resolutions that surpass more established additive techniques [183]. Again, much of the pioneering work in this area has focussed on structured cell culture scaffolds, however it has the potential to revolutionise micro- and nano-manufacturing by offering a low-cost, cleanroom-free alternative to lithographic processing [190].

3.1.1 Process Overview: liquid droplets to Taylor cones

A spheroidal meniscus (Figure 25a) will form when a small volume of liquid is ejected from a nozzle under normal conditions as the surface tension is the principal force dictating its shape. As the volume of liquid grows, gravity will become increasingly influential and droplets will start to fall from the nozzle.

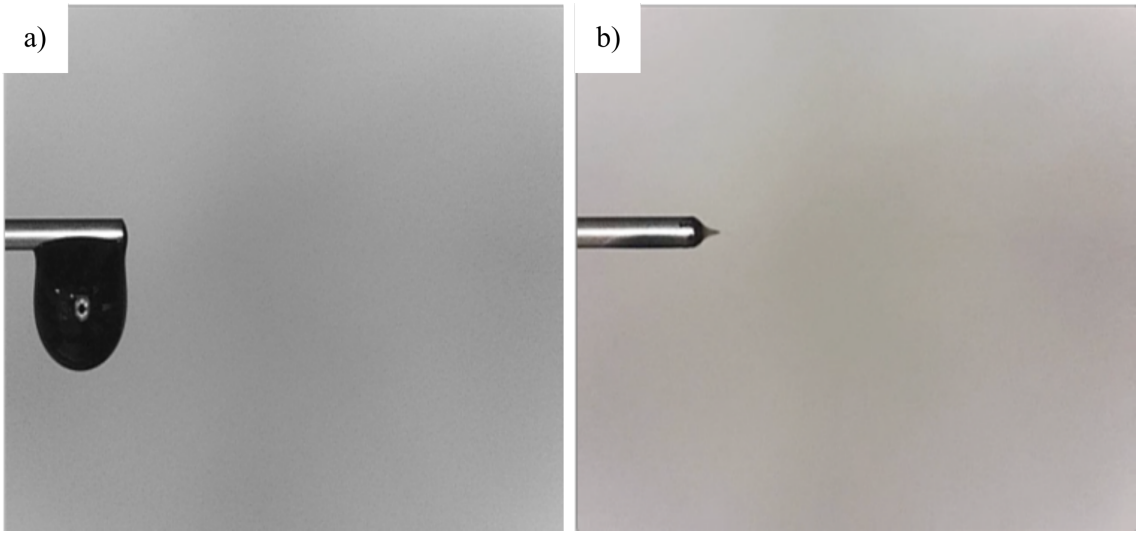

Figure 25 - a) liquid meniscus under no electric field and b) Taylor Cone formation under a high electric field

Electrical charging of the liquid can alter this behaviour as charge interactions become the predominant factor effecting the structure of the fluid. Beyond a critical charge, the spheroidal meniscus is pulled in to a conical shape (Figure 25b) referred to as a Taylor cone [191]. The apex of this cone emits a micro-jet that is used in all of the EHD processes.

Despite conceptual simplicity, cone formation is heavily dependent on the characteristics of the working fluid. Lee et al. [192] produced a useful study of the parameters effecting electrohydrodynamic deposition, where they identified 10 variables – density (ρ), viscosity (η), surface tension (ɣ), permittivity of free space (ε_0), permittivity of the fluid (ε'), conductivity (K), nozzle diameter (d), nozzle-substrate distance (L), fluid flow rate (Q_s), and applied voltage (V_a) – that determine the electro- and fluid dynamics of an EHD system. By applying the Buckingham π method, these parameters were broken in to six dimensionless variables (Table 4) that govern the process.

Table 4 - Dimensionless variables governing electrohydrodynamic deposition

Dimensionless Group	D_1	D_2	D_3	D_4	D_5	D_6
Expression	$\frac{\varepsilon_0 \varepsilon' Q_s}{KLd^2}$	$\frac{(\gamma^2 \rho \, \varepsilon_0 \varepsilon' / K)^{1/3}}{\eta}$	ε'	$\frac{d}{L}$	$\frac{\rho K Q_s}{\gamma \varepsilon_0 \varepsilon'}$	$\frac{V_a \sqrt{\varepsilon_0}}{\sqrt{\gamma d}}$
Notation	$\frac{T_q}{T_h}$	χ	ε'	$\frac{d}{L}$	α	β
Physical representation	*Jetting system*	*Material properties*		*Geometry*	*Process conditions*	

The first of these (D_1), which is the ratio of the characteristic time of charge transport (T_q) to the characteristic time of fluid supply (T_h), determines whether the deposition occurs in the classical electrohydrodynamic regime or a more recently described non-classical regime, known as an electrically forced jet [193]. High conductivity liquids, which operate in the classical EHD regime ($T_q/T_h < 1$), undergo a number of deposition regimes (Figure 26) depending on the magnitude of the applied voltage and flowrate for a given apparatus geometry. As discussed above, the first dripping mode occurs when surface tension and gravity are the predominant forces acting on the fluid. In the pulsating mode, a cyclic

imbalance occurs between the surface tension and electrostatic forces, which results in a difference in flowrate between the fluid supply, Q_s, and the micro-jet output. Increasing the magnitude of the electric field, corrects this imbalance to achieve the ideal cone-jet mode. The tilted-jet results from further increases as imbalances are re-introduced. Beyond this point, multi-jet regimes begin to occur in an attempt minimise energy through an increase in surface area.

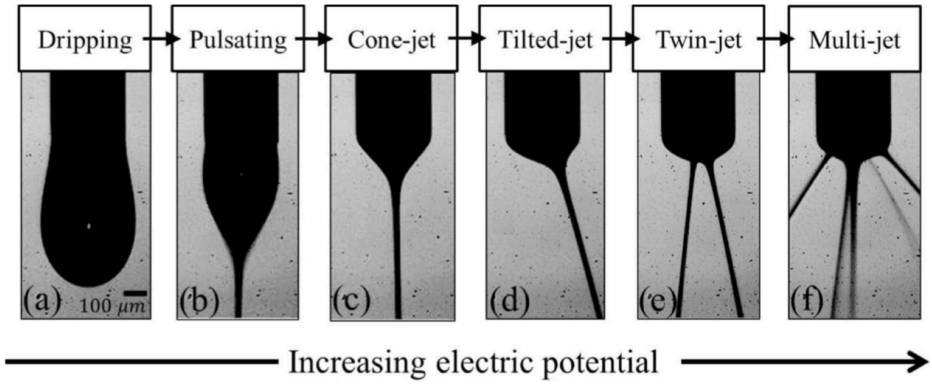

Figure 26 - Jet evolution with increasing electric potential [191]

When $T_q/T_h > 1$, the structure of the charged liquid shifts from the traditional cone-jet to a ball-jet [193]. In these cases, where the electrical relaxation time is greater than the hydrodynamic time, surface charge at the air-liquid interface does not exist which prevents the occurrence of the electrohydrodynamic jetting system. In these cases, the electric field and flow rate combine to induce an acceleration in the liquid that ejects a bead from the bulk liquid [194]. In practice, the primary consequence of the electrically forced jetting mode is increased feature size when compared to the classical jetting mode.

3.1.2 Process Overview: Fibres, Films and Direct-Write

Emission of the microjet is the starting point of all three of the common EHD processes. Variation in morphology is largely influenced by the material's behaviour in-flight; therefore, the properties of the deposit are dependent on the properties of the ink, the spatial relationship between the nozzle and the substrate, and the applied electric field. The key determinant between the three regimes is whether the ink remains as a jet or breaks into discrete droplets.

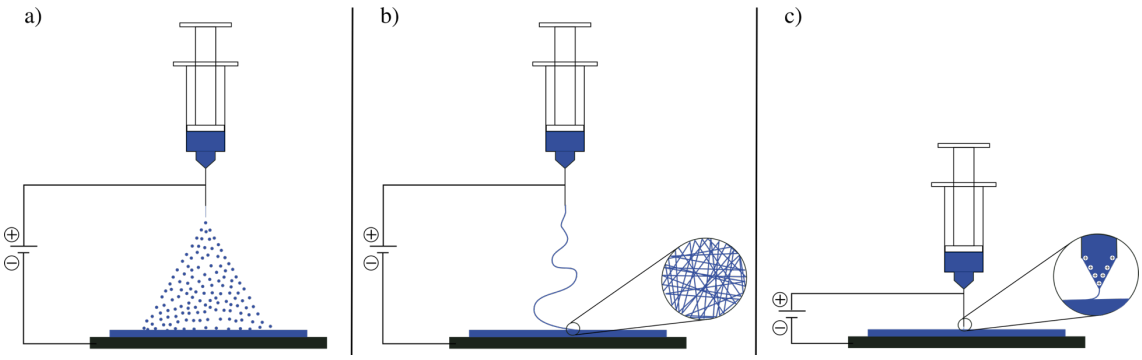

Figure 27 - Electrohydrodynamic deposition modes: a) electrospraying, b) electrospinning, and c) e-jet printing

Stable jet formation is achieved when any unstable perturbations are convected downstream faster than they can travel upstream (Plateau-Rayleigh instability) [195]. Growth of perturbations leads to the break-up of a liquid jet and forms the basis of electrospray deposition (Figure 27a). Perturbation growth is driven by surface tension for fluids with low Ohnesorge numbers; however, charge interactions become more influential for higher values [196]. Newtonian fluids - such as water, organic solvents, and dilute solutions or suspensions in those solvents – typically undergo jet break up if there is sufficient time of flight.

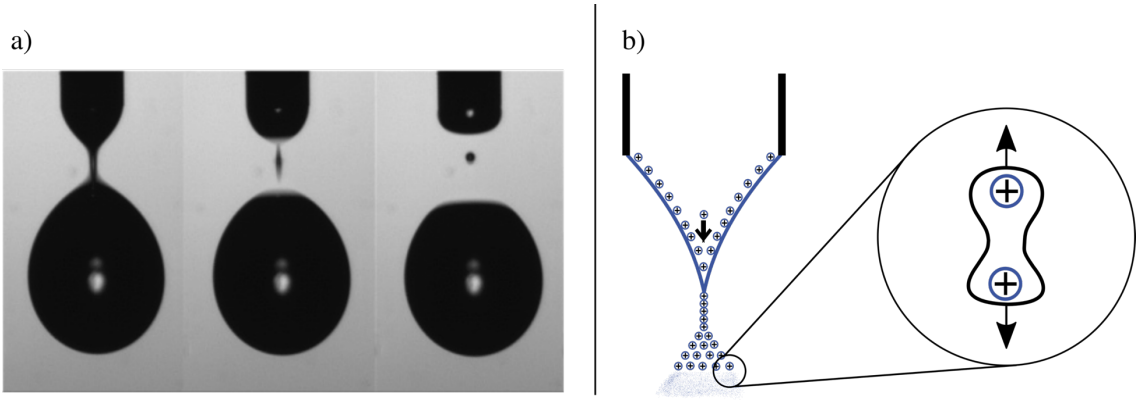

Figure 28 - a) Main and satellite droplets and b) coulombic fission in electrospray deposition (Charged Satellite Drop Avoidance in Electrohydrodynamic Dripping) [197]

This process often results in a bimodal distribution of droplet sizes through the production of large *'main'* and smaller *'satellite'* droplets (Figure 28a) [197]. Main droplets are produced at jet swells, whereas satellite droplets form as the jet necks down (Figure 28). After initial jet break-up, repulsive charges within droplets can lead to further droplet separation through Coulombic fission (Figure 28b). Through this electrospraying process quasi-monodisperse micro- and nano-droplets can be formed.

Viscoelastic fluids, such as polymer melts and high concentration polymeric solutions, are able to counteract the effects of surface tension and resist droplet break-up [198]. Chain entanglement – overlapping or interlocking of physical polymer chains - allows the material to remain as a continuous stream and produce a fibrous deposit through electrospinning (Figure 27b). The diameter of fibres can be reduced by altering the ink or by adjusting the process parameters Approaches centre around increasing the force provided to elongate fibres (voltage [199], conductivity [200]), decrease the resistance to elongation (viscosity [201]), or increase the time of flight (electrode-collector distance [202]).

Viscoelastic and Newtonian inks can be used for electro-hydrodynamic direct write (Figure 27c). The emission of material is achieved in the same manner as above, but the time in flight is significantly reduced by minimising the distance between the deposition head and substrate. The spatial resolution, deposition mechanism, and deposit morphology are still dependent on rheological differences and machine layout. For high-viscosity polymeric solutions, EHD direct write is often referred to as near-field electrospinning [183]. In this process, continuous fibres are deposited and the related effects of the whipping instability are visible in the deposit (Figure 29). Although fibres with sub-micron diameters can be deposited, the instability limits the spatial resolution of the deposit. These can be minimised by high-speed actuation. In contrast, low-viscosity fluids can be deposited as discrete droplets in a similar manner to common ink jetting techniques, which maintains minimum feature size while improving the spatial resolution [203]. However, this performance is usually achieved at the expense of process throughput.

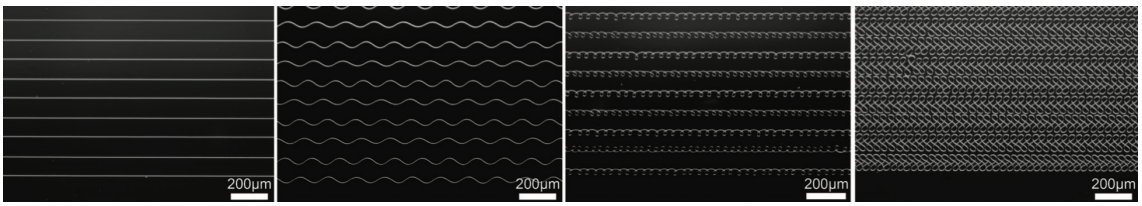

Figure 29 - Fibre pulsing in near-field electrospinning (Fibre pulsing during melt electrospinning writing) [183]

3.1.3 *Challenges for Electrohydrodynamic Deposition*

Multi-layer deposition: Build-up of Substrate Charge

Most common EHD apparatus rely on the application of a direct current (DC) source to drive a fluid towards a grounded substrate. Upon impaction, charge within the material dissipates through a grounded electrode to maintain the potential difference between the deposition head and the substrate. If low-conductivity or insulating substrates are used, then the time taken for charge dissipation can become greater than the rate of substrate charging. When this arises, interaction between incoming material and residual substrate charges can lead to a loss of resolution or process inhibition (Figure 30).

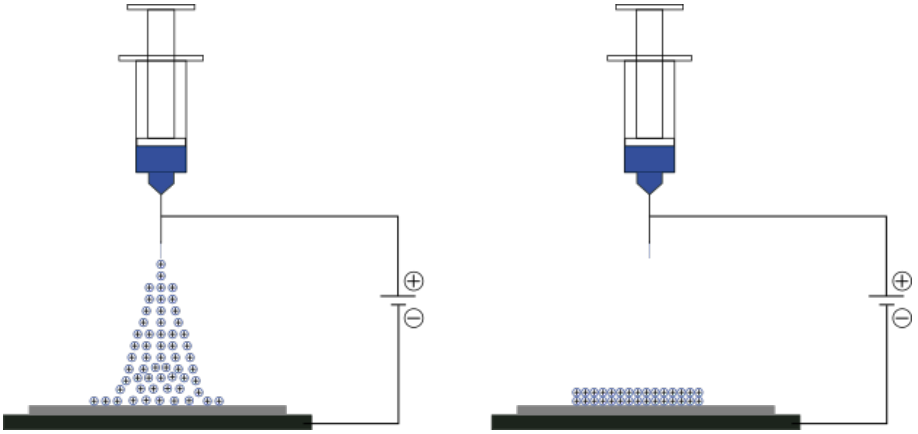

Figure 30 - Spray inhibition during Dc electrospray on to insulating substrates

This phenomenon can also arise when the deposited material is insulating [204], irrespective of the type of substrate used. If the deposited ink behaves as an insulator, it will eventually impede the route to ground for subsequent droplets. In practice, this places a limitation on the depth of features that can be produced using EHD techniques. Although the thickness of the films targeted in this work are small, this effect will likely present a challenge when transitioning to multi-layer structures.

Brown, Gladstone, and Chariot [205] investigated the evolution of polystyrene nanoparticle deposits during DC electrospray. By observing the development of nanoparticles during the early stages of deposit in DC electrospray through dark field microscopy, they were able to draw conclusions about the influence of residual charge and Coulombic interactions [206]. They discovered a bimodal

distribution in the spatial positioning of particles over time (Figure 31). This was explained by suggesting that early in the deposition (a) the particles were deposited centrally as it is the minimum path to the ground. After some time (b), charge begins to build in the central location and pushes the droplets radially through Coulombic repulsion. After more time (c), the central charge dissipates allowing droplets to once again be deposited. This could also coincide with repulsion from charges in the outer region. After more time (d), the deposition will become densely populated, but may not yet be completely uniform.

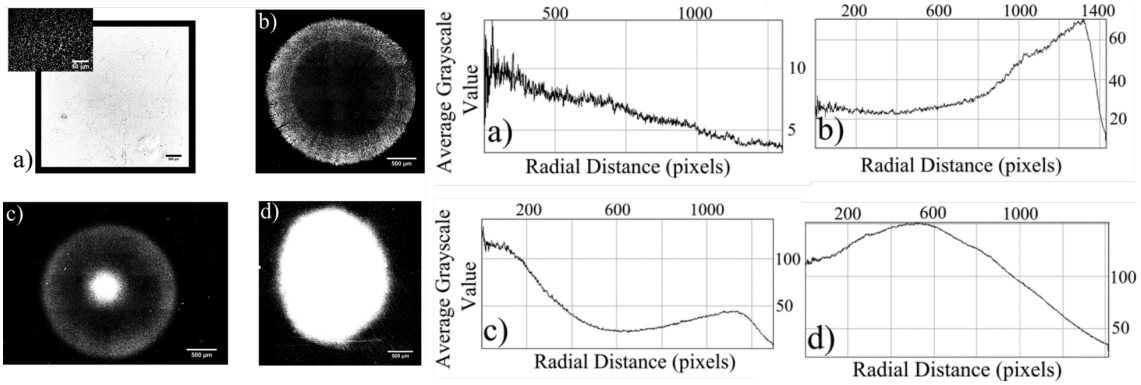

Figure 31 - Electrospray Deposits of 460nm Polystyrene after (a) 50ms, (b) 2s, (c) 7s and (d) 20s [205]

As the charge decay rate increases - through increased material thickness or the use of highly insulating substrates - the effects of residual charge repulsion become more extreme. If the charge is unable to dissipate in a useful timescale, then DC EHD techniques become ineffective as material cannot transfer from source to substrate. Kessick, Fenn, and Tepper [207] demonstrated this through the deposition of carboxymethylcellulose (CMC) on to an insulating polycarbonate substrate using a DC voltage up to 10kV (Figure 32). During the

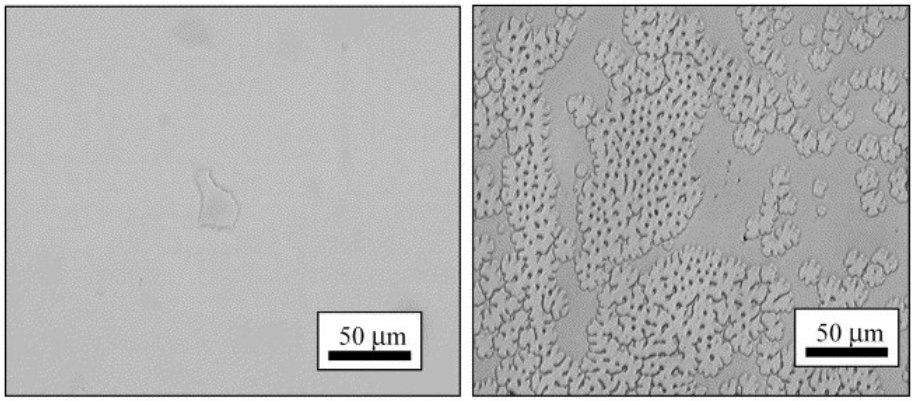

Figure 32 - Images of CMC on a Polycarbonate Substrate after Several Hours of Exposure using DC Electrospray [207]

early stages of deposition, a small volume of material was transferred, before charge accumulated and inhibited deposition. Even with exposure times of several hours they were only able to deposit small amounts of material. Although highlighted for electrospray, residual charge repulse presents a challenge for all modes of EHD deposition.

Alternating current (AC) electrospray is being increasingly investigated to overcome the challenges associated with surface charging. By sequentially depositing using positive and negative polarities, the net charge on the surface remains neutral. As a consequence, deposits can be achieved on highly insulating substrates over prolonged time periods. In Kessick's work, they demonstrated how AC allows improved coverage with voltages as low as 5kV. Weiss' work to deposit elastomer films used a similar approach [178]. In E-Jet printing AC is increasingly being explored for the production of higher aspect ratio features at the micron scale.

Increasing Deposition Rates

Increasing process throughput is a key challenge for film-based soft structures. Many of the manufacturing techniques are too slow or labour intensive for practical scale up. Even more commercially relevant techniques, such as gravure printing, have proven to be prohibitively expensive due to processing costs and the speed of electrode deposition. The only successful attempt to produce low-voltage DEAs, using molecular beam epitaxy, required two hours to produce a single dielectric layer of ~200nm. Early studies of electrospray deposition suggest speeds on 5.53nm/s are currently achievable, which offers a significant improvement over MBE whilst maintaining film quality. However, for a modestly sized actuator (millimetre scale) would still require days of continuous deposition.

Multiplexing, the introduction of multiple deposition heads, can be used to increase material deposition rate through parallel deposition. This area is being explored across industries to meet the throughput requirements of colloidal thrusters, mass spectrometry equipment, and manufacturing processes. Parhizkar et al.'s [208] recent study investigated four nozzle linear and circular arrays (Figure 33a) for their effect on the deposition speed. Through this simple

approach, the deposition mass increased from 50mg to 180mg for a three-hour exposure.

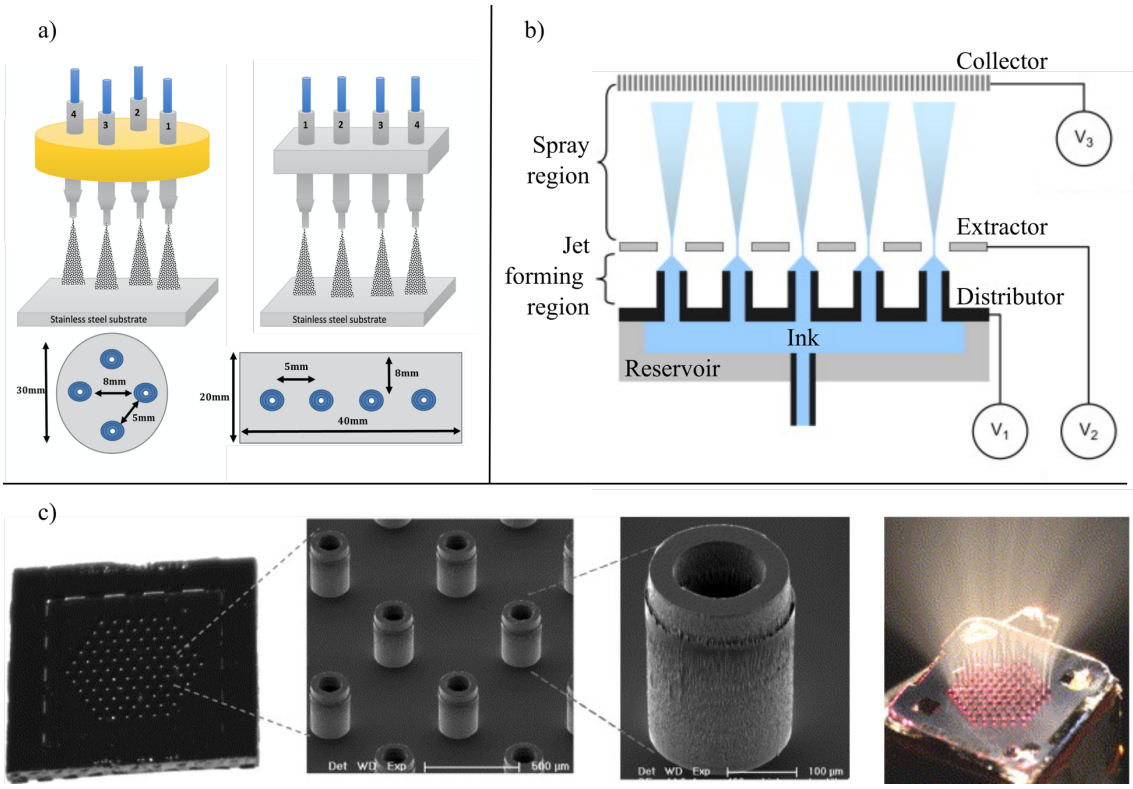

Figure 33 - Multiplexed nozzle arrangements for increased through put electrospray deposition: a) Performance of novel high throughput multi electrospray systems for forming of polymeric micro/nanoparticles [208], b) Compact multiplexing of monodisperse electrosprays [209], and c) Increase of electrospray throughput using multiplexed microfabricated sources for the scalable generation of monodisperse droplets [210]

Despite the success of this 'brute force' approach, simply mounting multiple stainless steel nozzles in close proximity is not a feasible approach for further increasing the material throughput[209]. Micro-machining [210] and lithography [211] processes have been implemented for producing high density nozzle arrays. Through a combination of photolithography and deep reactive ion etching, Deng et al. [212] have demonstrated the production of devices with up to 1027 individual nozzles on a single chip with a packing densities ranging from 253 to 11547 sources/cm^2 (Figure 33b). Although the flow was not characterised for the 11547 sources/cm^2 nozzle, a 91-nozzle array was shown to have a total throughput of 54.5cc/hour. Their highest stated value for a single nozzle is 2cc/hour, showing there are significant benefits of a multiplexed electrospray approach.

Additional challenges are introduced for multiplexed electro-hydrodynamic processes when compared to pressure backed extrusion techniques. Highly packed nozzle arrays require proximate points to be charged to voltages in the order of kilovolts. Doing this in a standard electrospraying arrangement, results in space charging: a phenomenon that causes a region of free space to become charged when exposed to excess charge [213]. To overcome this, more complex designs for electrospraying equipment, or at least nozzles need to be created. Deng's solution was to separate the electric fields used for deposition in to two distinct areas (Figure 33b): a jet forming region draws the fluid from the nozzles and then a spray region directs the aerosol to the substrate. This approach has been successfully demonstrated for DC electrospray, but it remains to be seen whether a similar approach will be applicable for AC systems.

3.1.1 Applications in soft robotics

Applications of EHD within soft robotics are limited due to the immaturity of the two fields. A number of pioneering publications have illustrated the technique for the production of either functional or structural soft matter applications, but with only a small number focussing more specifically on soft robotics.

Fibrous matts of electrospun elastomers have been explored for stretchable sensing by applying a thin conductive coating using secondary processes, such as roll or sputter coating. Lee et al. [214] presented a force sensitive touch interface by combining electrospinning of polyether block amide with a rolled PEDOT:PSS coating. Where materials do not naturally exhibit large elastic responses, they have been induced through the application of auxetic structures within the matt. Ko et al. [215] demonstrated this approach by patterning a PCL sheet using a femto-second laser. Electrical conductivity of the sensor was achieved by sputter coating a 15nm gold layer on to the surface of the PCL.

Rather than relying on bulk patterning, E-jet can be used to produce stretchable serpentine traces for strain measurement. Patterning of high aspect ratio silver nanowires in strain tolerant geometries allowed Cui et al. [216] to produce a number of heating and strain sensing elements on PET and PDMS substrates. When used as dry ECG electrodes, these devices where shown to perform comparably to commercially available wet solutions.

In thin film soft devices, the Nano-Tera Smart Sphincter project explored electrospray deposition as a high-speed alternative to molecular beam epitaxy of PDMS films for dielectric elastomer actuators. Preliminary studies with a simplified material demonstrated the potential for producing high-quality, low-roughness (< 1 nm) films with sub-micron resolution [30, 178]. A key challenge is the use of materials without the photo- or thermal initiators normally used to achieve cross-linking in elastomer materials. As a result, deep UV (<200nm) is required to cure the deposited material. The limited penetration depth of deep UV and cure times significantly lower than the electrosprayed film growth rate makes the material unsuitable for practical application [217]. Moreover, the mechanical properties of the simplified material are less suited to soft robotics than those used in competing technologies and the reported low roughness is only present over a small surface area. If electrohydrodynamic deposition is to make a significant impact on the field of soft robotics, processes that are tolerant of the rheology of existing materials need to be developed.

3.2 Machine design, layout, and validation

The equipment used by Weiss et al. manually placed a static spinneret (nozzle) 50mm from a stationary substrate to electrospray a simplified PDMS material. The point deposition of this system led to a limited coating area and required the use of low concentration solutions that are compatible with the electrospray regime. Here, it is hypothesised that the quality and coating area of films can be improved by introducing autonomous motion between the deposition head and substrate. Since equipment requirements are similar for all deposition modes, such a system will also allow investigation of alternate deposition modes (e-jet and electrospinning) by dynamically changing the material formulation and machine geometry. This should allow an extended range of material to be investigated as films could be made through electrospinning of wet fibres, consecutive direct-write of droplets, or aerosol deposition.

A system capable of transitioning on-the-fly also opens up opportunities for devices with spatially varying morphology as well as material composition. In wearable devices, for example, a three-layer device could consist of an

electrospun breathable interface, an electrosprayed dielectric elastomer actuator, and e-jet printed sensors and circuitry (Figure 34). This section documents the development of an experimental, proof-of-concept apparatus capable of all three deposition modes and serves a precursor to a more focussed study on the development of a soft film structure.

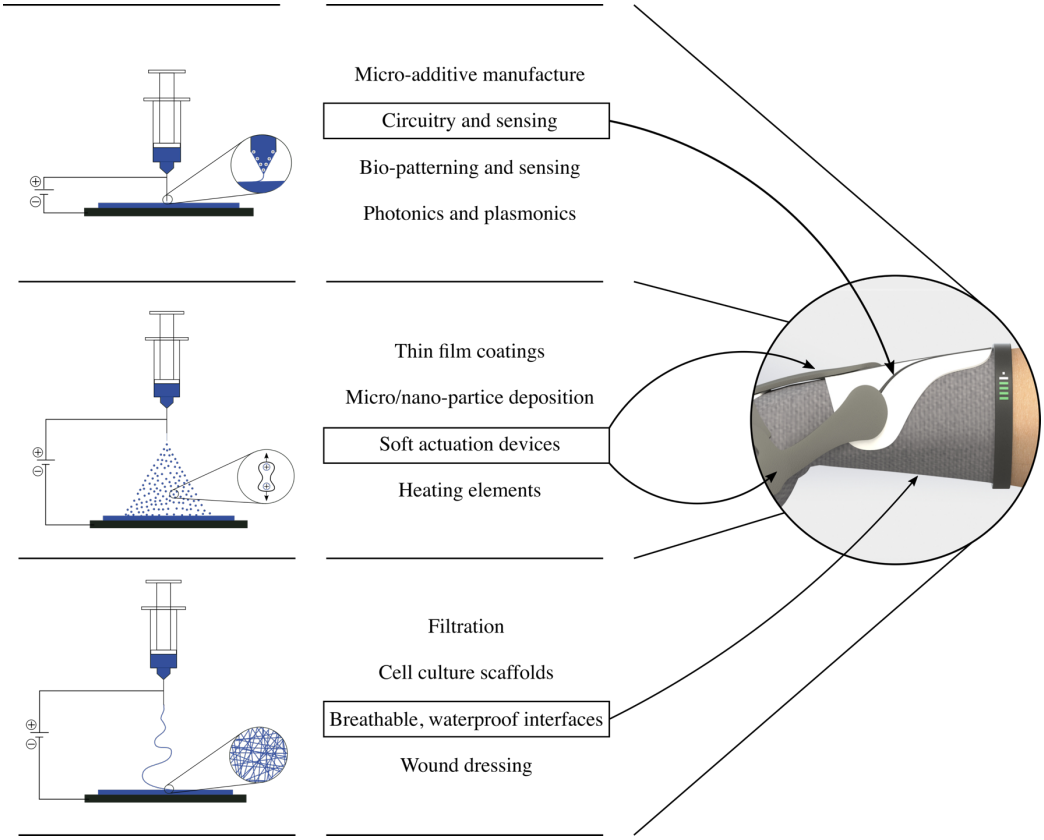

Figure 34 - Multi-modal electro-hydrodynamic deposition for functional, soft devices

Equipment for electrospray and electrospinning have similar requirements, with the transition between the two regimes being driven by the rheology of the ink. Deposition heads are usually static and placed at a relatively large distances from the substrate, providing the required time of flight for droplet fission or fibre elongation. Electrospinning typically features more complex substrates for fibre collection to encourage alignment. Perhaps the most common of these is a high-speed rotating mandrel. These similarities mean there are a small number of papers that have combined spinning and spraying [218, 219]. Conversely, E-Jet deposition requires significantly more complex equipment to enable synchronised motion for 3D patterning on small scales, while still tolerating the high voltage requirements. Furthermore, as the process is driven by the application of electric fields, control over the relative positions of the nozzle and

substrate is much more important at the small distances used during E-Jet printing. Compared to the other techniques, the low-speed of the E-Jet printing also contrasts with the high-speed rotation often used in electrospinning.

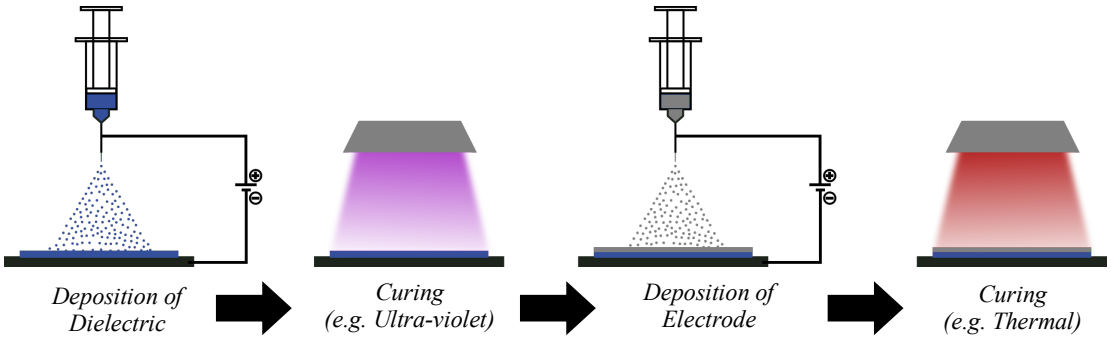

Figure 35 - Cartesian apparatus process flow

The use of a rotating mandrel, as per typical electrospinning arrangements, enables further opportunities for a continuous manufacturing process rather than a serial, lineated arrangement (Figure 35) that has been used for printed elastomer devices. A mandrel flanked by two, two axis platforms will enable the co-deposition of multiple inks and morphologies (Figure 36). For an application like DEAs, this approach has significant appeal as both the dielectric and conductive elements can be deposited in unison. Since they require a high number of layers, the continuous manufacturing approach could significantly reduce manufacturing time compared to lineated processing. In addition, this approach allows for co-deposition using two complementary processes. In this work, Aerosol Jet printing was eventually incorporated to overcome some of the challenges associated with direct write of conductive materials using the low-cost apparatus in this work.

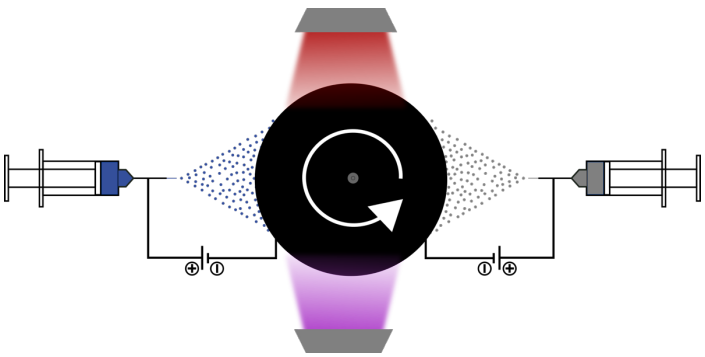

Figure 36 - Cylindrical apparatus process flow

3.2.1 Physical Machine Layout

Print Engine

The development of an effective print engine is essential for the development of a successful deposition system as it will likely define the limitations regarding material compatibility. The initial selection of the syringe pumps, tubing and connectors is relatively arbitrary as they are typical laboratory supplies. The main concern related to the selection of an appropriate power supply. In this type of experimental, exploratory study a power supply that allows process flexibility is essential. The literature review provided a framework for the selection of a power supply:

- Alternating Current
    - Alternating current prevents the build-up of charge on the surface of non-conducting substrates. The use of AC potentials will allow for deposition on to non-conducting substrates
- Voltages between 0-25kV
    - Review papers have suggested that voltages in the region of 0-25kV should be suitable for the deposition of most materials. Töpper et al. have shown electrospray deposition of PDMS from voltages as low as 5kV
- Low current requirements
    - Charge is carried through the material being deposited on the substrate. As a result, total flow of charge is on the order of a few milli-amperes.
- High Slew Rate
    - The slew rate of the power supply is the rate at which the voltage output can change. A high slew-rate allows for higher frequency AC potentials.

The final limitation on the selection of a power supply was cost. High voltage, low power alternating current power supplies are an order of magnitude more expensive than comparable direct current power supplies. Therefore, a selection had to be made within budgetary requirements. Ultimately, it was decided that a Trek 20-20 High Speed (20-20C-HS, TREK, USA) power supply would be used.

This high voltage amplifier is capable of producing ±20kV with a slew rate of 800V/µs.

Motion Platform

The translation axes of the machine are belt driven using the Core-XY arrangement (Figure 37) that has recently gained popularity in additive manufacturing equipment. Core-XY allows two-dimensional planar motion using two stationary motors, which reduces the deposition head carriage weight. Low weight reduces the forces required for acceleration, therefore allowing higher speed translation. As a secondary benefit, it also allows spatial isolation between the low-voltage motion electronics and high voltage deposition head.

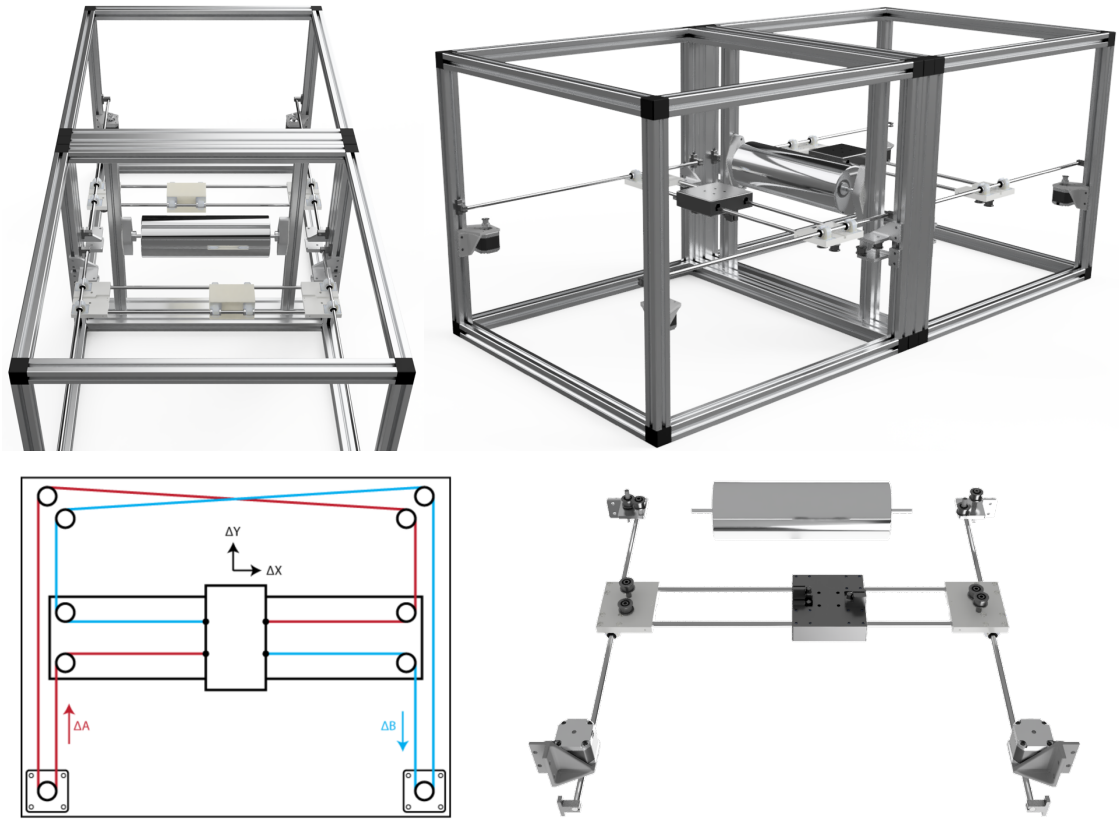

Figure 37 – a) Schematic of core-XY two-axis motion platform and b) the actual machine layout

The Core-XY implementation is a low-cost solution for relatively fast automation, especially when compared to lead or ball-screw based designs. Some sacrifices are made to precision and accuracy because of the belt's elasticity; however, for this early stage investigation, an expensive high-resolution stage would likely be superfluous. When using 1.8° stepper motors, 1/32 micro-stepping, 20 tooth pulleys, and a 2mm pitch timing belt the theoretical minimum step size on the gantry is 6.25µm.

The central mandrel was also belt driven from a stepper motor to provide isolation between substrate and drive electronics. This also allowed the mandrel to be adjusted for either high precision or speed by changing the gear ratio between the driven and driver pulleys. When a 1:1 ratio was used, this allowed a theoretical minimum step of 0.05625° that translates to a minimum surface travel of ~50μm. Adjusting the ratio to 1:5 led to resolution comparable to the x-y gantries.

Control

To limit development time, open-source machine control software libraries were used to achieve synchronised motion. Initially this combined an Arduino Mega microcontroller coupled with GRBL, which is a software package originally intended as a lightweight CNC controller. Since the current GRBL release is limited to three-axis motion, two microcontrollers were combined to control the five axes of this machine. Control of the timing between the two controllers was achieved using a second piece of software on the main PC.

This approach was successful for simple motion, but coordination between look ahead buffers proved challenging for more complex actuation. Furthermore, the reliability of the controllers provided an additional challenge, especially when trying to interface the system with the ancillary components. To simplify the system and reduce software development time, the Arduino based systems was replaced with the Smoothie platform. This platform combines an integrated CNC control board with modular software. The ability to quickly modify and create modules greatly simplified the interfacing with ancillary components, such as syringe pumps, the power supply, and heating elements. The controller is also compatible with 5-axis motion, which negated the need for software to control motion timing between the two axes. Motion commands were sent to the apparatus using G-CODE from a GUI developed using the tkinter library in python.

Toolpath planning

Time delays, caused by charge and pressure decays in continuous E-Jet and AJP, respectively, can present a challenge when frequently starting and stopping deposition. Toolpaths targeting continuous deposition were used to reduce the

need for intermittent deposition. The toolpaths to achieve this were generated from .DXF by converting them to G-CODE using a python program and the NetworkX library for network inspection.

The developed program extracted co-ordinates from the .DXF files to create a list of nodes and edges that represent the required geometry. If multiple discrete patterns are present within the design, then each is stored as an individual network. Each network is then inspected and defined a Eulerian, semi-Eulerian, or non-Eulerian circuits (Figure 38), where:

- Eulerian – each node in the network has an even degree
- Semi-Eulerian – exactly two nodes in the network have an odd degree
- Non-Eulerian – either one or more than two nodes in the network have an odd degree

Any Eulerian and semi-Eulerian graphs can be solved to find the minimum path that passes through each edge in the network. For semi-Eulerian graphs, deposition is required to commence and terminate at the nodes with an odd degree. For non-Eulerian networks dummy edges are added between nodes to produce a semi-Eulerian network. In practice, these manifest themselves as passing the shortest two edges twice during printing. A simple example of each type of network is presented below.

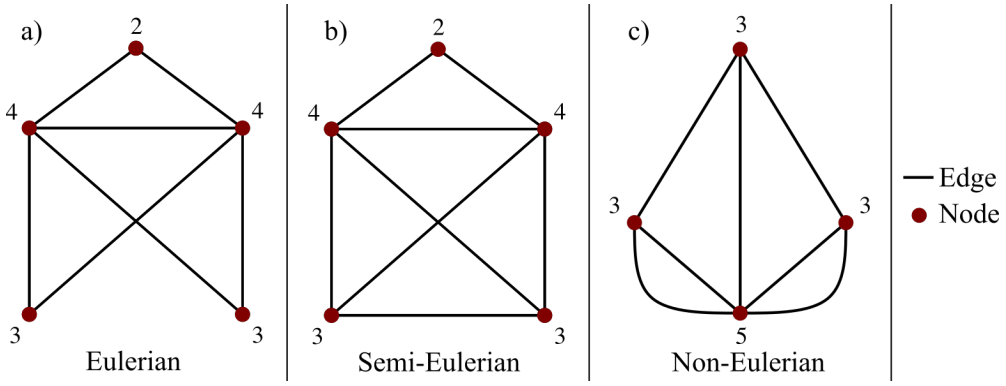

Figure 38 - Examples of a) Eulerian, b) Semi-Eulerian, and c) Non-Eulerian graphs

Mandrel alignment compensation

The 3030 aluminium extrusion frame of the machine was selected to provide a flexible construction, which was important for an early stage experimental apparatus. The low-cost allowed resources to be spared for critical machine

components, such as the power supply. A modular approach created a challenge to ensure alignment between the mandrel and the x-y translational stages. During installation, the mandrel was aligned by mounting a dial test indicator (DTI) to the deposition head and adjusting the mandrel and gantry to minimise deviations. Although the error could be minimised for a single side (~30-40µm), it proved difficult to achieve variation of less than 100µm for both gantries. Since EHD deposit morphology is driven by the magnitude of the electric field, this led to inconsistent printing and electrical shorting when the distance between the nozzle and substrate decreased.

To overcome this, a laser displacement sensor (IL-100, Keyence, Japan) was used to measure the position of the mandrel relative the deposition head. During a scanning cycle, the machine would record data in a grid pattern to produce a surface map of the substrate (Figure 39). This data could then be used to pre-process the G-Code ahead of deposition to compensate for any alignment errors. To define the correction value for points between the measured values, the three closest nodes were used to define a plane that captures the desired position. The required correction could then be calculated from the plane and the desired x-y position.

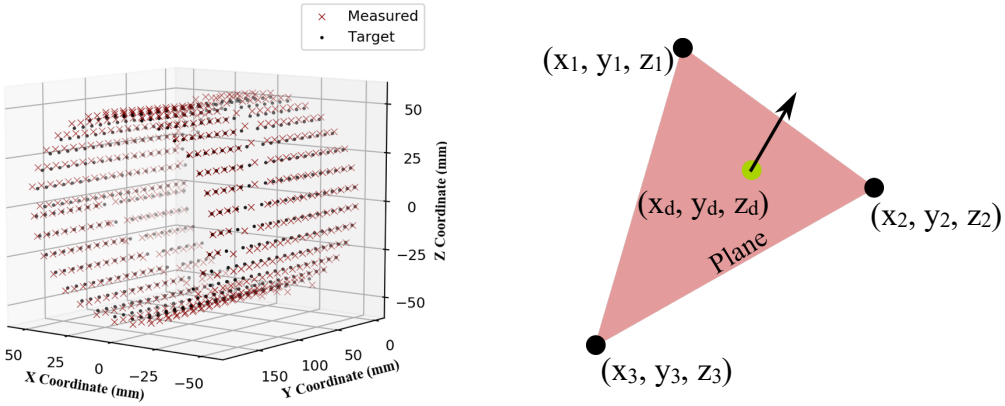

Figure 39 - a) Surface map of mandrel and b) finding the offset of the unknown point

To illustrate the efficacy of this approach the mandrel, a scanning cycle was run on a 40x200mm area of the mandrel and the data used to correct the G-Code for a second cycle. For the uncorrected and corrected scan, the standard deviation for the mandrel-deposition head distance was 1200µm and 40µm, respectively. The corrected deviation represents a 4% variation in distance at a nozzle substrate distance of 1mm. This reduction increased the reliability of the print

and prevented electrical arcing between the nozzle and substrate during direct write deposition. Despite the improvement, variation in distance likely contributed to the variation in deposit for the near-field process (Section 4). Further improvement could be achieved through more rigorous assembly approaches; however, the large span and limited stiffness of the machine meant vibrations of the machine were of a similar magnitude to the static error. Achieving lower errors would require an alternate and less modular approach to the machine design and construction, which would add significantly to the machine cost. A standard deviation of 40µm was found to be acceptable for this exploratory study. As an additional benefit, this software also allowed deposition of patterns on to non-planar substrates as illustrated in Section 5.4.

3.3 Initial Results

Initial validation of the machine was achieved using polyvinylpyrrolidone (PVP), which is an ink that has been widely studied and documented. This allowed exploration of the fundamental capabilities of the machine and provided a first insight into the factors that can affect the quality of the deposit. An attempt was made to validate that machine can transition between the three primary EHD deposition regime to produce three distinct morphologies through manipulation of the process parameters and ink concentration.

3.3.1 Materials and methods

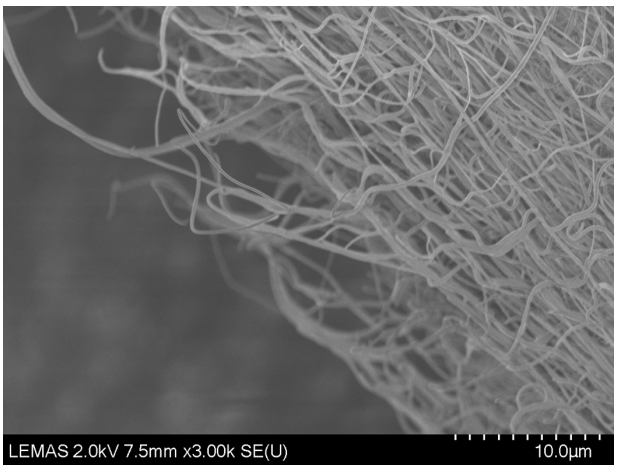

Figure 40 - SEM images of torn PVP fibres

Polyvinyl pyrrolidone (PVP) (Sigma Aldrich, Mw: 1300000) was dissolved in deionised water at 1, 5, 10, 15wt% for 24 hours at room temperature under

constant magnetic stirring at 200rpm. The ink was loaded in to 10ml syringes and supplied to the nozzle at a flow rate of 1ml/hr using a syringe pump (AL-2000, WPI, USA). A blunt 30-gauge dispensing tip (8001104, Fisnar, USA) was used as a spinneret in all instances. Deposits were conducted at distances of 60mm on to polyimide (50µm) backed copper (35µm) substrate (AN10, CIF, France) that was secured to the mandrel using a copper tape (Chomerics, UK). In the direct write mode, the fibre was deposited on to a PET sheets (125µm, Goodfellow, UK) as it simplified imaging through optical microscopy.

The morphology of the deposits was characterised using a combination of white light interferometry (NPFLEX, Bruker, USA), Scanning Electron Microscopy (SEM) (SU820, Hitachi, Japan), and optical microscopy (BX53M, Olympus, Japan). For comparison SEM micrographs of an untreated substrate have been supplied alongside the treated samples. SEM images were captured using samples that were sputter coated with a 5nm layer of iridium. Approximate measurements from the SEM images were taken using ImageJ.

3.3.2 Results and discussion

Electrospun fibres (Figure 41c-e), electrosprayed films (Figure 41b), and selective patterning of aqueous PVP has been demonstrated through variation of the solution concentration or machine layout. Qualitatively, reducing the solvent concentration from 12.5wt% to 1wt% led to a significant decrease in the viscosity of the PVP solution. During deposition, this change led to a decrease in mean fibre diameter from ~180nm (12.5wt%) to ~40nm (2.5wt%) (Figure 41f) from the same electric field. This reduction in fibre diameter is the direct result of a lower resistance to flow, and therefore elongation, for low-concentration, low-viscosity solutions. Once the polymer chain interaction is sufficiently low, continuous fibres can no longer be maintained and discrete droplets are deposited, which leads to the production of low-roughness films of PVP.

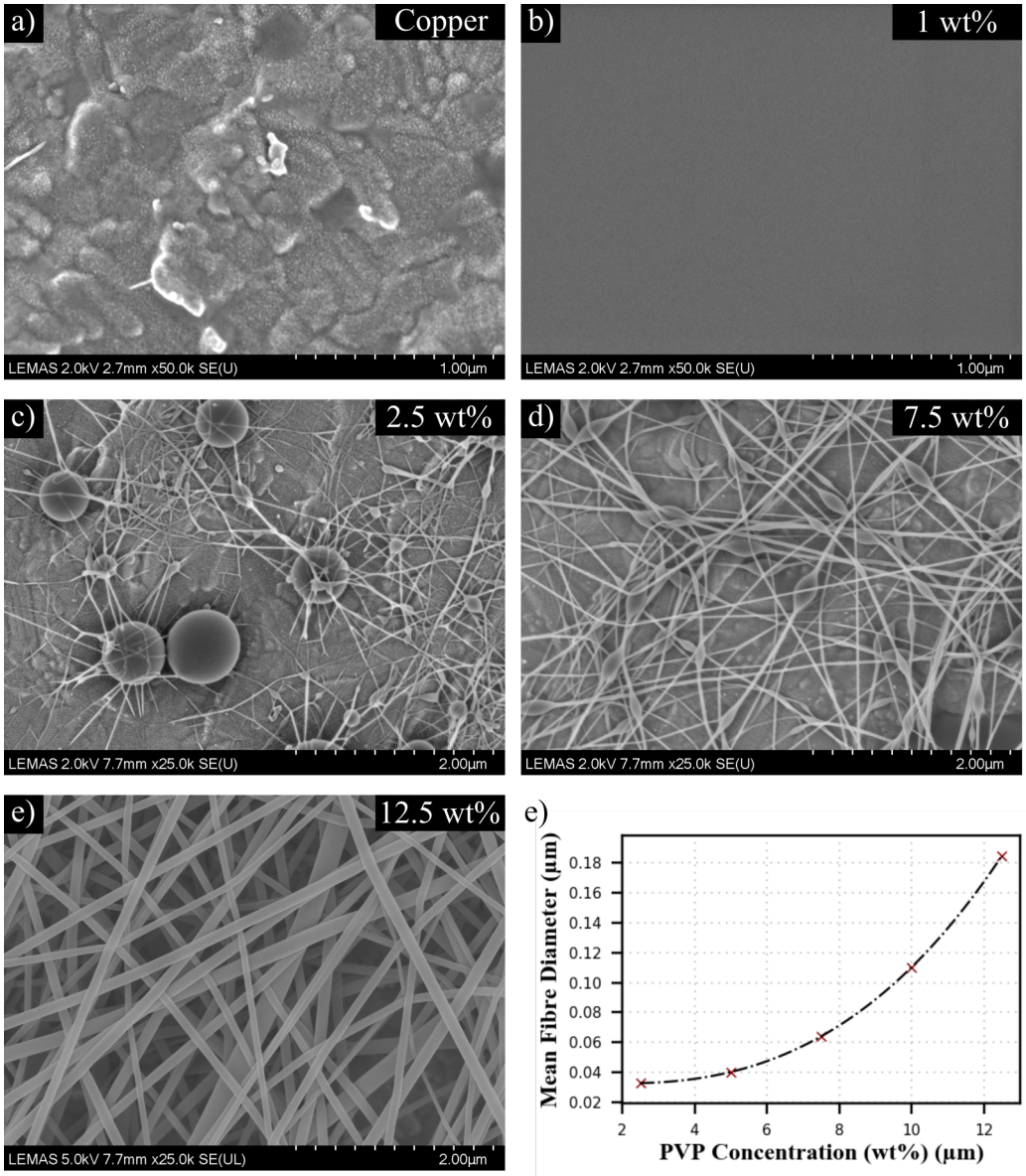

Figure 41 - Effect of solution concentration on electro-hydrodynamic deposition of PVP

At greater solvent concentrations, the uniformity of the deposit decreased and the number of bulbous artefacts, islands of PVP, and conjoined fibres all increased (Figure 42). Furthermore, deposition time of the solutions with PVP content <10wt% had to remain relatively low (<60 seconds) to produce micrographs with a high number of visible fibres. Prolonged exposure led to large islands of bulk PVP. These effects can be attributed to insufficient inflight solvent evaporation. Therefore, these effects can likely be eliminated by increasing evaporation rates by using higher volatility solvents or include enclosure heating.

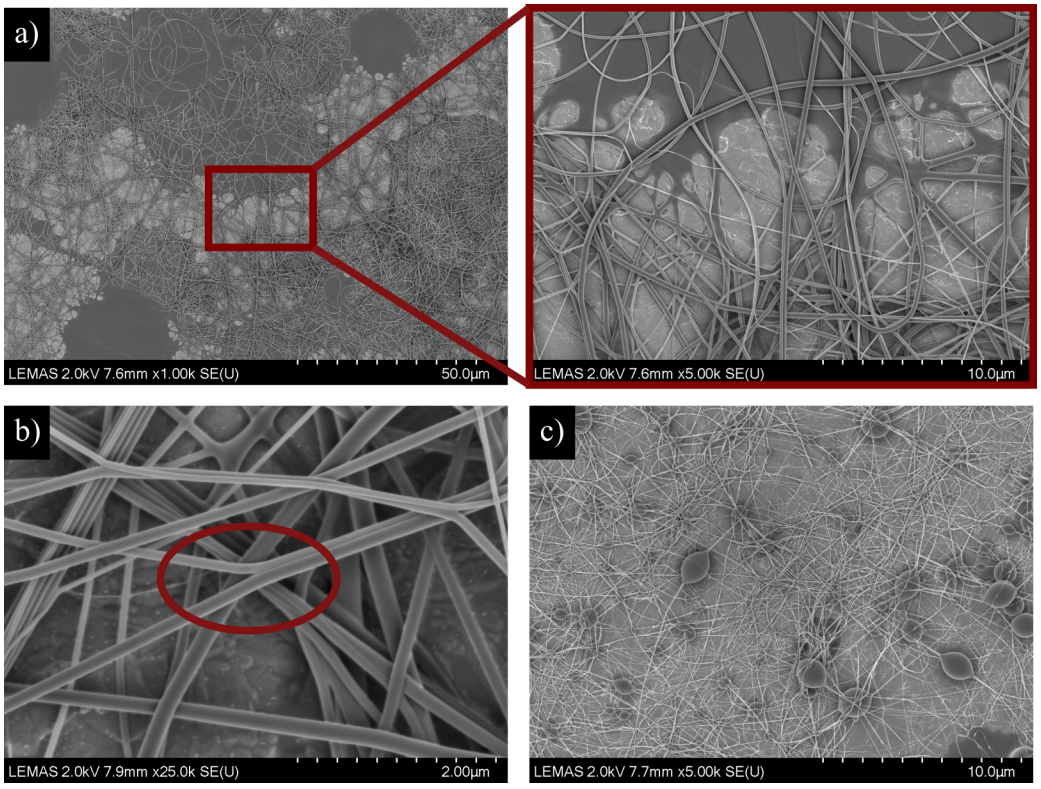

Figure 42 - a) Islands of bulk PVP, b) conjoined fibres, and c) bulbous fibres

3.4 Chapter summary

This chapter introduced electro-hydrodynamic deposition for the manufacture of soft films. The electrospinning, electrospraying, and E-Jet techniques were all introduced as ways of depositing material with varying rheological properties, therefore providing a versatile approach to thin film manufacture. Opportunities for a process that can dynamically switch between the processes, to spatially vary the morphology of the deposit were also introduced.

The design and build of an experimental apparatus that can dynamically change material and geometry to explore the different EHD regimes was presented. Software techniques to drive continuous deposition and minimise variation in nozzle-substrate distance were also developed. The machine allows deposition from distances up to 30mm on to a 100mm diameter substrate using AC electric fields up to ±20kV. Initial validation, using PVP as a model ink, allowed validation of the equipment and demonstrated the transition from direct write (5µm beads) to electrospun fibres (40nm) and electrosprayed films.

4 Electro-hydrodynamic deposition

The previous chapter introduced electro-hydrodynamic deposition; discussed the development of an apparatus for exploring EHD as a manufacturing technique; and presented result from initial deposits using materials that have previously been deposited used with the technique. This chapter explores the use of the machine for the deposition of elastomeric and conductive materials with a view towards applications in soft films.

4.1 Deposition of elastomers

Low electrical conductivity and high viscosity present barriers when attempting to deposit unmodified, commercially available PDMS elastomers. These materials often require tailoring through the addition solvents; simplification of the precursor solution [178]; using carrier materials within the solution [220]; or, more commonly, some combination of the two [30]. The addition of solvents typically increases the conductivity while lowering the viscosity, which combine to improve the material's affinity to the classical EHD regimes (Section 3). At low polymer concentration solutions, the degree of polymer entanglement is reduced, which increases the likelihood of droplet generation through the electrospray regime.

The addition of a carrier materials can be used to increase entanglement within the solution to encourage the deposition of fibres rather than droplets [220]. Co-axial extrusion of PDMS with a long chain polymer sheath material, which can be dissolved away post-deposition, has been demonstrated as a successful technique to produce structured fibrous meshes [221]. Although these modifications have been successful in enabling the deposition of PDMS materials, there has been limited research on their effect on the properties of the final material. Furthermore, the required development time to achieve this behaviour is of little value unless the application specifically requires a structured mesh.

A less common type of EHD deposition, known as electrically forced jets, may provide an opportunity to accelerate the adoption of EHD deposition of soft films. Initial studies demonstrated the compatibility of electrically forced jets with highly insulating dielectric fluids with viscosities similar to the elastomeric

materials often used for soft systems [194]. Silicone oils with viscosities ranging from 970-58200cP and conductivity as low as ~10^{-9}mS/m have been demonstrated [193]. Despite this, there has yet to be any comprehensive study on its application as a viable manufacturing technique for soft robotics. The process is perhaps overlooked since it lacks the resolution achievable in the classical regime. For many soft film applications, increased lateral resolution may present a suitable compromise for increased material compatibility, especially if axial resolution can be preserved. An initial scoping study using common materials was used to determine the most immediately practicable approach for thin elastomeric films.

4.1.1 Material screening

Four commercially available silicone materials were purchased and investigated for their response to the application of a high electric field. Materials were selected based on their viscosity, mechanical properties once cured, pot-life, and use within the literature. Biocompatibility was a secondary consideration driven by the technology's potential end use in cell culture platforms and implantable technologies. Since many of the materials targeted in this work are proprietary, viscosity was used as an indicator of polymer chain length and entanglement. Four types of PDMS were selected for the initial investigation: Sylgard 184, Sylgard 186, Sylgard 1-4128, and Gelest DMS-V21.

The Sylgard family of elastomers were chosen over alternatives from Smooth-on or Eco-flex due to their significantly greater pot-life despite their increased hardness. The properties and applications of Sylgard 184 and 186 are well documented and widely studied due to their use in microfluidics and soft robotics research. These two materials have the highest viscosities of the selected materials and are normally processed through soft lithography. Sylgard 1-4128 is less widely used in soft robotics, however it has significant application as a conformal coating for electronics, where its low hardness helps to relieve strain and absorb impacts. It is typically applied through dip coating or pneumatic spraying during automated PCB manufacture.

Table 5 - Properties of commercially available polydimethylsiloxanes

	DMS-V21	*184*	*186*	*1-4128*
Viscosity (cP)	*103*	*3500*	*66700*	*475*
Pot life (mins)	-	*90*	*99*	-
Cure method	*Deep UV*	*Thermal*	*Thermal*	*Thermal*
Cure time (mins)	*6nm/s*	*2880 (25°C)* *35 (100°C)* *10 (150°C)*	*25 (100°C)* *15 (150°C)*	*5 (105°C)*
Shore hardness	-	*43A*	*24A*	*64 OO*
Tensile Strength (MPa)	*4.7**	*6.7*	*2.1*	*0.2*
Strain (%)	-	-	-	*70*
Dielectric Strength (kV/mm)	-	*19*	-	*20*

**Young's Modulus has been provided as data for tensile strength is not available*

DMS-V21 from Gelest is a vinyl-terminated PDMS telechelic polymer normally used as a component within 2-part addition cure silicone elastomers. According to the supplier, the material is brittle and features a low-elastic modulus when cured without the addition of complementary monomers. It has been included in this initial scoping study since Weiss et al. [30] demonstrated its suitability to the electrospray deposition regime. Rudimentary mechanical analysis has shown the elastic modulus may be suitable for low-thickness (<1µm) films.

Gelest DMS-V21

DMS-V21 was combined with ethyl acetate in a ratio of 1:19 before being mixed in a planetary degasser (ARE-310, Thinky, Japan). The solution was then continuously stirred for at least 48 hours to ensure sufficient mixing and minimise chain entanglement. The solution was drawn in to a five-millilitre syringe and placed into a syringe pump. Using a flow of 3ml/hour, the nozzle was actuated to 30mm from the surface of the PET substrate, before electric field was applied to initiate deposition.

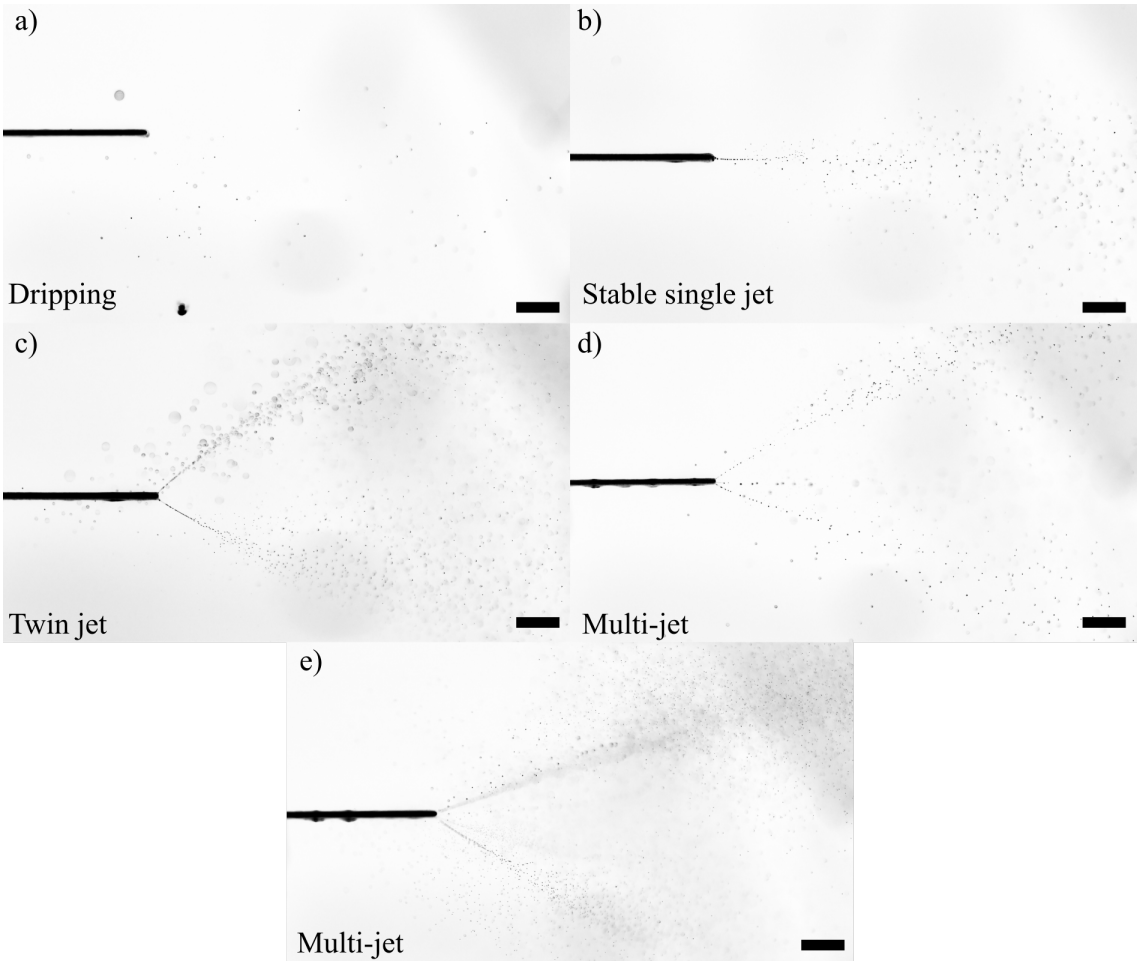

Figure 43 - Electrospraying modes of DMS-V21 solution in ethyl acetate: A) dripping, B) stable cone-jet, C) twinjet, D) & E) complex multi-jet. All scale bars are 2mm. (colour inverted for clarity)

At electric fields up to 1kV gravity remained as the predominant factor effecting deposition (Figure 43a), therefore droplets were ejected from the nozzle in the dripping mode. From ~1.8kV onwards (Figure 43b), the meniscus was pulled into a Taylor cone and the stable cone-jet was established, which broke down into a plume of droplets. As the voltage approached 3kV (Figure 43c), the twin-jet mode arose before complex multi-jets were established from 4kV upwards(Figure 43d-

e). Deposition through the twin and multi-jet modes were observed to be erratic, with jets appearing to flicker, initiate, and decay at random.

Deposition in the stable cone-jet was found to exhibit the classic target profile, with the amount of fluid present on the substrate reducing radially. As substrates were suspended vertically long exposure time led to the material running. Enclosure heating to more readily evaporate excess solvent may have helped minimise these effects; however, for the initial study, exposure times were kept below 60 seconds.

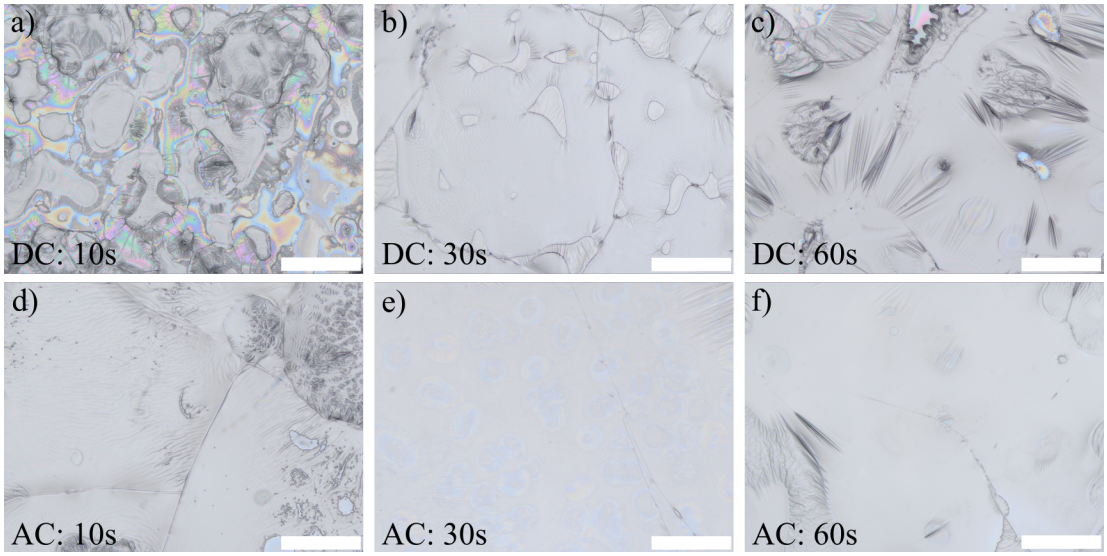

Figure 44 - Optical micrographs of electrosprayed DMS-V21 at varying exposure times from a A) 5kV DC applied voltage at 50mm and B) a 5kV, 18Hz electric field at 50mm. All scale bars are 500µm.

Figure 44 shows cured deposits of DMS-V21 produced using DC and AC electrospray at exposure times ranging from 10 to 60 seconds. At low exposure times, both AC and DC fields lead to isolated islands of material due to insufficient material delivery and spreading. Increasing exposure times reduced the number and size of gaps in the films for both field types, however pores and surface defects remained in DC films even at extended periods of deposition. In contrast, the use of an 18Hz, ±5kV AC field showed improved deposition at all exposure times with relatively large areas (2-3mm^2) with low roughness. Analysis using white light interferometry shows a roughness of 65.23nm (Sa) over an area of 1x0.8mm from a 30 seconds deposition time.

Although these results show promise, the absence of photo-initiators or crosslinking catalysts in the base material presented challenges when crosslinking the polymer. In this work, samples were baked at 100°C for 10

minutes to remove any residual solvent before being exposed to a broad wavelength UV source for one minute to cross-link the polymer. The low-wavelengths (~200nm) present in spectrum were able to cure the polymer despite the absence of photo-initiators; however, optical attenuation limited the penetration depth of the light source, and therefore achievable cure depth. When attempting to cure materials of greater depth, a 'skin' of cured material is produced on the surface of the uncured elastomer (Figure 45). Deposition times greater than 60 seconds led to inconsistent curing across the deposit area, which manifested as visible wrinkles in the optical micrographs. Literature suggests curing materials with thickness approaching 1μm can be challenging through this approach [217].

Figure 45 - Skin curing of DMS-V21 through exposure to deep UV

The films produced here were within a curable range, however this was only for single point depositions. Away from the centre, the deposit soon transitions from a confluent film to a series of islands. Achieving large area films will likely rely on an array of multiplexed nozzles, automated nozzle scanning, or a combination of the two. These approaches will allow improved coverage and will require a greater minimum film thickness to ensure uniform coverage.

This approach to materials presents several processing advantages and is immediately suitable to the electro-spraying regime, however the challenges with cross-linking, combined with limited bulk material properties and long cure times, means significant work is required to translate the approach to practical application.

Electrospray: Sylgard 184, 186, & 1-4128

The syringe pumps could not provide sufficient force to deliver the higher viscosity Sylgard 184 and 186 solutions; therefore, they were diluted using ethyl acetate prior to deposition as is common in solution processing. The base solutions were diluted using 5wt% ethyl acetate to decrease the viscosity. The pot life of Sylgard 184 and 186 – the time taken for viscosity to double – is reported as approximately 90 minutes, which meant long periods of mixing could not be used as for DMS-V21. Instead, the materials were mixed and degassed in a 4-minute cycle using planetary mixer (ARE-310, Thinky, Japan) before deposition.

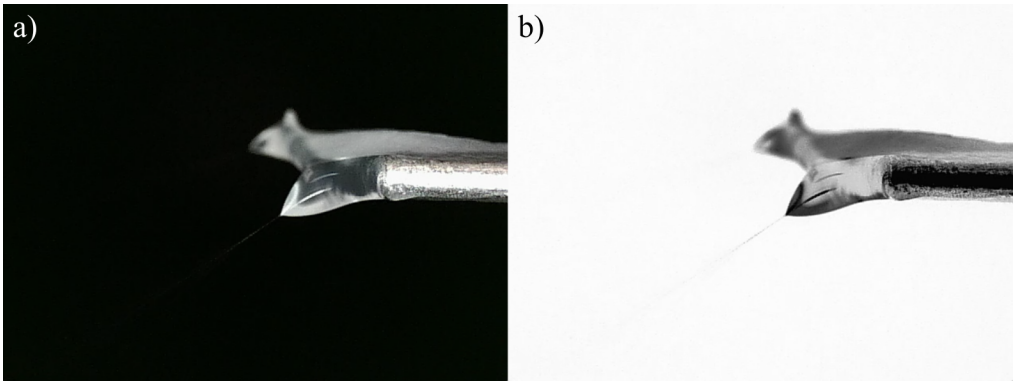

Figure 46 - Separation of Sylgard 184 and ethyl acetate at nozzle exit

Experimentation immediately highlighted challenges with this approach: firstly, the process was found to have a high time dependency, which is likely caused by solvent loss and partial cross-linking of the polymer. Secondly, as reported for EHD deposition of polymers in high volatility solvents [222], the solvent and PDMS appeared to separate at the nozzle exit (Figure 46). This led to either only the solvent being transferred to the substrate or, during extended deposition, nozzle clogging. If the solvent and temporal effects could be isolated, understood, and used to develop a suitable ink, the print stability would be limited due to the material's pot-life. Therefore, Sylgard 1-4128 became the focus of the study since it had an indefinite pot-life at room temperature. Droplet deposition of 1-4128 could be achieved without dilution and became the focus of this work

4.2 Droplet deposition of elastomers

Either the pulsating jet or pulse-on-demand modes are used to generate droplets during E-jet deposition. When using a pulsating jet, oscillation of the cone under

a constant, DC electric field is used to periodically emit a droplet from the nozzle. In pulse-on-demand, the selective application of an electric field is used to trigger droplet ejection. Although these regimes appear sub-optimal when compared to steady jetting – ejection of a continuous bead/fibre - it is parametrically distant from the unstable modes of deposition (multi-jet) that are difficult to direct and control. In practice, this has made the process the most useful for E-Jet applications as it is less sensitive to small deviations in local processing conditions. The following section provides a comparison of both droplet deposition techniques, before focussing on the pulse-on-demand technique and the primary factors effecting the deposits.

4.2.1 Method and Materials

Material and substrate preparation

Square substrates (50x50mm) were prepared from 300x300 sheets of 125µm polyethylene terephthalate (PET) (Goodfellow, UK). The silicone elastomer, Sylgard 1-4128, was prepared by mixing part A and B in a ratio of 10:1 as per the manufacturer's instruction. Once prepared the material was loaded in to a ten-millilitre syringe and secured into a syringe pump (Harvard Precision Instruments, USA). Using luer-lock connections, the syringe was attached to a 30-gauge (OD: 310µm, ID: 160µm) stainless steel blunt nozzle by a length of Tygon tubing. The nozzle was then mounted to the deposition head before deposition. Flow from the syringe pump was left to stabilise for 10 minutes prior to beginning deposition.

Deposit analysis

Images of the droplets were captured using optical microscopy (BX53M, Olympus) using 2.5x, 5x, or 10x objective depending on the radius of the droplets. The captured images were analysed using the OpenCV library in python. All images were converted to 8-bit grayscale and a median filter applied to remove defects from the images that may be mistaken droplets. Binary thresholding was used to allow pixel counting of the droplet area, while a canny edge detection algorithm was used to define the droplet boundaries. This data then allowed calculation of the mean distance from the centroid of the deposit to the edge of

the deposit (Figure 47). The variation in the mean distance is also used as a measure of droplet circularity. Validation of the automated analysis was accomplished by comparing results to manual measurement through ImageJ and the Olympus Stream Essentials. The figure below illustrates the analysis and provides example images at each stage of the analysis. A non-circular deposit is displayed since it exemplifies why alternate approaches, such as Hough transforms, struggle with the analysis.

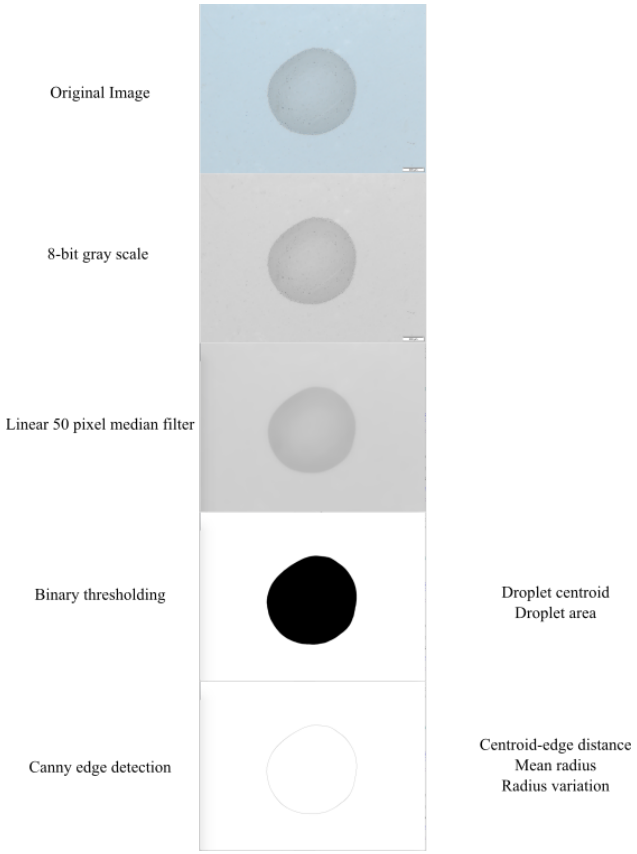

Figure 47 - Example analysis of optical micrographs for E-Jet printed PDMS droplets

Three-dimensional analysis was achieved using white light interferometry (NPFlex, Bruker) and analysed using open-source visualisation software (Gwyddion, Czech Republic). Deposition on to a cylindrical mandrel and curing at temperatures above the softening point of the PET substrate led to non-linear backgrounds, therefore data flattening was required to extract useful data from the deposit. A second-order, single axis polynomial background removal followed by a mean plane subtraction of the bare substrate was adequate in most cases. A 3-pixel median filter was also applied to minimise scan errors. Figure 48a-b shows example plots before and after processing. White light interferometry data was also used to generate a series of cross-sections for droplets to allow calculation of

the mean contact angle. Droplet volume was calculated from a plane at the level of the substrate and the surface of the masked area in Figure 48e.

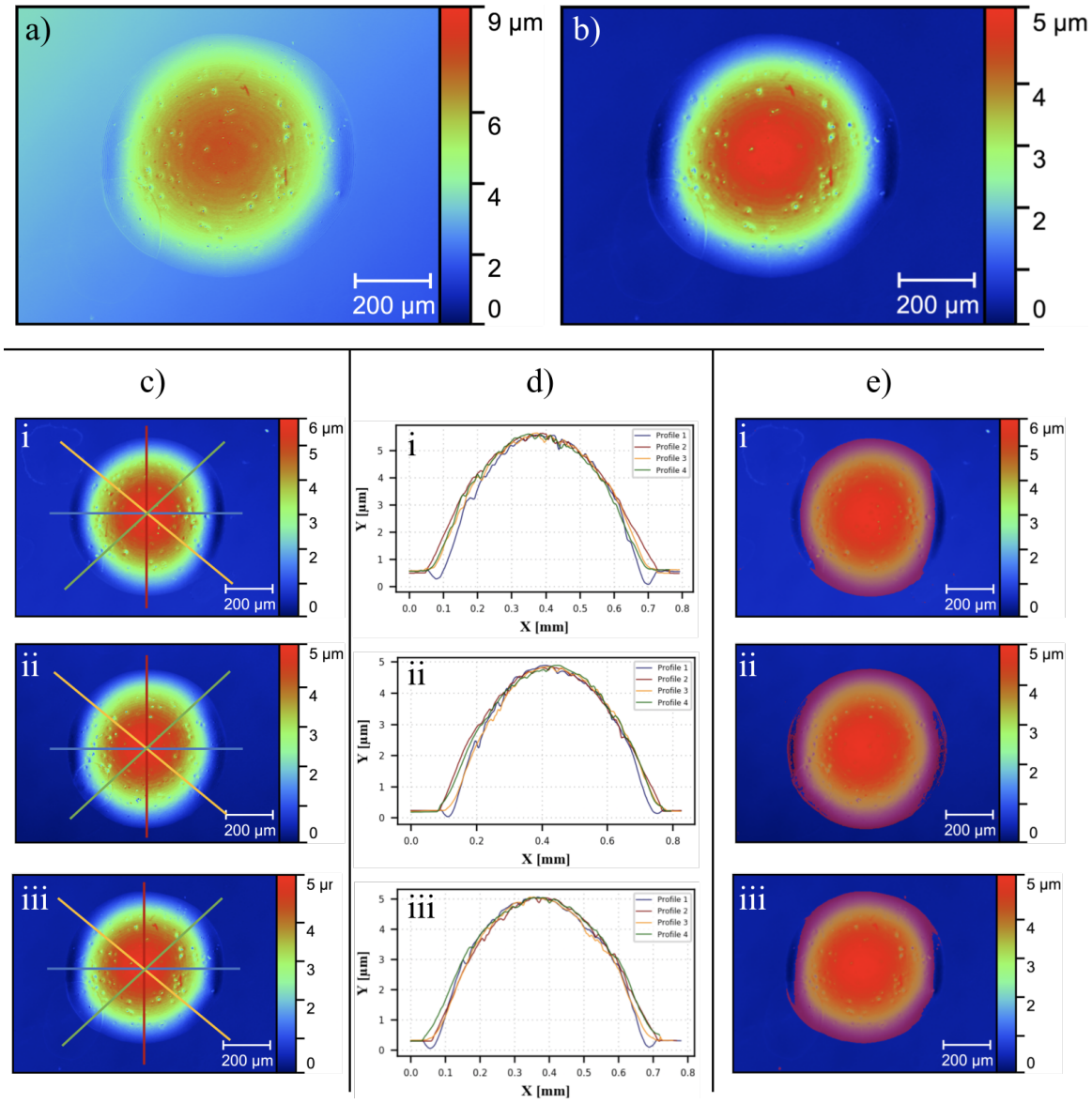

Figure 48 – White light interferometry plot before (a) and after (b) processing; c-i) Profiles used for generation of cross surface profiles, c-ii) examples of surface profiles used to measure contact angle, and c-iii) masked region to calculate the volume of the droplet

4.2.2 Droplets by Pulsating Jet

The pulsating jetting mode is the result of cyclic imbalances between the surface tension and electrostatic stresses within a droplet at the nozzle's tip. When no charge is present, the droplet is spheroidal as its shape is driven by its surface tension and mass. As charge, and therefore Maxwell stress, builds, the droplet is pulled into a conical shape with decreasing tip radius. A jet is then ejected when electrostatic stresses overcome the surface tension. This emission transfers

charge from the nozzle to the substrate, therefore reducing the charge-induced Maxwell stress within the liquid. This, in turn, causes the cone to recoil towards its original shape and the process is repeated.

Using this phenomenon to produce droplets means that the frequency of emission is driven by the properties of the ink, such as viscosity and conductivity, in combination with the applied voltage, nozzle-substrate distance, and material flowrate. Furthermore, the periodic ejection of droplets means that their spacing is dependent on the translational velocity of the deposition head. As such, the first step to characterise the deposition was to determine the effect of the feed rate on the shape and distribution before investigating how the frequency and size of the droplets are influenced by the remaining parameters.

Feed rate

For a given set of process parameters, the emission of droplets in the pulsating jet mode should occur at a consistent frequency. Therefore, the effect of increasing the travel speed of the deposition head was expected to maintain droplet diameter, while increasing the spacing between subsequent droplets. Through testing at various rates, calculation of the droplet frequency should be possible based on the translational speed of the head and the relative spacing between droplets.

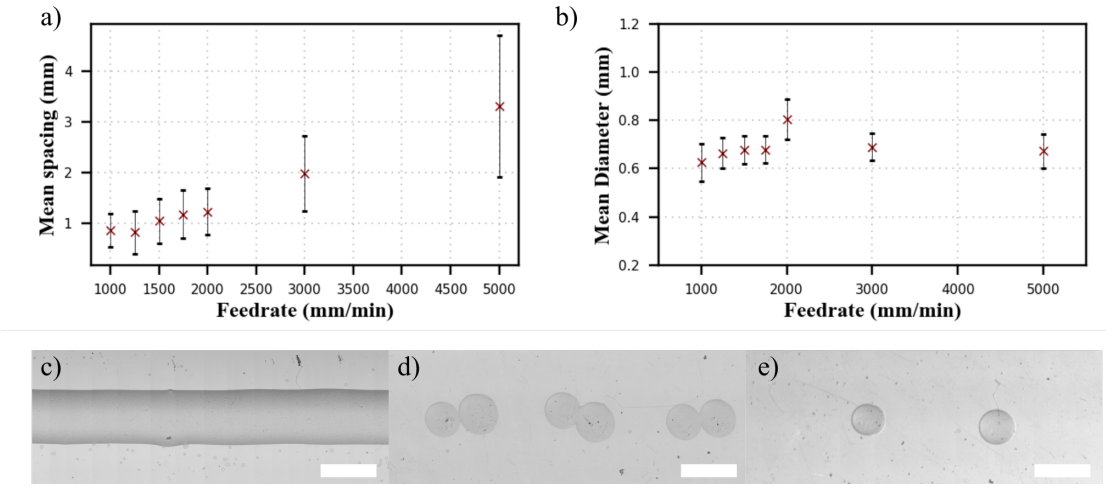

Figure 49 – a) Droplet spacing and b) mean diameter with increasing feed rates. Error bars represent 1 standard deviation. Microscope images of deposits at feed rates of c) 100mm/min, d) 2000mm/min, and e) 5000mm/min. Scale bars are 1mm.

Samples were prepared by setting a flowrate of 100ul/hr, applied voltage of 2000V, and then travelling at feed rates ranging from 1000-5000mm/min for

30mm. The diameter of the droplets and the spacing between consecutive droplets were measured using optical microscopy. Three repeats were conducted for each feed rate and the mean, minimum and maximum are plotted in Figure 49. As expected, the droplet spacing increases linearly with feed rate, while the mean droplet area remains relatively constant. At low feed rates, the mean droplet area is comparable to the droplet spacing, which caused challenges when distinguishing between droplets.

The standard deviation in droplet spacing was found to increase significantly with nozzle speed. Examination of optical micrographs show that droplets are grouped together in pairs and, although the droplets are of comparable size, the leading droplet is consistently larger than the trailing droplet. This observation suggests 'main' and 'satellite' droplets are being produced as the material jet necks down and droplets. If these droplets are treated individually, the mean droplet ejection frequency was calculated to be 25.3Hz with a standard deviation of 1.06Hz for the given parameter set.

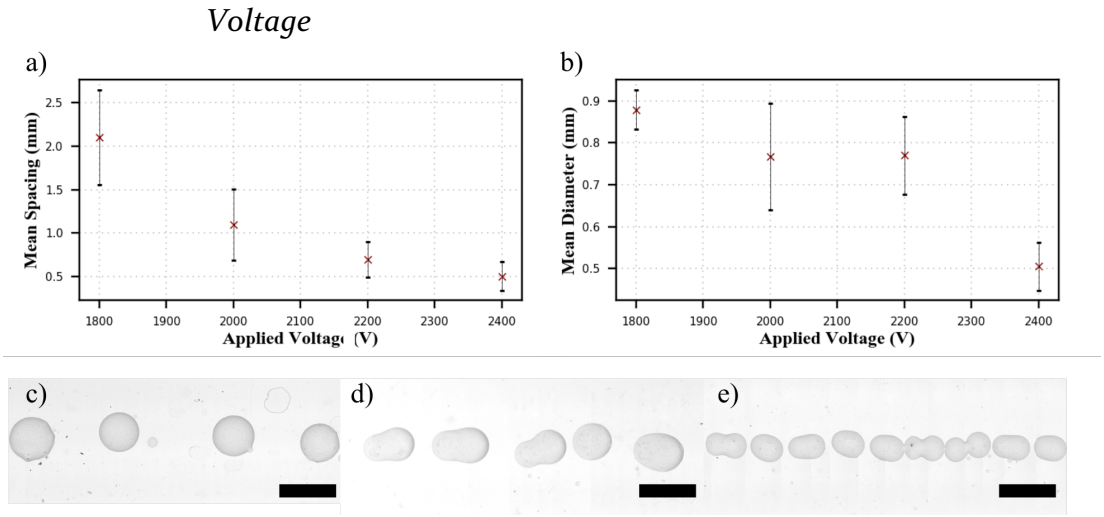

Figure 50 - a) Droplet spacing and b) mean diameter with increasing applied voltage. Error bars represent ±1 standard deviation. Microscope images of deposits at voltages of c) 1800V, d) 2000V, and e) 2400V. Scale bars are 1mm. For each voltage 10 samples were taken. Each sample consisted of 10 droplets

Bounds of the pulsating jet deposition mode were determined by increasing the voltage from 1kV-3kV and examining the response of the jet under stroboscopic optical microscopy (AM3715TB, Dino-lite, Taiwan). Deposits were then produced with a nozzle-substrate distance of 5mm and a feed rate of 1000mm/min over a distance of 30mm. Five samples were produced and the results are presented in Figure 50.

Increasing the magnitude of the applied voltage led to a reduction in the diameter of the deposited droplets. As expected for a constant ink flow rate, the this decrease in diameter was accompanied by an increased in the droplet ejection frequency (8Hz at 1800V to 33Hz at 2400V). Satellite droplets were less obviously present in droplets produced at the lowest voltage (1800V).

Flowrate

For a voltage of 2000V and a stand-off height of 5mm, the flowrate was increased from 10ul/hr until the limit of the syringe pump was reached (8ml/hr). Both the droplet diameter and the frequency of emission was found to increase with flow rate. The flowrate was found to have the most significant effect on the volume of the deposit, with a more than 200% increase in droplet diameter between the lowest and greatest flow rate (Figure 51). The droplet ejection frequency had the inverse relationship, falling from ~16Hz at the lowest flowrate (0.01ml/hr) to ~8Hz at the greatest (8ml/hr). The standard deviation of the spacing and droplet diameter reduced with flowrate, which is likely caused by a more consistent droplet volume being present at the nozzle's tip during printing.

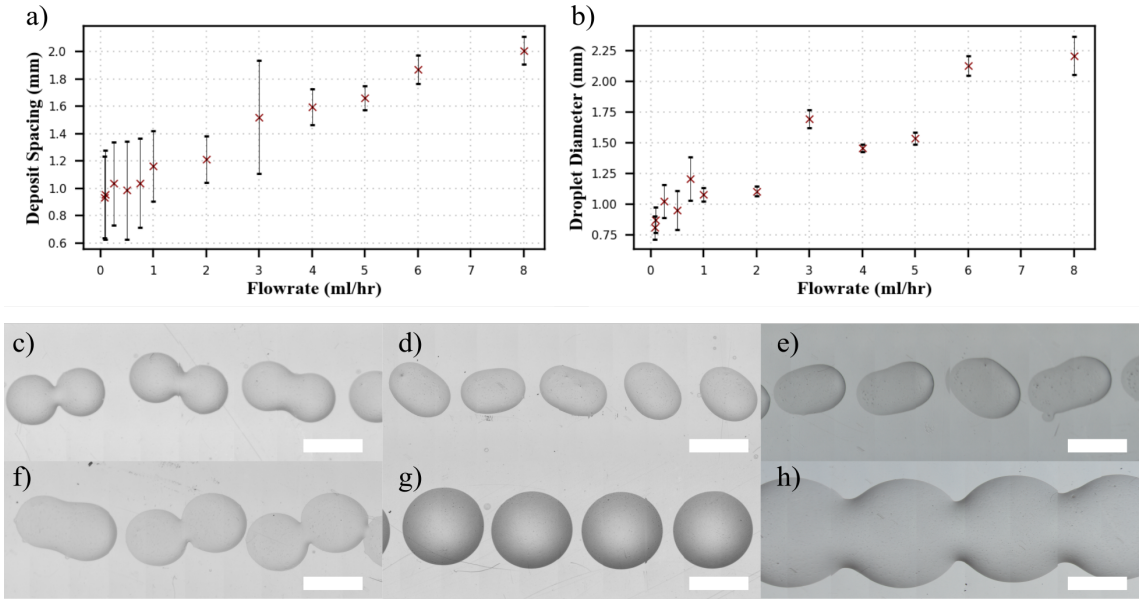

Figure 51 - a) Droplet spacing and b) mean diameter with increasing flowrate. Error bars represent ±1 standard deviation. Microscope images of deposits at flowrates of c) 0.01ml/hr, d) 0.1ml/hr, e) 0.5ml/hr, f) 1ml/hr, g) 5ml/hr, and h) 8ml/hr. Scale bars are 1mm. For each test point 10 samples were taken. Each sample consisted of 10 droplets

4.2.3 *Droplets by pulse-on-demand*

Conceptually, pulse-on-demand (PoD) is closer aligned to DoD inkjet techniques as the timing of droplet release can be directly controlled, rather than as a consequence of material and process conditions. This is achieved by selectively supplying a high-voltage pulses to trigger the release of a droplet, or series of droplets, from the nozzle. The period, or distance for constant velocity motion, between droplets is controlled by configuring the time between consecutive pulses. Although this is more complex to control than a pulsating jet system, it can achieve improved spatial positioning of droplets as well as allowing the waveform to be varied on a droplet by droplet basis. Using a similar approach to above, here a systematic approach is taken to gain an understanding of the effects of processing conditions on the shape and size of the deposits. By selectively applying the electric field, these results should demonstrate the volume and frequency of the droplets can be controlled independently while improving the spatial positioning of the droplets.

Voltage and minimum pulse width

When a voltage of sufficient magnitude is applied to a neutral meniscus, it is pulled into a conical shape that emits a jet as the electrostatic stresses overcome the surface tension. In PoD deposition, both the width and magnitude of the pulse needs to be sufficient to allow the initiation of jetting. To determine the minimum pulse width required to establish jetting at a given voltage, pulses of increasing duration were applied until a deposit could be detected on the PET substrate (Figure 52). This minimum pulse width provides the upper bound for the maximum jetting frequency. The non-biased jetting frequency can often be

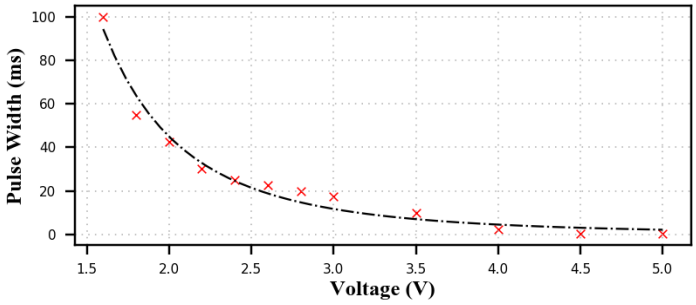

Figure 52 - Minimum pulse width required to trigger droplet ejection at increasing electric field strengths

lower than this boundary as the meniscus needs to time to recover and stabilise to avoid driving unwanted oscillations. Increased jetting frequency can be increase by biasing the material with a voltage just below the jetting onset voltage, therefore reducing the time taken for charge build-up.

Pulse Width

The value of the pulse width above the minimum value was investigated to determine its effect on the deposition volume. For a voltage of 2kV and a stand-off height of 2mm, the diameter of deposits was measured for increasing pulse widths. For pulses of 35-80ms, the diameter of deposits increases linearly. However, for pulses with a duration of greater than 90ms there is a step-change increase in the volume of droplets (Figure 53). Inspection of the deposition under

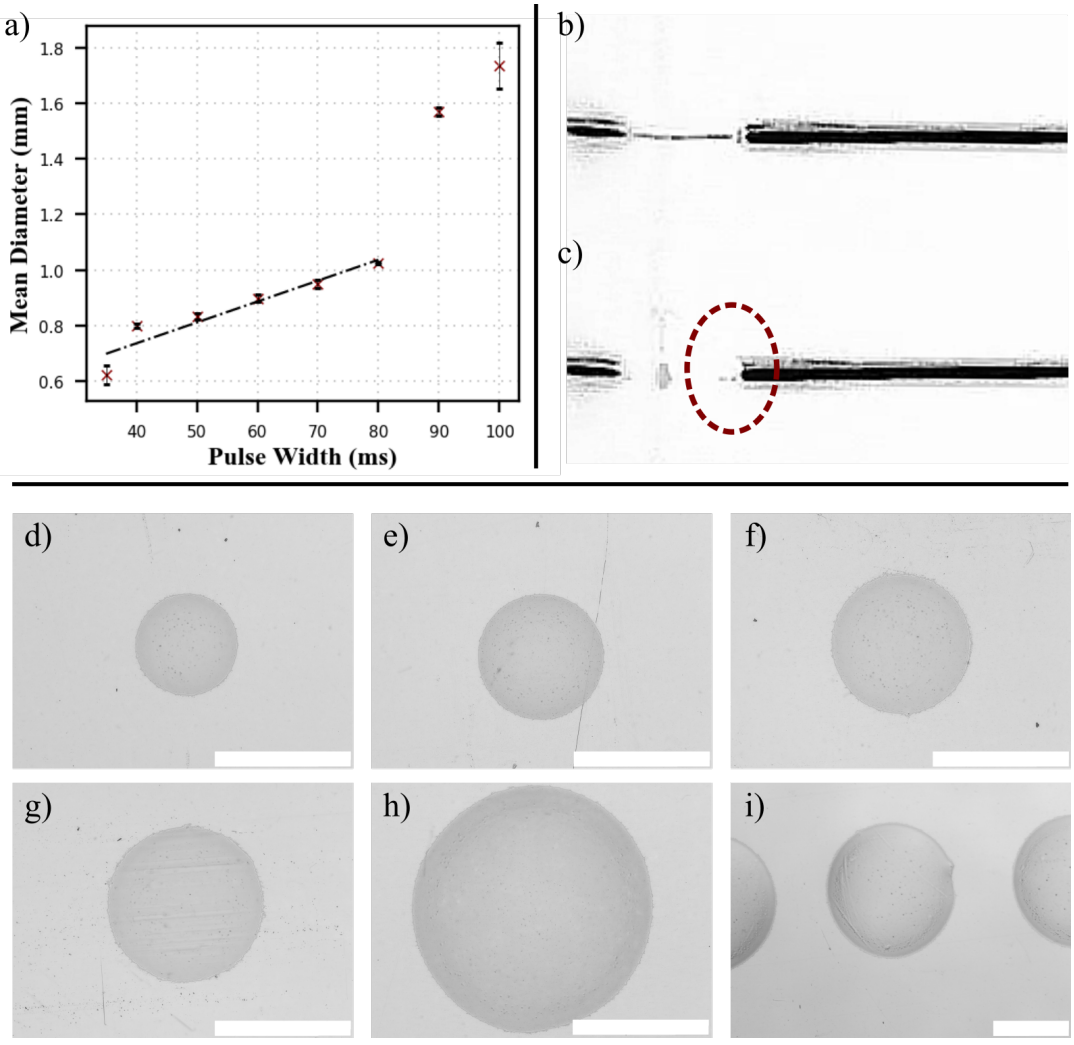

Figure 53 – a) Mean droplet diameter with increasing pulse width. Error bars represent ±1 standard deviation. b) Initial and c) secondary material ejection from a 100ms pulse width. Droplets produced with d) 35ms, e) 50ms, f) 60ms, g) 80ms, h) 90, and i) 100ms. All scale bars are 1mm. For each test point 10 samples were taken. Each sample consisted of 10 droplets

stroboscopic microscopy showed a primary and secondary deposit. In effect, a pulse width greater than 90ms appeared to be sufficient for the onset of the pulsating jet mode.

Voltage

For a constant pulse width of 100ms, increasing the applied electric field was found to increase the droplet diameter from ~600um to ~1500um (Figure 54). This is in contrast with the results from the pulsating jet, where an increased electric field resulted in a reduced droplet volume but increased the frequency of emission. In POD jetting the deposits for a given pulse took place from a static nozzle. Therefore, sequential ejection of droplets during the same pulse can lead to an increased magnitude in the size of the deposit. Again, optical microscopy at the deposition head showed the ejection of several deposits at greater voltages.

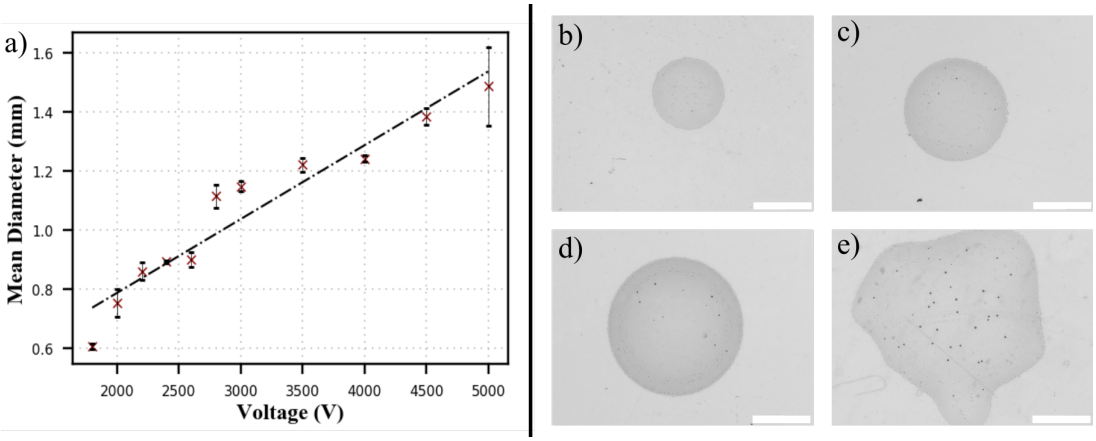

Figure 54 - Deposit diameter with increasing voltage and deposits at 2000, 3000, & 4000V. Error bars represent ±1 standard deviation. For each test point 10 samples were taken. Each sample consisted of 10 droplets

4.2.4 A comparison of pulsating jet and pulse-on-demand deposition mechanisms

Both deposition techniques are effective in producing droplets of PDMS, however the close coupling between jetting frequency and droplet volume presents a significant challenge for the pulsating mode. Significant empirical work is required to understand the interdependence and the factors that drives it. In practice, the simplest approach tailored the parameters for a specific droplet size before the nozzle head speed was adjusted to account for the corresponding ejection frequency. This approach will dictate print speed and droplet throughput.

Across all experiments, the variation in droplet diameter was found to be larger for pulsating jet deposition. The use of flow-based ink control, rather than pressure, led to temporal variation in meniscus volume at the nozzle tip. Qualitatively, this was found to have a significant impact on the volume of the deposited droplets. In the pulse-on-demand experiments, periodic cleaning of the nozzle to minimise material build up led to the deposition of more consistent droplet volumes. Such an approach was less feasible in the pulsating jet mode due to the continuous nature of deposition. In addition, high-speed translation of the nozzle is required to achieve suitable spacing at high droplet ejection frequencies in the pulsating jetting mode. Resonant vibration at certain actuation speeds led to increased variation in droplet size and position (Figure 55) due to changes in the relative position of the nozzle and substrate. This could perhaps be improved by adding stiffness or mass to the system to shift the system's natural frequency beyond the operating range.

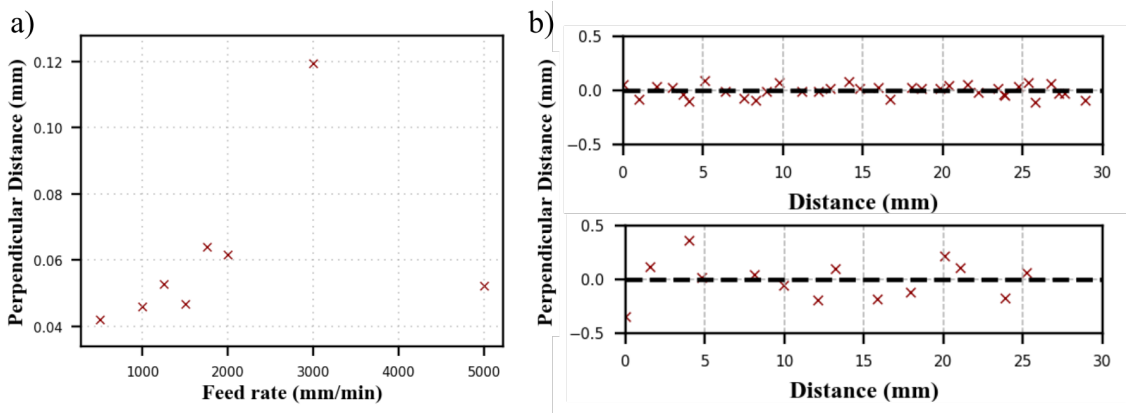

Figure 55 - Perpendicular distance of droplets from the mean print line and b) droplet positions relative to mean print line for feed rates of 1000mm/min and 3000mm/min.

Pulse-on-demand overcame many of the above challenges by de-coupling droplet size and volume through the selective application of a high magnitude electric field. Independent control of the droplet frequency and volume allows the size and spacing of the deposit to be driven by the requirements of the applications, while dynamic control of the pulse width and volume provides scope for on-the-fly changes in deposit volume. The sacrifice for this is reduced throughput for a given electric field and increased machine complexity. Increasing the voltage while reducing the pulse width can help increase the ejection frequency, however it is unlikely to match the higher frequency of biased pulsating jet printing.

Increasing the voltage beyond the usual stable jetting range was found to be effective but led to increased variation in droplet size.

In this work, deposition through the pulse-on-demand technique was conducted using a static deposition head to overcome challenges in vibration. Laser profilometry was used to decrease variation in the nozzle-substrate distance through pre-processing of G-Code, however this may be improved by transitioning to in-process monitoring of the nozzle-substrate distance or by monitoring material transfer by measuring the substrate current. Alternatively, improvements in alignment and machine stiffness could be achieved by moving away from the modular aluminium extrusion design.

4.2.5 Confluent elastomer features

Reducing the spacing between consecutive droplets allows the production of confluent features, however the magnitude of the spacing needs to be considered with respect to the volume of the droplets. Inadequate spacing can cause consecutive droplets to coalesce into a single larger droplet rather than forming a linear feature. In contrast, over-spacing can lead to poor edge definition with periodic bulging or the deposition of discrete droplets. In this work, the production of continuous features was made difficult due to the relatively large variation in droplet size during printing.

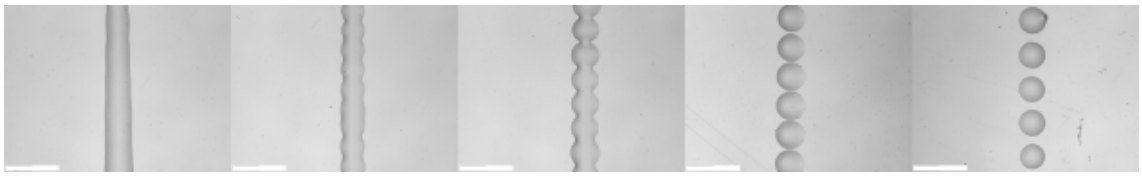

Figure 56 - Deposition of PDMS droplets with decreasing spacing. All scale bars are 500µm.

A series of experiments were conducted to evaluate the effect of decreased droplet spacing on the edge quality of printed lines (Figure 56). Droplets with an approximate diameter of 500µm produced through the pulse-on-demand deposition mode by applying a 1.8kV pulse for 80ms to the nozzle at 1mm distance from the substrate. Droplets were deposited over a distance of 20mm with decreasing spacing, ranging from 700µm to 300µm on to a PET substrate. This represented a maximum droplet overlap of approximately 60% (Figure 57).

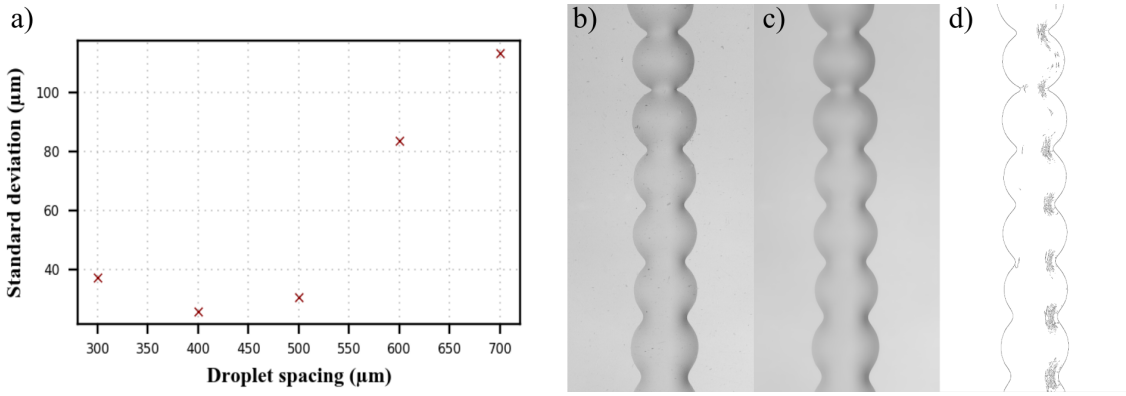

Figure 57 - Standard deviation as a measure of line quality

To define edge quality, optical micrographs of vertically aligned deposits were examined on a row-by-row basis to identify mean line width and variation in along the edge. At high spacings, discrete droplets were formed, however as the spacing decreased, 'necking' between droplets began to arise as deposits coalesced into confluent features. At droplet spacing of 300µm, or about 40% droplet overlap, continuous features with a mean width similar to the diameter of the individual droplets was produced. Beyond this point, confluent features with increasing width were produced.

The production of films extended this approach by depositing droplets with an overlap of approximately 40% in two directions. Experiments for investigating individual droplet and short linear deposits were achieved using positive polarity pulses. However, when transitioning to larger area films, the accumulation of charge on the insulating PET substrate introduced challenges with edge definition. Charge repulsion within the deposited fluid led to the production of dendrites, or fingers, that severely impacted the edge definition of the deposits. By altering the polarity of consecutive pulses accumulation was minimised and the edge definition improved (Figure 58b-c).

The polarity of the applied pulse was found to have minimal effect on the droplet volume, especially when compared to magnitude or duration of the pulse (Figure 58a). The surface roughness of the films was found to be ~0.26µm (Sa) over a 2mm^2 surface area. Inspection of the surface plots and microscopy data showed the surface roughness was negatively impacted by atmospheric dust ingress during manufacture.

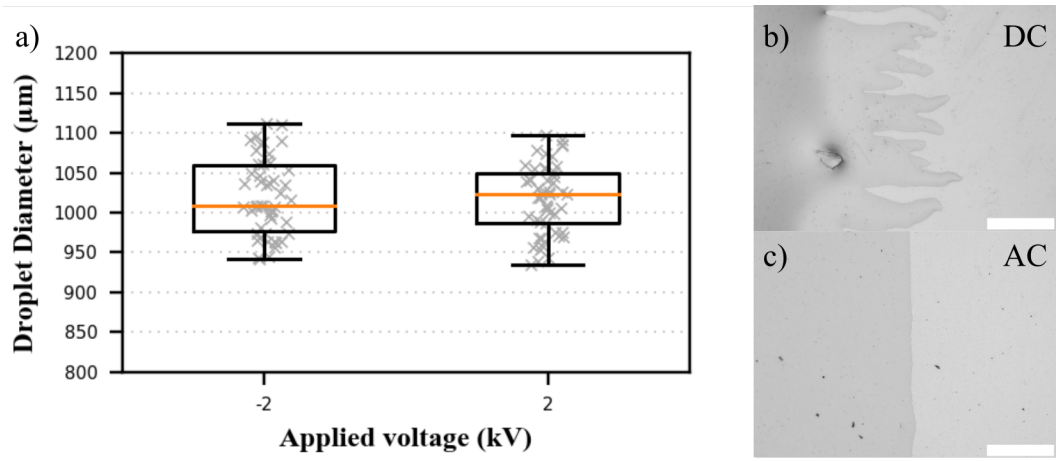

Figure 58 – a) Variation in diameter for droplets produced using positive and negative pulses with equal magnitude and duration and film edges produced using b) DC and c) AC fields. All scale bars are 500µm.

4.2.6 Challenges with electrohydrodynamic printing of elastomer features

A high variance in the diameter of droplets has been observed during the experiments in this chapter. Therefore, producing larger features with closely controlled geometry can be a challenge, especially during extended periods of printing. Transitioning to the pulse-on-demand approach improved the variance as it allowed in-process cleaning of the nozzle, however this had a detrimental effect on deposit time and mechanical cleaning of a thin, flexible nozzle had a tendency to permanently deform the nozzle tip. On occasion, this would vary the distance between the deposition head and substrate, which changed the characteristics of the deposit. Transitioning the process to a pressure-controlled ink supply, rather than a flow-controlled syringe pump, would help control the meniscus volume and minimise variation of the deposit dimensions.

Furthermore, challenges were discovered when examination of the deposits before curing showed temporal variation in the droplet diameter as the material wet to the substrate. Due to the low-contact angle and time frames of approximately 270 seconds, 2D measurements of the droplet diameter were used to define the relaxation behaviour of the droplet at room temperature. Droplets were ejected from the deposition head before the substrate was actuated into the field-of-view of a USB microscope for inspection. Actuation times meant the droplet response could only be monitored from 5 seconds after deposition until the droplet remained stationary. Through this approach, the droplet diameter increased by ~200% in the 70 seconds after deposition (Figure 60). Inspection with white light interferometry showed the final contact angle to be 1.2°. This time dependent variation means droplet diameter is driven by time to cure as well as the specific process parameters.

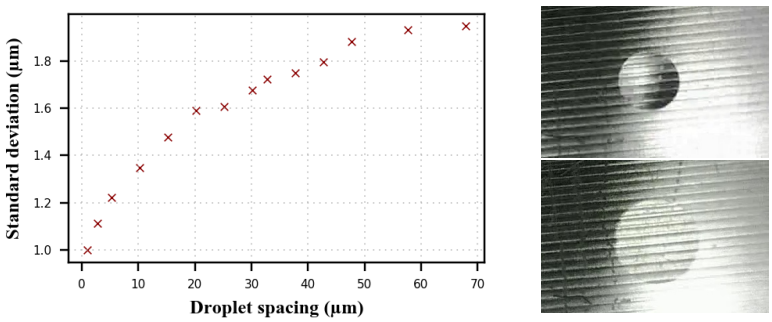

Figure 59 - Effect of material wetting on the final droplet area: a) droplet area with increasing time, b-i) droplet imaged ~0.95s after deposition, and b-ii) droplet imaged ~66s after deposition

The minimum volume of the droplets presented here are estimated to be ~800pL by assuming constant volume during deposition and curing. Although lateral and axial resolutions of ~500µm and ~5µm were realised, this is lower than demonstrated by McCoul et al. [171] through inkjet printing. Improving the resolution will require improvements in fluid delivery as well as a reduction in the internal diameter of the deposition nozzle, which may cause challenges for high viscosity, functionally loaded materials

4.3 Deposition of graphene platelet conductive features

EHD deposition was also explored for the production of conductive features alongside PDMS tracks. However, apparatus challenges, which did not provide sufficient value for the required development effort, meant that only a limited

feasibility study occurred as part of this work. Similar to the study for elastomeric inks, the use of direct vs alternating current is explored before a discussion of large area coverings using the electrospray mode and finer features using e-jet printing.

4.3.1 Conductive features through electrohydrodynamic deposition

The graphene ink was loaded into the syringe pump and a 22-gauge nozzle (413µm) was fitted to the deposition head. A PET substrate was then loaded into the machine and the nozzle moved 50mm away from the substrate. The flow rate was set to 25µl/min and the magnitude of the electrical field increased until a stable cone could be identified at the tip of the nozzle.

At 7.5kV (1.5kV/mm) the Taylor cone appears stable in both the AC and DC regimes (Figure 60a-b), which allowed a direct comparison of deposit morphology with increasing deposition time. Figure 60c-f shows the DC electrospraying technique transferred the graphene ink to the substrate during the early stages of deposition but then became reduced as time progressed. Imaging of the Taylor cone reinforced this observation as droplets stopped being emitted after approximately 50s. In contrast, under the AC regime (100Hz) material continued to be deposited throughout the exposure. Building on this to actuate the deposition head allowed the production of large area coatings of the graphene platelet ink through the spraying mode(Figure 60g-h).

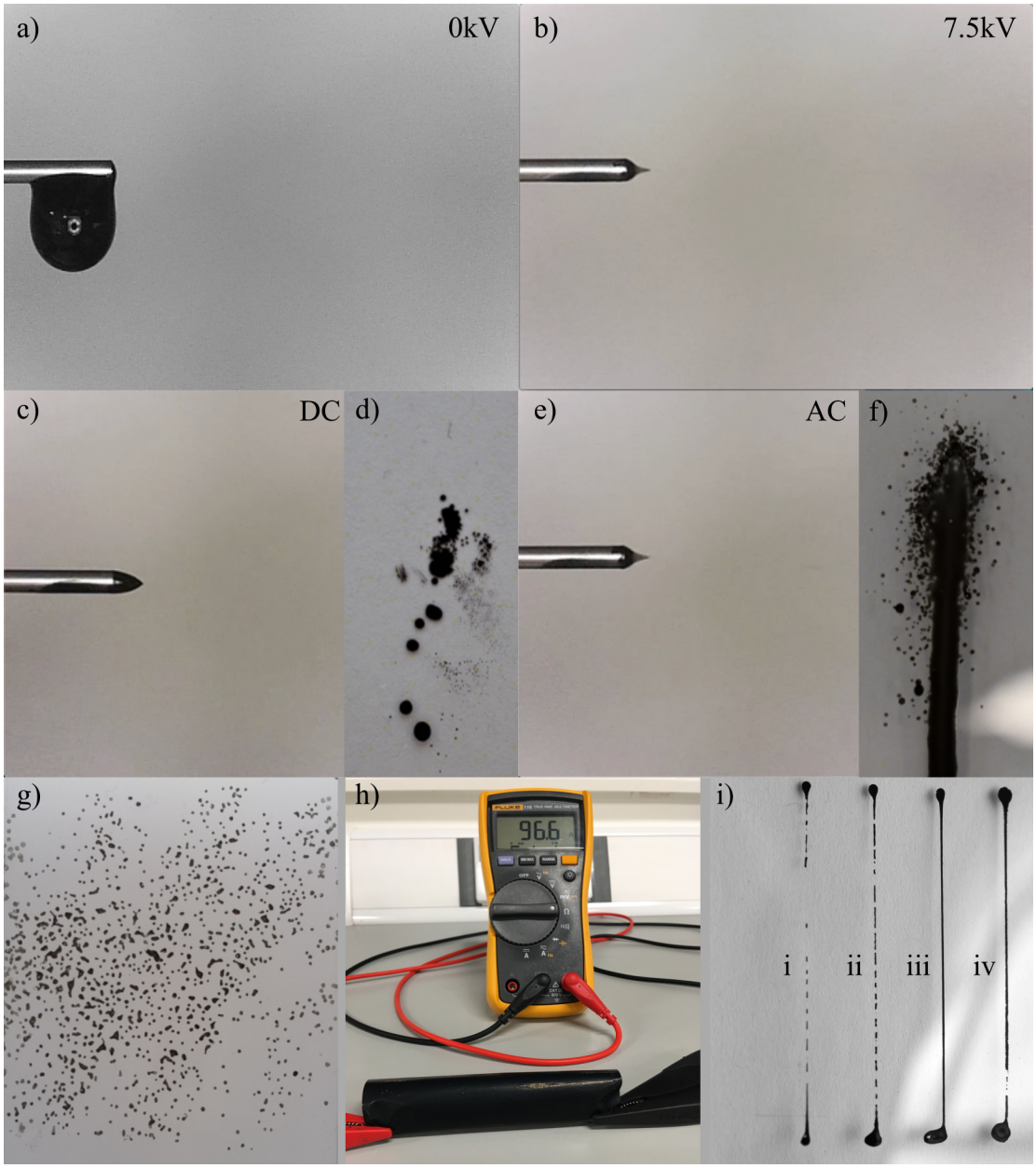

Figure 60 – a-b) Taylor cone formation under a DC electric field, c-f) direct current and alternating current electrospray, g) droplets of graphene platelet ink, h) conductivity measurement of electrospray printed sample, i) e-jet printed graphene platelet lines

Direct write patterning was explored to selectively produce conductive traces for use in sensing and actuation devices. E-jet was successfully applied to produce confluent lines with a width of 200µm and length of 30mm using an applied voltage of 2kV at 1mm stand-off distance (Figure 60i). Increasing the frequency of field to 100Hz produced consistent patterning at a federate of 1000mm/min. The hurdles demonstrated while using e-jet for elastomer materials were also present for the patterning of conductive features. However, since the targeted lateral resolution is greater for conductive materials and the rheology of conductive inks

are less challenging. Consequently, it was decided to explore more robust processes for printing conductive elements.

4.4 Chapter summary

Electro-hydrodynamic deposition was explored for the deposition of elastomeric inks. An initial scoping study using electrospray and e-jet printing was conducted for a number of silicone elastomer materials. A simplified PDMS precursor was successfully deposited using the electrospray regime following dilution with ethyl acetate. The lack of cross-linking agents in the ink presented challenges with material curing and required exposure to deep-UV wavelengths. The limited penetration depth (~200nm) of short wavelength UV presents challenges when curing films approaching 1µm and led to a skin-forming on the surface of the elastomer. Furthermore, the unknown mechanical properties of the deposited material creates additional hurdles in practical application.

Using more conventional silicone formulations, deposition using droplet based e-jet printing was demonstrated as a feasible technique for patterning silicone elastomers. Both the pulsating jet and pulse on demand deposition modes were demonstrated with droplet sizes (~800pL) comparable to more conventional direct write techniques. The parameters for initiating pulsating jet and PoD modes were investigated for their suitability for producing soft thin films. Direct spatial control of the droplets was found to be difficult to achieve in the pulsating jet mode and required multiple process parameters to be balanced. The PoD technique was found to simplify printing and increase the reliability of deposits. Droplets with maximum heights of 5µm and diameters of 500µm could reliably be produced. Using an overlap of 40% the droplet diameter allowed the production of confluent features using PoD e-jet deposition.

Deposition of conductive inks was also investigated using e-jet and electrospraying techniques. The production of films through electrospray was found to be successful and relatively simple owing to the higher conductivity and lower viscosity of the ink. Selective patterning, through e-jet printing, had severe challenges with the size and repeatability of the deposit. Since the targeted resolution of the features are significantly smaller then for the elastomer inks, the development time and cost were decided to be prohibitive – especially when

more conventional, robust, and commercially available techniques can achieve the required resolution.

5 Aerosol jet printing of carbon conductive inks

The production of soft devices with embedded actuation and sensing requires the integration of functional materials alongside the structural elastomer. Although the previous chapter demonstrated the deposition of a conductive ink using electrohydrodynamic deposition, the repeatability and robustness of the process presented challenges that are compounded as resolution increases. This chapter aims to complement the previous by investigating Aerosol Jet, a more established direct-write technique, to additionally provide the patterning of carbon-based conductive materials. Although leveraging an existing technique overcomes many challenges in materials and apparatus development, significant empirical work is still required to develop reliable deposition. This chapter explores the process, the effect of process parameters on the shape and structure of the deposit, and then correlates these to conductivity. As an extension of this work, and an illustration of its potential beyond film-based devices, deposition on to complex non-planar structures is presented using the toolpath generation tools discussed in chapter 3.

5.1 Introduction to Aerosol Jet printing

Aerosol jet (AJ) printing emerged from the DARPA-funded MICE (Mesoscale Integrated Conformal Electronics) project in the late 1990s, which aimed to develop manufacturing processes capable of depositing a range of materials on to virtually any substrate [223]. To date, AJ has been the most successful outcome of the project with commercialisation through Optomec Inc. and Integrated Deposition Systems. Through the use of a directed aerosol stream rather than sequential droplet ejection, AJ introduced improved material compatibility, increased resolution, and allowed consistent deposition at offsets of 1-5mm [224]. This helped accelerate direct write technologies into a range of environments, including active and passive electronics; actuation and sensing technologies; and even selective chemical and biological processing. A review of the technology was published as part of this work and can be found in Appendix A [225].

5.1.1 *Process Overview*

During AJ (Figure 61), ink is atomised, suspended within a carrier gas, and directed towards a substrate that is articulated with respect to the deposition head to achieve spatial patterning. By combining an effective focussing mechanism with the production of a uniform aerosol, deposits that approach 10µm can be achieved [226, 227]. Any material that can be suspended within an aerosol can be processed using the AJ deposition technique. Commercial systems use ultrasonic or Collison atomisation to generate an aerosol from inks with viscosities that range from 1 to 1000cp [228].

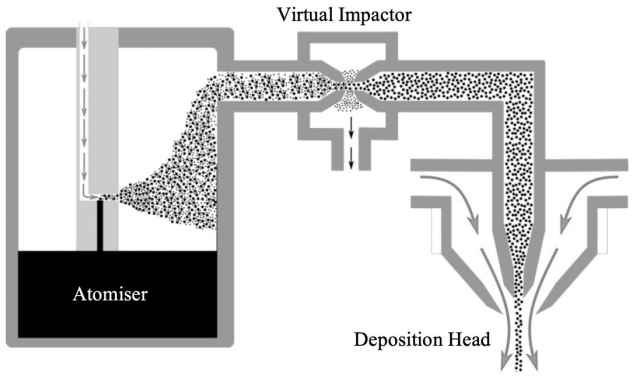

Figure 61 - Schematic of Aerosol Jet Printing Process

Aerosol generation

Ultrasonic atomisation produces an aerosol from small volumes (~2ml) of low viscosity (1-10cp) inks, which limits material throughput and material compatibility. This approach is attractive in many contexts as the distribution of droplet sizes (dispersity) is narrower than competing methods [172]. For AJ, this removes the need for secondary refinement of the aerosol. In contrast, pneumatic atomisation is tolerant of a greater range of viscosities (1-1000cp) and atomises from a reservoir of approximately 50ml at the expense of an aerosol with high dispersity.

In ultrasonic atomisation a transducer is submerged within a transfer medium, typically water, where it oscillates at high frequency (Figure 62a-1). A wave is propagated through the transfer medium to a vial suspended above the transducer (Figure 62a-2). Within the vial, a standing wave is formed on the surface and the superposition of consecutive waves results in the formation of large peaks (Figure 62a-3). Local shear at the top of these peaks results in small

droplets being ejected from the bulk ink. Finally, a positive pressure is applied to the vial to drive the aerosol from the vial towards the deposition head (Figure 62a-4).

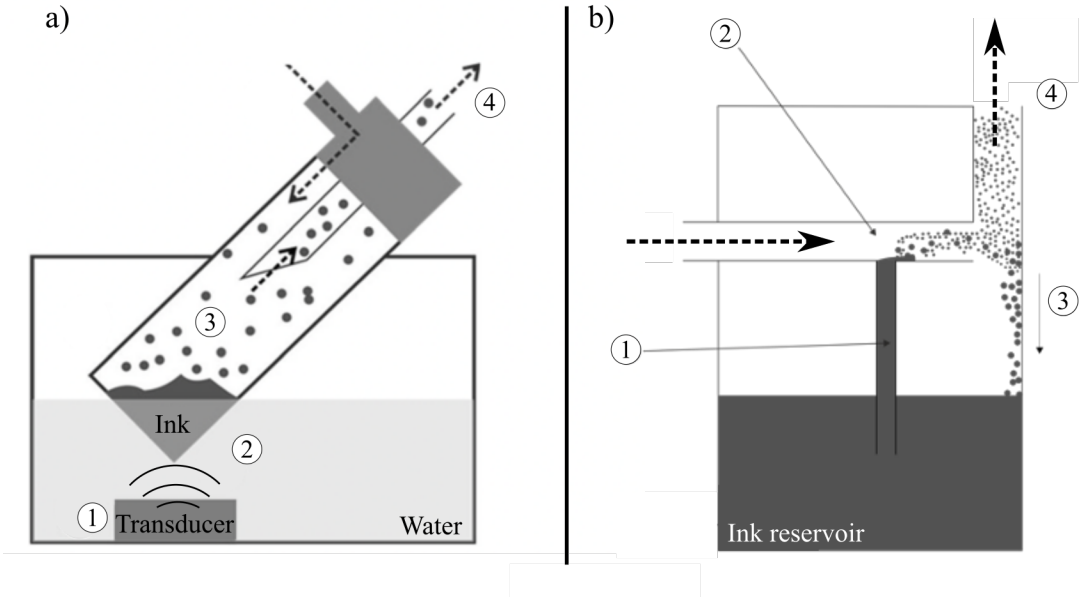

Figure 62 - Schematic of an ultrasonic atomiser used for Aerosol Jet printing

During atomisation with a Collison atomiser, a carrier gas is accelerated across the top of an ink supply channel (Figure 62b-1). This creates a region of reduced static pressure that draws the ink to the carrier gas flow. When the ink reaches the level of the carrier gas stream, the topmost layer is sheared producing a series of polydisperse droplets (Figure 62b-2). Large, high-inertia droplets within this stream are impacted on the side wall of the atomising chamber and return to the reservoir (Figure 62b-3), while lower inertia droplets remain as an aerosol and are exhausted from the atomiser towards the virtual impactor (Figure 62b-4).

Aerosol refinement

Aerosols produced using a Collison atomiser are polydisperse due to the inconsistent, chaotic perturbation introduced to the fluid stream. Although the sidewall of the atomisation chamber acts as a low-pass filter for removing the largest droplets, refinement of the aerosol through virtual impaction is required to produce deposits suitable for deposition. The virtual impactor uses a region of stagnant flow to separate droplets within an aerosol stream based on their inertia (Figure 63). Small droplets, those with insufficient inertia to pass through this region, are ejected radially and collected in the major flow. As low-inertia

droplets are often the cause of overspray in AJ, these small droplets can be vented to atmosphere or collected and recycled into the main reservoir. The larger, high-inertia droplets pass through the stagnant flow region and continue towards the deposition head.

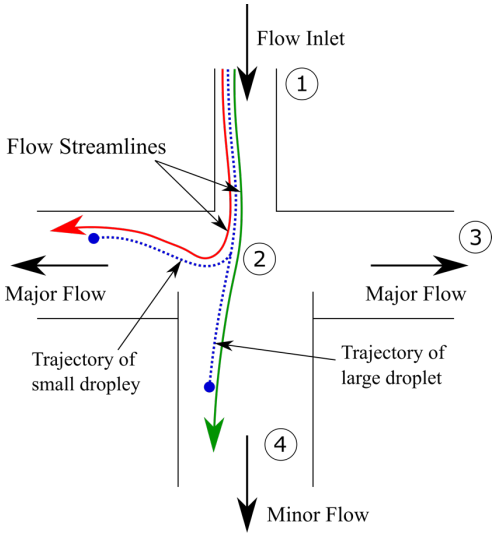

Figure 63 - Schematic of a virtual impactor used for flow refinement during aerosol jet printing

Aerosol Deposition

Following the production of a suitable aerosol, it is transferred to deposition head by the carrier gas flow. Here, it is focussed using a combination of a virtual and physical nozzle (Figure 64). The introduction of a secondary flow constrains and constricts the aerosol within an annular sheath that forms an interlayer between the aerosol and the physical components. The aerosol and sheath gas are further focussed by passing through a physical nozzle before being deposited on to the substrate.

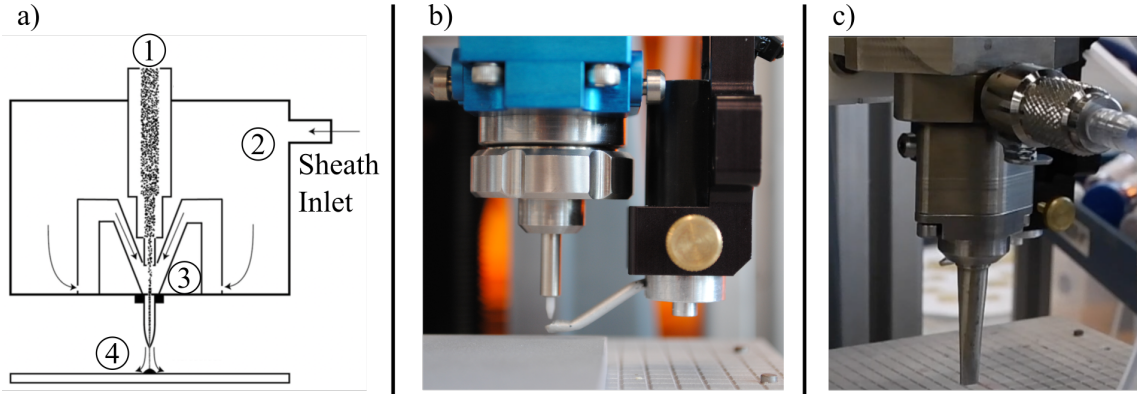

Figure 64 - Schematic of the aerosol jet deposition head

The application of a sheath gas results in process characteristics that are unique to AJP: the aerosol flow is collimated, which supposedly enables consistent deposition at a 1–5 mm stand-off distances; the inter-layer between the aerosol stream and the physical nozzle reduces the instances of nozzle clogging; and, through the manipulation of the aerosol flow rate relative to the sheath, it enables in-process control of the deposition geometry without changes in hardware. The combination of virtual and physical nozzles can allow deposits that are one tenth the size of the nozzle's orifice [229].

5.2 Effect of process conditions on the geometry of Aerosol Jet printed features

Deposit quality is reliant on a multitude of factors (Figure 66). The apparatus, process and design are readily configurable, while the substrate and environmental factors are more difficult to control. Materials development is an active research area for AJ and the development of bespoke inks contribute to the development of reliable, high-quality deposits. Due to the long lead times associated with materials development, commercially available inks were targeted for this work. Two inks were deposited: a graphene nano-platelet ink, which has formed the primary focus of this thesis; and a carbon black-glycerol ink developed by Maria Lukic-Mann, who led the materials development aspects of the wider project. This section explores the effects of process and design parameters on the quality of printed features using the graphene ink.

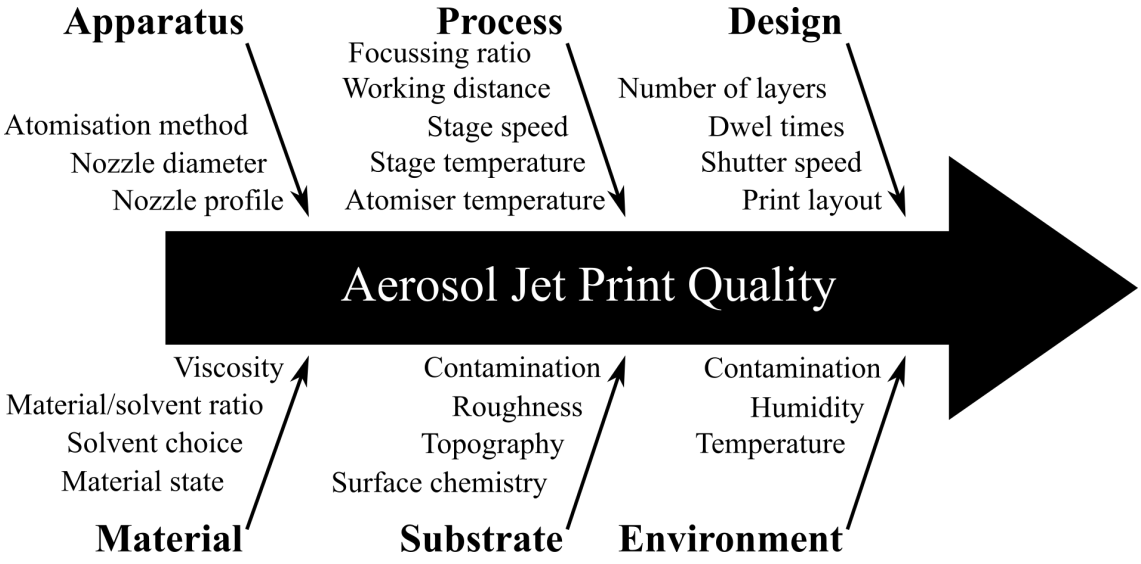

Figure 65 - Factors that affect Aerosol Jet printing

5.2.1 *Methods for evaluating Aerosol Jet printed features*

Control of the nozzle output is achieved through manipulation of the airflows used to generate the aerosol (atomiser gas flow), vent excess (exhaust gas flow), and focus the aerosol (sheath gas flow). The effects of these parameters are investigated alongside the effects of substrate velocity and temperature through systematic variation. Unless otherwise stated, 10mm single width lines were deposited on to precleaned glass slides and then analysed using optical microscopy and white light interferometry. Precleaned glass slides were selected to minimise the effect of dust ingress and to simplify measurement from a flat glass surface.

A 50ml volume of graphene platelet ink (CamGraph IJ3, Cambridge Nanosystems, UK) was loaded into the pneumatic atomiser, held at a temperature of 30°C, and stirred continuously at 200rpm using a magnetic stir bar. When atomiser or sheath flow was applied, the flow rates and pressure were left to stabilise before initiating a deposit. The glass slides were loaded on to a bespoke 5-axis deposition platform (Thorlabs, USA & Aerotech, USA) before initiating deposition.

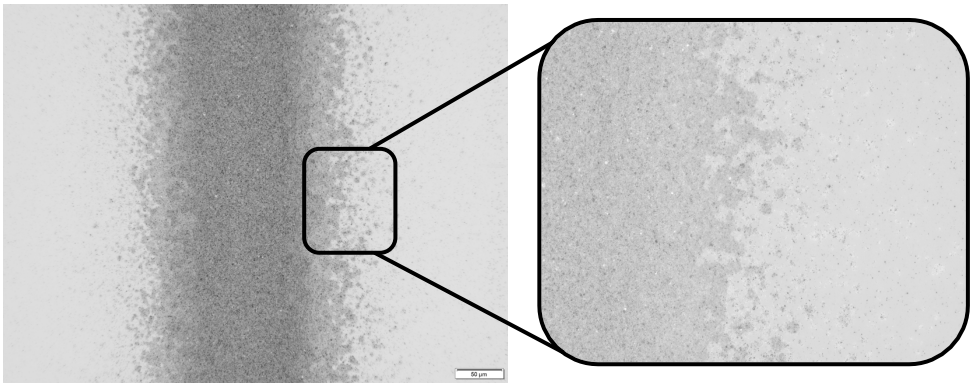

Figure 66 - Overspray in aerosol jet printed features

Deposits were characterised based on their peak height and width; however, since the aerosol flow consists of a distribution of droplet sizes, their position from the central axis of the line varies dependent on the volume of each droplet. This results in deposits with gradated edges (Figure 66), rather than a sharp well-defined edge. This makes objective measurement of feature width challenging when comparing between samples prepared with differing process inputs. To

overcome this the full width at half maximum height (FWHM) of printed features has been used.

For parameters sets that led to deposits with a central, high-aspect feature and a large amount of overspray, FWHM and peak height (Figure 68) presented these as positive outcomes despite much of the deposit not contributing to the functional capacity of the printed features [230]. Therefore, a subjective measure of the width of the overspray was compared to the FWHM as a measure of line quality. The ratio of the FWHM to the overspray width has bene defined as the quality ratio. Since the FWHM typically fell within the confluent portion, this provided a good indication of the portion of the line that contributed to the function of the printed feature.

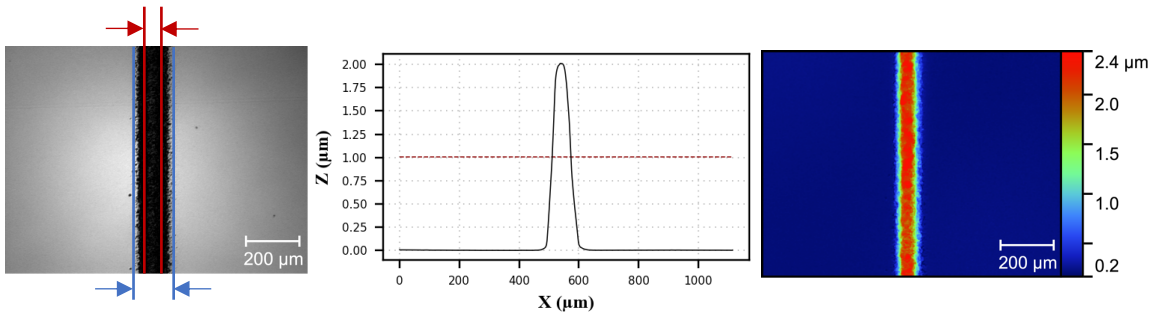

Figure 67 - Quality ratio for AJ printed lines: a) optical micrograph with annotations for FWHM and overspray, b) Average surface profile of an AJ printed line with the FWHM and c) white light interferometry scan of AJ printed line

$$Quality\ Ratio = \frac{FWHM}{Overspray\ width}$$

Estimation of print height through optical microscopy

Beyond the geometric limits for design, two observations from the characterisation of process parameters can be drawn that have practical consequences for this project: firstly, the exact geometry of AJ printed traces can be highly variable even with fixed process parameters, especially in environments with changeable conditions (temperature, humidity etc.); and secondly, three-dimensional characterisation of profiles using white light interferometry does not represent a time efficient way of comparing the geometry or quality of deposits between print runs.

Reducing temporal variation required improved control of the environment that added increased cost and complexity that was not feasible in the apparatus used in this work; therefore, it was decided to use ad hoc iterative test prints to compensate for any change in print geometry before initiating the process. To achieve this, grayscale values were taken from two-dimensional optical microscopy images and correlated to line height data gathered through white light interferometry to allow more rapid calibration of print parameters.

Grayscale as an indication of printed feature height

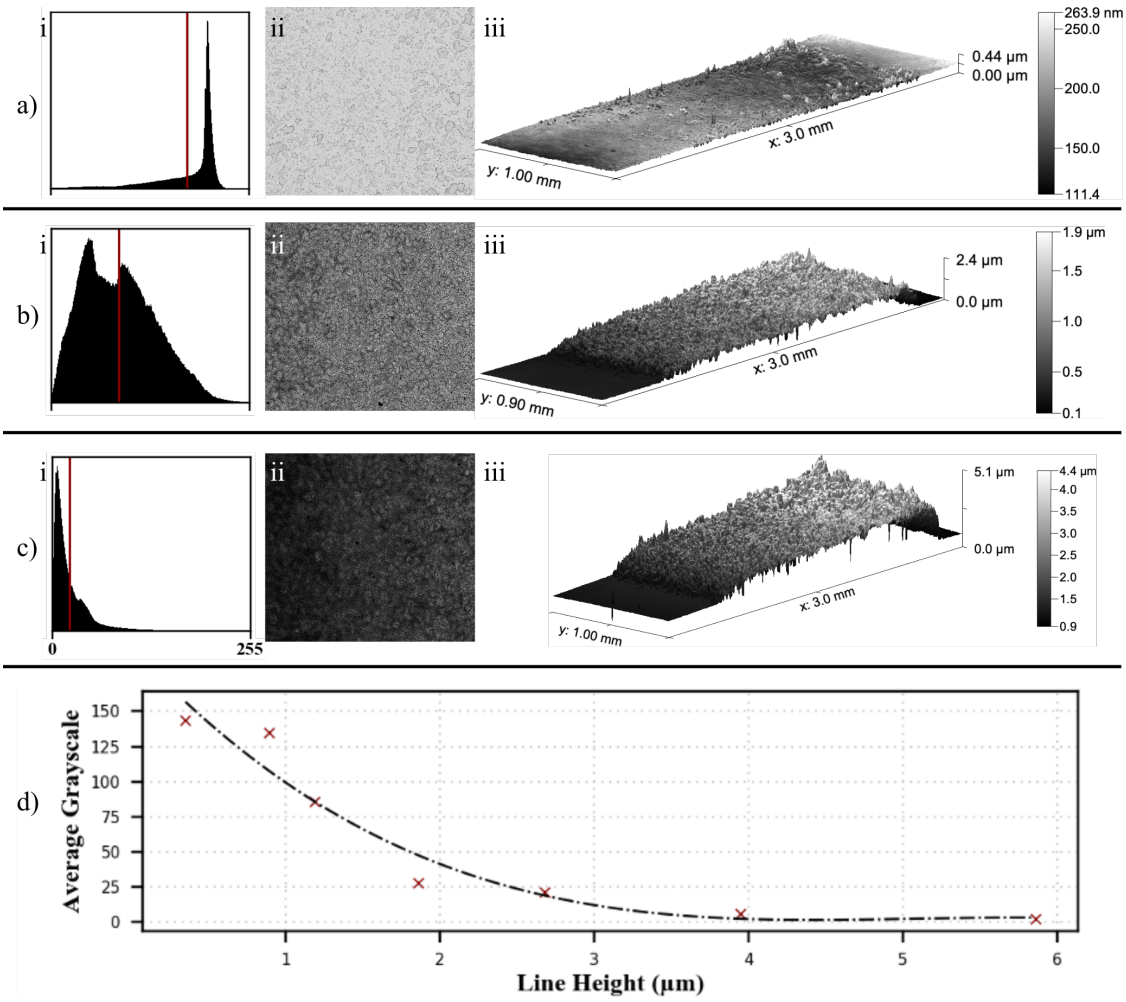

Figure 68 - Grayscale as an indication of print height. a-c) (i) Histograms, (ii) optical micrographs, and (iii) 3D surface plots of printed features with 1, 6, and 10 layers, respectively. d) Effect of line height on the average grayscale of printed features.

A series of depositions were created using a 3mm slotted nozzle travelling at 2mm/s at a distance of 2mm with a sheath and atomiser flows of 400 and 500sccm, respectively. The height of the deposits was varied by increasing the number of nozzle passes from 1-20 before being imaged using optical microscopy

and white light interferometry. Initially through ImageJ, and later through OpenCV, the distribution of grayscale and mean grayscale were plotted in histograms (Figure 68). The mean grayscale provided a strong indication of thickness, with opacity found from features with approximately 4µm onwards. This initial set of results provided a useful tool for the comparative performance of the printer between print runs. Collection of data over longer periods should allow improved prediction of layer height.

5.2.2 *Effect of substrate heating on Aerosol Jet printed features*

Substrate heating helps drive residual solvent from deposited features and, if the degree of heating is sufficiently high, sinters the material to increase the conductivity of traces. For AJ, accelerated solvent evaporation can be important to prevent the sheath gas from interacting with previously deposited material. These effects are most prevalent when printing features in close proximity, for example in fine pitch electronics, large areas of infill, or with low nozzle speeds. In this work, substrates were heated to 120°C using a silicone heater applied to the rear of the aluminium bed. The effect of deposits produced on heated and non-heated substrate can be seen in Figure 69.

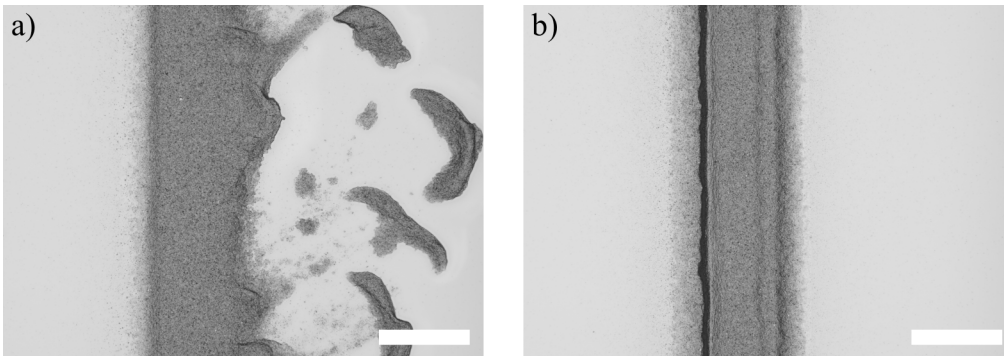

Figure 69 - Aerosol Jet deposition a) without substrate heating and b) with substrate heating

5.2.3 *Effect of nozzle height on Aerosol Jet printed features*

Datasheets describe Aerosol Jet as producing a collimated jet that provides consistent deposition at stand-off distances of 1-5mm. In academic studies, this has largely been reaffirmed with only a moderate increase in the line width with working distance [231]. Here, the relationship between the geometry of the deposit and the working distance is investigated for the graphene platelet ink. The distance from the nozzle to the substrate was varied from 1-8mm in

increments of 0.5mm during a single-pass print at 2mm/s to produce 15 traces on to a glass substrate heated to 120°C. The atomiser and sheath gas flow rates were set to 600sccm and 300sccm, respectively. This process was repeated five times before the samples were analysed.

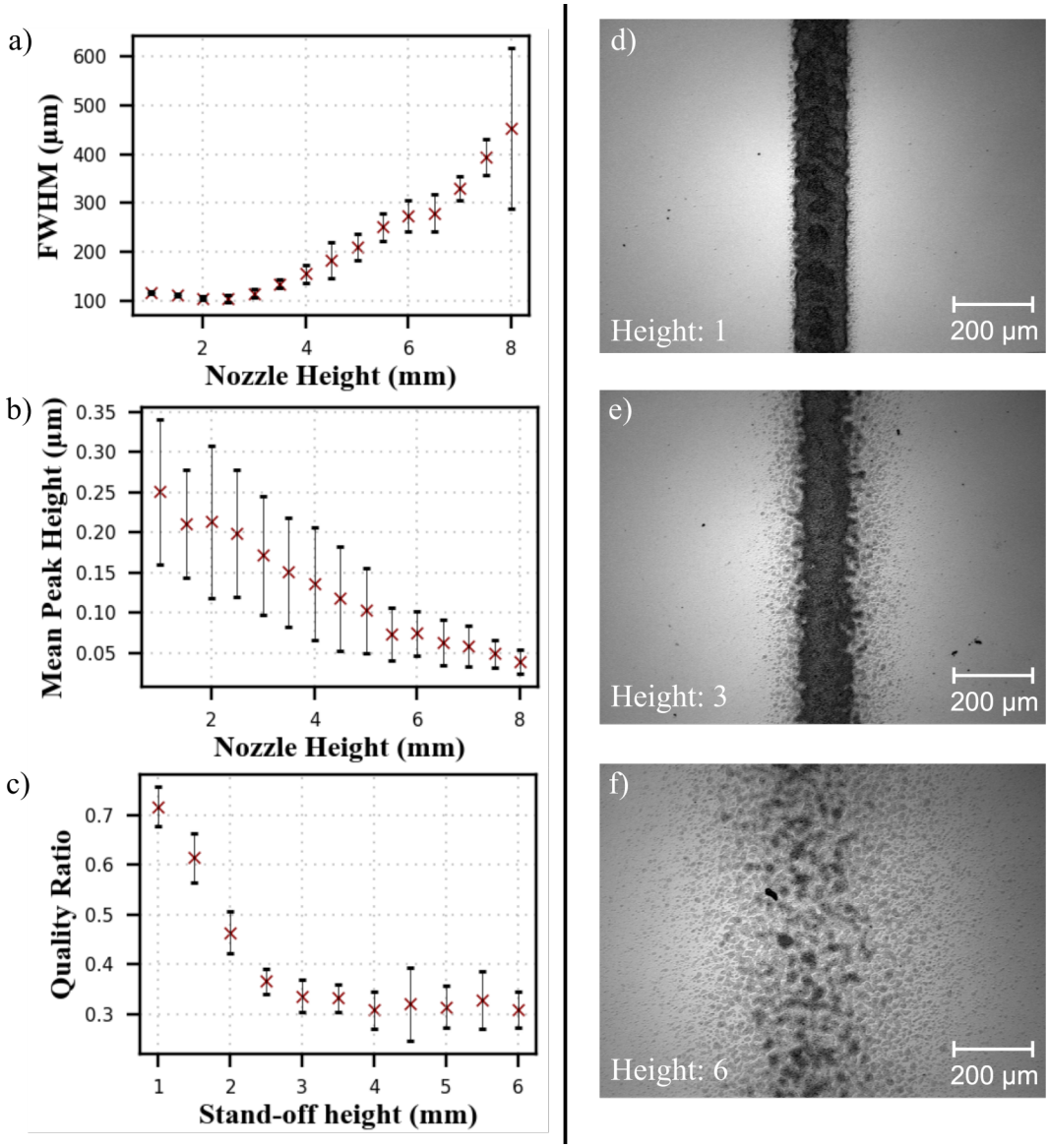

Figure 70 - The effect of nozzle-substrate distance on the mean peak height, FWHM, and quality of Aerosol Jet printed features. Error bars represent ±1 standard deviation. n=10

The mean width of the deposits was found to be relatively stable at stand-off distances ranging from 1-3mm, with a moderate focus point around 2mm (Figure 70a). From distances of 3-8mm, the maximum height of printed traces were found to decrease from ~0.25µm to 0.05µm (Figure 70b), while the full width at half maximum height increased from ~100µm to over 450µm. The standard deviation of deposit height was found to decrease with deposit height; however,

the coefficient of variation, or relative standard deviation, was found to be independent of nozzle height and remained consistent at approximately 0.4.

The quality of the printed lines was found to have the inverse relationship to the width of features as the quality is stable for moderate to high stand-off distances (3-6mm) but decreases significantly when the substrate is in close proximity to nozzle exit (1-3mm) (Figure 70c). This can be explained by expansion of the jet as it enters atmospheric conditions and a reduction in droplet mass caused by inflight solvent evaporation. This reduces droplet inertia and increases the material's tendency to follow gas flow rather than impact on the substrate. As small droplets have a greater surface area to volume ratio, they will evaporate more readily and lead to a loss of edge resolution, increase in overspray, and reduction in line quality.

5.2.4 Effect of nozzle velocity on Aerosol Jet printed features

Increasing the translational velocity of the nozzle was expected to decrease the volume of material deposited over a given area since the gas and, therefore material, flow rates are held constant. Nozzle velocities ranging from 0.1-3mm/s were investigated their effect on the droplet geometry when deposited on to glass slides held at 120°C with a nozzle stand-off distance of 2mm.

The maximum height of printed features decayed with nozzle velocity, starting from approximately 65µm at 0.1mm/s and tending towards 200nm at 3mm/s (Figure 71b). With increasing velocity, deposits transitioned from confluent features to a series of discrete droplets. Further increases in velocity would be expected continue this trend until the maximum height is equivalent to the solid content within the largest droplets. The FWHM was found to moderately increase with velocity (Figure 71a); however, this is the result of the normal distribution of droplets within the aerosol stream and the reduced deposit volume at high nozzle speeds, as evidenced by the consistent width of the

overspray and a comparison of cross-sections. The quality of the printed deposits shows a similar trend due to its dependence on the FWHM.

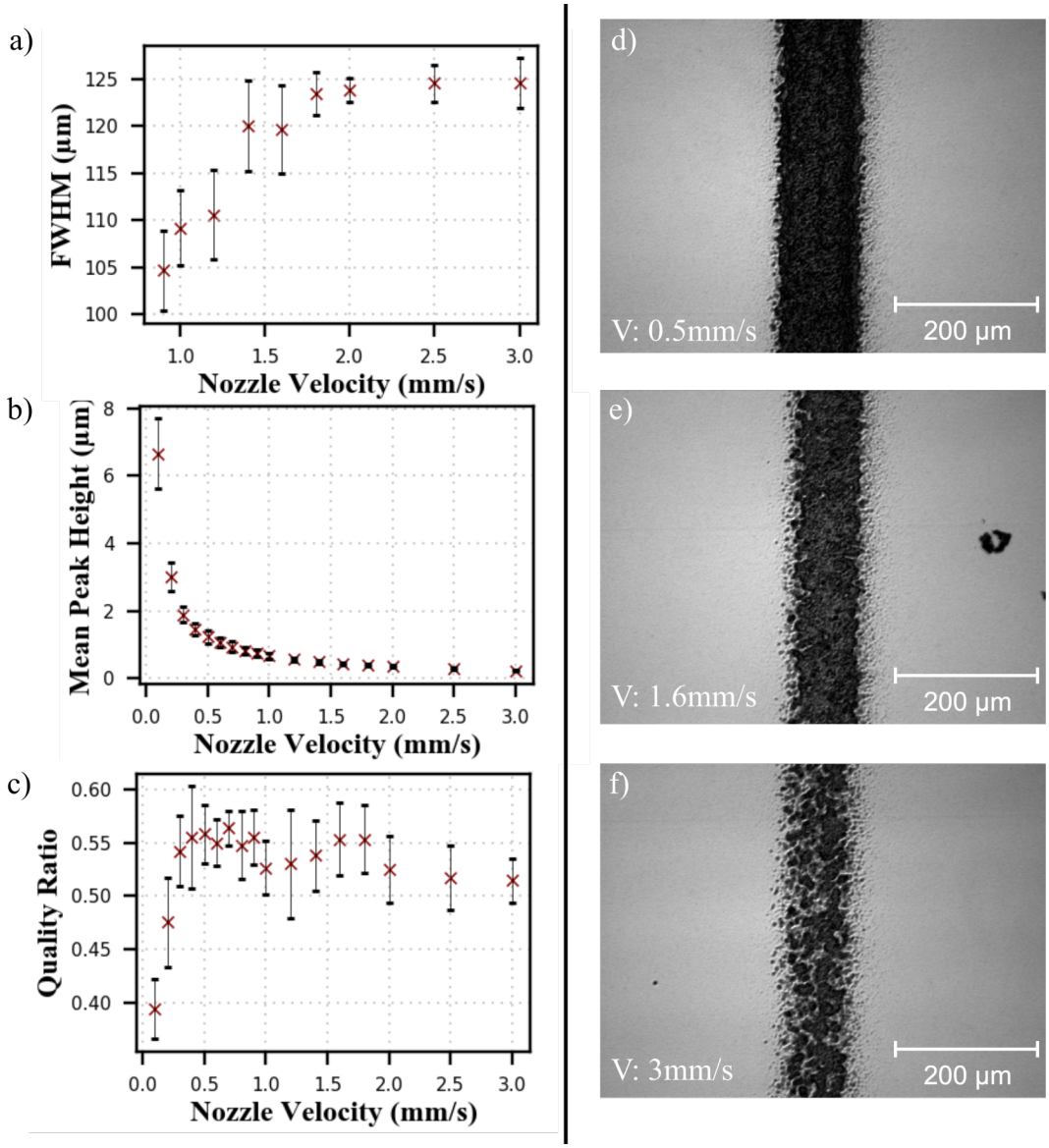

Figure 71 - The effect of nozzle velocity on the mean peak height, FWHM, and quality of Aerosol Jet printed features. Error bars represent ±1 standard deviation. n=10.

At speeds below 1mm/s, the width and height of features were found to have a high degree of variance. Since the material is in the liquid state upon deposition, solvent evaporation takes longer to accomplish due a lower time in flight. This makes the wet deposit vulnerable to interaction with residual gas flows, which can lead to a loss of resolution and line quality (Figure 71).

5.2.5 *Effect of gas flow rates on Aerosol Jet printed features*

Material flow and delivery is controlled through the manipulation of the atomiser and sheath gas flow rates. The effect of these parameters was investigated in

isolation before their combined effects were explored through investigation of the focussing ratio:

$$Focusing\ Ratio\ = \frac{Sheath\ flow\ rate}{Atomiser\ flow\ rate}$$

Initial experiments showed that increasing the sheath flow leads to increased mean peak height and reduced FWHM (Figure 72). Excessive increases of the atomiser, or reduction of the sheath flow, were found to introduce nozzle clogging. Flow rates of approximately 350-600sccm 2atomiser) and 175-300sccm (sheath) were found to minimise the instances of nozzle clogging. Moderate focusing ratios (~1-2) were found to produce higher quality deposits compared to more extreme values (Figure 72c). In practice, controlling the width of printed

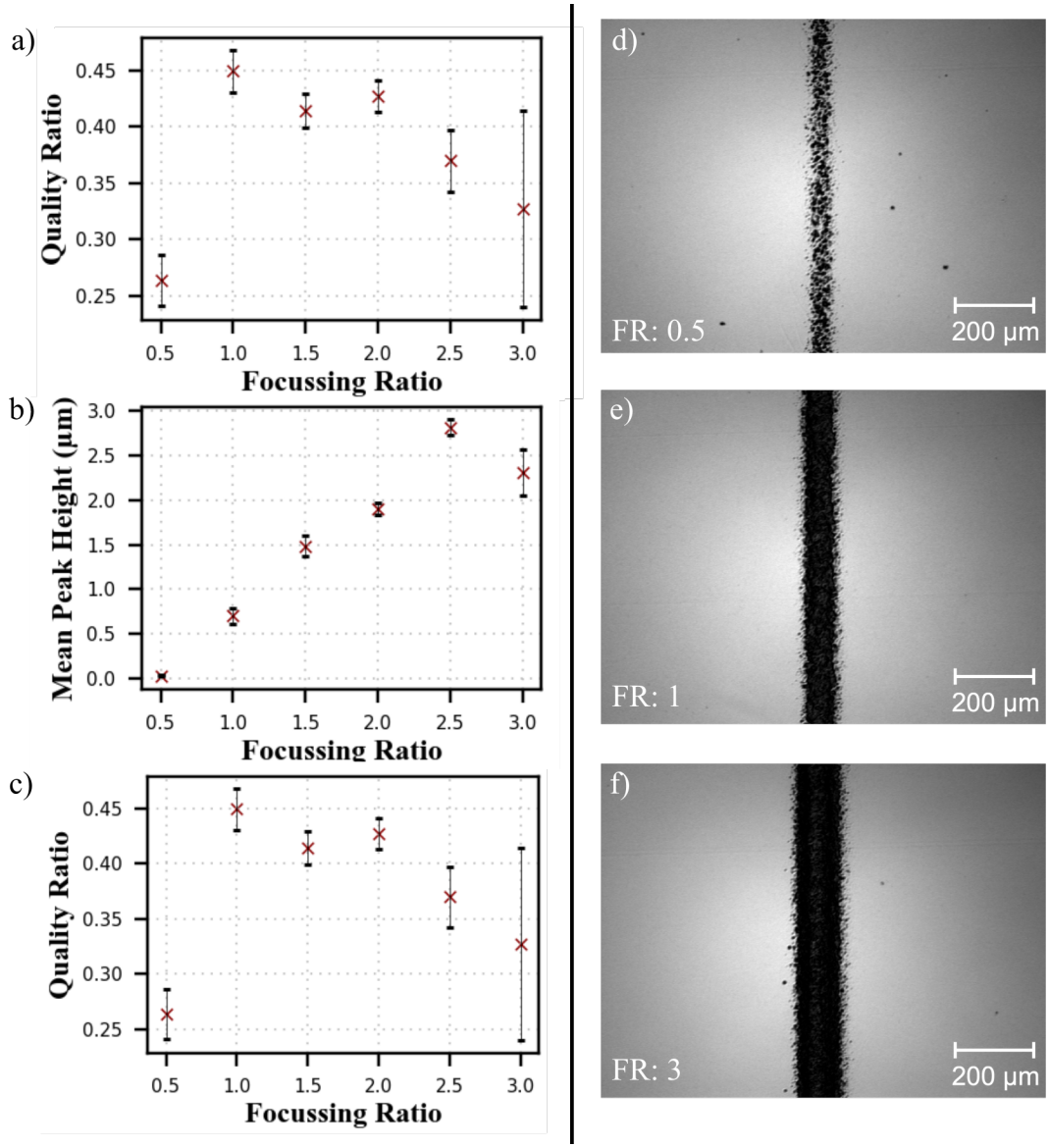

Figure 72 - The effect of the focussing ratio on the mean peak height, FWHM, and quality of Aerosol Jet printed features. Error bars represent ±1 standard deviation. n=10

features was achieved by increasing atomiser flow with a constant focusing ratio of two. The sheath was then adjusted within a closer window to tune the width of the printed lines.

5.3 Conductivity of Aerosol Jet printed features

Two- and four-point probing were used to assess the conductivity of AJ printed features. Two-point probing was used as a comparison of printed traces with varying aspect ratios. This experiment was designed to indicate whether multiple print passes should target increasing trace width (low aspect ratio) or trace height (high aspect ratios). Since the print time is driven by the nozzle travel distance required, understanding the most time efficient method of producing traces with sufficient conductivity is useful in a design context.

Four-point probing and measurements of the sample's thickness were used to determine the dimensionless conductivity of the material. Four-point probing accounts for contact and test lead resistance to give more accurate reporting of the sample's conductivity. This allows simpler comparisons between results from different research groups, experimental setups, materials, and manufacturing processes. Four terminal measurements were not used for all conductivity test due to limited availability of suitable probes.

5.3.1 Two-point probe measurement of AJ printed samples

Two sets of 5 samples were produced with the number of print passes increasing from 1 to 8. In the first set, each pass of the AJ nozzle deposited material at the same location increasing the height of the printed feature with each pass

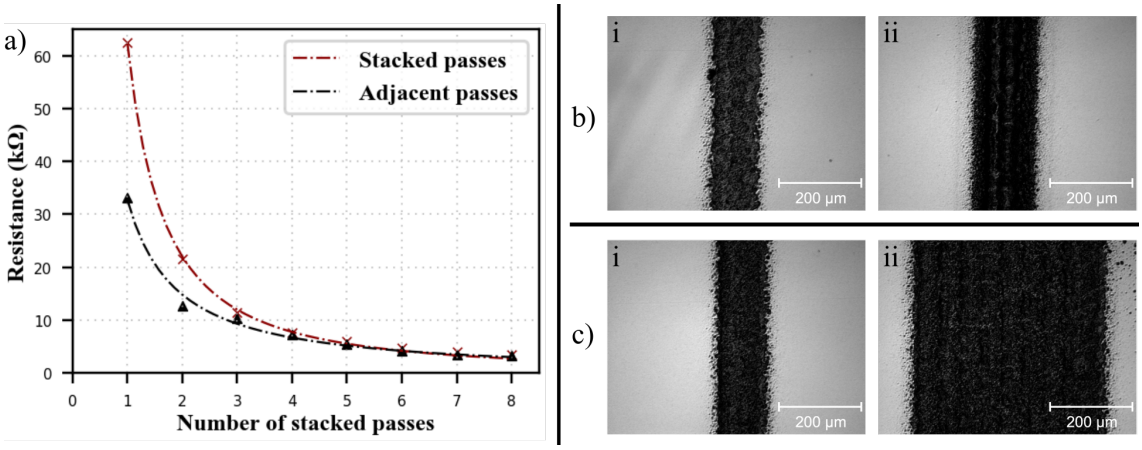

Figure 73 - a) Conductivity of stacked and adjacent multi-pass printing, b & c) single and eight pass printing in stacked and adjacent arrangements, respectively

(stacked). In the second set of samples, each pass of the nozzle was offset by half a line width to increase the width of the printed feature (adjacent). Each sample consisted of two 3mm contact pads connected by a 10mm feature . All samples were produced on glass substrates heated to 120°C at a nozzle height of 1mm with sheath and atomiser flows of 250 and 500sccm, respectively. The geometry of each sample was measured using white light interferometry (NP-Flex, Bruker) and the resistance measured using was measured using a calibrated multi-meter (2110, Keithley). From 5 repeats, the mean height, FWHM, and resistance were calculated, and the results plotted in Figure 73. Full results can be found in Table 6 & 7, in Appendix C.

The conductivity of single pass lines were found to show a high degree of variance, with a standard deviation of 13.84kΩ across 8 samples. In both stacked and adjacent printing arrangements, the standard deviation in the resistance decreased with the number of passes and reached less than 1kΩ for six or more passes. The resistance values were approximately equivalent after 4 nozzles passes in both approaches; however, before this point the adjacent arrangement has a significantly lower resistance. This can be attributed to the increased role the region of overspray plays in prints with a low number of passes, which can be evidenced through the quality ratio. In practice, adjacent track designs should be targeted to minimise the influence of overspray on device performance if the number of printed passes is lower than four.

5.3.2 Four-point probing of AJ printed samples

Measurements of sheet resistivity were completed using 20mm circular samples printed on to glass slides. The samples were printed using the same parameters as above, with infill spacing of 50µm. The samples were placed on to a platform and a 60g contact probe (1 mm Spacing, 60g, Tungsten Carbide Tip, Rµ 100, Jandel Engineering Ltd.) was lowered on to the centre of the substrate. The probe was connected to a source meter unit (SMU) (2450, Keithley) that was set to deliver 100µA and record the voltage to calculate the resistance of the sample. The average of ten readings were taken for each of the three samples and the bulk resistivity was calculated to be 62.6Ω/sq using equation:

$$\rho = \frac{C}{R_s t}$$

5.4 Conformal patterning of conductive inks

Many direct write, or surface functionalization techniques are reliant on close proximity of the nozzle substrate distance to achieve consistent deposits. As such, printing on conformal surfaces requires more complex articulation and often imposes geometric limitations when trying to produce toolpaths that track a substrate with non-planar, topographically complex geometry. For example, printing on small concave radii can be difficult owing to bulky deposition heads.

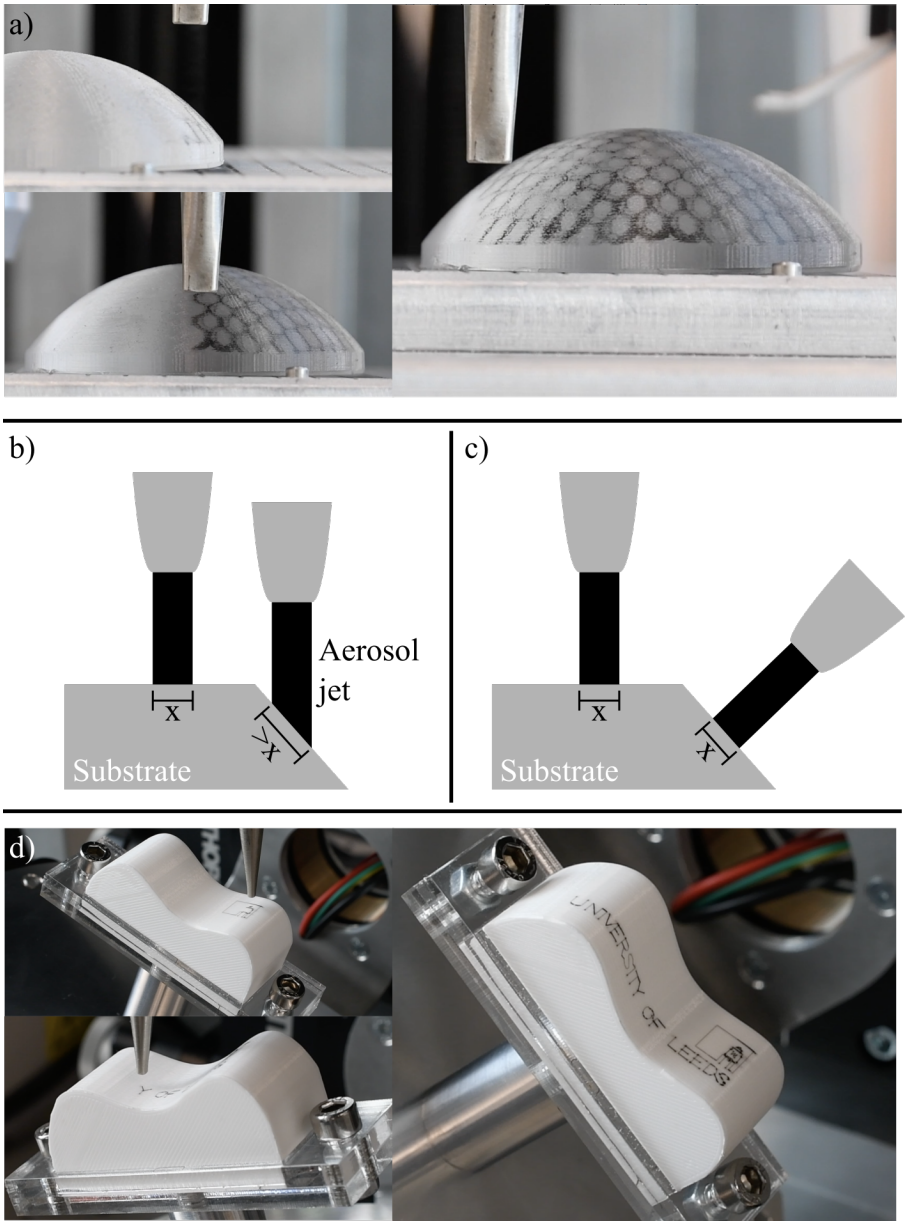

Figure 74 - a) 3-axis conformal patterning and b) associated pattern distortion. c) 5-axis patterning schematic and d) 5-axis conformal deposition

The ability of AJP to deposit consistently at stand-off heights of 1-5mm presents an opportunity to simplify this by reducing the degree to which the motion of the deposition head needs to replicate the surface. Furthermore, as the nozzle does not need to maintain perpendicularity to the surface, printing on to conformal surfaces can be achieved even with relatively simple 3-axis motion systems (Figure 74a). This simplified approach does introduce new challenges with pattern distortion as it projected on to non-planar surfaces (Figure 74b-c). Transitioning to a five-axis platform allowed patterning on to complex surfaces while keeping the nozzle perpendicular to the surface (Figure 74d). In this, AJ still simplifies the process and allows deposition on to concave surfaces that would be inaccessible for physical nozzles.

In soft robotics, patterning on to complex surfaces will become increasingly important as designs evolve to meet the needs of applications. Furthermore, if film based devices are going to be incorporated within soft devices, then flexible methods for interconnection and integration will be needed.

5.5 Chapter summary

Aerosol jet printing was introduced for its potential to more reliably pattern functional inks within soft robotics. This chapter first introduced the underlying principles of AJ before developing before developing a methodology for assessing printed features. Exploration of the parameters effecting the quality of the deposit was conducted and minimum feature sizes of <1µm and 50µm were demonstrated for the axial and lateral resolution, respectively.

The conductivity of printed features were evaluated using two and four point probing techniques and, when printing a small number of passes, it was found that adjacent printing had a greater reduction on conductivity than stacked passes. This can be attributed to the lower portion of the line consisting of overspray, as verified by the quality ratio. Finally, patterning on to more complex surfaces was demonstrated for its wider impact on soft robotics.

6 Application and Hybridisation

The previous chapters have characterised individual manufacturing techniques capable of depositing conductive and elastomeric materials. This final chapter applies these techniques to produce functional, proof-of-concept demonstrators of the manufacturing technologies. These simple devices were created to highlight how the manufacturing processes developed in this work can be used to enable emerging soft technologies. This chapter describes the challenges with material wetting and thin film handling that needed to be overcome. A working dielectric elastomer actuator and resistive sensor based on aerosol jet printed features are produced and, finally, the chapter culminates in the production of a fully printed capacitive sensor by combining AJ with electro-hydrodynamic deposition of a silicone elastomer.

6.1 Material compatibility

6.1.1 Substrate wetting

Patterning multiple inks can introduce challenges caused by the interaction of materials. The low porosity and surface energy of PDMS, coupled with the relatively high surface tension of aqueous inks, leads to limited material wetting and adhesion. These hurdles are more apparent for conductive inks where additives to promote adhesion can have a detrimental effect on the functionality of the deposit.

To encourage adhesion, spreading, and the production of confluent features, PDMS was exposed to an oxygen plasma treatment to increase the surface energy of the substrate. The sessile drop imaging technique was used to provide an indication of the efficacy of the plasma treatment and to understand the effect of exposure time on material wetting. Samples of PDMS (1cm^2, Sylgard 1-4128, Dow Corning) were placed within a plasma oven (PE-25, Inseto, UK) and exposed to a 75W oxygen plasma under a vacuum of 17torr. The samples were then loaded on to the micro-adjustable tilt stage of a contact angle goniometer (Ossila, UK). The sample was backlit using blue light and imaged with a 2MP camera. A micro-dispensing pipette (613-2894, VWR, USA) was used to dispense 25µl on to the surface of the PDMS. This approach was taken over the white light method used

previously as the contact angles were much larger and measurements needed to be taken more quickly to limit the effects of solvent evaporation.

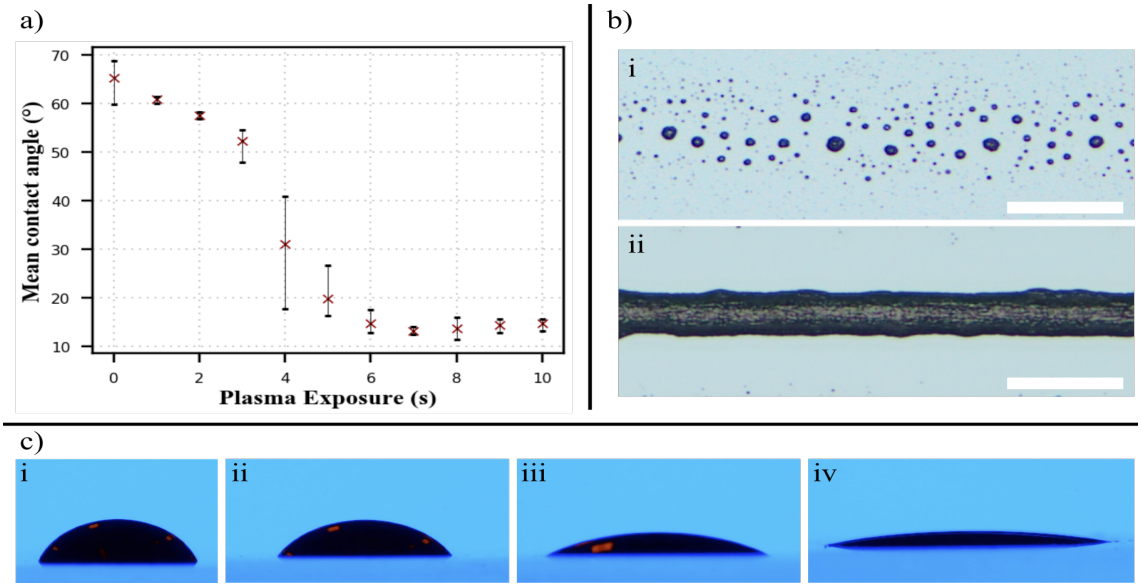

Figure 75 - Effect of oxygen plasma surface treatment on the contact angle of an aqueous graphene ink on PDMS. All scale bars are 50µm. Error bars represent ±1 standard deviation. n=5

The contact angle with untreated PDMS was found to be ~65°, and reduced to 15° after six seconds of treatment (Figure 75a). Further plasma treatment had little effect on the contact angle and, therefore, adhesion of the ink to the plasma surface. Excessive exposure to oxygen plasma treatment can lead to surface oxidation, therefore 6 seconds was used in all printing on to PDMS surfaces. In practice, printing on to untreated surfaces led to material beading on the surface in discrete droplets. Post plasma treatment, the graphene ink wet to the surface to produce confluent, conductive features (Figure 75b).

6.1.2 Thin film handling and multi-layer structures

Thin elastomer films, on the order of 10µm, were found to be difficult to handle due to the low Young's modulus of the material. This caused frequent tearing while handling or bundling of the film as a result of internal stress and electrostatic interactions. Therefore, elastomer films were deposited on to higher stiffness PET substrates to provide mechanical stability. This approach allowed multiple layers to be built up before removal, which reduced the potential for film damage.

Manual mechanical peeling of the films was found to have a low-yield and imparted variable stress across the films that can lead to variation in the material's mechanical response due to the Mullin's effect. As an alternative, a sacrificial support layer that could be dissolve post-print, was applied to the substrate. An aqueous solution of polyvinyl alcohol (PVA) was spin coated on to the PET films using a 500rpm spin speed for 60s. The PVA solution was prepared by gradually mixing PVA granules (PVA, MP Biomedicals) to deionised water at 80°C under constant stirring for 48 hours until a 3wt% solution was achieved. Dip coating was used in some experiments, how beading at the material edge was found to give less consistent results. After printing, the printed film could be removed from the substrate by submersion in an ultrasonic bath at 80°C.

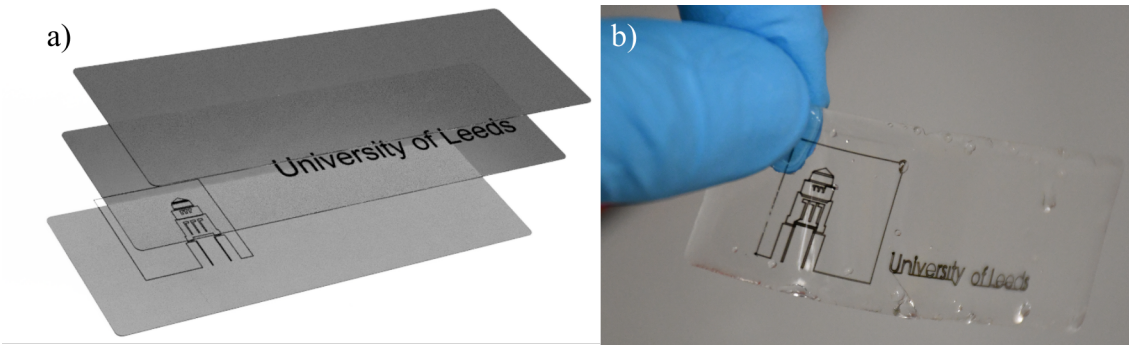

Figure 76 - a) schematic of multi-layer print and b) printed device

6.2 Device development: Aerosol Jet printed functional devices

The devices described here have been created using substrates produced using conventional soft fabrication techniques combined with aerosol jet printing. This work formed part of a presentation and publication at the 2019 IEEE International Conference on Soft Robotics in Seoul, South Korea (Robosoft, 2019) [232].

6.2.1 Dielectric Elastomer Actuators

As covered in Section 2.1.2, dielectric elastomer actuators consist of an dielectric elastomer layer sandwiched between to stretchable electrodes. When a voltage is applied between the electrodes, electrostatic attraction result in radial and axial strain. The most common method of manufacture is through manual application of carbon electrodes on to pre-strained VHB elastomer films, which lacks the dimensional accuracy, resolution, and repeatability of automated patterning.

Furthermore, pre-strained films can be prone to tearing due to the loads imparted during contact-based material transfer techniques. AJ was investigated as a technique for improving the ability to patterned suspended films for prototyping dielectric elastomer actuators.

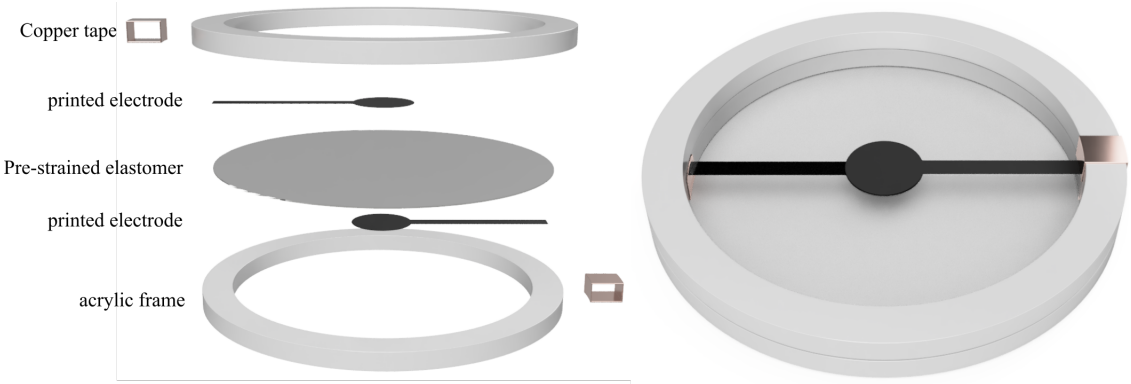

Figure 77 - Design of dielectric elastomer actuator

A 20mm diameter acrylic elastomer (VHB4910, 3M, USA) disk with a thickness of 1mm was stretched over a circular laser cut (Epilog Mini 50W, Epilog Laser, UK) acrylic frame (3mm, OD/ID: 60/50mm). Copper tape was applied to the acrylic frame to allow connection to the printed elastomer (Figure 77). Electrodes were then printed on to both sides of the acrylic elastomer (Figure 78a) and small amount of conductive carbon grease was used as a compliant interconnect between the printed electrodes and rigid copper foils. A high voltage amplifier (20/20HS, TREK, USA) was driven using a function generator (2110, Keithley, USA) from square-wave frequencies varying from 1Hz to 6kHz. For the electrodes, CamGraph IJ3 was used as well as a high strain tolerance ink produced using a carbon conductive paste diluted with water and glycerol (10:8:2) originally developed by a research group colleague, M. Lukic-Mann.

The actuator's response was recorded at 60fps using a DSLR (D7500, Nikon, Japan) and analysed using the OpenCV library in python. All frames were converted to grayscale and the region of interest (ROI) isolated by inscribing a square from the inner diameter of the acrylic frame. A threshold was then applied to produce a binary image. The areal strain could then be calculated by comparing the unactuated and actuated area in any given frame:

$$Strain = \frac{(Area_{frame} - Area_{unactuated})}{Area_{Unactuated}}$$

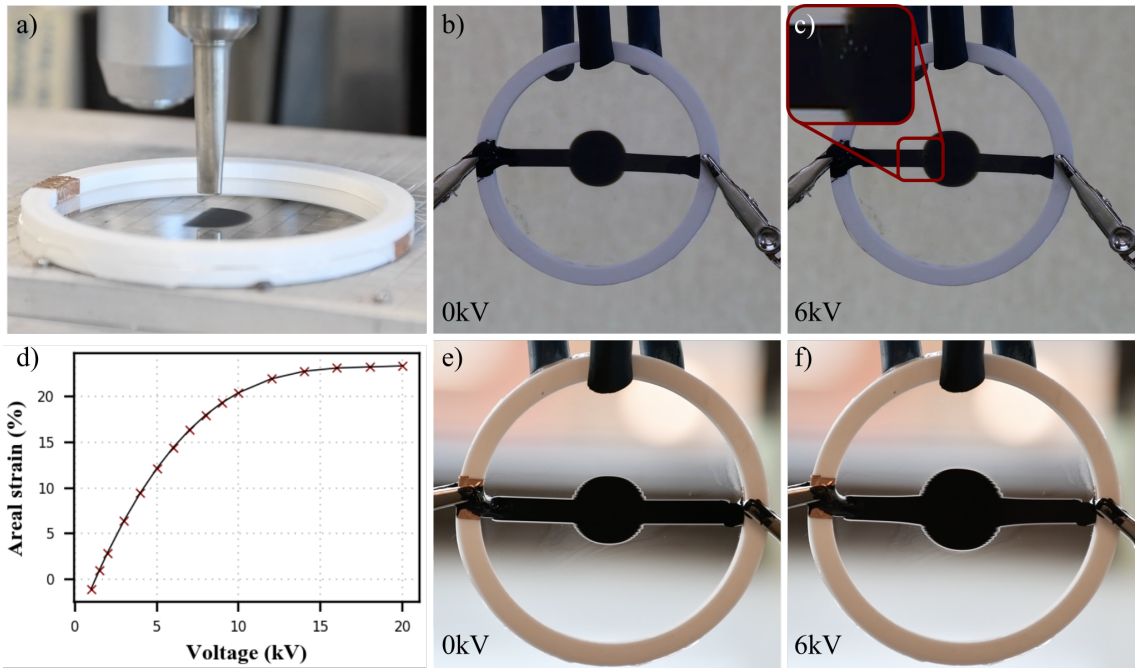

Figure 78 - a) Printing of electrodes for a DEA; b) unactuated DEA with graphene platelet ink; c) actuated DEA with graphene platelet ink (inset: cracking and arcing of electrode); d) Areal strain response of DEA at 1Hz with high strain tolerance ink; e) unactuaded DEA with high strain ink; and f) actuated DEA with high strain ink

The limited strain tolerance of the graphene platelet ink caused cracking of the electrodes at moderate strains of ~8% (Figure 78b-c). With this electrode material, a small number of actuation cycles led to device failure due to loss of electrode conductivity. Transitioning to the ink with higher strain tolerance enabled actuation strains of ~25% at a frequency of 1Hz and electric fields of 15-20kV (Figure 78d-f). This second type of actuator presented a near linear increase in strain for voltages of 1-10kV before it began to plateau. This behaviour is likely cause by an increase in apparent stiffness at increased strain rates or strain-stiffening as the polymer approaches the limits of chain extensibility.

Increasing actuator strains to the extreme values reported within the literature requires the duration of the applied pulse to be increased. Modelling and empirical investigation VHB has shown two phases of actuation upon application of an electric field [233]: an initial, short-lived linear elastic response followed by an extended period of creep until a steady-state is reached. High strain values reported are typically achieved after the steady state has been reached. The viscoelastic relaxation time of the elastomer is on the order of 10^2 seconds at room temperature, which makes it impractical for most applications. This demonstration proves AJ as available technique for developing and

experimenting with actuator electrode configuration while also overcoming the challenges faced with manual application of electrodes. Furthermore, characterisation of the devices in an application context should be enabled by increased repeatability and process reliability.

6.2.2 Resistive strain sensing

The possible degrees of freedom in soft robotics makes the development of reliable and repeatable sensors important for the development of closed loop control strategies and more complex performance. The most widely investigated are resistive sensors, which monitor the change in electrical resistance of a conductive material as it undergoes strain. Traditional strain gauge technologies provide high resolution, but are not tolerant of the high strains exhibited in soft systems. Here, the strain response of the carbon-black glycerol ink investigated with a view towards integrated printed sensors.

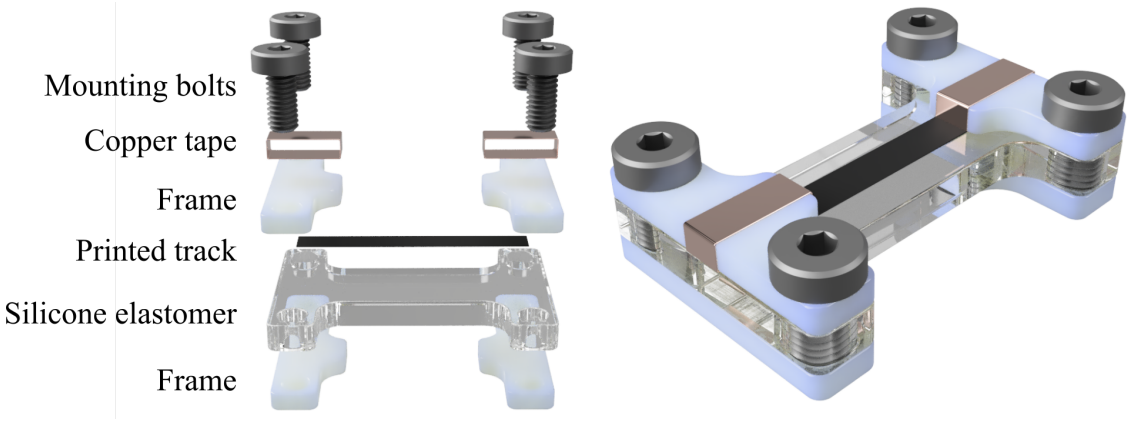

Figure 79 - Design of high strain resistive sensor

Resistive sensors monitor the change in resistance of a conductive material as it undergoes strain. Since soft robotics often exhibit strains greater than 100% it can be challenging for conductive materials to maintain conductivity during operation. To test the strain tolerance and performance of a printed sensor, an AJ printed trace was deposited on to an elastomer dog bone (Figure 79). Elastosil P7670 was selected as a substrate material as it can withstand strains of 600% without failure, which is significantly more than maximum strain of the ink and Sylgard materials (<100%). The elastomer was shaped using soft lithography in to a fuse filament fabricated (FFF) mould. Once mixed, degassed, and poured, the elastomer and mould were placed in to a vacuum chamber to remove any

residual bubbles. The elastomers were then left to cure at room temperature for at least 48 hours. Samples were then aligned on a glass slide for printing. Connections to the soft sensor were made in a similar way to the DEAs in the previous section (Figure 79). The sensor was mounted in to a bespoke linear strain test rig and the change in resistance was monitored using an SMU (2450, Keithley, USA).

The devices were strained between 0-140% in 10% increments. The sensor was cycled through each set point 100 times and the strain response plotted in Figure 80. This test was extended to include 150% strain, however at this point continuity errors begin to present within the sensor. A secondary test was carried out that tested the performance of a sensor over 1000 cycles at a 70% strain set point to evaluate any performance drift over time. The strain sensor presented here is relatively small in size, with a total length of 20mm and an unstrained thickness of 2mm.

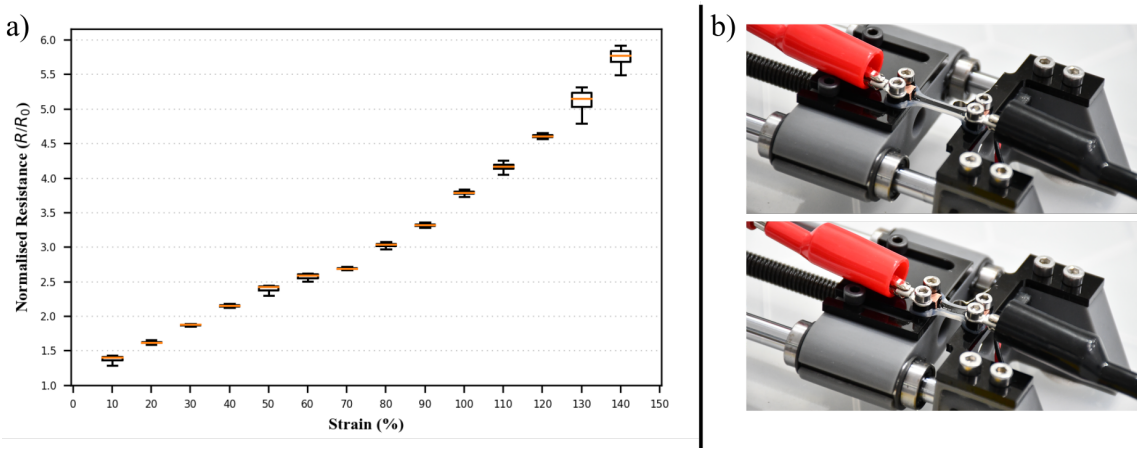

Figure 80 - a) Resistive sensor response to increasing strain and b) testing of strain sensor.

The normalized resistance response was found to be stable for any given value of strain and exhibited near linear performance, particularly for strain values below 60%. However, some challenges remain in both the manufacture and characterization of the strain sensing devices. Firstly, the starting resistance (R_0) of different gauges was found to vary significantly (5-30MOhm). Although the reason for this is yet to be quantified, it is possibly a result of inconsistencies in both the printing and assembly process. Connection between the rigid electrodes and soft elastomer was guaranteed through the manual placement of a small amount of conductive carbon grease, which likely had an impact. It is also expected that the resistance of these devices can be decreased by increasing the

volume of deposited material. The data collected above was produced by actuating to a set point, taking a series of measurements, and then returning to the unstrained position. This was then repeated for 100 cycles for each value of strain. As such, hysteresis effects have been observed but not yet been characterized. Future work expects to address some of these challenges through optimization and improvements to the manufacturing methodology. A better transition from the rigid and soft components will likely help overcome some of the challenges with inconsistent values for resistance.

6.3 Device development: hybrid Aerosol Jet and electro-hydrodynamic deposition

Combining E-jet of elastomers films; AJ of conductive traces; oxygen plasma surface treatment; and spin-coating of sacrificial supports in to a single device creates opportunity for soft films with integrated functionality. Here, a proof-of-concept five-layer film - consisting of three PDMS and two electrodes layers – capable of capacitive touch sensing is presented.

Square substrates (50x50mm) of PET were prepared and coated with a layer of PVA as per Section 6.1.2. The silicone elastomer (Sylgard 1-4128) was prepared and loaded in to a 10ml syringe. The PET sheets were then loaded on to the mandrel of EHD apparatus and a 30x30mm layer film was deposited using AC pulses with a magnitude of 2kV from a deposition distance of 3mm. Two print passes were used to increase the uniformity of the film and minimise the presence of pin-holes caused by dust ingress or surface contamination. Once printed, the elastomer films were cured for 120 seconds on a hot plate at 100°C. The films were then placed in a plasma oven and treated as per Section 6.1.1.

The elastomer films were then loaded on to the AJ apparatus and manually aligned using an USB CMOS camera (EO-5012M) and a 5x objective. The stage was heated to 120°C and 3 layers of electrodes were printed. Upon completion, the samples were replaced in to the EHD apparatus and the cycle continued until the desired number of layers were produced. Electrical connection to the sensors were achieved using carbon grease (MG Chemicals, USA) in combination with an acrylic frame and cyanoacrylate (3M, UK) for strain relief (Figure 81). A thicker

layer of PDMS was cast before removal from the PET films to protect the sensor and increase its mechanical robustness.

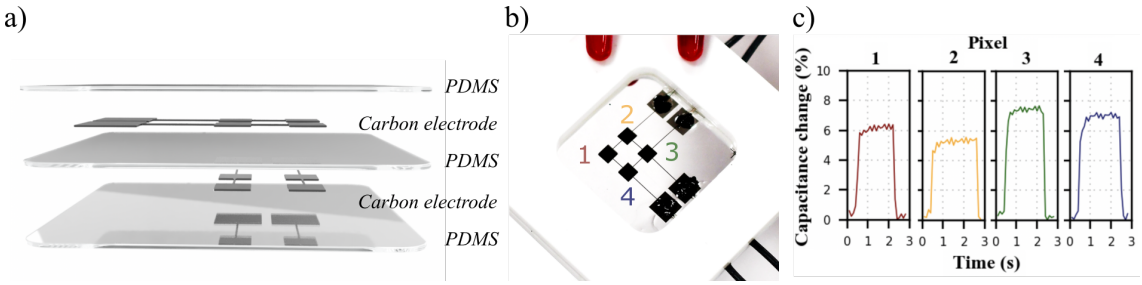

Figure 81 - a) design of capacitive sensor, b) physical device, and c) response of sensor to touch

Geometric analysis of the samples was achieved using white light interferometry. For testing the sensor, a capacitance-to-digital development board (AD7746, Analog Devices, USA) was used. Since the development board had a single input, pixel selection and cycling was achieved by combination an Arduino Mega with a multiplexer (CD74HC4067, Sparkfun, USA). This allowed readings to be taken with a frequency of ~100Hz.

The thickness of the electrode and elastomer films were found to be 3µm and 65µm, respectively, which lead to a total device thickness of approximately 200µm. The surface roughness of the elastomer layers were found to be 0.26µm (Sa) when measured over an area of 2mm^2. Upon touch, each pixel was found to exhibit 5-8% change in capacitance (Figure 81), which allowed reliable identification of individual pixels. A key challenge for the device was the limited strain tolerance of the materials. Moderate deformation of the film led to cracking in the conductive traces and a loss of electrical continuity. Use of the higher strain tolerance ink was investigated; however, it did not have sufficient conductivity for operation (~100kΩ vs. 10MΩ).

Although simple in design operation, this device demonstrates the potential of the manufacturing processes developed in this thesis for the production of thin film soft robotics. By using E-Jet printing alongside Aerosol Jet in a single process, inks with disparate rheology can be selectively and repeatably patterned to produce soft thin film devices.

6.4 Chapter summary

Manufacturing soft devices with sensing, actuation, or other forms of embedded intelligence requires the development of processes for both elastomeric and functional inks. Additionally, methodologies to ensure the compatibility of dissimilar materials need to be established. This chapter first showed how oxygen plasma surface treatment and sacrificial support can be used to overcome challenges in material wetting and substrate adhesion.

Functionality in soft structures is then shown by printing conductive carbon inks on to elastomer substrates to produce working DEAs and resistive strain sensors. Combining AJ with E-Jet printing is then used to successfully demonstrate the manufacture of a fully printed, soft capacitive touch sensor; therefore, demonstrating the fusion of the two core technologies of this work.

Challenges with dust and air ingress, alongside the limited strain tolerance of the CamGraph ink, prevented application of the printing technology to high strain sensing or even dielectric elastomer actuators. However, the work in this chapter demonstrates that these goals may well be in reach of a hybridised version of the manufacturing technology, provided the hurdles in process refinement and materials science can be overcome.

7 Conclusions and future work

7.1 Conclusions

Through this work, a new manufacturing approach that combines alternating current electro-hydrodynamic deposition of high-viscosity, low-conductivity elastomer films with aerosol jet direct write for conductive traces is developed to overcome the rheological constrains of the respective processes. Using electrically forced jets for the deposition of silicone elastomers has addressed the high frequency of nozzle blocking associated with the direct write of elastomer films. Droplet sizes of 800pL allowed the fabrication of features with a peak height of 5µm using a nozzle with a 160µm internal diameter. Integration of oxygen plasma surface treatment and aerosol jet printing enabled the production of functional devices without the development time or cost required for high-resolution e-jet printing. Functional actuation and sensing devices were produced to highlight the potential of the manufacturing technologies.

During the literature review, six core requirements (material compatibility, solution processing, resolution, roughness, throughput, and cleanliness) were highlighted for any new process. Here, the capabilities of the developed process are compared to the initial requirements:

Material compatibility – Initial targets for material compatibility centred around their viscosity as it the primary limiting factor in many deposition techniques (aerosol jet, ink jet, direct ink write). For electro-hydrodynamic processes, the development of inks was found to be equally dependent on the electrical and rheological properties, which can make ink formulation more challenging. In spite of this, a number of silicone elastomer materials were deposited with viscosities ranging from ~100-3500cp using the electro-hydrodynamic technique. Instances of nozzle blocking were reduced to instances of user error (nozzle-substrate shorting).

The deposition of low-viscosity carbon conductive inks were also shown using the same process, however aerosol jet printing provided a more robust solution for aqueous inks at the targeted resolutions. The conductive inks used in this work presented a compromise between strain tolerance and electrical

performance. The graphene platelet ink provided superior conductivity but was found to fail at strains of 8% when used for dielectric elastomer actuators. In contrast, the carbon-glycerol ink could undergo over 100% strain before failure but had a 3 orders of magnitude greater resistance. Although solutions are emerging in research contexts, the lack of commercially available functional inks with the required electro-mechanical properties continues to be a restriction for the field.

Resolution – The targeted feature sizes for the elastomer ink (X-Y: 500µm, Z: 10µm) and conductive ink (X-Y: 150µm, Z <1µm) were selected based on the state of the art for spin coating and inkjet printing. Through the pulsating jet, a lateral resolution of ~500µm was achieved; however, limited spatial positioning and droplet inconsistencies meant that PoD was carried forward as the predominant jetting technique despite demonstrating minimum feature sizes of ~600µm. Although greater than the initial target, the lateral resolution achieved is comparable to existing inkjet technologies for PDMS elastomers while significantly reducing instances of nozzle clogging. Refinement of the process, apparatus, and use of smaller nozzles may provide a pathway to high resolution patterning. Both jetting modes demonstrated Z resolution of ~5µm, which shows promise for the production of low-voltage dielectric elastomers.

For the conductive features, aerosol jet printed tracks with FWHM of less than 50µm were produced with minimum heights on the order of 200nm. The thickness of the conductive traces were an order of magnitude smaller than the printed elastomer films, even when multiple print passes were required to increase conductivity and reduce variation.

Roughness – Roughness is important for thin film technologies as variation in the film height can lead to electrical stress raisers and premature device failure due to dielectric breakdown. Inkjet printing of elastomer films has been shown to produce layers with a roughness of 0.32µm (Sa). Through droplet spreading and mutual coulombic repulsion, elastomer films with a roughness of 0.26µm were produced using the e-jet technique.

Solution processing – solution processing was targeted to minimise the requirements for special environmental conditions. Existing processes, such as

molecular beam epitaxy, were limited by build speeds and expense due to the requirements for a vacuum. Both of the deposition systems were developed in atmosphere. Vacuum oxygen plasma treatment was used due to its availability in the lab, however atmospheric plasma has been demonstrated to be equally effective at improving the wettability in preliminary lab studies.

Cleanliness – This proved to be a significant challenge for the current apparatus. Operating in an open, non-cleanroom lab environment led to significant dust ingress that was on a similar scale to the thickness of the films. Attempts to produce functional printed actuators led to premature electrical breakdown. The current approach of transferring samples between work stations contributed to these challenges.

Throughput – Droplet sizes from PoD deposition were approximately 800pL from a 2kV, 40ms pulse. Assuming no pauses between pulses, a 25Hz ejection frequency would generate a material throughput of 20µL/s (1.2ml/s, 72ml/hr). This represents a significant improvement on molecular beam epitaxy while also providing greater geometric freedom. Challenges will persist if this approach is to be transferred for high volume production, but multiplexing and improved nozzle designs are promising approaches to increase material throughput.

7.2 Future work

This work has developed an apparatus and shown a manufacturing approach that can underpin ongoing research for the production of soft films with integrated sensing and actuation. Translating this initial exploratory study to achieve wider impact will require continued development in process refinement and material formulation. The success of any process is driven by the capabilities it enables, therefore there is also work to be conducted in applying the manufacturing technology to products with tangible societal impact.

7.2.1 Process development

The current fabrication strategy required samples to be transferred between workstations, which contributed to sample contamination and dust ingress. For high electric field applications, such as DEAs, this led to premature failure due to dielectric breakdown. The logical next step would be the integration of the

individual processes in to a single apparatus to minimise dust exposure. Operation in a clean environment, or at least in a positive pressure enclosure, would likely be required for manufacturing over any significant period, especially if micron scale films are targeted.

The modularity of the apparatus proved essential to the success of this project as it helped reduce cost, permitted wider exploration of the experimental space, and enabled the addition/removal of ancillary equipment (imaging equipment, heaters etc.) when necessary. However, this also contributed to the limited stiffness of the system and introduced challenges with alignment. For the e-jet deposition technique, which proved most useful for the targeted application, this manifested itself in variation droplet volume due to changes in the relative distance between the nozzle and substrate. Refinement of the mechanical apparatus; improved alignment and construction techniques; and more advanced offset compensation could help minimise the errors. However, implementation of closed loop control of the droplet volume would likely be the most effective strategy in the short term. Initial work monitoring the current transferred during droplet ejection appears to be shows promise for achieving this.

Improved resolution can likely be achieved by reducing the diameter of the nozzles used for deposition. This work centred on small-gauge, commercially-available, steel blunt nozzles. Transitioning to blown-glass needles should allow testing with nozzle diameters down from a few hundred microns down to the nano-scale. Using these types of nozzles, E-jet printing of nano-meter sized features has been demonstrated with more conventional, higher conductivity inks.

This exploratory study allowed an experimental understanding; however, further gains will be equally reliant on the developing models to understand the complex relationship between the rheological and electrical responses. Significant work has been conducted for low-viscosity Newtonian fluids in the classical regimes but, apart from the experimental studies of Jayasinghe et al., there is limited work on the deposition of viscoelastic materials using electrically forced jets.

As covered in the published review (Appendix A), aerosol jet still faces some challenges as its maturity grows. Primarily, a better understanding of the process

and its requirements will be required to accelerate application development since its dependence on large bodies of empirical work to develop robust printing is hampering adoption [234]. For soft robotics, 5-axis AJ presents opportunities for more complex sensing and actuation arrangements that could unlock new functionality. Existing patterning techniques are largely limited to 2 or 2.5D features that restrains design.

7.2.2 Materials

Following the creation of the apparatus, a challenge of this work was sourcing of materials with the properties suitable for deposition. Off-the-shelf elastomers were used to demonstrate the potential of EHD deposition; however, ink flow led to a loss of resolution when depositing a larger volumes of material in the existing machine format. Increasing the yield stress of the fluid and inducing thixotropic behaviour would enable increased lateral resolution and provide more stable, consistent prints. The addition of fumed silica has been demonstrated as an effective way of achieving this when patterning elastomers with DIW.

The development of functional inks with sufficient strain tolerance is a challenge across soft robotics, with few commercially available solutions the most significant developments are confined to a small number of labs. In this work, two inks were explored: a graphene platelet ink that could achieve relatively high conductivity but was found to fail at moderate strains of ~8%, and another carbon black ink that exhibited low-conductivity but could withstand strains up to 140%. Rearrangement of the conductive network within the materials leads to a high degree of hysteresis in their response, which limits the use in resistive strain sensing. The development of materials with appropriate properties for processing and application will continue to be one the biggest development areas for soft robotics.

References

1. Polygerinos P, Wang Z, Galloway KC, et al (2015) Soft robotic glove for combined assistance and at-home rehabilitation. In: Robotics and Autonomous Systems. pp 135–143
2. Park YL, Chen BR, Pérez-Arancibia NO, et al (2014) Design and control of a bio-inspired soft wearable robotic device for ankle-foot rehabilitation. Bioinspiration and Biomimetics. https://doi.org/10.1088/1748-3182/9/1/016007
3. Cianchetti M, Laschi C, Menciassi A, Dario P (2018) Biomedical applications of soft robotics. Nat. Rev. Mater.
4. Cianchetti M, Ranzani T, Gerboni G, et al (2014) Soft Robotics Technologies to Address Shortcomings in Today's Minimally Invasive Surgery: The STIFF-FLOP Approach. Soft Robot. https://doi.org/10.1089/soro.2014.0001
5. Shintake J, Rosset S, Schubert B, et al (2016) Versatile Soft Grippers with Intrinsic Electroadhesion Based on Multifunctional Polymer Actuators. Adv Mater 28:231–238. https://doi.org/10.1002/adma.201504264
6. Shintake J, Cacucciolo V, Floreano D, Shea H (2018) Soft Robotic Grippers. Adv. Mater.
7. Polygerinos P, Correll N, Morin SA, et al (2017) Soft Robotics: Review of Fluid-Driven Intrinsically Soft Devices; Manufacturing, Sensing, Control, and Applications in Human-Robot Interaction. Adv. Eng. Mater.
8. Kühne M, Wolf S, Bahls T, et al (2015) Soft robotics with variable stiffness actuators: Tough robots for soft human robot interaction. In: Soft Robotics: Transferring Theory to Application
9. Ilievski F, Mazzeo AD, Shepherd RF, et al (2011) Soft robotics for chemists. Angew Chemie - Int Ed. https://doi.org/10.1002/anie.201006464
10. Martinez R V., Glavan AC, Keplinger C, et al (2014) Soft actuators and robots that are resistant to mechanical damage. Adv Funct Mater. https://doi.org/10.1002/adfm.201303676
11. Marchese AD, Onal CD, Rus D (2014) Autonomous Soft Robotic Fish

Capable of Escape Maneuvers Using Fluidic Elastomer Actuators. Soft Robot. https://doi.org/10.1089/soro.2013.0009

12. Katzschmann RK, DelPreto J, MacCurdy R, Rus D (2018) Exploration of underwater life with an acoustically controlled soft robotic fish. Sci Robot. https://doi.org/10.1126/scirobotics.aar3449

13. Rich SI, Wood RJ, Majidi C (2018) Untethered soft robotics. Nat. Electron.

14. Truby RL, Santina CD, Rus D (2020) Distributed Proprioception of 3D Configuration in Soft, Sensorized Robots via Deep Learning. IEEE Robot Autom Lett 5:3299–3306. https://doi.org/10.1109/LRA.2020.2976320

15. Truby RL, Wehner M, Grosskopf AK, et al (2018) Soft Somatosensitive Actuators via Embedded 3D Printing. Adv Mater. https://doi.org/10.1002/adma.201706383

16. Hines L, Petersen K, Lum GZ, Sitti M (2017) Soft Actuators for Small-Scale Robotics. Adv. Mater.

17. Kim J, Kim JW, Kim HC, et al (2019) Review of Soft Actuator Materials. Int. J. Precis. Eng. Manuf.

18. Mirvakili SM, Hunter IW (2018) Artificial Muscles: Mechanisms, Applications, and Challenges. Adv. Mater.

19. Pelrine R (2000) High-Speed Electrically Actuated Elastomers with Strain Greater Than 100%. Science (80-) 287:836–839. https://doi.org/10.1126/science.287.5454.836

20. Keplinger C, Sun J-Y, Foo CC, et al (2013) Stretchable, Transparent, Ionic Conductors. Science (80-) 341:984–987. https://doi.org/10.1126/science.1240228

21. Ji X, Liu X, Cacucciolo V, et al (2019) An autonomous untethered fast soft robotic insect driven by low-voltage dielectric elastomer actuators. Sci Robot. https://doi.org/10.1126/scirobotics.aaz6451

22. Jung K, Kim KJ, Choi HR (2008) A self-sensing dielectric elastomer actuator. Sensors Actuators, A Phys. https://doi.org/10.1016/j.sna.2007.10.076

23. Zhang Y, Ellingford C, Zhang R, et al (2019) Electrical and Mechanical Self-Healing in High-Performance Dielectric Elastomer Actuator Materials. Adv Funct Mater. https://doi.org/10.1002/adfm.201808431

24. Yang G-Z, Bellingham J, Dupont PE, et al (2018) The grand challenges of *Science Robotics*. Sci Robot. https://doi.org/10.1126/scirobotics.aar7650

25. Rosset S, Shea HR (2016) Small, fast, and tough: Shrinking down integrated elastomer transducers. Appl Phys Rev 3:. https://doi.org/10.1063/1.4963164

26. Zhao H, Hussain AM, Duduta M, et al (2018) Compact Dielectric Elastomer Linear Actuators. Adv Funct Mater. https://doi.org/10.1002/adfm.201804328

27. Lotz P, Matysek M, Schlaak HF (2011) Fabrication and application of miniaturized dielectric elastomer stack actuators. IEEE/ASME Trans Mechatronics 16:58–66. https://doi.org/10.1109/TMECH.2010.2090164

28. Vudayagiri S (2014) Large Scale Processing of Dielectric Electroactive Polymers

29. Rosset S, Ararom OA, Schlatter S, Shea HR (2016) Fabrication process of silicone-based dielectric elastomer actuators. J Vis Exp 2016:. https://doi.org/10.3791/53423

30. Weiss FM, Töpper T, Osmani B, et al (2016) Electrospraying Nanometer-Thin Elastomer Films for Low-Voltage Dielectric Actuators. Adv Electron Mater 2:1500476. https://doi.org/10.1002/aelm.201500476

31. Luo M, Skorina EH, Tao W, et al (2017) Toward modular soft robotics: Proprioceptive curvature sensing and sliding-mode control of soft bidirectional bending modules. Soft Robot. https://doi.org/10.1089/soro.2016.0041

32. Homberg BS, Katzschmann RK, Dogar MR, Rus D (2015) Haptic identification of objects using a modular soft robotic gripper. In: IEEE International Conference on Intelligent Robots and Systems

33. Dickey MD (2017) Stretchable and Soft Electronics using Liquid Metals. Adv. Mater.

34. Wang X, Guo R, Liu J (2019) Liquid Metal Based Soft Robotics: Materials,

Designs, and Applications. Adv. Mater. Technol.

35. Larson C, Peele B, Li S, et al (2016) Highly stretchable electroluminescent skin for optical signaling and tactile sensing. Science (80-). https://doi.org/10.1126/science.aac5082

36. Truby RL, Katzschmann RK, Lewis JA, Rus D (2019) Soft robotic fingers with embedded ionogel sensors and discrete actuation modes for somatosensitive manipulation. In: RoboSoft 2019 - 2019 IEEE International Conference on Soft Robotics

37. Sun JY, Keplinger C, Whitesides GM, Suo Z (2014) Ionic skin. Adv Mater 26:7608–7614. https://doi.org/10.1002/adma.201403441

38. Yeo JC, Yap HK, Xi W, et al (2016) Flexible and Stretchable Strain Sensing Actuator for Wearable Soft Robotic Applications. Adv Mater Technol. https://doi.org/10.1002/admt.201600018

39. Guo SZ, Qiu K, Meng F, et al (2017) 3D Printed Stretchable Tactile Sensors. Adv Mater. https://doi.org/10.1002/adma.201701218

40. Liu H, Li Q, Zhang S, et al (2018) Electrically conductive polymer composites for smart flexible strain sensors: a critical review. J. Mater. Chem. C

41. Zhao H, O'Brien K, Li S, Shepherd RF (2016) Optoelectronically innervated soft prosthetic hand via stretchable optical waveguides. Sci Robot. https://doi.org/10.1126/scirobotics.aai7529

42. Xu PA, Mishra AK, Bai H, et al (2019) Optical lace for synthetic afferent neural networks. Sci Robot. https://doi.org/10.1126/scirobotics.aaw6304

43. George Thuruthel T, Ansari Y, Falotico E, Laschi C (2018) Control Strategies for Soft Robotic Manipulators: A Survey. Soft Robot.

44. Palza H, Zapata PA, Angulo-Pineda C (2019) Electroactive smart polymers for biomedical applications. Materials (Basel).

45. Brochu P, Pei Q (2010) Advances in Dielectric Elastomers for Actuators and Artificial Muscles. Macromol Rapid Commun 31:10–36. https://doi.org/10.1002/marc.200900425

46. Pelrine RE, Kornbluh RD, Joseph JP (1998) Electrostriction of polymer dielectrics with compliant electrodes as a means of actuation. Sensors Actuators A Phys 64:77–85. https://doi.org/10.1016/S0924-4247(97)01657-9

47. Keplinger C, Li T, Baumgartner R, et al (2012) Harnessing snap-through instability in soft dielectrics to achieve giant voltage-triggered deformation. Soft Matter. https://doi.org/10.1039/c1sm06736b

48. Majidi C (2014) Soft Robotics: A Perspective - Current Trends and Prospects for the Future. Soft Robot.

49. Coyle S, Majidi C, LeDuc P, Hsia KJ (2018) Bio-inspired soft robotics: Material selection, actuation, and design. Extrem. Mech. Lett.

50. Pelrine R, Kornbluh R, Joseph J, et al (1997) Electrostriction of Polymer Films for. IEEE Micro Electro Mech Syst 1:238–243. https://doi.org/10.1109/MEMSYS.1997.581811

51. Zhao X, Suo Z (2010) Theory of dielectric elastomers capable of giant deformation of actuation. Phys Rev Lett 104:. https://doi.org/10.1103/PhysRevLett.104.178302

52. Zhao X, Suo Z (2007) Method to analyze electromechanical stability of dielectric elastomers. Appl Phys Lett 91:. https://doi.org/10.1063/1.2768641

53. Zhang X, Wissler M, Jaehne B, et al (2004) Effects of crosslinking, prestrain, and dielectric filler on the electromechanical response of a new silicone and comparison with acrylic elastomer. pp 78–86

54. Kornbluh RD, Pelrine R, Pei Q, et al (2000) Ultrahigh strain response of field-actuated elastomeric polymers. Proc. SPIE 3987:51–64

55. Ha SM, Yuan W, Pei Q, et al (2006) Interpenetrating polymer networks for high-performance electroelastomer artificial muscles. Adv Mater 18:887–891. https://doi.org/10.1002/adma.200502437

56. Brochu P, Stoyanov H, Niu X, Pei Q (2013) All-silicone prestrain-locked interpenetrating polymer network elastomers: Free-standing silicone artificial muscles with improved performance and robustness. Smart Mater Struct. https://doi.org/10.1088/0964-1726/22/5/055022

57. Maffli L, Rosset S, Ghilardi M, et al (2015) Ultrafast all-polymer electrically tunable silicone lenses. Adv Funct Mater 25:1656–1665. https://doi.org/10.1002/adfm.201403942

58. Carpi F, Frediani G, Turco S, De RD (2011) Bioinspired tunable lens with muscle-like electroactive elastomers. Adv Funct Mater 21:4152–4158. https://doi.org/10.1002/adfm.201101253

59. Imboden M, de Coulon E, Poulin A, et al (2019) High-speed mechano-active multielectrode array for investigating rapid stretch effects on cardiac tissue. Nat Commun. https://doi.org/10.1038/s41467-019-08757-2

60. Poulin A, Imboden M, Sorba F, et al (2018) An ultra-fast mechanically active cell culture substrate. Sci Rep. https://doi.org/10.1038/s41598-018-27915-y

61. Romasanta LJ, Lopez-Manchado MA, Verdejo R (2015) Increasing the performance of dielectric elastomer actuators: A review from the materials perspective. Prog Polym Sci 51:188–211. https://doi.org/10.1016/j.progpolymsci.2015.08.002

62. Renukappa NM, Siddaramaiah, Sudhaker Samuel RD, et al (2009) Dielectric properties of carbon black: SBR composites. J Mater Sci Mater Electron 20:648–656. https://doi.org/10.1007/s10854-008-9780-4

63. Park I-S, Kim KJ, Nam J-D, et al (2007) Mechanical, dielectric, and magnetic properties of the silicone elastomer with multi-walled carbon nanotubes as a nanofiller. Polym Eng Sci 47:1396–1405. https://doi.org/10.1002/pen.20833

64. Dang Z-M, Wang L, Yin Y, et al (2007) Giant Dielectric Permittivities in Functionalized Carbon-Nanotube/ Electroactive-Polymer Nanocomposites. Adv Mater 19:852–857. https://doi.org/10.1002/adma.200600703

65. Tian M, Zhang J, Zhang L, et al (2014) Graphene encapsulated rubber latex composites with high dielectric constant, low dielectric loss and low percolation threshold. J Colloid Interface Sci 430:249–256. https://doi.org/10.1016/j.jcis.2014.05.034

66. Lewis TJ (2005) Interfaces: nanometric dielectrics. J Phys D Appl Phys

38:202–212. https://doi.org/10.1088/0022-3727/38/2/004

67. Galantini F, Bianchi S, Castelvetro V, Gallone G (2013) Functionalized carbon nanotubes as a filler for dielectric elastomer composites with improved actuation performance. Smart Mater Struct 22:55025

68. Jiang L, Betts A, Kennedy D, Jerrams S (2015) Improving the electromechanical performance of dielectric elastomers using silicone rubber and dopamine coated barium titanate. Mater Des 85:733–742. https://doi.org/10.1016/j.matdes.2015.07.075

69. Bele A, Cazacu M, Stiubianu G, Vlad S (2014) Silicone–barium titanate composites with increased electromechanical sensitivity. The effects of the filler morphology. RSC Adv 4:58522–58529. https://doi.org/10.1039/C4RA09903F

70. Yang D, Tian M, Li D, et al (2013) Enhanced dielectric properties and actuated strain of elastomer composites with dopamine-induced surface functionalization. J Mater Chem A 1:12276–12284. https://doi.org/10.1039/C3TA12090B

71. Romasanta LJ, Leret P, Casaban L, et al (2012) Towards materials with enhanced electro-mechanical response: CaCu3Ti4O12-polydimethylsiloxane composites. J Mater Chem 22:24705–24712. https://doi.org/10.1039/C2JM34674E

72. Carpi F, De Rossi D (2005) Improvement of electromechanical actuating performances of a silicone dielectric elastomer by dispersion of titanium dioxide powder. IEEE Trans Dielectr Electr Insul 12:835–843. https://doi.org/10.1109/TDEI.2005.1511110

73. Yang D, Tian M, Dong Y, et al (2013) A high-performance dielectric elastomer consisting of bio-based polyester elastomer and titanium dioxide powder. J Appl Phys 114:. https://doi.org/10.1063/1.4824805

74. Stoyanov H, Kollosche M, Risse S, et al (2011) Elastic block copolymer nanocomposites with controlled interfacial interactions for artificial muscles with direct voltage control. Soft Matter 7:194–202. https://doi.org/10.1039/C0SM00715C

75. Zhang QM, Li H, Poh M, et al (2002) An all-organic composite actuator material with a high dielectric constant. Nature 419:284–287. https://doi.org/10.1038/nature01021

76. Huang C, Zhang QM, deBotton G, Bhattacharya K (2004) All-organic dielectric-percolative three-component composite materials with high electromechanical response. Appl Phys Lett 84:4391–4393. https://doi.org/10.1063/1.1757632

77. Gallone G, Galantini F, Carpi F (2010) Perspectives for new dielectric elastomers with improved electromechanical actuation performance: composites versus blends. Polym Int 59:400–406. https://doi.org/10.1002/pi.2765

78. Tian M, Yan B, Yao Y, et al (2014) Largely improved actuation strain at low electric field of dielectric elastomer by combining disrupting hydrogen bonds with ionic conductivity. J Mater Chem C 2:8388–8397. https://doi.org/10.1039/c4tc01140f

79. Stoyanov H, Kollosche M, McCarthy DN, et al (2010) Flexible enhanced energy density composites for dielectric elastomer actuators. In: Bar-Cohen Y (ed) Proc. SPIE. p 76422G

80. Stoyanov H, Kollosche M, McCarthy DN, Kofod G (2010) Molecular composites with enhanced energy density for electroactive polymers. J Mater Chem 20:7558. https://doi.org/10.1039/c0jm00519c

81. Dünki SJ, Ko YS, Nüesch FA, Opris DM (2015) Self-repairable, high permittivity dielectric elastomers with large actuation strains at low electric fields. Adv Funct Mater 25:2467–2475. https://doi.org/10.1002/adfm.201500077

82. Dünki SJ. b, Dascalu M., Nüesch FA. b, Opris DM. (2016) Silicones with enhanced permittivity for dielectric elastomer actuators. In: Proceedings of SPIE - The International Society for Optical Engineering

83. Rosset S, Shea HR (2013) Flexible and stretchable electrodes for dielectric elastomer actuators. Appl Phys A 110:281–307. https://doi.org/10.1007/s00339-012-7402-8

84. Huang JC (2002) Carbon black filled conducting polymers and polymer blends. Adv. Polym. Technol. 21:299–313

85. Rwei S-P, Ku F-H, Cheng K-C (2002) Dispersion of carbon black in a continuous phase: Electrical, rheological, and morphological studies. Colloid Polym Sci 280:1110–1115. https://doi.org/10.1007/s00396-002-0718-8

86. Pelrine R, Kornbluh R, Joseph J, et al (2000) High-field deformation of elastomeric dielectrics for actuators. Mater Sci Eng C 11:89–100. https://doi.org/10.1016/S0928-4931(00)00128-4

87. Lotz P, Matysek M, Lechner P, et al (2008) Dielectric elastomer actuators using improved thin film processing and nanosized particles. In: Proceedings of SPIE - The International Society for Optical Engineering

88. Lotz P, Matysek M, Schlaak HF (2009) Peristaltic pump made of dielectric elastomer actuators. Proc. SPIE 7287:72872D-72872D–8

89. Huang J, Yang J, Jin L, et al (2016) Pattern formation in plastic liquid films on elastomers by ratcheting. Soft Matter 12:3820–3827. https://doi.org/10.1039/c6sm00124f

90. Sumita M, Sakata K, Asai S, et al (1991) Dispersion of fillers and the electrical conductivity of polymer blends filled with carbon black. Polym Bull 25:265–271. https://doi.org/10.1007/BF00310802

91. Kim Y, Zhu J, Yeom B, et al (2013) Stretchable nanoparticle conductors with self-organized conductive pathways. Nature 500:59–63. https://doi.org/10.1038/nature12401

92. Kan W, Chang Y-H, Zhang C, Wang B (2016) Conductive-on-demand: Tailorable polyimide/carbon nanotube nanocomposite thin film by dual-material aerosol jet printing. Carbon N Y 98:397–403. https://doi.org/http://dx.doi.org/10.1016/j.carbon.2015.11.032

93. Feng L, Xie N, Zhong J (2014) Carbon nanofibers and their composites: A review of synthesizing, properties and applications. Materials (Basel). 7:3919–3945

94. Li J, Ma PC, Chow WS, et al (2007) Correlations between percolation

threshold, dispersion state, and aspect ratio of carbon nanotubes. Adv Funct Mater 17:3207–3215. https://doi.org/10.1002/adfm.200700065

95. Sandler JKW, Kirk JE, Kinloch IA, et al (2003) Ultra-low electrical percolation threshold in carbon-nanotube-epoxy composites. Polymer (Guildf) 44:5893–5899. https://doi.org/10.1016/S0032-3861(03)00539-1

96. Sumfleth J, Buschhorn ST, Schulte K (2011) Comparison of rheological and electrical percolation phenomena in carbon black and carbon nanotube filled epoxy polymers. J Mater Sci 46:659–669. https://doi.org/10.1007/s10853-010-4788-6

97. Ruschau GR, Yoshikawa S, Newnham RE (1992) Resistivities of conductive composites. J Appl Phys 72:953–959. https://doi.org/10.1063/1.352350

98. Kaur G, Adhikari R, Cass P, et al (2015) Electrically conductive polymers and composites for biomedical applications. RSC Adv 5:37553–37567. https://doi.org/10.1039/C5RA01851J

99. Yuan W, Lam T, Biggs J, et al (2007) New electrode materials for dielectric elastomer actuators. In: Proceedings of SPIE - The International Society for Optical Engineering

100. Yuan W, Lam T, Pei Q (2009) Durable dielectric elastomer actuators via self-clearable compliant electrode materials. In: Materials Research Society Symposium Proceedings. pp 183–190

101. Lam T, Tran H, Yuan W, et al (2008) Polyaniline nanofibers as a novel electrode material for faulttolerant dielectric elastomer actuators. In: Proceedings of SPIE - The International Society for Optical Engineering

102. Yao S, Zhu Y (2015) Nanomaterial-Enabled Stretchable Conductors: Strategies, Materials and Devices. Adv Mater 27:1480–1511. https://doi.org/10.1002/adma.201404446

103. Park M, Park J, Jeong U (2014) Design of conductive composite elastomers for stretchable electronics. Nano Today 9:244–260

104. Wu J, Zang J, Rathmell AR, et al (2013) Reversible sliding in networks of nanowires. Nano Lett 13:2381–2386. https://doi.org/10.1021/nl4000739

105. Ye S, Rathmell AR, Chen Z, et al (2014) Metal nanowire networks: The next generation of transparent conductors. Adv Mater 26:6670–6687. https://doi.org/10.1002/adma.201402710

106. Jeong GS, Baek DH, Jung HC, et al (2012) Solderable and electroplatable flexible electronic circuit on a porous stretchable elastomer. Nat Commun. https://doi.org/10.1038/ncomms1980

107. Baëtens T, Pallecchi E, Thomy V, Arscott S (2018) Cracking effects in squashable and stretchable thin metal films on PDMS for flexible microsystems and electronics. Sci Rep. https://doi.org/10.1038/s41598-018-27798-z

108. Rosset S, Niklaus M, Dubois P, et al (2007) Mechanical properties of electroactive polymer microactuators with ion-implanted electrodes. In: Electroactive Polymer Actuators and Devices (EAPAD) 2007

109. Hammock ML, Chortos A, Tee BCK, et al (2013) 25th anniversary article: The evolution of electronic skin (E-Skin): A brief history, design considerations, and recent progress. Adv Mater. https://doi.org/10.1002/adma.201302240

110. Verplancke R, Bossuyt F, Cuypers D, Vanfleteren J (2012) Thin-film stretchable electronics technology based on meandering interconnections: Fabrication and mechanical performance. J Micromechanics Microengineering 22:. https://doi.org/10.1088/0960-1317/22/1/015002

111. Matsuhisa N, Chen X, Bao Z, Someya T (2019) Materials and structural designs of stretchable conductors. Chem. Soc. Rev.

112. Zhang Y, Fu H, Su Y, et al (2013) Mechanics of ultra-stretchable self-similar serpentine interconnects. Acta Mater. https://doi.org/10.1016/j.actamat.2013.09.020

113. Cheng T, Zhang Y, Lai WY, Huang W (2015) Stretchable thin-film electrodes for flexible electronics with high deformability and stretchability. Adv. Mater.

114. Pimpin A, Suzuki Y, Kasagi N (2007) Microelectrostrictive actuator with large out-of-plane deformation for flow-control application. J

Microelectromechanical Syst. https://doi.org/10.1109/JMEMS.2007.895222

115. Jahanshahi A, Gonzalez M, van den Brand J, et al (2013) Stretchable Circuits with Horseshoe Shaped Conductors Embedded in Elastic Polymers. Jpn J Appl Phys 52:05DA18

116. Fan JA, Yeo WH, Su Y, et al (2014) Fractal design concepts for stretchable electronics. Nat Commun. https://doi.org/10.1038/ncomms4266

117. Gray DS, Tien J, Chen CS (2004) High-Conductivity Elastomeric Electronics. Adv Mater. https://doi.org/10.1002/adma.200306107

118. Benslimane M, Gravesen P, Sommer-Larsen P (2002) Mechanical properties of dielectric elastomer actuators with smart metallic compliant electrodes. In: Smart Structures and Materials 2002: Electroactive Polymer Actuators and Devices (EAPAD)

119. Vudayagiri S, Junker MD, Skov AL (2013) Factors affecting the surface and release properties of thin polydimethylsiloxane films. Polym J 45:871–878. https://doi.org/10.1038/pj.2012.227

120. Benslimane M, Kiil H-E, Tryson MJ (2010) Electromechanical properties of novel large strain PolyPower film and laminate components for DEAP actuator and sensor applications. In: Electroactive Polymer Actuators and Devices (EAPAD) 2010

121. Kiil H-E, Benslimane M (2009) Scalable industrial manufacturing of DEAP. In: Proceedings of SPIE - The International Society for Optical Engineering

122. Jun K, Kim D, Ryu S, Oh IK (2017) Surface Modification of Anisotropic Dielectric Elastomer Actuators with Uni-A nd Bi-axially Wrinkled Carbon Electrodes for Wettability Control. Sci Rep. https://doi.org/10.1038/s41598-017-06274-0

123. Wang H, Wang Z, Yang J, et al (2018) Ionic Gels and Their Applications in Stretchable Electronics. Macromol. Rapid Commun.

124. Keplinger C, Sun JY, Foo CC, et al (2013) Stretchable, transparent, ionic conductors. Science (80-). https://doi.org/10.1126/science.1240228

125. Cao Y, Morrissey TG, Acome E, et al (2017) A Transparent, Self-Healing,

Highly Stretchable Ionic Conductor. Adv Mater 29:. https://doi.org/10.1002/adma.201605099

126. Hall DB, Underhill P, Torkelson JM (1998) Spin Coating of Thin and Ultrathin Polymer Films. Polym Eng Sci 38:2039–2045. https://doi.org/10.1002/pen.10373

127. Duduta M, Wood RJ, Clarke DR (2016) Multilayer Dielectric Elastomers for Fast, Programmable Actuation without Prestretch. Adv Mater. https://doi.org/10.1002/adma.201601842

128. Krishnan S (2007) On the Manufacture of Very Thin Elastomeric Films by Spin-Coating. Thesis

129. Bračič M, Mohan T, Kargl R, et al (2014) Preparation of PDMS ultrathin films and patterned surface modification with cellulose. RSC Adv. https://doi.org/10.1039/c3ra47380e

130. Liu M, Sun J, Sun Y, et al (2009) Thickness-dependent mechanical properties of polydimethylsiloxane membranes. J Micromechanics Microengineering. https://doi.org/10.1088/0960-1317/19/3/035028

131. Chen Y, Zhao H, Mao J, et al (2019) Controlled flight of a microrobot powered by soft artificial muscles. Nature. https://doi.org/10.1038/s41586-019-1737-7

132. Duduta M, Hajiesmaili E, Zhao H, et al (2019) Realizing the potential of dielectric elastomer artificial muscles. Proc Natl Acad Sci U S A. https://doi.org/10.1073/pnas.1815053116

133. CTSystems. http://ct-systems.ch/index.php. Accessed 25 Mar 2020

134. Müller B, Deyhle H, Mushkolaj S, Wieland M (2009) The challenges in artificial muscle research to treat incontinence. Swiss Med. Wkly.

135. Rosset S, Ararom OA, Schlatter S, Shea HR (2016) Fabrication process of silicone-based dielectric elastomer actuators. J Vis Exp. https://doi.org/10.3791/53423

136. Poulin A, Saygili Demir C, Rosset S, et al (2016) Dielectric elastomer actuator for mechanical loading of 2D cell cultures. Lab Chip 16:3788–3794.

https://doi.org/10.1039/C6LC00903D

137. Rosset S, Shea H (2015) Towards fast, reliable, and manufacturable DEAs: Miniaturized motor and Rupert the rolling robot. In: Proceedings of SPIE - The International Society for Optical Engineering

138. Maffli L, Rosset S, Ghilardi M, et al (2015) Ultrafast all-polymer electrically tunable silicone lenses. Adv Funct Mater. https://doi.org/10.1002/adfm.201403942

139. Shi H, Al-Rubaiai M, Holbrook CM, et al (2019) Screen-Printed Soft Capacitive Sensors for Spatial Mapping of Both Positive and Negative Pressures. Adv Funct Mater. https://doi.org/10.1002/adfm.201809116

140. Suikkola J, Björninen T, Mosallaei M, et al (2016) Screen-Printing Fabrication and Characterization of Stretchable Electronics. Sci Rep 6:25784. https://doi.org/10.1038/srep25784

141. Poulin A, Rosset S, Shea HR (2015) Printing low-voltage dielectric elastomer actuators. Appl Phys Lett. https://doi.org/10.1063/1.4937735

142. Poulin A, Rosset S, Shea H (2016) Fully printed 3 microns thick dielectric elastomer actuator. In: Proceedings of SPIE - The International Society for Optical Engineering

143. Poulin A, Rosset S, Shea HR (2015) Printing low-voltage dielectric elastomer actuators. Appl Phys Lett 107:244104. https://doi.org/10.1063/1.4937735

144. Mäkelä T, Haatainen T, Majander P, Ahopelto J (2007) Continuous roll to roll nanoimprinting of inherently conducting polyaniline. Microelectron Eng 84:877–879. https://doi.org/10.1016/j.mee.2007.01.131

145. Lee J-W, Mun KK, Yoo YT (2009) A comparative study on roll-to-roll gravure printing on PET and BOPP webs with aqueous ink. Prog Org Coatings 64:98–108. https://doi.org/10.1016/j.porgcoat.2008.07.011

146. Benslimane MY, Gravesen P (2003) Dielectric actuator or sensor structure and method of making it

147. Sarban R, Jones RW, MacE BR, Rustighi E (2011) A tubular dielectric

elastomer actuator: Fabrication, characterization and active vibration isolation. Mech Syst Signal Process 25:2879–2891. https://doi.org/10.1016/j.ymssp.2011.06.004

148. Wallin TJ, Pikul J, Shepherd RF (2018) 3D printing of soft robotic systems. Nat. Rev. Mater.

149. Truby RL, Lewis JA (2016) Printing soft matter in three dimensions. Nature 540:371–378. https://doi.org/10.1038/nature21003

150. Peele BN, Wallin TJ, Zhao H, Shepherd RF (2015) 3D printing antagonistic systems of artificial muscle using projection stereolithography. Bioinspiration and Biomimetics. https://doi.org/10.1088/1748-3190/10/5/055003

151. Yirmibesoglu OD, Morrow J, Walker S, et al (2018) Direct 3D printing of silicone elastomer soft robots and their performance comparison with molded counterparts. In: 2018 IEEE International Conference on Soft Robotics, RoboSoft 2018

152. Muth JT, Vogt DM, Truby RL, et al (2014) Embedded 3D printing of strain sensors within highly stretchable elastomers. Adv Mater. https://doi.org/10.1002/adma.201400334

153. Wehner M, Truby RL, Fitzgerald DJ, et al (2016) An integrated design and fabrication strategy for entirely soft, autonomous robots. Nature 536:451–455. https://doi.org/10.1038/nature19100

154. Lewis JA (2006) Direct Ink Writing of 3D Functional Materials. Adv Funct Mater 16:2193–2204. https://doi.org/10.1002/adfm.200600434

155. Skylar-Scott MA, Mueller J, Visser CW, Lewis JA (2019) Voxelated soft matter via multimaterial multinozzle 3D printing. Nature. https://doi.org/10.1038/s41586-019-1736-8

156. Lewis JA (2006) Direct Ink Writing of 3D Functional Materials. Adv Funct Mater 16:2193–2204. https://doi.org/10.1002/adfm.200600434

157. Chortos A, Hajiesmaili E, Morales J, et al (2020) 3D Printing of Interdigitated Dielectric Elastomer Actuators. Adv Funct Mater.

https://doi.org/10.1002/adfm.201907375

158. Mei J, Lovell MR, Mickle MH (2005) Formulation and processing of novel conductive solution inks in continuous inkjet printing of 3-D electric circuits. IEEE Trans Electron Packag Manuf. https://doi.org/10.1109/TEPM.2005.852542

159. Martin GD, Hoath SD, Hutchings IM (2008) Inkjet printing - The physics of manipulating liquid jets and drops. J Phys Conf Ser. https://doi.org/10.1088/1742-6596/105/1/012001

160. Tekin E, Smith PJ, Schubert US (2008) Inkjet printing as a deposition and patterning tool for polymers and inorganic particles. Soft Matter. https://doi.org/10.1039/b711984d

161. Wijshoff H (2010) The dynamics of the piezo inkjet printhead operation. Phys. Rep.

162. De Gans BJ, Duineveld PC, Schubert US (2004) Inkjet printing of polymers: State of the art and future developments. Adv. Mater.

163. Kim E, Baek J (2012) Numerical study on the effects of non-dimensional parameters on drop-on-demand droplet formation dynamics and printability range in the up-scaled model. Phys Fluids. https://doi.org/10.1063/1.4742913

164. Gao M, Li L, Song Y (2017) Inkjet printing wearable electronic devices. J Mater Chem C. https://doi.org/10.1039/C7TC00038C

165. Kamyshny A, Magdassi S (2014) Conductive nanomaterials for printed electronics. Small 10:3515–3535

166. Umedachi T, Vikas V, Trimmer BA (2013) Highly deformable 3-D printed soft robot generating inching and crawling locomotions with variable friction legs. In: IEEE International Conference on Intelligent Robots and Systems

167. Maccurdy R, Katzschmann R, Kim Y, Rus D (2016) Printable hydraulics: A method for fabricating robots by 3D co-printing solids and liquids. In: Proceedings - IEEE International Conference on Robotics and Automation

168. Bartlett NW, Tolley MT, Overvelde JTB, et al (2015) A 3D-printed, functionally graded soft robot powered by combustion. Science (80-). https://doi.org/10.1126/science.aab0129

169. Rossiter J, Walters P, Stoimenov B (2009) Printing 3D dielectric elastomer actuators for soft robotics. Proc SPIE 7287:1–10. https://doi.org/10.1117/12.815746

170. Shih B, Mayeda J, Huo Z, et al (2018) 3D printed resistive soft sensors. In: 2018 IEEE International Conference on Soft Robotics, RoboSoft 2018

171. McCoul D, Rosset S, Schlatter S, Shea H (2017) Inkjet 3D printing of UV and thermal cure silicone elastomers for dielectric elastomer actuators. Smart Mater Struct. https://doi.org/10.1088/1361-665X/aa9695

172. Huang Q, Zhu Y (2019) Printing Conductive Nanomaterials for Flexible and Stretchable Electronics: A Review of Materials, Processes, and Applications. Adv Mater Technol 0:1800546. https://doi.org/10.1002/admt.201800546

173. Al-Halhouli A, Qitouqa H, Alashqar A, Abu-Khalaf J (2018) Inkjet printing for the fabrication of flexible/stretchable wearable electronic devices and sensors. Sens. Rev.

174. Araromi OA, Conn AT, Ling CS, et al (2010) A novel fabrication set-up for the flexible production of silicone based EAP “artificial muscle” actuators. WIT Trans Ecol Environ 138:289–300. https://doi.org/10.2495/DN100251

175. Reitelshofer S, Landgraf M, Graf D, et al (2015) A new production process for soft actuators and sensors based on dielectric elastomers intended for safe human robot interaction. In: 2015 IEEE/SICE International Symposium on System Integration (SII). IEEE, pp 51–56

176. Forrest SR (1997) Ultrathin Organic Films Grown by Organic Molecular Beam Deposition and Related Techniques. Chem Rev 97:1793–1896. https://doi.org/10.1021/cr9410140

177. Töpper T, Weiss F, Osmani B, et al (2015) Siloxane-based thin films for biomimetic low-voltage dielectric actuators. Sensors Actuators A Phys 233:32–41. https://doi.org/10.1016/j.sna.2015.06.014

178. Weiss FM, Töpper T, Osmani B, et al (2016) Thin Film Formation and Morphology of Electrosprayed Polydimethylsiloxane. Langmuir 32:3276–3283. https://doi.org/10.1021/acs.langmuir.6b00476

179. Hartmann F, Drack M, Kaltenbrunner M (2018) Meant to merge: Fabrication of stretchy electronics for robotics. Sci. Robot.

180. Cooley JF (1902) Apparatus for electrically dispersing fluids.

181. Bhardwaj N, Kundu SC (2010) Electrospinning: A fascinating fiber fabrication technique. Biotechnol. Adv. 28:325–347

182. Jaworek A, Sobczyk AT (2008) Electrospraying route to nanotechnology: An overview. J Electrostat. https://doi.org/10.1016/j.elstat.2007.10.001

183. Onses MS, Sutanto E, Ferreira PM, et al (2015) Mechanisms, Capabilities, and Applications of High-Resolution Electrohydrodynamic Jet Printing. Small

184. Xue J, Xie J, Liu W, Xia Y (2017) Electrospun Nanofibers: New Concepts, Materials, and Applications. Acc Chem Res. https://doi.org/10.1021/acs.accounts.7b00218

185. Kenawy ER, Bowlin GL, Mansfield K, et al (2002) Release of tetracycline hydrochloride from electrospun poly(ethylene-co-vinylacetate), poly(lactic acid), and a blend. J Control Release. https://doi.org/10.1016/S0168-3659(02)00041-X

186. Sill TJ, von Recum HA (2008) Electrospinning: Applications in drug delivery and tissue engineering. Biomaterials

187. Fenn JB, Mann M, Meng CK, et al (1989) Electrospray ionization for mass spectrometry of large biomolecules. Science (80-.).

188. Fukuda T, Toda A, Takahira K, et al (2017) Improved performance of organic photovoltaic cells with PTB7-Th:PC71 BM by optimized solvent evaporation time in electrospray deposition. Org Electron. https://doi.org/10.1016/j.orgel.2017.05.049

189. Dalton PD, Vaquette C, Farrugia BL, et al (2013) Electrospinning and additive manufacturing: Converging technologies. Biomater. Sci.

190. Engstrom DS, Porter B, Pacios M, Bhaskaran H (2014) Additive nanomanufacturing - A review. J. Mater. Res.

191. Fernández de la Mora J (2006) The Fluid Dynamics of Taylor Cones. Annu Rev Fluid Mech. https://doi.org/10.1146/annurev.fluid.39.050905.110159

192. Lee A, Jin H, Dang HW, et al (2013) Optimization of experimental parameters to determine the jetting regimes in electrohydrodynamic printing. Langmuir. https://doi.org/10.1021/la403111m

193. Jayasinghe SN, Edirisinghe MJ (2004) Electrically forced jets and microthreads of high viscosity dielectric liquids. J Aerosol Sci. https://doi.org/10.1016/j.jaerosci.2003.08.004

194. Jayasinghe SN, Edirisinghe MJ (2004) Electric-field driven jetting from dielectric liquids. Appl Phys Lett. https://doi.org/10.1063/1.1812574

195. Eggers J, Villermaux E (2008) Physics of liquid jets. Reports Prog Phys. https://doi.org/10.1088/0034-4885/71/3/036601

196. Collins RT, Harris MT, Basaran OA (2007) Breakup of electrified jets. J Fluid Mech. https://doi.org/10.1017/S0022112007007409

197. Tang K, Gomez A (1994) On the structure of an electrostatic spray of monodisperse droplets. Phys Fluids. https://doi.org/10.1063/1.868182

198. Yu DG, Branford-White CJ, Chatterton NP, et al (2010) Electrospinning of concentrated polymer solutions. Macromolecules. https://doi.org/10.1021/ma1024363

199. Wang X, Cao J, Hu Z, et al (2006) Jet shaping nanofibers and the collection of nanofiber mats in electrospinning. J Mater Sci Technol

200. Zong X, Kim K, Fang D, et al (2002) Structure and process relationship of electrospun bioabsorbable nanofiber membranes. Polymer (Guildf). https://doi.org/10.1016/S0032-3861(02)00275-6

201. Tan SH, Inai R, Kotaki M, Ramakrishna S (2005) Systematic parameter study for ultra-fine fiber fabrication via electrospinning process. Polymer (Guildf). https://doi.org/10.1016/j.polymer.2005.05.068

202. Mazoochi T, Hamadanian M, Ahmadi M, Jabbari V (2012) Investigation on

the morphological characteristics of nanofiberous membrane as electrospun in the different processing parameters. Int J Ind Chem. https://doi.org/10.1186/2228-5547-3-2

203. Park J-U, Hardy M, Kang SJ, et al (2007) High-resolution electrohydrodynamic jet printing. Nat Mater 6:782–789. https://doi.org/10.1038/nmat1974

204. Altmann K, Schulze RD, Hidde G, Friedrich J (2013) Electrospray ionization for deposition of ultra-thin polymer layers-principle, electrophoretic effect and applications. J Adhes Sci Technol. https://doi.org/10.1080/01694243.2012.727170

205. Brown N a., Gladstone JN, Chiarot PR (2015) Evolution of Nanoparticle Deposits Printed Using Electrospray. J Micro Nano-Manufacturing 3:014502. https://doi.org/10.1115/1.4029198

206. Brown NA, Gladstone JN, Chiarot PR (2014) Materials Printing Using Electrospray. In: Volume 2B: Advanced Manufacturing. ASME, p V02BT02A049

207. Kessick R, Fenn J, Tepper G (2004) The use of AC potentials in electrospraying and electrospinning processes. Polymer (Guildf) 45:2981–2984. https://doi.org/10.1016/j.polymer.2004.02.056

208. Parhizkar M, Reardon PJT, Knowles JC, et al (2017) Performance of novel high throughput multi electrospray systems for forming of polymeric micro/nanoparticles. Mater Des 126:73–84. https://doi.org/10.1016/j.matdes.2017.04.029

209. Lojewski B, Yang W, Duan H, et al (2013) Design, fabrication, and characterization of linear multiplexed electrospray atomizers micro-machined from metal and polymers. Aerosol Sci Technol 47:146–152. https://doi.org/10.1080/02786826.2012.734936

210. Arnanthigo Y, Yurteri CU, Biskos G, et al (2011) Out-scaling electrohydrodynamic atomization systems for the production of well-defined droplets. Powder Technol 214:382–387. https://doi.org/10.1016/j.powtec.2011.08.036

211. Deng W, Klemic JF, Li X, et al (2006) Increase of electrospray throughput using multiplexed microfabricated sources for the scalable generation of monodisperse droplets. J Aerosol Sci 37:696–714. https://doi.org/10.1016/j.jaerosci.2005.05.011

212. Deng W, Waits CM, Morgan B, Gomez A (2009) Compact multiplexing of monodisperse electrosprays. J Aerosol Sci 40:907–918. https://doi.org/10.1016/j.jaerosci.2009.07.002

213. Deng W, Gomez A (2007) Influence of space charge on the scale-up of multiplexed electrosprays. J Aerosol Sci 38:1062–1078. https://doi.org/10.1016/j.jaerosci.2007.08.005

214. Lee GY, Lee HT, Ryu W, et al (2018) Resistive pressure sensor based on cylindrical micro structures in periodically ordered electrospun elastic fibers. Smart Mater Struct. https://doi.org/10.1088/1361-665X/aae041

215. Ko J, Bhullar S, Cho Y, et al (2015) Design and fabrication of auxetic stretchable force sensor for hand rehabilitation. Smart Mater Struct. https://doi.org/10.1088/0964-1726/24/7/075027

216. Cui Z, Han Y, Huang Q, et al (2018) Electrohydrodynamic printing of silver nanowires for flexible and stretchable electronics. Nanoscale. https://doi.org/10.1039/c7nr09570h

217. Leung V, Fattorini E, Karapetkova M, et al (2016) Biomimetic artificial sphincter muscles: status and challenges. In: Martín-Palma RJ, Lakhtakia A, Knez M (eds) Bioinspiration, Biomimetics, and Bioreplication 2016. p 97970M

218. Braghirolli DI, Zamboni F, Acasigua GAX, Pranke P (2015) Association of electrospinning with electrospraying: A strategy to produce 3D scaffolds with incorporated stem cells for use in tissue engineering. Int J Nanomedicine. https://doi.org/10.2147/IJN.S84312

219. Al Kayal T, Losi P, Pierozzi S, Soldani G (2020) A New Method for Fibrin-Based Electrospun/Sprayed Scaffold Fabrication. Sci Rep 10:5111. https://doi.org/10.1038/s41598-020-61933-z

220. Ren L-F, Xia F, Shao J, et al (2017) Experimental investigation of the effect

of electrospinning parameters on properties of superhydrophobic PDMS/PMMA membrane and its application in membrane distillation. Desalination 404:155–166. https://doi.org/https://doi.org/10.1016/j.desal.2016.11.023

221. Niu H, Wang H, Zhou H, Lin T (2014) Ultrafine PDMS fibers: Preparation from in situ curing-electrospinning and mechanical characterization. RSC Adv. https://doi.org/10.1039/c4ra00232f

222. Liu W, Huang C, Jin X (2015) Electrospinning of Grooved Polystyrene Fibers: Effect of Solvent Systems. Nanoscale Res Lett. https://doi.org/10.1186/s11671-015-0949-5

223. Maher M, Smith A, Margiotta J (2014) A synopsis of the Defense Advanced Research Projects Agency (DARPA) investment in additive manufacture and what challenges remain. pp 897002–897009

224. Tait JG, Witkowska E, Hirade M, et al (2015) Uniform Aerosol Jet printed polymer lines with 30μm width for 140ppi resolution RGB organic light emitting diodes. Org Electron 22:40–43. https://doi.org/10.1016/j.orgel.2015.03.034

225. Wilkinson NJ, Smith MAA, Kay RW, Harris RA (2019) A review of aerosol jet printing—a non-traditional hybrid process for micro-manufacturing. Int J Adv Manuf Technol 105:4599–4619. https://doi.org/10.1007/s00170-019-03438-2

226. Grunwald I, Groth E, Wirth I, et al (2010) Surface biofunctionalization and production of miniaturized sensor structures using aerosol printing technologies. Biofabrication 2:. https://doi.org/10.1088/1758-5082/2/1/014106

227. Cai F, Chang Y-H, Wang K, et al (2016) Low-Loss 3-D Multilayer Transmission Lines and Interconnects Fabricated by Additive Manufacturing Technologies. IEEE Trans Microw Theory Tech PP: https://doi.org/10.1109/TMTT.2016.2601907

228. Optomec (2017) Aerosol Jet Technology for 3D Printed Electronics. https://www.optomec.com/printed-electronics/aerosol-jet-technology/

229. Saleh MS, Hu C, Panat R (2017) Three-dimensional microarchitected materials and devices using nanoparticle assembly by pointwise spatial printing. Sci Adv 3:e1601986. https://doi.org/10.1126/sciadv.1601986

230. Smith M, Choi YS, Boughey C, Kar-Narayan S (2017) Controlling and assessing the quality of aerosol jet printed features for large area and flexible electronics. Flex Print Electron 2:. https://doi.org/10.1088/2058-8585/aa5af9

231. Mahajan A, Frisbie CD, Francis LF (2013) Optimization of Aerosol Jet Printing for High-Resolution, High-Aspect Ratio Silver Lines. ACS Appl Mater Interfaces 5:4856–4864. https://doi.org/10.1021/am400606y

232. Wilkinson NJ, Lukic-Mann M, Shuttleworth MP, et al (2019) Aerosol jet printing for the manufacture of soft robotic devices. In: RoboSoft 2019 - 2019 IEEE International Conference on Soft Robotics. pp 496–501

233. Chiang Foo C, Cai S, Jin Adrian Koh S, et al (2012) Model of dissipative dielectric elastomers. J Appl Phys. https://doi.org/10.1063/1.3680878

234. Secor EB (2018) Principles of aerosol jet printing. Flex Print Electron. https://doi.org/10.1088/2058-8585/aace28

8 Appendix A

Wilkinson, N.J.; Smith, M.A.A.; Kay, R.W.; and Harris, R.A. 'A review of aerosol jet printing—a non-traditional hybrid process for micro-manufacturing.' *Int J Adv Manuf Technol* **105,** 4599–4619 (2019). DOI: 10.1007/s00170-019-03438-2.

The International Journal of Advanced Manufacturing Technology
https://doi.org/10.1007/s00170-019-03438-2

ORIGINAL ARTICLE

A review of aerosol jet printing—a non-traditional hybrid process for micro-manufacturing

N. J. Wilkinson[1] · M. A. A. Smith[1] · R. W. Kay[1] · R. A. Harris[1]

Received: 5 May 2018 / Accepted: 11 February 2019

Abstract
Aerosol Jet Printing (AJP) is an emerging contactless direct write approach aimed at the production of fine features on a wide range of substrates. Originally developed for the manufacture of electronic circuitry, the technology has been explored for a range of applications, including, active and passive electronic components, actuators, sensors, as well as a variety of selective chemical and biological responses. Freeform deposition, coupled with a relatively large stand-off distance, is enabling researchers to produce devices with increased geometric complexity compared to conventional manufacturing or more commonly used direct write approaches. Wide material compatibility, high resolution and independence of orientation have provided novelty in a number of applications when AJP is conducted as a digitally driven approach for integrated manufacture. This overview of the technology will summarise the underlying principles of AJP, review applications of the technology and discuss the hurdles to more widespread industry adoption. Finally, this paper will hypothesise where gains may be realised through this assistive manufacturing process.

Keywords Aerosol jet · Hybrid manufacture · Micro-manufacturing · Printed electronics · Direct write

1 Introduction

Direct write covers a range of processes that can selectively deposit material to produce freeform patterns. These processes are often investigated for the production of conductive traces [1–3]; however, the capabilities of direct write are being increasingly explored for the deposition of other functional [4–6] and structural inks [7–9]. Digitally driven and independent of orientation, direct write techniques are attractive for applications desiring conformity and design flexibility [10]. The high-value sectors of aerospace and healthcare provide significant motivation; however, as technologies mature, they are likely to be adopted more widely as engineers seek new functionality alongside improved performance and packaging. The diversity of applications provides a significant incentive for the development of capable direct-write processes. This opportunity was recognised in the DARPA-funded MICE (Mesoscale Integrated Conformal Electronics) project in the late 1990s, which aimed to develop manufacturing processes capable of depositing a range of materials on to virtually any substrate [11]. The outcome was the development of a number of deposition mechanisms, most notably the Aerosol Jet and Nanojet systems that have since been commercialised by Optomec Inc. and Integrated Deposition Systems (IDS), respectively. The first research publications featuring Aerosol Jet Printing (AJP) began to emerge around 2001–2002 [12].

AJP (Fig. 1) introduced new capabilities to direct write through its use of a directed aerosol stream to provide consistent deposition at nozzle–substrate offsets of 1–5 mm [13]. This approach enables the patterning of more complex surfaces, which was well illustrated through the deposition of a spiral pattern on the surface of a golf ball [14]. For an assistive manufacturing technology—one that is intended to be used as part of a greater, hybrid manufacturing process—this flexibility simplifies control, accommodates less precise articulation and enables patterning on surfaces that cannot be reached by physical nozzles. This combination greatly simplifies process integration when compared with other direct write technologies.

Wilkinson and Smith have made an equal contribution in the creation of this review.

✉ N. J. Wilkinson
mnnjw@leeds.ac.uk

[1] Future Manufacturing Processes Research Group, University of Leeds, Leeds, UK

Published online: 09 May 2019

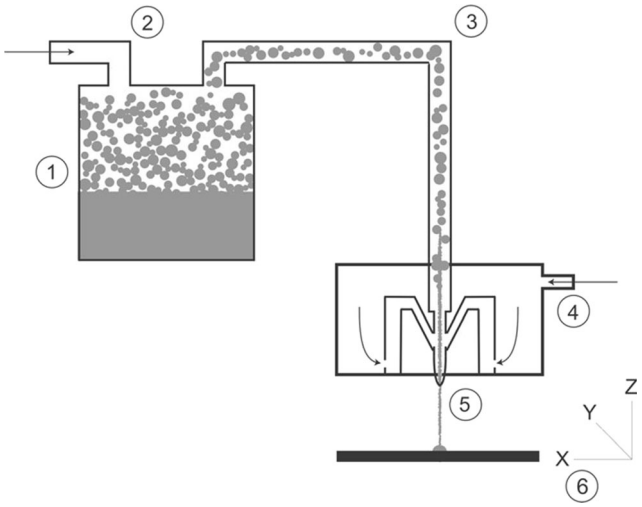

Fig. 1 An overview of AJP: (1) aerosol generation using either ultrasonic or pneumatic atomiser, (2) introduction of a carrier gas to transport the aerosol, (3) transportation and refinement, (4) focussing and (5) deposition and (6) computer-controlled translation of the substrate

In theory, any material that can be suspended within an aerosol is compatible with the AJP technique. Commercial systems use ultrasonic or pneumatic atomisation to generate an aerosol from inks with viscosities that range from 1 to 1000 cp. Tolerance of a wide range of materials presents opportunities beyond competing inkjet technologies, which are often limited to viscosities below 20 cp. Examples of materials deposited using AJP range from silver inks [15] and ceramics [16] to biological matter, such as proteins and strands of DNA [17]. Material flexibility does not come at the expense of resolution, with research groups claiming depositions in the region of 10 μm [17, 18].

The above-mentioned novelties provide promise for the field of AJP and the wider direct write approach. This review provides an overview of the process before discussing the current-state-of-the-art from an applications perspective. The future of AJP is, then, explored to provide an insight in to how it can mature for more widespread industry adoption. This review has avoided a comprehensive comparison with similar direct write technologies, such as inkjet printing, as this is can be found in existing literature [3, 19].

2 Atomisation techniques

Production of an aerosol with characteristics suitable for jetting requires an understanding of both the atomisation techniques and the rheological properties of the ink. The interplay between the surface tension, viscosity, volatility, and density of the material with the method of aerosolization presents unique challenges in process development. These issues are compounded by a high degree of process variability between inks of different types.

An ideal aerosol would be monodispersed, highly dense and contain droplets with sufficient inertia to be impacted on the substrate. Droplets must not be so large that they negatively affect the minimum feature size or cause nozzle clogging. Aerosolization is achieved through the application of either ultrasonic or pneumatic atomisation. The ultrasonic atomiser produces highly uniform aerosols; however, it is limited to inks with viscosities in the range of 1–10 cp. The pneumatic approach enables the atomisation of materials with a viscosity up to 1000 cp [20], but it sacrifices the uniformity, or monodispersity, of the aerosol that is produced and requires extra flow refinement steps before deposition.

2.1 Ultrasonic atomisation

Ultrasonic atomisation produces an aerosol from small volumes (~2 ml) of low-viscosity (1–10 cp) inks. Its operation principle is illustrated in Fig. 2; a transducer is submerged within a transfer medium, typically water, where it oscillates at high frequency (Fig. 2—1). A wave is propagated through the transfer medium to a vial suspended above the transducer (Fig. 2—2). Within the vial, a standing wave is formed on the surface and the superposition of consecutive waves results in the formation of large peaks (Fig. 2—3). Local shear at the top of these peaks results in small droplets being ejected from the bulk ink. Finally, a positive pressure is applied to the vial to drive the aerosol from the vial towards the deposition head (Fig. 2—4).

Aerosols produced using this technique are typically of low dispersity, with droplet sizes ranging from 2 to 5 μm [19]. In practice, a user is likely to tailor the atomisation parameters and ink formulation to modify the droplet size and distribution in an attempt to minimise small satellite deposits at the edges of a deposition known as overspray (Section 3.1). The

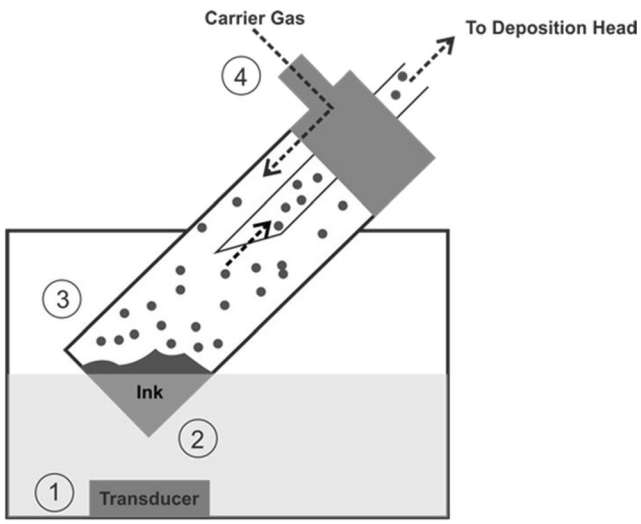

Fig. 2 Schematic of ultrasonic atomisation

relatively low dispersity of the aerosol negates the need for secondary refinement stages.

2.2 Pneumatic atomisation

The pneumatic approach is tolerant of a greater range of viscosities—usually reported to be 1–1000 cp; however, Optomec's more recent datasheets suggest a conservative 1–500 cp. Atomisation is achieved using a variant of the well-documented Collison-style atomiser that has previously been used for the aerosolization of bacterial suspensions. Designs, descriptions and applications of this type of atomiser can be found in the literature; with May's 1972 report providing a detailed design study [21].

Figure 3 shows a schematic of a typical Collison atomiser. During atomisation, a carrier gas is accelerated across the top of an ink supply channel (Fig. 3—1). This creates a region of reduced static pressure that draws the ink to the carrier gas flow. When the ink reaches the level of the carrier gas stream, the topmost layer is sheared producing a series of polydisperse droplets (Fig. 3—2). Large, high-inertia droplets within this stream are impacted on the side wall of the atomising chamber and return to the reservoir (Fig. 3—3), while lower inertia droplets remain as an aerosol and are exhausted from the atomiser towards the virtual impactor (Fig. 3—4).

Following atomisation, the aerosol is transported to the virtual impactor (Fig. 4—1), which uses a region of stagnant flow to separate droplets within an aerosol stream based on their inertia (Fig. 4—2). Small droplets, which have insufficient inertia to overcome this region, are ejected radially in to the major flow (Fig. 4—3). As low inertia droplets contribute

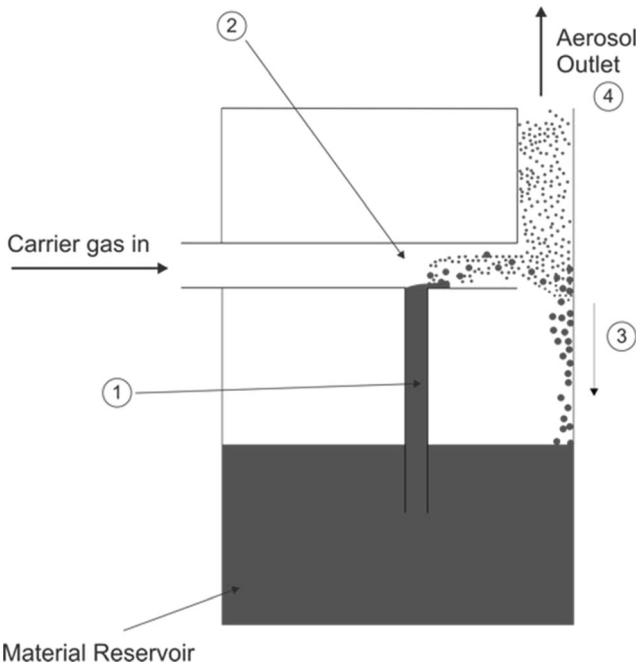

Fig. 3 A schematic of pneumatic atomisation

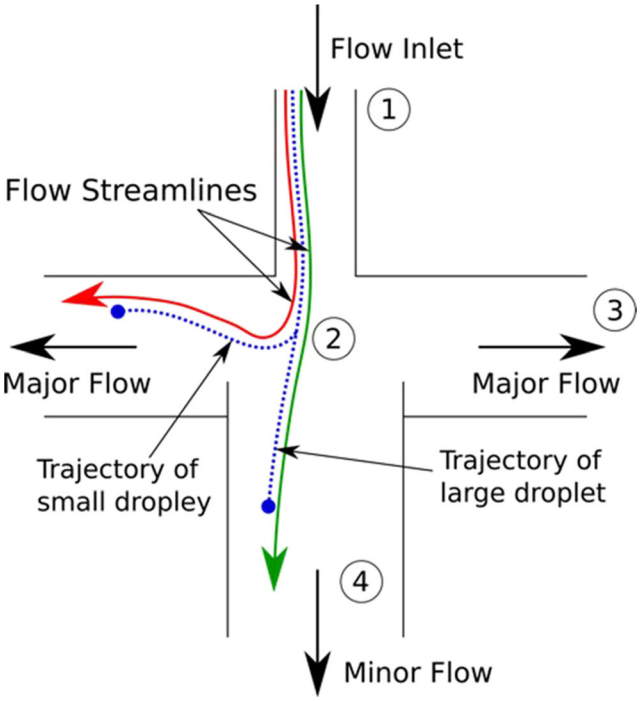

Fig. 4 Schematic of a virtual impactor

to overspray in AJ, these are usually collected or vented to the atmosphere. Large, high-inertia droplets are able to pass through the stagnant flow region and continue towards the deposition head (Fig. 4—4).

3 Focussing and deposition

Once a suitable aerosol has been produced, it is transferred to the deposition head by a carrier gas flow (Fig. 5—1) where it is focussed using a virtual and physical nozzle. The introduction of a secondary flow (Fig. 5—2) constrains and constricts the aerosol within an annular sheath that forms an interlayer between the aerosol and the physical components (Fig. 5—3). The aerosol and its annular sheath are further focussed through a physical nozzle before being deposited on to the substrate (Fig. 5—4).

The application of a sheath gas results in characteristics that are unique to AJP; the aerosol flow is collimated, which enables consistent deposition at a 1–5 mm stand-off; the interlayer between the aerosol stream and the material reduces the instances of nozzle clogging; and, through the manipulation of the aerosol flow rate relative to the sheath, it enables in-process control of the deposition geometry without changes in hardware. The combination of virtual and physical nozzles allows deposits that are one tenth the size of the nozzle's orifice [9]. A challenge for focussing using a sheath comes from its interaction with the substrate and previous deposits, especially if they are in liquid or powdered forms.

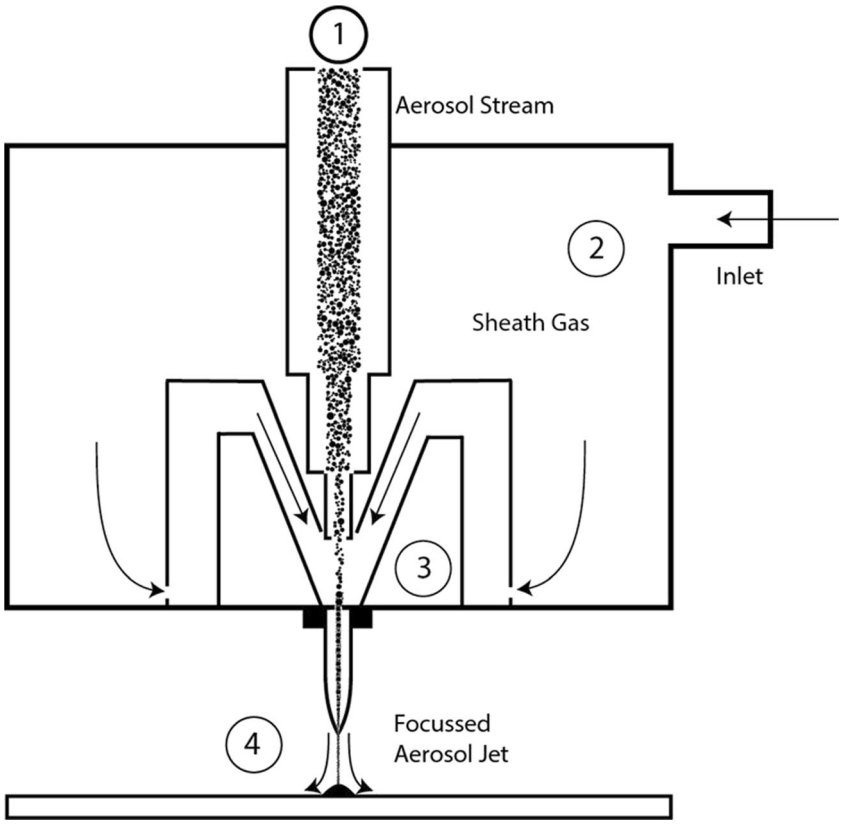

Fig. 5 Schematic of a deposition head [1]

3.1 Factors affecting deposition

Deposit quality is reliant on a multitude of factors (Fig. 6); the apparatus, process and design are readily configurable, while the substrate and environmental factors are more difficult to control, especially in the context of industrial production lines. Material and ink formulation present arguably the biggest challenge, and their development is discussed at more length in Section 4. Research groups have begun investigating the effect of process parameters [1, 22, 23], and the fundamental principles of AJP have, recently, been well presented [24]. Goth et al. [22] conducted a study with a focus on the adhesiveness, conductivity and wetting characteristics for silver and palladium inks at varying processing parameters and substrate surface energies. They report that plasma treatment of the substrate's surface prior to AJP increases material spreading and adhesion. Mahajan et al. [1] built on this work and were the first to identify the focussing ratio—the ratio of the sheath gas flow rate to the carrier gas flow rate—as a key parameter for the printing of fine features using AJP. The importance of the focussing ratio was reaffirmed during an analytical study on AJP by Binder et al. [25]. More recently, Smith et al.

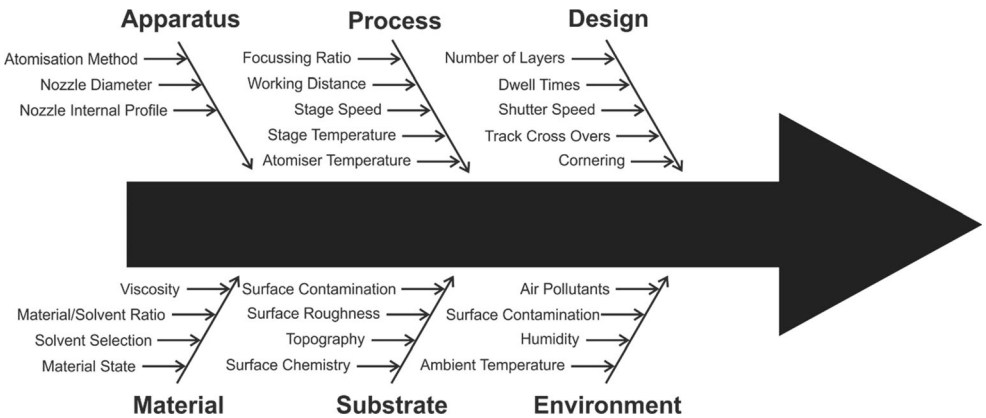

Fig. 6 Parameters effecting aerosol jet printing (adapted from [22])

[23] conducted an investigation of processing parameters and expanded the study to include the substrate temperature.

In all of these studies, minimising overspray is identified as a challenge for AJP during initial process development. The overspray deposits (Fig. 7) are the result of droplets with insufficient inertia to be impacted close to the centre line of the aerosol flow before spreading with the carrier and sheath gas [24]. Assuming the droplets all have the same density and velocity, these inertial differences will result from variation in the volume of the droplets, which can be controlled to a degree though the ink composition, atomisation parameters and virtual impaction. For any reasonably developed process, overspray is merely an artefact of deposition mechanism and its consequence is primarily as a metric for defining line quality.

Improving edge definition and overall line quality by minimising overspray is currently achieved through empirical optimisation. Analytical models aiming to increase understanding of the deposition mechanism are starting to be developed, which will lead to a greater appreciation of the interdependence of process parameters and accelerate the development of robust print recipes [24, 26].

Objective metrics that can distinguish between poor- and high-quality lines will be important for AJP as it transitions away from a reliance on user intuition. For conductive traces, Smith et al. [23] developed a method for quantitatively defining line quality by comparing the full-width at half-maximum height (FWHM) to a measurement of the distance between the edges of the overspray. If this measurement, known as the effective width, was found to be significantly greater than the FWHM, then the line was deemed to be of poor quality as much of the deposit did not contribute to its current carrying capacity. Salary et al. [27] have started to develop an in-process monitoring tool that extracts six metrics (line width, line density, edge smoothness, overspray index, line discontinuity and Fiedler number) from optical micrographs to determine the quality of deposit. They hope to eventually implement a system for closed-loop control of the AJP process.

Often overlooked, transportation losses can also have a large impact on the quality of the final deposit. Secor [24] published a model for the transportation losses and highlighted gravitational settling as the predominant factor with diffusion, machine geometry and ink formulation also playing important roles. Losses during transportation can account for non-linearities in the deposition rate with increasing aerosol flow, if it is assumed that the density of the aerosol is constant. In practice, longer transportation tubing requires greater aerosol flow rates for equivalent losses, meaning machine configurations that generate an aerosol at a distance from the deposition head will experience greater losses than those that generate the aerosol locally. More recent iterations of the Optomec and Nanojet systems have integrated the atomisation assembly on to the deposition head, which is perhaps indicative of this effect.

Secor [24] argues that through considered design of these flow pathways, the losses could be harnessed to narrow the distribution of droplets within an aerosol flow. Although attractive in principle, the limited gains achievable through this approach are unlikely to be worth the empirical efforts compared to other techniques, such as virtual impaction or optimisation of the ink and processing parameters.

4 Material development

The formulation of a suitable ink is key for depositions with desirable morphologies and functional characteristics and, as a result, is one of the most active areas of research for AJP. Although accommodating of a wide variety of ink solutions, suspensions and viscosities (Table 1), initial formulation and optimisation are achieved through large, isolated bodies of empirical work due to a lack of fundamental understanding and process models. A description of the conditions required to develop a jettable ink, comparable to the "Z number" used for inkjet printing, would likely accelerate development times and research outputs [28].

Part of this challenge is understanding and effectively controlling evaporation during atomisation, transportation and deposition. Low-boiling point solvents evaporate in flight and, when used alone, can result in the deposition of discrete, dry particles that produce features with high surface roughness

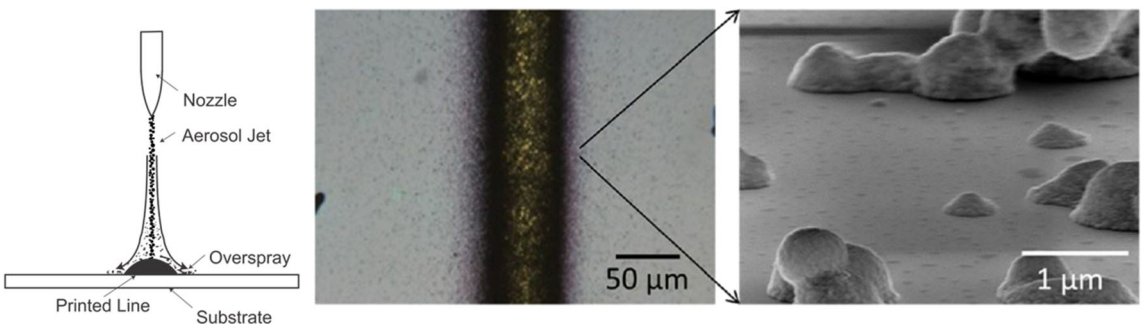

Fig. 7 Overspray in AJP deposits [1] (Reprinted with permission from [1])

Table 1 Material recommendations

	Ultrasonic atomisation	Pneumatic atomisation
Suitable phase	Solvents, solutions, dispersions	Solutions, dispersions, liquid monomers, melts
Maximum viscosity	5 cP	1000 cP
Maximum solid loading (dispersions)	55 wt.%	75 wt.%
Maximum particle size (dispersions)	50 nm	500 nm
Predominant solvent type	Low boiling point	High boiling point

and porosity. A loss of mass through evaporation can lead to droplets with insufficient inertia for impaction, which can prevent patterning and emit more particles in to the atmosphere than on to the substrate [24]. Yang et al. [29] stipulated that the production of flat features requires the deposition of a thin liquid layer that can be dried in situ through the effects of the sheath gas and a heated substrate. This behaviour is commonly achieved through a combination of high and low volatility solvents. The high volatility solvent is evaporated shortly after atomisation, which saturates the carrier gas and leads to a stable droplet volume during transportation until the aerosol stream interacts with the sheath gas. At this point, the low volatility solvent will begin to evaporate. Total drying of the particles before deposition can usually be avoided by including ~ 10% of low volatility co-solvent within the ink [24].

These hurdles, combined with the adhesion, wetting and drying challenges facing nearly all direct write process, are being readily addressed for AJP in both research and commercial settings. Continued development is likely to lead to a better understanding of the process that will decrease development timescales, drive down cost and ultimately lead to more widespread industrial adoption.

5 Applications

An array of applications have been identified for AJP that hope to deploy its material and spatial freedom to create new types of products with increased functionality. Most work, to date, has been centred on the production of printed electronic devices using unconventional materials and substrates. However, the technology is starting to be explored to expand capabilities in diverse research topics. For the purposes of this review, the different bodies of work have been grouped based on their primary application area (Fig. 8).

5.1 Passive electronic components

Passive electronic components are those that do not increase the net power of the circuit and whose output is not controlled by another signal (e.g. resistors [30], capacitors [16, 31] and inductors [32]). Their relative simplicity makes them an achievable application for most implementations of AJP, provided the material can be printed reliably. Printing passive electronic components reduces their space claim and allows greater integration of electronic circuitry with fewer processing steps, while the ability to print onto non-planar surfaces surpasses other technology in this area.

5.1.1 Interconnects

AJP is widely demonstrated as a technique for printing conductive traces designed to connect two or more electronic components. This approach is a promising free-form, three-dimensional and mask-less substitute for template-driven technologies, such as photolithography, chemical etching and screen printing. AJP has an opportunity to enable a new era of electronics on unconventional substrates. The simplicity of electrical interconnects has made them the primary structure for the evaluation of conductive materials.

Early work on interconnects used a silver nanoparticle ink as a seed layer for a secondary light-induced plating process on glass and silicone substrates for the front side metallisation of solar cells [33, 34]. The AJP nanoparticle ink was used to produce a high-quality electrical and mechanical contact with the silicon solar cell, while the light-induced plating process provided a higher conductivity finger for more efficient transfer of charge. Fraunhofer ISE have continued to develop the seed-plating process through investigation of scale-up [34] and material development [35, 36]. Functional circuitry using only AJP followed shortly after when Padovani at al. [37] deposited silver nanoparticle inks on glass as 35 μm interconnects between LEDs in a transparent head-up display (Fig. 9).

The flexibility in stand-off heights enables the production of vertical interconnects for multi-layer circuitry and stacked componentry. Vertical interconnects, or vias, were developed by Zhan et al. [38]. By shaping holes between circuit layers in to trapezoidal and reverse-trapezoidal geometries, they were able to create effective connections by jetting a silver ink in to the recesses. Once sintered, the vias were functional provided that the cooling rate was controlled to prevent cracking through the thermal shock. Out-of-plane interconnection of stacked components on a PCB substrate using 25-μm AJP silver lines has been shown to be an effective way to produce compact packaging (Fig. 10) [39]. The conductivity of the silver tracks produced during this work was found to be 8%

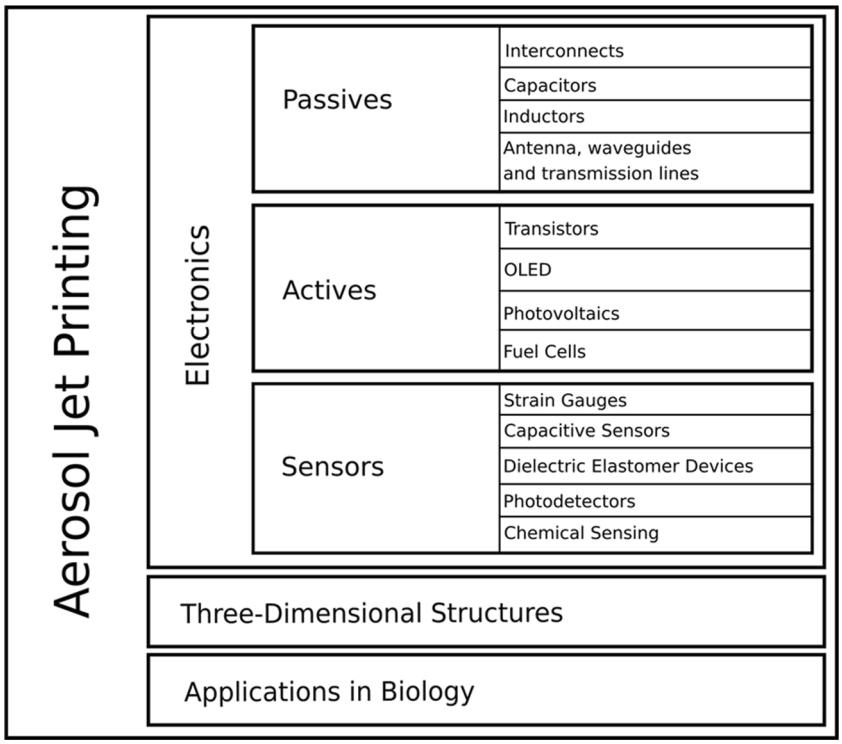

Fig. 8 Applications of AJP

of bulk silver. Syed-Khaja et al. [40] have shown die attachment through the sintering of AJP silver pads.

An investigation in to the compatibility of AJP-deposited silver ink and conventional wire bonding has shown limited bond strength for Au and Al wire bonding. In their work, Stoukatch et al. [41] suggested that silver inks themselves may prove to be an alternative for substrates with low thermal capabilities. Ultrasonic wire bonding has been shown to be a more effective technique for joining AJP silver deposits to components on both glass and polythalamide substrates [42]. The attachment of micro-electromechanical systems (MEMS) to circuits has also been achieved through AJP [43].

One of the primary advantages of AJP is its ability to produce fine features [44]. Kopola et al. [45] demonstrated improved device performance by decreasing the width of tracks in the current collection grid of an inverted, ITO-free solar cell. In this preliminary work, comparatively large mean line widths of 58.1 μm were achieved. Mahajan et al. [1] conducted a more comprehensive study on the optimisation of high-resolution (20 μm), high-aspect ratio (0.1) silver lines, in

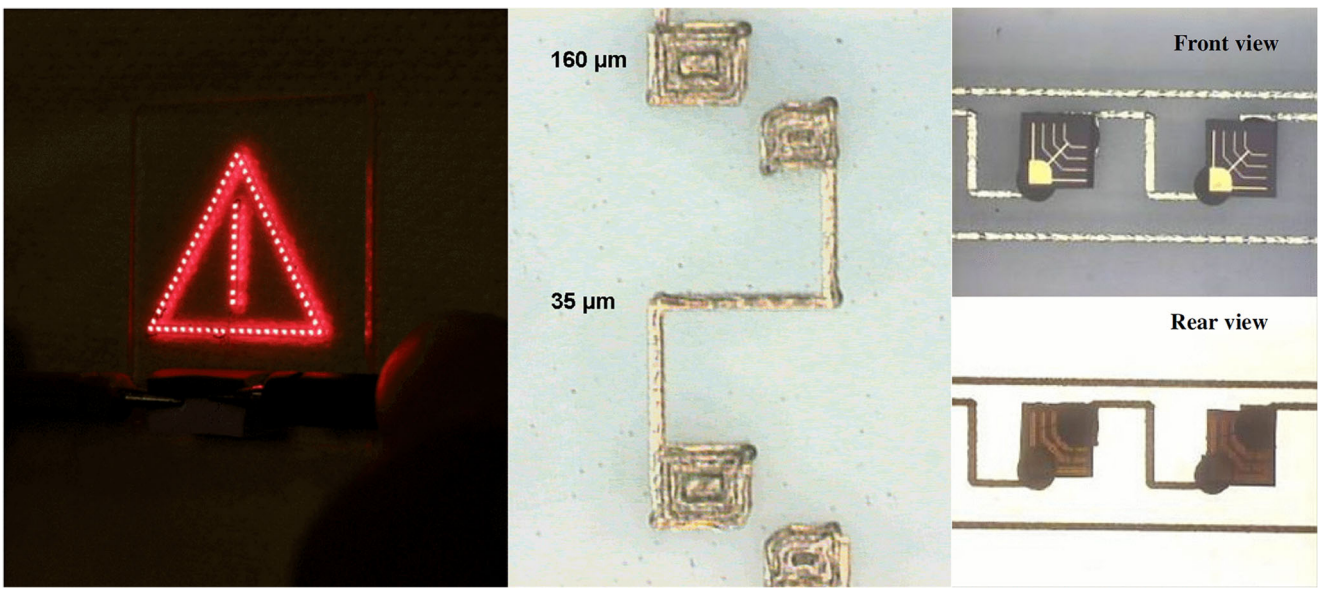

Fig. 9 AJP deposited silver interconnects in a head-up display (© 2010 IEEE. Reprinted, with permission, from [37])

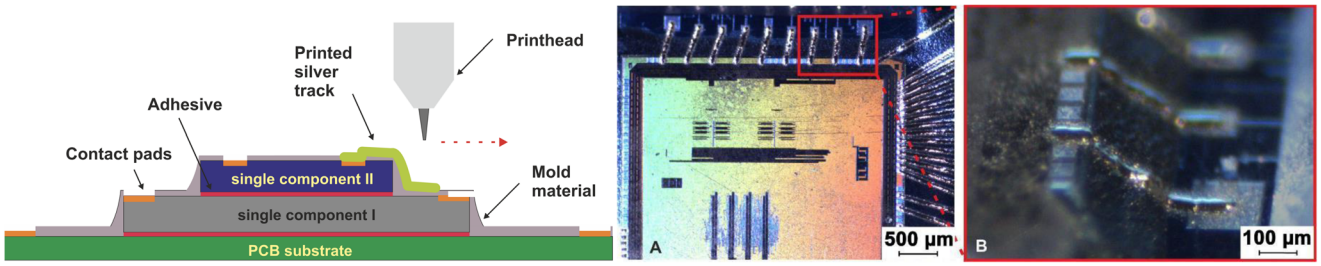

Fig. 10 Interconnection between stacked PCB components (Reprinted with permission from [39])

which the electrical properties of the deposit were correlated to the processing parameters. Resistances roughly double that of bulk silver were achieved; however any variation in processing parameters (low focussing ratio and high translational velocities) leads to increased porosity and, therefore, increased resistance [1]. To the best of the authors' knowledge, the finest reported conductive metallic lines produced using AJP were produced by Cai et al. [18] who presented line widths of 10 µm using a silver ink (Fig. 11).

Although AJP has been shown useful in the production of fine pitch interconnects, Mashayekhi et al. [46] argue that it is limited when producing tracks with lengths less than 100 µm. During a comparison of printing techniques for electronic applications, their work shows that the characteristic bulges at the end of AJP tracks coalesce and form a droplet-like deposition, effectively limiting the print resolution [46].

Wetting characteristics of the substrate are well known to affect the morphology of any deposit. Vunnam et al. [47] investigated the effects of air plasma and self-assembled monolayer treatments on the adhesion of AJP-deposited silver ink on an indium tin oxide substrate. Ultimately, they found the ink spreading to be strongly dependent on the substrate's surface free energy, ink properties and sheath flow [47]. Mahajan et al. [48] have shown how AJ printing on to low energy substrates can facilitate a transfer process for producing low roughness (< 10 nm) silver ink tracks (Fig. 12). Chang et al. [49] have used a similar print-transfer-peel technique to produce circuitry on to flexible substrates. As well as producing low surface roughness interconnects, this approach allowed the researchers to overcome capillary action-induced wicking in channels caused by stair-steps on the surface of additively manufactured components. This approach also facilitated patterning on low-temperature substrates as the ink could be sintered before transfer.

Thermal sintering is an important processing step in the development of highly conductive traces. Both Shankar et al. [50] and Werner et al. [51] have demonstrated, quantitatively, the impact of thermal sintering on the conductivity of silver deposits. Their results show that higher sintering temperatures can lead to increased conductivity through more complete evaporation of ligands and a greater degree of coalescence. At a similar time, however, Goth et al. [2] showed that thermal sintering can present issues with interconnect cracking due to differences in the coefficient of thermal expansion between the ink and the substrate. Seifert et al. [39] showed that multi-layered (> 10) printed silver tracks tend to peel during sintering as result of residual stresses. Rahman et al. [52] conducted a study investigating the high-temperature stability of AJP silver nanoparticle ink post-sintering, finding that the post-sintering impedance of the deposit increases up to 150 °C, decreases between 150 and 300 °C and, then, increases again as the temperature approaches 500 °C. Decreases in conductivity were largely attributed to grain growth at elevated temperatures.

For materials that are not compatible with the temperatures associated with sintering (e.g. common thermoplastics), Hoerber et al. [53] showed that non-sintered deposits with larger interconnect dimensions can be used, while Werner et al. [51] presented electrical sintering as an alternative for thermally sensitive substrates. In later work, Schuetz et al. [54]

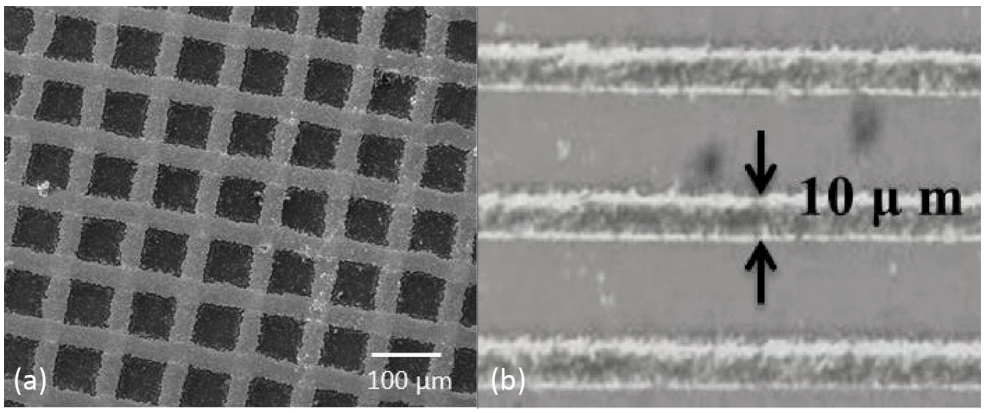

Fig. 11 AJP silver ink tracks at (**a**) 20 µm grid (Reprinted with permission from [1] and (**b**) 10 µm tracks (© [2016] IEEE. Reprinted, with permission, from [18])

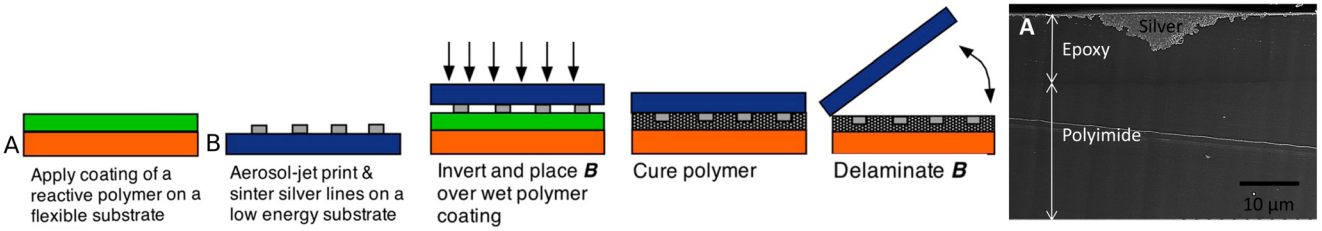

Fig. 12 Transfer process for highly flat conductive tracks adapted from (Reprinted with permission from [48])

developed a new technique for sintering metallic deposits using selective exposure to a xenon light source. Their approach allowed for the sintering of silver tracks on a polycarbonate substrate with limited substrate damage.

The use of nanoparticle inks presents serious limitations for the application of AJP interconnects. The high surface area-to-volume ratio of metallic nanoparticles makes them highly susceptible to loss of conductivity through oxidation. Silver ink is most commonly used as it is less prone to oxidation than copper-based inks. A comprehensive review of ink development is beyond the scope of this report. Reviews of conductive inks are readily available [19, 55].

AJ printing of metallic inks is a promising technique for the production of conformal, rigid circuitry. However, as determined by Reboun et al. [56], metallic-sintered conductive patterns have insufficient bending endurance (< 10,000 cycles) for flexible applications (Fig. 13). Alternative conductive materials based on polymers, polymer matrices or forms of carbon are often presented as solutions.

Jabari and Toyserkani [57] investigated the deposition of graphene-based interconnects and achieved resistivity as low as 0.018 Ω cm. Low concentrations of graphene inks are required to reduce instances of nozzle clogging, which limits the conductivity of the interconnects. A follow-up study attempted to overcome this through the combination of graphene and silver nanoparticle inks [58], which provided the flexibility of the graphene electrodes with a 100 factor increase in conductivity.

Wang et al. [59] demonstrated a "Conductive-On-Demand" approach to produce composite polyimide/carbon nanotube conductive devices that use inherent process characteristics to facilitate in-process mixing of multiple materials (Fig. 14). Two materials were atomised separately then combined in a static mixer before entering the deposition head. Through control of the relative flow rates, the conductivity of the composite could be spatially varied by adjusting the weighting of carbon nanotubes during the process (Fig. 14).

Beyond electrical circuitry, optical waveguides are a promising alternative for applications that need higher speed communication and data transfer than is achievable using conductive traces. Current manufacturing techniques are limited to planar designs connected by inefficient optical junctions [60]. Additive techniques that enable freeform optical waveguides are an attractive pathway for compact and efficient optical circuitry. The first demonstration of polymer optical waveguides (POW) using AJP was achieved by depositing a UV curable photopolymer on to a glass substrate [61]. Wetting of the photopolymer proved challenging and required a ten-minute exposure to ethylene glycol to adapt the surface energy of the substrate. Attenuation of the light source was found to be 2.8 dB/cm, which showed poor performance compared with other POW techniques (< 0.5 dB/cm). Subsequent work improved the quality of the POW by using flexography to deposit conditioning lines that locally alter the contact angle of the substrate [62]. By increasing the aspect ratio of the AJP structures, POWs with a significantly improved attenuation of 0.7 dB/cm were achieved. The repeatability of both the flexographic and AJP process has been identified as key challenges for printed POWs [63].

5.1.2 Capacitors

Ha et al. [64] sequentially deposited poly(3-hexylthiophene) (P3HT) and an electrolyte ion-gel on to pre-patterned gold electrodes to form the dielectric layer of a thin film capacitor. The top electrode was applied by printing PEDOT:PSS on to the surface of the ion gel. The time delay of the device was

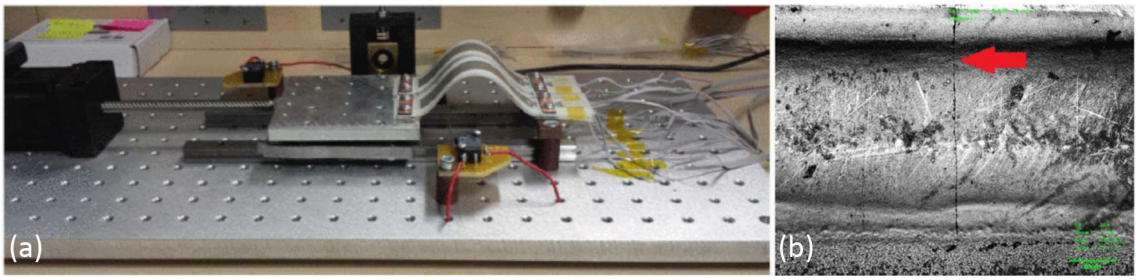

Fig. 13 (**a**) Apparatus for the testing of bending endurance of AJ-printed tracks and (**b**) cracks in AJ-printed tracks after 10,000 cycles (Reprinted with permission from [56])

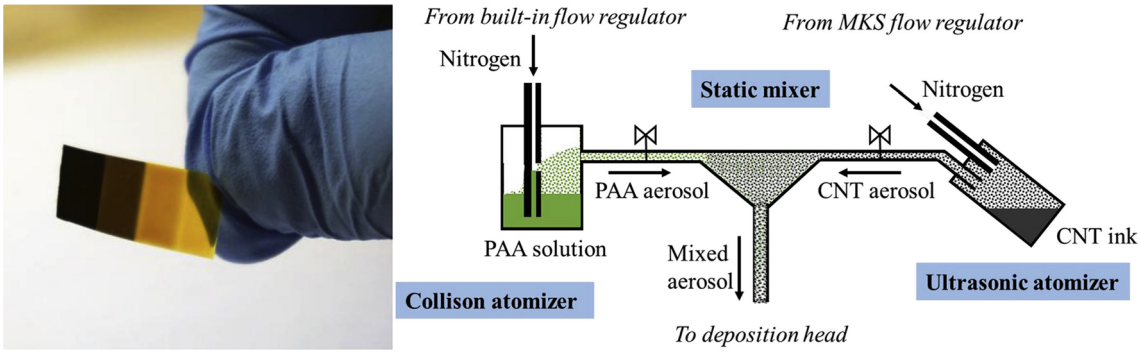

Fig. 14 "Conductive-on-demand" through the selective introduction of CNTs in to polyimide (Reprinted from [59])

found to linearly increase with the thickness of P3HT layer up to 400 nm. A fully printed capacitor was produced by Gupta et al. [15] by printing silver traces alongside SU-8 photoresist as a dielectric medium. Increasing the area of overlap on the printed devices showed a linear increase in capacitance, which provides a simple pathway for tuning the capacitance to match the requirements of the circuit.

Folgar et al. [16] investigated the production of ceramic capacitors by depositing barium titanate particles before using selective laser sintering to form a continuous film. Development of an ink that was compatible with both processes proved challenging as ceramic binders inhibited the sintering process. Functional devices, with a capacitance of 17.5 pF at 1 MHz, were produced by introducing silver electrodes either side of the ceramic along with a PMMA interlayer to minimise diffusion. The tested devices featured green state (non-sintered) ceramic as challenges with high porosity and delamination were difficult to overcome.

5.1.3 Inductors

AJP has been used to successfully print inductors by the deposition of a silver-based conductive ink, a magnetic nickel iron core and a muscovite mica dielectric [32]. The rudimentary nine-and-a-half turn inductor was produced in five processing steps, with conductive coils being the first and last printed layers to form a coil around the magnetic material. The coils were insulated from the magnetic core through the deposition of the dielectric on either side. The total thickness of the five layer device was less than 70 μm with a length of 20 mm and width of 8 mm. Besides ink development, the key step in this process was the removal of oxygen from the iron oxide and subsequent alloying with the nickel material post-deposition. Complete sintering is typically achieved at 80% of the melting point of the permalloy (1440 °C); however, the sample produced using AJP was able to be sintered at 500 °C and 350 °C on glass and Kapton, respectively. The final device was found to have a fairly stable inductance 1.5 μH at frequencies above 100 kHz. Devices with commercially relevant inductances have been produced using silver ink in combination with polymer, iron and ferrite cores [65]. Polymer core inductors were printed in situ, while the iron and ferrite cores were placed before an insulating polymer layer was deposited. A number of inductor geometries showed the flexibility of the manufacturing process for printed inductors.

5.1.4 Antenna, waveguides and transmission lines

Single-layer, planar antenna has been presented in several forms, with most research focussing on the deposition of a silver-based ink to produce the conductive traces on a dielectric substrate. When investigating the production of radio-frequency identification (RFID) tags, Cai et al. [66] printed a silver seed for electroless copper plating, which increased the conductivity of the deposit and improved the quality factor of the antenna. The electroless plating process was found to strip the silver seed from the substrate unless an adhesive interlayer was applied. Although the final adhesive strength was not quantified, RFID tags with inductances in the range of 2.87–2.97 uH were successfully produced.

Three-dimensional antennas were produced through the deposition and UV curing of a dielectric ink to form pillars and hollow cylinders (Fig. 15). Conductive silver ink was, then, printed on the vertical walls of these structures using a tilted print head to produce functional, three-dimensional millimetre-wave antenna. In the work, the authors argue that this approach to antenna design and manufacture opens up the possibility of an entirely new class of three-dimensional antenna [68, 69].

Deposition of dielectric materials alongside the conductive material has been presented as a technique for multi-layer co-planar waveguides capable of operation up to 50 GHz with losses of 0.5 dB/mm [70]. In this case, a polyimide ink was deposited as the dielectric alongside the silver to produce multilayer devices. Further work investigated single layer, radio-frequency waveguides on a diamond substrate [71]. Similar techniques have been used to produce other high-frequency electronic components, such as transmission lines [72] and power dividers [73]. Oakley et al. [74] did a direct benchmarking of AJP terahertz filters with equivalent copper filters produced using photolithographic techniques and found

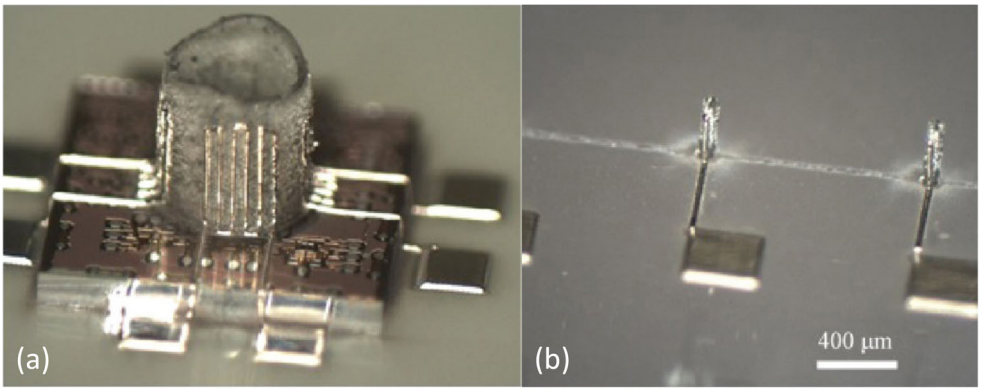

Fig. 15 (**a**) Vertical metal antenna on a dielectric pillar and (**b**) antenna microstructures (© IOP Publishing. Reproduced with permission from [69]. All rights reserved)

comparable performance. As a result, AJP is again presented as an attractive technique for low-cost fabrication and prototyping, especially when combined with other additive techniques [75].

5.2 Active electronic components

Active electronic components either require power to work or can introduce net power into a circuit. Active electronic components tend to be multi-material structures which are more complex when compared to passive electronics. Many implementations of active components use AJP as part of a hybrid process chain to produce the final components. AJP is attractive for the deposition of these devices by allowing their implementation on non-standard substrates, such as paper, fabric and low-temperature polymers.

5.2.1 Transistors and switches

The ubiquity of transistors in modern electronics has made them one of the primary research areas in AJP. A key challenge has been the development of high-capacitance dielectric inks for the gate insulators of thin film transistors (TFTs) while maintaining compatibility with solution processing. Cho et al. [76] were the first to demonstrate the potential of ion gels by using AJP to manufacture a series of organic TFTs with switching speeds up to 10 kHz (Fig. 16), which represented a significant increase over solid polymer electrolytes that were limited to sub-100 Hz operation.

A subsequent body of work designing and characterising circuits—low-voltage (< 3 V) invertors and ring oscillators Fig. 17 [77, 78]—based on these AJP electrolyte-gated TFTs immerged showing high efficiency and performance. Later optimisation and characterisation showed current ratios of up to 10^6, off-state drain currents as low as 10^{-10} A and threshold voltages of − 0.3 V [5]. Other approaches to develop solution processable, high-capacitance dielectrics have focussed on the development of poly(methylsilsesquioxane) as a gate dielectric in indium–gallium–zinc–oxide transistors [79] or polyfluorinated electrolytes for applications that require higher thermal stability [80].

TFTs manufactured using AJP were found to differ in performance when compared to equivalent devices manufactured using conventional solution processes, such as spin coating. Wu et al. [79] attributed these variances to differences in the electrolyte structure (pin holes), ingress of impurities or residual solvents in the deposit.

The other main body of research in the development of TFTs focusses on the deposition of single-walled carbon nanotubes as a semi-conductor. Transistors with operating frequencies in the region of 5 GHz have been demonstrated through the deposition of high-purity SWCNT inks [81]. The primary hurdle for using semi-conducting SWCNTs is the production and purification of the CNTs and the associated ink formulations [82]. Recently, refinement techniques that can scale have begun to emerge, with Rother et al. [83] showing a stable polymer-sorted semi-conducting SWCNT ink for

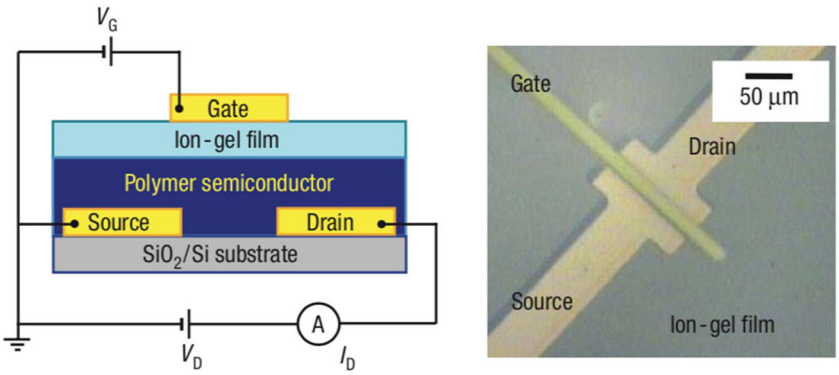

Fig. 16 Schematic and optical micrograph of electrolyte-gated thin film transistor (Reprinted with permission from [76])

TFTs with high reproducibility. TFTs using semi-conducting SWCNTs have been shown to go through 1000 bending cycles with minimal performance degradation, showing their application to flexible electronics [84]. Other research has focussed on the use of SWCNTs for temperature-stable TFTs [80] and the effect of substrate wetting through oxygen plasma surface treatments [85]. Selective deposition of ethanolamine doping agent on to semiconducting SWCNTs has been shown to change the polarity of TFTs, with P-type transistors being selectively converted to N-type [86]. Through this approach, the researchers could produce a complementary metal oxide semiconductor (CMOS).

Ha et al. [64] demonstrated the potential of AJP-printed transistors by printing an electrochromic pixel along with a H-bridge drive circuit. The final device featured 23 transistors, 20 resistors, 12 capacitors and 9 dielectric crossovers, all printed in situ using AJP. The interconnecting circuitry was produced using photolithography and electron beam evaporation on to a PET substrate. The final circuit was found to operate at 1 V with a high degree of stability over 600 test cycles. Although the individual components in this work had been previously demonstrated, this work is the first that demonstrates their application in a more complex circuit.

5.2.2 Organic light-emitting diodes

The growth of modern display technology has stirred interest in techniques for the production of high-efficiency displays that do not require conventional vacuum processing techniques. AJP at ambient conditions could lead to a cost reduction while enabling increased performance through design flexibility—even a relatively simple implementation of AJPs, which deposited a PEDOT:PSS grid on the anode of an organic light-emitting diode (OLED), saw efficiency improvements over conventional devices by a factor of 2.3 [88].

Tait et al. [89] took this further by demonstrating the deposition poly(N-vinylcarbazole), PEDOT:PSS and $Mo0_3$ as part of functional OLED structures (Fig. 18) while studying the effects of flow rates, stand-off height (up to 15 mm), nozzle speed and temperature on the deposition quality. The remaining components of the OLED—the top electron transport layer, cathode and metal oxide layer—were patterned using more conventional shadow mask vacuum evaporation. Their conservative devices produced RGB pixels at a density of 144 ppi; however, through optimisation, they suggest that densities as high as 500 ppi may be feasible. Although unlikely to compete with the high-pixel densities of other techniques, it is an attractive approach for large-scale devices that are dimensionally and financially constrained by masked vacuum manufacture.

5.2.3 Photovoltaics

As with display technologies, AJP is being used as a tool to transition towards atmospheric processing of photovoltaics (PV). Contactless techniques that allow processing of thinner silicon wafers without damage are increasingly being investigated over more widely adopted screen printing techniques to further reduce manufacturing cost and increase size scales. Initial applications of AJP to PV applications focussed on the metallisation of silicon cells, which was achieved through direct printing of a conductive ink (silver [90], aluminium [91]) or printing of a seed material followed by an electroplating process in a similar way to the techniques discussed in Section 5.1.1. As metallisation aims to minimise the shadowing of the cell while maintaining high conductivity to improve the efficiency, the relatively high-resolution of AJP

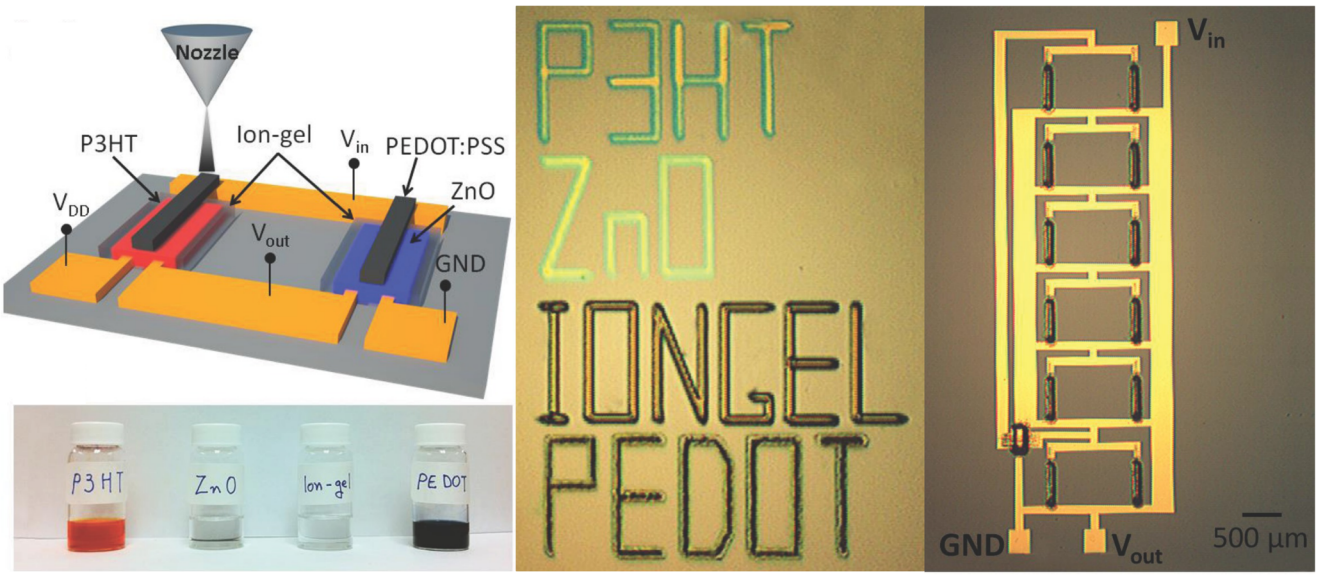

Fig. 17 AJP deposition of P3HT, Zno, PEDOT:PSS, and an Ion-gel for a 5-stage ring oscillator (Reproduced from [77])

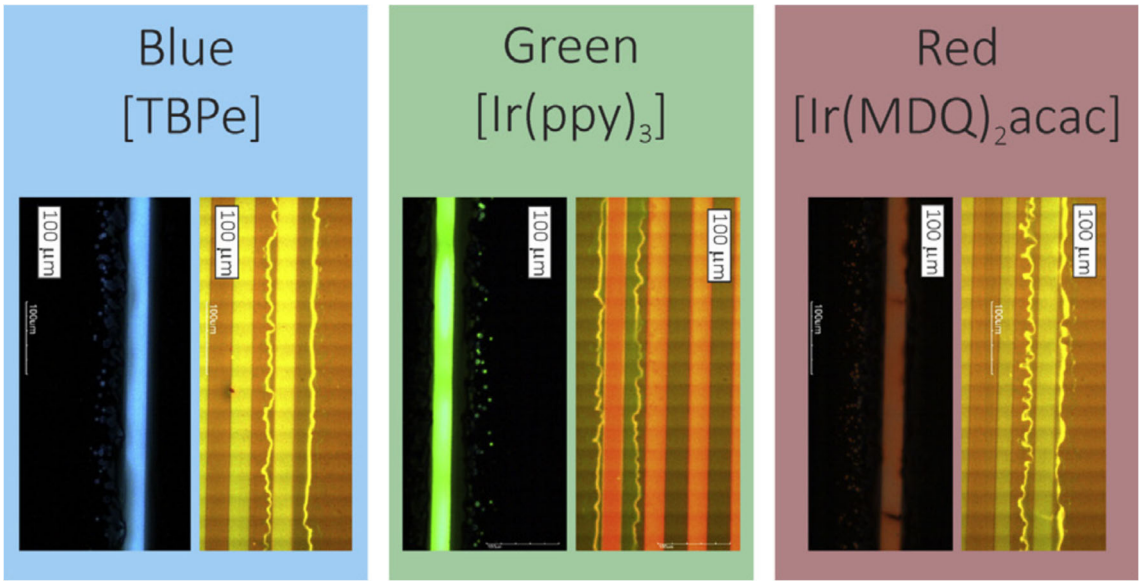

Fig. 18 Printed blue, green and red OLEDs (Reprinted from [89])

when compared to other large area patterning techniques presents an attractive approach.

The manufacture of PVs using direct write processes is dependent on the development of suitable solution processable materials. Earth-abundant materials, particularly perovskite and kesterite materials, are gaining attention for their ease of processing and relatively low cost. Williams et al. [92] investigated the deposition of material precursors that can be annealed to form copper–zinc–tin–sulfide features. Deposits with low solvent content were preferred as it limited cracking during drying. However, as is typical of dry deposits, this led to porous films that required secondary annealing and compaction processes to produce dense, crack-free nanocrystal films. More recently, Bag et al. [93] used AJP to deposit perovskite films as part of a functional solar cell that achieved power conversion efficiencies as high as 15.4%. Their work extended the process to investigate the production of solar cells on non-planar surfaces, demonstrating a hemispherical device with efficiencies of ~ 5.4%.

A technique for patterning dielectric materials, which are used for insulating and passivation layers in solar cells, used AJP's selective deposition to produce localised chemical etching on a series of silicon substrates coated with silicon dioxide, silicon nitride, silicon oxynitride and aluminium oxide [94]. In this approach, a bulk layer of polyacrylic acid was spin-coated on to the coated silicon substrate before AJP was used to deposit an ammonium fluoride solution. The combination of polyacrylic acid and ammonium fluoride formed localised areas of hydrofluoric acid that etched the underlying dielectric with a minimum feature size approaching 20 μm. The remaining hydrofluoric acid and polyacrylic acid can, then, be rinsed from the substrate using DI water.

5.2.4 Fuel cells

Sukeshini et al. [95–97] published a series of papers investigating the deposition of a yttria-stabilised zirconia (YSZ) electrolyte, a strontium-doped lanthanum manganate (LSM) cathode and a YSZ/LSM composite interlayer for use in solid oxide fuel cells (SOFCs). The interlayer material was facilitated by a dual atomisation configuration that combined two aerosol streams prior to deposition. Despite substandard performance of the developed button cell, an investigation of processing parameters highlighted how the geometry and microstructure can be manipulated to improve device performance. Subsequent optimisation efforts explored this and found that the power densities of the button cell could be varied from 200 to 460 mW/cm^2 simply by controlling the process parameters [96].

Further improvements in performance were found by grading the composition of a YSZ/NiO interlayer through on-demand mixing. This approach allowed the ratio of the composite to be varied on consecutive layers, thereby reducing the ohmic resistance of the device and improving overall performance. Despite this, the button cell still presented substandard performance and further optimisation, in terms of processing, materials and ink formulation, is required before AJP becomes a serious technique for the manufacture of SOFCs. An initial study using a gadolinia-doped ceria (GDC)–lanthanum strontium cobalt ferrite (LSCF) cathode as an alternative to LSM has already led to a 2-fold increase in performance [97].

5.3 Sensors

AJP is an effective technique for the manufacture of high-resolution sensors that enable researchers to rapidly iterate

designs through the modification of geometry and materials. New types of sensors are being produced on a greater range of substrates. Embedding sensors within components by direct printing also presents an opportunity for a deeper understanding of how a component behaves in service.

5.3.1 Strain gauges

A number of strain gauges have been developed by Fraunhofer IFAM [98, 99] and the Georgia Institute for Technology [100]. At their most simple, strain gauges are patterned conductive traces that experience a change in resistance in response to mechanical strain. Traditionally, these devices are manufactured as part of a film before being adhered to the surface for testing. AJP allows the manufacture of the part directly on to the surface of the component, which removes the need for secondary bonding processes while allowing deposition on to complex surfaces. To produce a strain gauge, Maiwald et al. [98] first deposited a polymer isolation layer before using a commercially available silver ink (Advanced Nano Products) to produce the strain gauge geometry (Fig. 19). Their results show a device with a reliable output for a 500 N load over 1000 cycles at 0.5 Hz. Similar approaches have been adopted by Zhao et al. [100] to embed silver ink strain gauges in carbon–fibre composite devices without significant impact on the mechanical properties. Their work suggests that AJP is a promising approach for embedded sensors; further work is required to remove defects, optimise curing processes and investigate the interface between the sensor and the carbon fibre prepreg. Recently, Rahman et al. [101] demonstrated a ceramic/metal strain sensor for high-temperature applications.

5.3.2 Capacitive sensors

Rahman et al. [102] developed interdigitated capacitive touch sensors through the deposition of silver ink on to a planar glass slide (Fig. 20). The interdigitated fingers of the sensor were approximately 50 μm, 1.5–55 mm long, 0.5 μm thick and had a native capacitance of 1–5 pF. A degree of repeatability was shown with an 8% variance in sensor capacitance over three samples. Simulation and experimental observations showed the capacitance to be insensitive to variation in electrode height, meaning the high surface roughness of their AJ deposits has little impact on device performance. The capacitive sensor's output was shown to be largely dependent on the electrode width as a fraction of electrode pitch. Current work has deposited on to planar glass substrates, but more novelty is expected as researchers use AJP for non-planar and flexible substrates. Andrews et al. [103] printed a capacitive sensor from a carbon nanotube ink that, when pressed to a material, exhibits a linear response between capacitance and material thickness. Another interesting application that uses similarly interdigitated AJP structures for electrostatic adhesion has been proposed for use in miniaturised robotics [104].

5.3.3 Dielectric elastomer devices

The Factory Automation and Production Systems (FAPS) group is investigating the use of AJP to produce soft dielectric elastomer devices (DEDs) that can be used for sensing, actuation and energy harvesting [105]. These layered structures consist of a soft dielectric sandwiched between two compliant electrodes. Current DED actuation technology is limited by high driving voltages (> 1 kV). Reducing the layer thickness of both the dielectric and electrode is a promising approach to producing a low-voltage DEA. AJP's layer-by-layer approach, combined with its ability to produce thin films, makes it a promising approach to produce DEDs in a single processing step [106, 107]. Although the production of a functional part has yet to be presented, the deposition of two-part silicone (Elastosil P760) has been achieved using a dual atomisation configuration [108]. It is feasible that the current state-of-the-art could be used for DED-based sensing.

5.3.4 Photodetectors

Photodetectors are a good example of how AJP can be integrated in to a range of fabrication strategies to produce functional devices. The combination of inkjet printing,

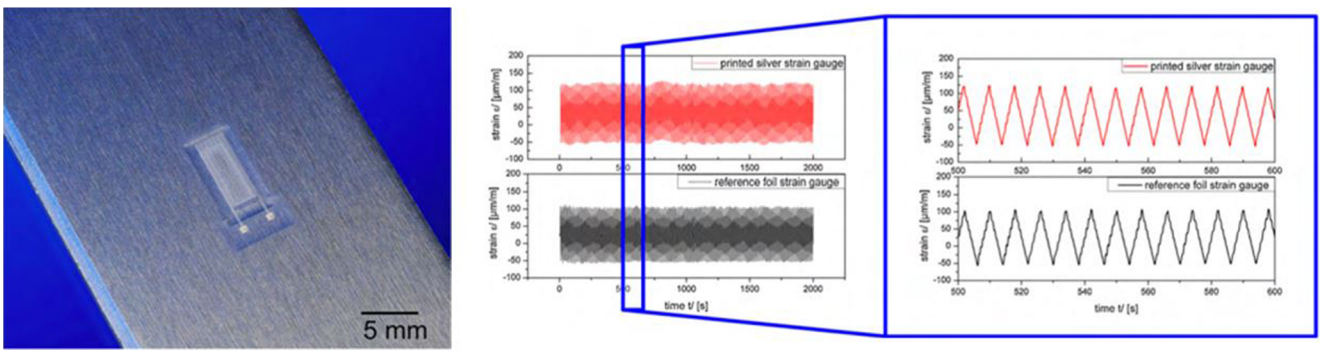

Fig. 19 An AJP gauge and its response compared to a reference foil strain gauge (Reprinted from [98])

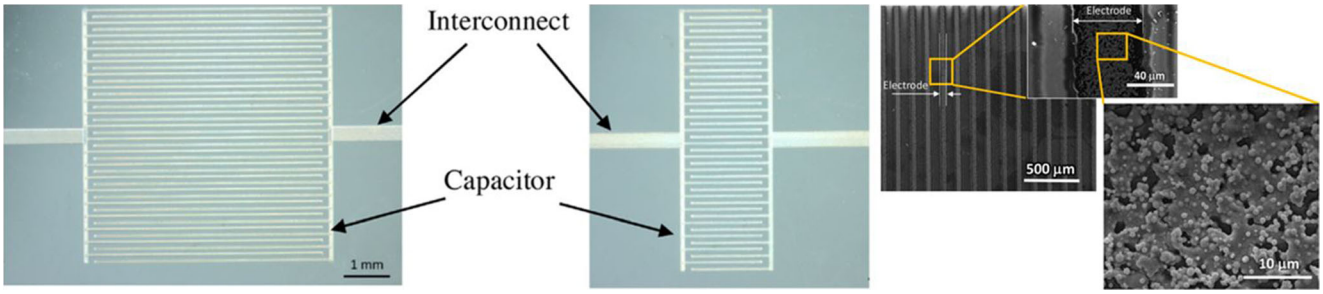

Fig. 20 AJP interdigitated capacitive sensor (Reprinted from [102])

AJP and drop casting leads to the development of a low-cost paper-based photo detector for the visible spectrum [109]. In this work, PEDOT:PSS and P3HT:PCBM layers were deposited by AJP, the silver bottom electrode was deposited using inkjet and a DNA biopolymer was drop-cast. An interlayer of PEDOT:PSS was required to increase the adhesion of the silver to P3HT:PCBM, while the DNA biopolymer was required to facilitate a confluent PEDOT:PSS top electrode. A number of different processing and material strategies have been deployed to produce photodetectors [110], including a fully AJP sensor with performance comparable to the state-of-the-art [111]. Ichiyama et al. have used AJP as a technique for the deposition of a fluorescent quantum dot film, with the intention of enabling deep-UV capability in standard CMOS and CCD detector arrays [112].

5.3.5 Chemical sensors

Functionalised single-walled carbon nanotube (SWCNT) networks are used in a number of gas-sensing applications. Solution processing of these devices, rather than high-temperature in situ growth, is required to enable manufacture on low-cost polymer and paper substrates. Reduced drying effects, such as the coffee ring effect, in AJP present a simpler pathway to manufacture over inkjet printing or spin coating and have been, recently, demonstrated in the production of a platinum-decorated SWCNT hydrogen sensor [113]. Kuberský et al. [114] demonstrated a NO_2 sensor with AJP-printed top CNT electrodes on a series of drop-cast polymer electrolytes. An alternative approach that monitors the current drawn by an AJP electrode array to reduce hydrogen peroxide has also been developed [115]. By introducing glucose oxidase, an enzyme that catalyses the oxidation of glucose to hydrogen peroxide, the sensor was able to detect the concentration of glucose, which could prove useful for biosensing applications. The same group who produced paper-based photo detectors (see Section 5.3.4), refined their technique to produce a sensor capable of vapour-phase chemical detection of water and other volatile organic compounds [116].

5.4 Three-dimensional structures

AJP has primarily been used for surface patterning, and researchers are beginning to explore its potential for expanding additive manufacturing with the hope that it can help bridge the gap between size scales. Saleh et al. [9] demonstrated the production of hierarchical structures with features that span 5 orders of magnitude (Fig. 21). Rapid solvent evaporation in a 90–110 °C environment was required to solidify the ink on deposition, while secondary processing was used to remove the binder and sinter the nanoparticle ink. Control of the binder content, nanoparticle size and sintering conditions allowed the authors to manipulate the porosity of the trusses within the lattices. This work was completed using a silver nanoparticle ink; however, it has been stipulated that the approach can be readily transferred to any ink that can form a nanoparticle suspension. Subsequent work has presented these lattices as candidates for electrodes in lithium ion batteries [117] and characterised the mechanical strength of micropillars under compressive load [118].

An alternative approach to produce 3D structures used AJP to deposit thin layers (5–35 μm) of inks on to non-planar surfaces that were subsequently cured through exposure to a UV laser. This hybrid approach combines the thin layer capabilities of AJP with the fine feature capabilities of laser-based direct write to produce high-resolution structures. Although these studies were completed with PDMS [8] and pentaerythritol triacrylate (PETA) [7] (Fig. 22), it is easy to see how this can be expanded to accommodate any UV-curable material. The combination of AJP and laser-based direct write may also present a pathway to multi-material stereolithography that is difficult using conventional VAT-based processes.

5.5 Applications in biology

Biological applications of AJP have focussed on techniques for either patterning cellular structures or printing biological molecules, such as proteins, enzymes and strands of DNA. Early work attempted to spatially position mammalian (3T3 mouse fibroblast) cells by direct deposition of the cells and surrounding growth media on the surface of a Petri dish [12]. A viability study showed the deposited cells to have 87%

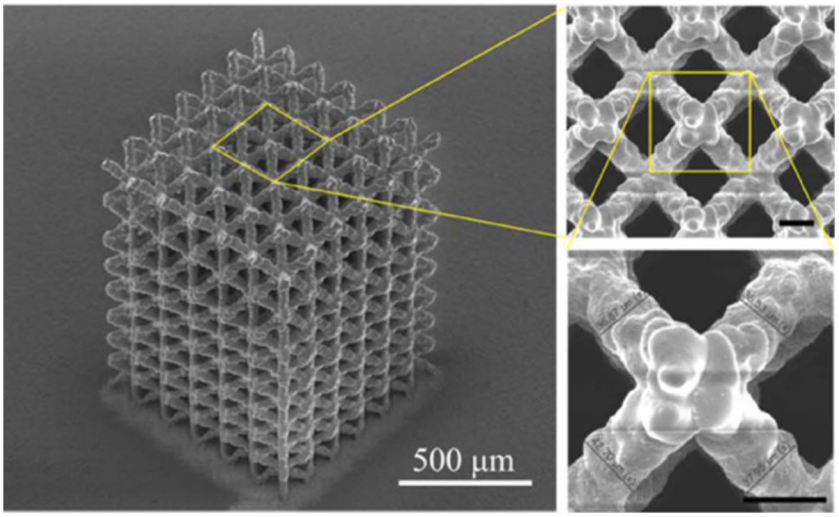

Fig. 21 3D AJP hierarchical silver lattices spanning 5 length scales (Reprinted from [9])

viability compared to 97% of the control group. Low viability and an inability to control cell migration post-deposition present a significant challenge for this type of approach.

An alternative created regions of preferential adhesion for cells on the surface of a substrate through either positive or negative patterning. In this work, De Silva et al. [119] created regions of preferential adhesion on PDMS-coated Petri dishes by AJP of laminin and poly-ethylenimine. After patterning, the cells were cultured on the surface of the substrate, and higher cell densities were found in the patterned region. Certain cell types were, even, found to elongate and align in the direction of the printed features. The inverse effect—negative patterning—was also shown by patterning glass substrates with PDMS and PTFE. In the negative case, the cells were identified as migrating towards the less hydrophobic glass surface over time, demonstrating their preference for adhesion to intermediate to high-surface tension substrates.

The production of ceramic calcium phosphate substrates for bone cell growth studies has been completed as part of a comparison between AJP, laser ablation and microcontact printing [120]. Geometric and cell proliferation analysis showed AJP to be a useful tool for investigating cell growth on ceramic microstructures with minimal toxicity; however, it does highlight issues relating to system variability and slow processing times when compared to the other techniques.

The deposition of bio-molecules with high spatial resolution is a key to the development of miniaturised test platforms that can be used for fundamental studies, drug/toxicology screening and biological sensing. Grunwald et al. [17] demonstrated the deposition of a series of fluorescent proteins, strands of DNA and active enzymes with minimal impact on their biological activity before going on to compare the technique with other printing processes. The low shear forces present in the AJP process enable the deposition of complex high-molecular weight molecules without denaturing their structure, as shown by the deposition of DNA molecules suspended in a phosphate-buffered saline solution. Although successful in deposition, the authors argue that the slow processing time and lack of parallel deposition in most AJP configurations present a hurdle for the mass production of microarray structures and other test platforms.

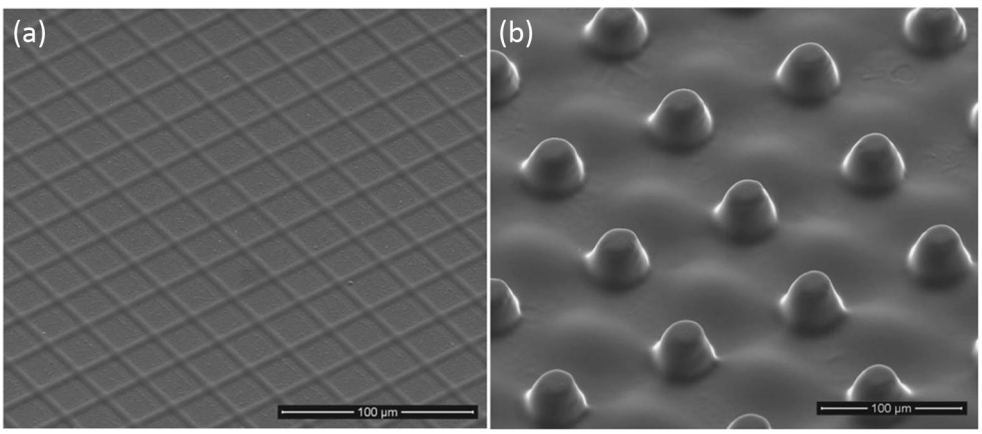

Fig. 22 SEM images of (**a**) 2S square grid pattern and (**b**) 3D cone array structures (Reprinted from [7])

6 Future direction of aerosol-based direct write

Printed electronics has been a key driver for the development of the AJP process and is likely to continue as a commercial motivation. Basic circuit elements have been demonstrated in isolation, with examples of complete circuitry only beginning to emerge more recently through hybrid processing. Improving the capability of printed devices will be important in the development of AJP technology, but its lower resolution than lithographic processes means that the greatest short-term impact of AJP will be in applications that harness the flexible nature of the process along with unique characteristics to provide increased function and value. For example, the high conformity offered by AJP increases the design freedom for electronics packaging and conformal antenna [68], while large-area, ambient processing is appealing [19] for economical manufacture of photovoltaics and display technologies.

Beyond the technology's original scope, researchers are using AJP to impact fast-growing topics as diverse as biotechnology and robotics. Novel design and manufacturing has led to innovation in lab-on-a-chip devices [121], and the convergence of these techniques with advanced printing, such as AJP, will provide further opportunities through sensing, selective catalysation, cell seeding and directed cell growth [119].

Additive techniques in soft robotics have been well demonstrated [122], with their ability to selectively and spatially vary stiffness enabling new functionality in soft systems. AJP offers to build on this through the deposition of sensing elements and other electronics within their bodies, paving the way for improved proprioceptive and environmental sensing. Material and process flexibility makes AJP an ideal candidate for implementation alongside other additive techniques for the repeatable, hybrid manufacture of soft robotics—a goal that has recently been highlighted by the research community [123].

Many applications of AJP are facilitated through the formulation of materials with the required processing and functional characteristics. Although AJP has expanded the range of printable viscosities and enabled the deposition of two-part and composites, ink formulation requires a large body of empirical work for consistent deposition. Defining the criteria for a suitable ink through process modelling and experimental observation will accelerate the adoption of the process in commercial settings by decreasing development time scales and cost [24].

Given wider manufacturing research and industrial developments, such as the Internet of Things and Industry 4.0, AJP is well positioned to become an underpinning technology for enabling the creation of more connected and intelligent products. Its extreme versatility gives it the potential to disrupt a host of manufacturing environments; from conventional electronics and sensing to biological and chemical manufacturing applications. As investment increases and applications are recognised, the reliability of the system will increase through improved understanding of material and processing conditions. Its increased adoption will likely be driven by the development of devices with increased performance that reflect the unique capabilities of the process.

Acknowledgments We kindly acknowledge our research funding from the Engineering and Physical Sciences Research Council. This includes a number of our activities which incorporate AJP as a Hybrid Manufacturing Process, namely grants EP/L02067X/2, EP/M026388/1, and EP/P027687/1.

References

1. Mahajan A, Frisbie CD, Francis LF (2013) Optimization of aerosol jet printing for high-resolution, high-aspect ratio silver lines. ACS Appl Mater Interfaces 5:4856–4864. https://doi.org/10.1021/am400606y
2. Goth C, Putzo S, Franke J (2011) Aerosol jet printing on rapid prototyping materials for fine pitch electronic applications. In: 2011 IEEE 61st Electronic Components and Technology Conference (ECTC). IEEE, pp 1211–1216
3. Seifert T, Sowade E, Roscher F, Wiemer M, Gessner T, Baumann RR (2015) Additive manufacturing technologies compared: morphology of deposits of silver ink using inkjet and aerosol jet printing. Ind Eng Chem Res 54:769–779. https://doi.org/10.1021/ie503636c
4. Meruga JM, Baride A, Cross W, Kellar JJ, May PS (2014) Red-green-blue printing using luminescence-upconversion inks. J Mater Chem C 2:2221. https://doi.org/10.1039/c3tc32233e
5. Kim SH, Hong K, Lee KH, Frisbie CD (2013) Performance and stability of aerosol-jet-printed electrolyte-gated transistors based on poly(3-hexylthiophene). ACS Appl Mater Interfaces 5:6580–6585. https://doi.org/10.1021/am401200y
6. Secor EB, Hersam MC (2015) Emerging carbon and post-carbon nanomaterial inks for printed electronics. J Phys Chem Lett 6:620–626. https://doi.org/10.1021/jz502431r
7. Obata K, Klug U, Koch J et al (2014) Hybrid micro-stereolithography by means of aerosol jet printing technology. J Laser Micro Nanoeng 9:242–247. https://doi.org/10.2961/jlmn.2014.03.0012
8. Obata K, Schonewille A, Slobin S, Hohnholz A, Unger C, Koch J, Suttmann O, Overmeyer L (2017) Hybrid 2D patterning using UV laser direct writing and aerosol jet printing of UV curable polydimethylsiloxane. Appl Phys Lett 111:121903. https://doi.org/10.1063/1.4996547
9. Saleh MS, Hu C, Panat R (2017) Three-dimensional microarchitected materials and devices using nanoparticle assembly by pointwise spatial printing. Sci Adv 3:e1601986. https://doi.org/10.1126/sciadv.1601986
10. Paulsen JA, Renn M, Christenson K, Plourde R (2012) Printing conformal electronics on 3D structures with aerosol jet technology. In: FIIW 2012—2012 Future of Instrumentation International Workshop Proceedings. pp 47–50

11. Maher M, Smith A, Margiotta J (2014) A synopsis of the Defense Advanced Research Projects Agency (DARPA) investment in additive manufacture and what challenges remain. pp 897002–897009
12. Marquez GJ, Renn MJ, Miller WD (2001) Aerosol-based direct-write of biological materials for biomedical applications. MRS Proc 698:Q5.2.1. https://doi.org/10.1557/PROC-698-Q5.2.1
13. Tait JG, Witkowska E, Hirade M, Ke TH, Malinowski PE, Steudel S, Adachi C, Heremans P (2015) Uniform aerosol jet printed polymer lines with 30 ??m width for 140 ppi resolution RGB organic light emitting diodes. Org Electron physics, Mater Appl 22:40–43. https://doi.org/10.1016/j.orgel.2015.03.034
14. Optomec aerosol jet videos. https://www.optomec.com/resources/3d-printing-application-videos/. Accessed 19 Mar 2018
15. Gupta AA, Bolduc A, Cloutier SG, Izquierdo R (2016) Aerosol jet printing for printed electronics rapid prototyping. In: 2016 IEEE International Symposium on Circuits and Systems (ISCAS). IEEE, pp 866–869
16. Folgar CE, Suchicital C, Priya S (2011) Solution-based aerosol deposition process for synthesis of multilayer structures. Mater Lett 65:1302–1307. https://doi.org/10.1016/j.matlet.2011.01.069
17. Grunwald I, Groth E, Wirth I, Schumacher J, Maiwald M, Zoellmer V, Busse M (2010) Surface biofunctionalization and production of miniaturized sensor structures using aerosol printing technologies. Biofabrication 2:014106. https://doi.org/10.1088/1758-5082/2/1/014106
18. Cai F, Chang Y-H, Wang K, Zhang C, Wang B, Papapolymerou J (2016) Low-loss 3-D multilayer transmission lines and interconnects fabricated by additive manufacturing technologies. IEEE Trans Microw Theory Tech 64:3208–3216. https://doi.org/10.1109/TMTT.2016.2601907
19. Huang Q, Zhu Y (2019) Printing conductive nanomaterials for flexible and stretchable electronics: a review of materials, processes, and applications. Adv Mater Technol 0:1800546. https://doi.org/10.1002/admt.201800546
20. Optomec (2017) Aerosol jet technology for 3D printed electronics. https://www.optomec.com/printed-electronics/aerosol-jet-technology. Accessed 01 April 2019
21. May KR (1973) The collison nebulizer: description, performance and application. J Aerosol Sci 4:235–243. https://doi.org/10.1016/0021-8502(73)90006-2
22. Goth C, Putzo S, Franke J (2011) Aerosol jet printing on rapid prototyping materials for fine pitch electronic applications. In: Proceedings—Electronic Components and Technology Conference. pp 1211–1216
23. Smith M, Choi YS, Boughey C, Kar-Narayan S (2017) Controlling and assessing the quality of aerosol jet printed features for large area and flexible electronics. Flex Print Electron 2. https://doi.org/10.1088/2058-8585/aa5af9
24. Secor EB (2018) Principles of aerosol jet printing. Flex Print Electron. https://doi.org/10.1088/2058-8585/aace28
25. Binder S, Glatthaar M, Rädlein E (2014) Analytical investigation of aerosol jet printing. Aerosol Sci Technol 48:924–929. https://doi.org/10.1080/02786826.2014.940439
26. Chen G, Gu Y, Tsang H, Hines DR, Das S (2018) The effect of droplet sizes on overspray in aerosol-jet printing. Adv Eng Mater 20:1701084. https://doi.org/10.1002/adem.201701084
27. Salary R, Lombardi JP, Samie Tootooni M, Donovan R Rao PK, Poliks MD (2016) In situ sensor-based monitoring and computational fluid dynamics (CFD) modeling of aerosol jet printing (AJP) process. In: ASME 2016 11th International Manufacturing Science and Engineering Conference
28. Deiner LJ, Reitz TL (2017) Inkjet and aerosol jet printing of electrochemical devices for energy conversion and storage. Adv Eng Mater 19
29. Yang C, Zhou E, Miyanishi S, Hashimoto K, Tajima K (2011) Preparation of active layers in polymer solar cells by aerosol jet printing. ACS Appl Mater Interfaces 3:4053–4058. https://doi.org/10.1021/am200907k
30. Paulsen JA, Renn MJ (2006) Maskless printing of miniature polymer thick film resistors for embedded applications. IPC 3rd Int Conf Embed Technol 2
31. Christenson KK, Paulsen JA, Renn MJ, et al (2011) Direct printing of circuit boards using aerosol jet®. In: 27th International Conference on Digital Printing Technologies, Technical Program and Proceedings. pp 433–436
32. Carter M, Amundson T, Colvin J, Sears J (2007) Characterization of soft magnetic nano-material deposited with M3D technology. J Mater Sci 42:1828–1832. https://doi.org/10.1007/s10853-006-0695-2
33. Mette A, Richter PL, Hörteis M, Glunz SW (2007) Metal aerosol jet printing for solar cell metallization. Prog Photovolt Res Appl 15:621–627. https://doi.org/10.1002/pip.759
34. Drew K, Hopman S, Hörteis M, Glunz SW, Granek F (2011) Combining laser chemical processing and aerosol jet printing: a laboratory scale feasibility study. Prog Photovolt Res Appl 19:253–259. https://doi.org/10.1002/pip.1014
35. Kalio A, Leibinger M, Filipovic A, Krüger K, Glatthaar M, Wilde J (2012) Development of lead-free silver ink for front contact metallization. Sol Energy Mater Sol Cells 106:51–54. https://doi.org/10.1016/j.solmat.2012.05.044
36. Tamari Y, Gautrein A, Schmiga C, Binder S, Glatthaar M, Glunz SW (2014) Synthesis of a lead- and particle-free metal-organic ink for front side metallization of crystalline silicon solar cells. Energy Procedia 55:708–714. https://doi.org/10.1016/j.egypro.2014.08.049
37. Padovani S, Sinesi S, Priante S, et al (2010) New method for head-up display realization by mean of chip on board and aerosol jet process. In: 3rd Electronics System Integration Technology Conference (ESTC). IEEE, pp 1–3
38. Zhan Z, Yu L, Wei J, Zheng C, Sun D, Wang L (2014) Application of aerosol jet technology in through-via interconnection for MEMS wafer-level packaging. Microsyst Technol 21:451–455. https://doi.org/10.1007/s00542-014-2107-x
39. Seifert T, Baum M, Roscher F, Wiemer M, Gessner T (2015) Aerosol jet printing of nano particle based electrical chip interconnects. Mater Today Proc 2:4262–4271. https://doi.org/10.1016/j.matpr.2015.09.012
40. Syed-Khaja A, Hoerber J, Gruber C, Franke J (2016) A novel approach for thin-film Ag-sintering process through aerosol jet printing in power electronics. In: 20th European Microelectronics and Packaging Conference and Exhibition: Enabling Technologies for a Better Life and Future, EMPC 2015
41. Stoukatch S, Laurent P, Dricot S, et al (2012) Evaluation of aerosol jet printing (AJP) technology for electronic packaging and interconnect technique. 2012 4th Electron Syst Technol Conf ESTC 2012. https://doi.org/10.1109/ESTC.2012.6542067
42. Kaestle C, Hoerber J, Oechsner F, Franke J (2015) Prospects of wire bonding as an approach for contacting additive manufactured aerosol jet printed structures. In: 2015 European Microelectronics Packaging Conference (EMPC). pp 1–6
43. Khorramdel B, Torkkeli A, Mantysalo M (2017) Electrical contacts in SOI MEMS using aerosol jet printing. IEEE J Electron Devices Soc 6. https://doi.org/10.1109/JEDS.2017.2764498
44. Verheecke W, Van Dyck M, Vogeler F, et al (2012) Optimizing aerosol jet® printing of silver interconnects on polyimide film for embedded electronics applications. In: 8th Int DAAAM Balt Conf "INDUSTRIAL Eng". pp 373–379
45. Kopola P, Zimmermann B, Filipovic A, Schleiermacher HF, Greulich J, Rousu S, Hast J, Myllylä R, Würfel U (2012) Aerosol jet printed grid for ITO-free inverted organic solar cells. Sol Energy Mater Sol Cells 107:252–258. https://doi.org/10.1016/j.solmat.2012.06.042

46. Mashayekhi M, Winchester L, Evans L, Pease T, Laurila MM, Mantysalo M, Ogier S, Teres L, Carrabina J (2016) Evaluation of aerosol, superfine inkjet, and photolithography printing techniques for metallization of application specific printed electronic circuits. IEEE Trans Electron Devices 63:1246–1253
47. Vunnam S, Ankireddy K, Kellar J, Cross W (2013) Surface modification of indium tin oxide for direct writing of silver nanoparticulate ink micropatterns. Thin Solid Films 531:294–301. https://doi.org/10.1016/j.tsf.2013.01.047
48. Mahajan A, Francis LF, Frisbie CD (2014) Facile method for fabricating flexible substrates with embedded, printed silver lines. ACS Appl Mater Interfaces 6:1306–1312. https://doi.org/10.1021/am405314s
49. Chang Y-HY, Wang K, Wu C, Chen Y, Zhang C, Wang B (2015) A facile method for integrating direct-write devices into three-dimensional printed parts. Smart Mater Struct 24:065008. https://doi.org/10.1088/0964-1726/24/6/065008
50. Shankar R, Groven L, Amert A, Whites KW, Kellar JJ (2011) Non-aqueous synthesis of silver nanoparticles using tin acetate as a reducing agent for the conductive ink formulation in printed electronics. J Mater Chem 21:10871. https://doi.org/10.1039/c0jm04521g
51. Werner C, Godlinski D, Zöllmer V, Busse M (2013) Morphological influences on the electrical sintering process of aerosol jet and ink jet printed silver microstructures. J Mater Sci Mater Electron 24:4367–4377. https://doi.org/10.1007/s10854-013-1412-y
52. Rahman MT, McCloy J, Ramana CV, Panat R (2016) Structure, electrical characteristics, and high-temperature stability of aerosol jet printed silver nanoparticle films. J Appl Phys 120:075305. https://doi.org/10.1063/1.4960779
53. Hoerber J, Goth C, Franke J, Hedges M (2011) Electrical functionalization of thermoplastic materials by aerosol jet printing. In: 2011 IEEE 13th Electronics Packaging Technology Conference. IEEE, pp 813–818
54. Schuetz K, Hoerber J, Franke J (2014) Selective light sintering of aerosol-jet printed silver nanoparticle inks on polymer substrates. In: AIP Conference Proceedings. pp 732–735
55. Kamyshny A, Magdassi S (2014) Conductive nanomaterials for printed electronics. Small 10:3515–3535
56. Reboun J, Pretl S, Navratil J, Hlina J (2016) Bending endurance of printed conductive patterns on flexible substrates. In: 2016 39th International Spring Seminar on Electronics Technology (ISSE). IEEE, pp 184–188
57. Jabari E, Toyserkani E (2015) Micro-scale aerosol-jet printing of graphene interconnects. Carbon N Y 91:321–329. https://doi.org/10.1016/j.carbon.2015.04.094
58. Jabari E, Toyserkani E (2016) Aerosol-jet printing of highly flexible and conductive graphene/silver patterns. Mater Lett 174:40–43. https://doi.org/10.1016/j.matlet.2016.03.082
59. Kan W, Chang Y-H, Zhang C, Wang B (2016) Conductive-on-demand: tailorable polyimide/carbon nanotube nanocomposite thin film by dual-material aerosol jet printing. Carbon N Y 98:397–403. https://doi.org/10.1016/j.carbon.2015.11.032
60. Reitberger T, Franke J, Hoffmann G-A, et al (2016) Integration of polymer optical waveguides by using flexographic and aerosol jet printing. In: 2016 12th International Congress Molded Interconnect Devices (MID). IEEE, pp 1–6
61. Reitberger T, Hoerber J, Schramm R et al (2015) Aerosol jet printing of optical waveguides. In: 2015 38th International Spring Seminar on Electronics Technology (ISSE). IEEE, pp 5–10
62. Hoffmann G, Reitberger T, Franke J, Overmeyer L (2016) Conditioning of surface energy and spray application of optical waveguides for integrated intelligent systems. Procedia Technol 26:169–176. https://doi.org/10.1016/j.protcy.2016.08.023
63. Reitberger T, Hoffmann G-A, Wolfer T, et al (2016) Printing polymer optical waveguides on conditioned transparent flexible foils by using the aerosol jet technology. In: List-Kratochvil EJW (ed) Proceedings volume 9945, printed memory and circuits II. p 99450G
64. Ha M, Zhang W, Braga D, Renn MJ, Kim CH, Frisbie CD (2013) Aerosol-jet-printed, 1 volt H-bridge drive circuit on plastic with integrated electrochromic pixel. ACS Appl Mater Interfaces 5:13198–13206. https://doi.org/10.1021/am404204q
65. Gu Y, Park D, Bowen D, et al (2018) Direct-write printed, solid-core solenoid inductors with commercially relevant inductances. Adv Mater Technol
66. Xu BL, Zhao Y, Yu LK, Xu B, Zhang HE, Lv WL, Sun DH (2013) Aerosol jet printing on radio frequency IDentification tag applications. Key Eng Mater 562–565:1417–1421. https://doi.org/10.4028/www.scientific.net/KEM.562-565.1417
67. Rahman MT, Panat R, Heo D (2015) 3-D antenna structures using novel direct-write additive manufacturing method. In: ASME 2015 International Technical Conference and Exhibition on Packaging and Integration of Electronic and Photonic Microsystems, InterPACK 2015, collocated with the ASME 2015 13th International Conference on Nanochannels, Microchannels, and Minichannels. American Society of Mechanical Engineers, School of Mechanical and Materials Engineering, Washington State University, Pullman, WA, United States
68. Rahman MT, Panat R, Heo D (2015) 3-D antenna structures using novel direct-write additive manufacturing method. In: Volume 3: Advanced fabrication and manufacturing; emerging technology frontiers; energy, health and water-applications of nano-, micro- and mini-scale devices; MEMS and NEMS; technology update talks; thermal management using micro channels, jets, sprays. ASME, p V003T03A002
69. Rahman T, Renaud L, Heo D, Renn M, Panat R (2015) Aerosol based direct-write micro-additive fabrication method for sub-mm 3D metal-dielectric structures. J Micromech Microeng 25:107002. https://doi.org/10.1088/0960-1317/25/10/107002
70. Fan Cai, Pavlidis S, Papapolymerou J, et al (2014) Aerosol jet printing for 3-D multilayer passive microwave circuitry. In: 2014 44th European Microwave Conference. IEEE, pp 512–515
71. He Y, Becker M, Grotjohn T, et al (2017) RF characterization of coplanar waveguide (CPW) transmission lines on single-crystalline diamond platform for integrated high power RF electronic systems. IEEE MTT-S Int Microw Symp Dig 517–520. https://doi.org/10.1109/MWSYM.2017.8058613
72. Cai F, Chang Y, Wang K, et al (2014) High resolution aerosol jet printing of D-band printed transmission lines on flexible LCP substrate. In: 2014 IEEE MTT-S International Microwave Symposium (IMS2014). IEEE, pp 1–3
73. Lan X, Lu X, Blumenthal T, et al (2015) Ultra-wideband microwave components fabricated using low-cost aerosol-jet printing technology. In: 2015 IEEE Radio and Wireless Symposium (RWS). IEEE, pp 156–158
74. Oakley C, Kaur A, Byford JA, Chahal P (2017) Aerosol-jet printed quasi-optical terahertz filters. In: 2017 IEEE 67th Electronic Components and Technology Conference (ECTC), Orlando, FL, 2017, IEEE, pp 248–253. https://doi.org/10.1109/ECTC.2017.233
75. Hester J, Nguyen E, Tice J, Radisic V (2017) A novel 3d-printing-enabled "roller coaster" transmission line. In: 2017 IEEE Antennas Propag Soc Int Symp Proc 2017–Janua:2639–2640. https://doi.org/10.1109/APUSNCURSINRSM.2017.8073362
76. Cho JH, Lee J, Xia Y, Kim BS, He Y, Renn MJ, Lodge TP, Daniel Frisbie C (2008) Printable ion-gel gate dielectrics for low-voltage polymer thin-film transistors on plastic. Nat Mater 7:900–906. https://doi.org/10.1038/nmat2291
77. Hong K, Kim YH, Kim SH, Xie W, Xu WD, Kim CH, Frisbie CD (2014) Aerosol jet printed, sub-2 V complementary circuits

constructed from P- and N-type electrolyte gated transistors. Adv Mater 26:7032–7037. https://doi.org/10.1002/adma.201401330
78. Hong K, Kim SH, Lee KH, Frisbie CD (2013) Printed, sub-2V ZnO electrolyte gated transistors and inverters on plastic. Adv Mater 25:3413–3418. https://doi.org/10.1002/adma.201300211
79. Wu X, Chen Z, Zhou T, Shao S, Xie M, Song M, Cui Z (2015) Printable poly(methylsilsesquioxane) dielectric ink and its application in solution processed metal oxide thin-film transistors. RSC Adv 5:20924–20930. https://doi.org/10.1039/C4RA17234E
80. Li H, Tang Y, Guo W, Liu H, Zhou L, Smolinski N (2016) Polyfluorinated electrolyte for fully printed carbon nanotube electronics. Adv Funct Mater 26:6914–6920. https://doi.org/10.1002/adfm.201601605
81. Jones CS, Lu X, Renn M, Stroder M, Shih WS (2010) Aerosol-jet-printed, high-speed, flexible thin-film transistor made using single-walled carbon nanotube solution. Microelectron Eng 87:434–437. https://doi.org/10.1016/j.mee.2009.05.034
82. Qian L, Xu W, Fan X, Wang C, Zhang J, Zhao J, Cui Z (2013) Electrical and photoresponse properties of printed thin-film transistors based on poly(9,9-dioctylfluorene-co-bithiophene) sorted large-diameter semiconducting carbon nanotubes. J Phys Chem C 117:18243–18250. https://doi.org/10.1021/jp4055022
83. Rother M, Brohmann M, Yang S, Grimm SB, Schießl SP, Graf A, Zaumseil J (2017) Aerosol-jet printing of polymer-sorted (6,5) carbon nanotubes for field-effect transistors with high reproducibility. Adv Electron Mater 3:1700080. https://doi.org/10.1002/aelm.201700080
84. Cao C, Andrews JB, Franklin AD (2017) Completely printed, flexible, stable, and hysteresis-free carbon nanotube thin-film transistors via aerosol jet printing. Adv Electron Mater 3:1700057. https://doi.org/10.1002/aelm.201700057
85. Liu Z, Zhao J, Xu W, Qian L, Nie S, Cui Z (2014) Effect of surface wettability properties on the electrical properties of printed carbon nanotube thin-film transistors on SiO_2/Si substrates. ACS Appl Mater Interfaces 6:9997–10004. https://doi.org/10.1021/am502168x
86. Xu Q, Zhao J, Pecunia V, Xu W, Zhou C, Dou J, Gu W, Lin J, Mo L, Zhao Y, Cui Z (2017) Selective conversion from p-type to n-type of printed bottom-gate carbon nanotube thin-film transistors and application in complementary metal–oxide–semiconductor inverters. ACS Appl Mater Interfaces 9:12750–12758. https://doi.org/10.1021/acsami.7b01666
87. Liu R, Shen F, Ding H, Lin J, Gu W, Cui Z, Zhang T (2013) All-carbon-based field effect transistors fabricated by aerosol jet printing on flexible substrates. J Micromech Microeng 23:065027. https://doi.org/10.1088/0960-1317/23/6/065027
88. Zhou L, Zhuang JY, Song MS, Su WM, Cui Z (2014) Enhanced performance for organic light-emitting diodes by embedding an aerosol jet printed conductive grid. J Phys D Appl Phys 47:115504. https://doi.org/10.1088/0022-3727/47/11/115504
89. Tait JG, Witkowska E, Hirade M, Ke TH, Malinowski PE, Steudel S, Adachi C, Heremans P (2015) Uniform aerosol jet printed polymer lines with 30 μm width for 140 ppi resolution RGB organic light emitting diodes. Org Electron 22:40–43. https://doi.org/10.1016/j.orgel.2015.03.034
90. van Hest MFAM, Habas SE, Underwood JM, et al (2010) Direct write metallization for photovoltaic cells and scaling thereof. In: 2010 35th IEEE Photovoltaic Specialists Conference. IEEE, pp 003626–003628
91. Platt HAS, Li Y, Novak JP, van Hest MFAM (2012) Non-contact printed aluminum metallization of Si photovoltaic devices. In: 2012 38th IEEE Photovoltaic Specialists Conference. IEEE, pp 002244–002246
92. Williams BA, Mahajan A, Smeaton MA, Holgate CS, Aydil ES, Francis LF (2015) Formation of copper zinc tin sulfide thin films from colloidal nanocrystal dispersions via aerosol-jet printing and compaction. ACS Appl Mater Interfaces 7:11526–11535. https://doi.org/10.1021/acsami.5b02484
93. Bag S, Deneault JR, Durstock MF (2017) Aerosol-jet-assisted thin-film growth of CH 3 NH 3 PbI 3 perovskites—a means to achieve high quality, defect-free films for efficient solar cells. Adv Energy Mater 1701151:1701151. https://doi.org/10.1002/aenm.201701151
94. Rodriguez J, Lennon AJ, Luo M, Li Z, Yao Y, Lu PH, Chan C, Wenham SR (2012) Dielectric patterning using aerosol jet printing. J Imaging Sci Technol 56:1–7. https://doi.org/10.2352/J.ImagingSci.Technol.2012.56.4.040502
95. Sukeshini AM, Jenkins T, Gardner P, et al (2010) Investigation of aerosol jet deposition parameters for printing SOFC layers. In: ASME 2010 8th International Fuel Cell Science, Engineering and Technology Conference: Volume 1. ASME, pp 325–332
96. Sukeshini AM, Gardner P, Meisenkothen F, et al (2011) Aerosol jet printing and microstructure of SOFC electrolyte and cathode layers. pp 2151–2160
97. Sukeshini AM, Meisenkothen F, Gardner P, Reitz TL (2013) Aerosol jet?? Printing of functionally graded SOFC anode interlayer and microstructural investigation by low voltage scanning electron microscopy. J Power Sources 224:295–303. https://doi.org/10.1016/j.jpowsour.2012.09.094
98. Maiwald M, Werner C, Zoellmer V, Busse M (2010) INKtelligent printed strain gauges. Sensors Actuators A Phys 162:198–201. https://doi.org/10.1016/j.sna.2010.02.019
99. Maiwald M, Werner C, Zöllmer V, Busse M (2010) INKtelligent printing ® for sensorial applications. Sens Rev 30:19–23. https://doi.org/10.1108/02602281011010763
100. Zhao D, Liu T, Zhang M, Liang R, Wang B (2012) Fabrication and characterization of aerosol-jet printed strain sensors for multifunctional composite structures. Smart Mater Struct 21:115008. https://doi.org/10.1088/0964-1726/21/11/115008
101. Rahman MT, Moser R, Zbib HM, Ramana CV, Panat R (2018) 3D printed high performance strain sensors for high temperature applications. J Appl Phys 123:024501. https://doi.org/10.1063/1.4999076
102. Rahman MT, Rahimi A, Gupta S, Panat R (2016) Microscale additive manufacturing and modeling of interdigitated capacitive touch sensors. Sensors Actuators A Phys 248:94–103. https://doi.org/10.1016/j.sna.2016.07.014
103. Andrews JB, Cao C, Brooke MA, Franklin AD (2017) Noninvasive material thickness detection by aerosol jet printed sensors enhanced through metallic carbon nanotube ink. IEEE Sensors J 17:4612–4618. https://doi.org/10.1109/JSEN.2017.2710085
104. Fessl J, Mach F, Navratil J (2017) Numerical and experimental analysis of electrostatic adhesion force generated by interdigital electrodes. In: 2017 18th Int Symp Electromagn Fields Mechatronics, Electr Electron Eng ISEF 2017 c:1–2. https://doi.org/10.1109/ISEF.2017.8090706
105. Reitelshöfer S, Göttler M, Schmidt P, Treffer P, Landgraf M, Franke J (2016) Aerosol-jet-printing silicone layers and electrodes for stacked dielectric elastomer actuators in one processing device. In: Proc. SPIE 9798, Electroactive Polymer Actuators and Devices (EAPAD)
106. Landgraf M, Reitelshofer S, Franke J, Hedges M (2013) Aerosol jet printing and lightweight power electronics for dielectric elastomer actuators. In: 2013 3rd International Electric Drives Production Conference (EDPC). IEEE, pp 1–7
107. Yoo IS, Landgraf M, Ramer C, Reitelshöfer S, Ziegler C, Franke J (2014) My new colleague has artificial muscles: a DEA based approach for inherently compliant robotic systems. Prod Eng 8:711–717. https://doi.org/10.1007/s11740-014-0564-9
108. Reitelshofer S, Landgraf M, Graf D, et al (2015) A new production process for soft actuators and sensors based on dielectric

elastomers intended for safe human robot interaction. In: 2015 IEEE/SICE International Symposium on System Integration (SII). IEEE, pp 51–56

109. Aga RS, Lombardi JP, Bartsch CM, Heckman EM (2014) Performance of a printed photodetector on a paper substrate. IEEE Photon Technol Lett 26:305–308. https://doi.org/10.1109/LPT.2013.2292830
110. Wang F-X, Lin J, Gu W-B, Liu YQ, Wu HD, Pan GB (2013) Aerosol-jet printing of nanowire networks of zinc octaethylporphyrin and its application in flexible photodetectors. Chem Commun 49:2433–2435. https://doi.org/10.1039/c3cc38996k
111. Eckstein R, Rödlmeier T, Glaser T, Valouch S, Mauer R, Lemmer U, Hernandez-Sosa G (2015) Aerosol-jet printed flexible organic photodiodes: semi-transparent, color neutral, and highly efficient. Adv Electron Mater 1:1500101. https://doi.org/10.1002/aelm.201500101
112. Ichiyama R, Ninkov Z, Williams S, et al (2017) Using quantum-dots to enable deep-UV sensitivity with standard silicon-based imaging detectors. In: Soskind YG, Olson C (eds) Proceedings of SPIE. p 1011011
113. Liu R, Ding H, Lin J, Shen F, Cui Z, Zhang T (2012) Fabrication of platinum-decorated single-walled carbon nanotube based hydrogen sensors by aerosol jet printing. Nanotechnology 23:505301. https://doi.org/10.1088/0957-4484/23/50/505301
114. Kuberský P, Altšmíd J, Hamáček A, Nešpůrek S, Zmeškal O (2015) An electrochemical NO_2 sensor based on ionic liquid: influence of the morphology of the polymer electrolyte on sensor sensitivity. Sensors 15:28421–28434. https://doi.org/10.3390/s151128421
115. Yang H, Rahman MT, Du D et al (2016) 3-D printed adjustable microelectrode arrays for electrochemical sensing and biosensing. Sensors Actuators B Chem 230:600–606. https://doi.org/10.1016/j.snb.2016.02.113
116. Lombardi J, Poliks MD, Zhao W, et al (2017) Nanoparticle based printed sensors on paper for detecting chemical species. In: 2017 IEEE 67th Electronic Components and Technology Conference (ECTC). IEEE, pp 764–771
117. Saleh MS, Li J, Park J, Panat R (2018) 3D printed hierarchically-porous microlattice electrode materials for exceptionally high specific capacity and areal capacity lithium ion batteries. Addit Manuf 23:70–78. https://doi.org/10.1016/j.addma.2018.07.006
118. Sadeq Saleh M, HamidVishkasougheh M, Zbib H, Panat R (2018) Polycrystalline micropillars by a novel 3-D printing method and their behavior under compressive loads. Scr Mater 149:144–149. https://doi.org/10.1016/j.scriptamat.2018.02.027
119. De Silva MN, Paulsen J, Renn MJ, Odde DJ (2006) Two-step cell patterning on planar and complex curved surfaces by precision spraying of polymers. Biotechnol Bioeng 93:919–927. https://doi.org/10.1002/bit.20787
120. Große Holthaus M, Rezwan K (2008) Comparison of three microstructure fabrication methods for bone cell growth studies. In: ASME 2008 International Manufacturing Science and Engineering Conference, Volume 2. ASME, pp 483–490
121. Kitsara M, Kontziampasis D, Agbulut O, Chen Y (2019) Heart on a chip: micro-nanofabrication and microfluidics steering the future of cardiac tissue engineering. Microelectron Eng 203–204:44–62. https://doi.org/10.1016/j.mee.2018.11.001
122. Wehner M, Truby RL, Fitzgerald DJ, Mosadegh B, Whitesides GM, Lewis JA, Wood RJ (2016) An integrated design and fabrication strategy for entirely soft, autonomous robots. Nature 536:451–455. https://doi.org/10.1038/nature19100
123. Wallin TJ, Pikul J, Shepherd RF (2018) 3D printing of soft robotic systems. Nat Rev Mater 3:84–100

9 Appendix B

1wt%

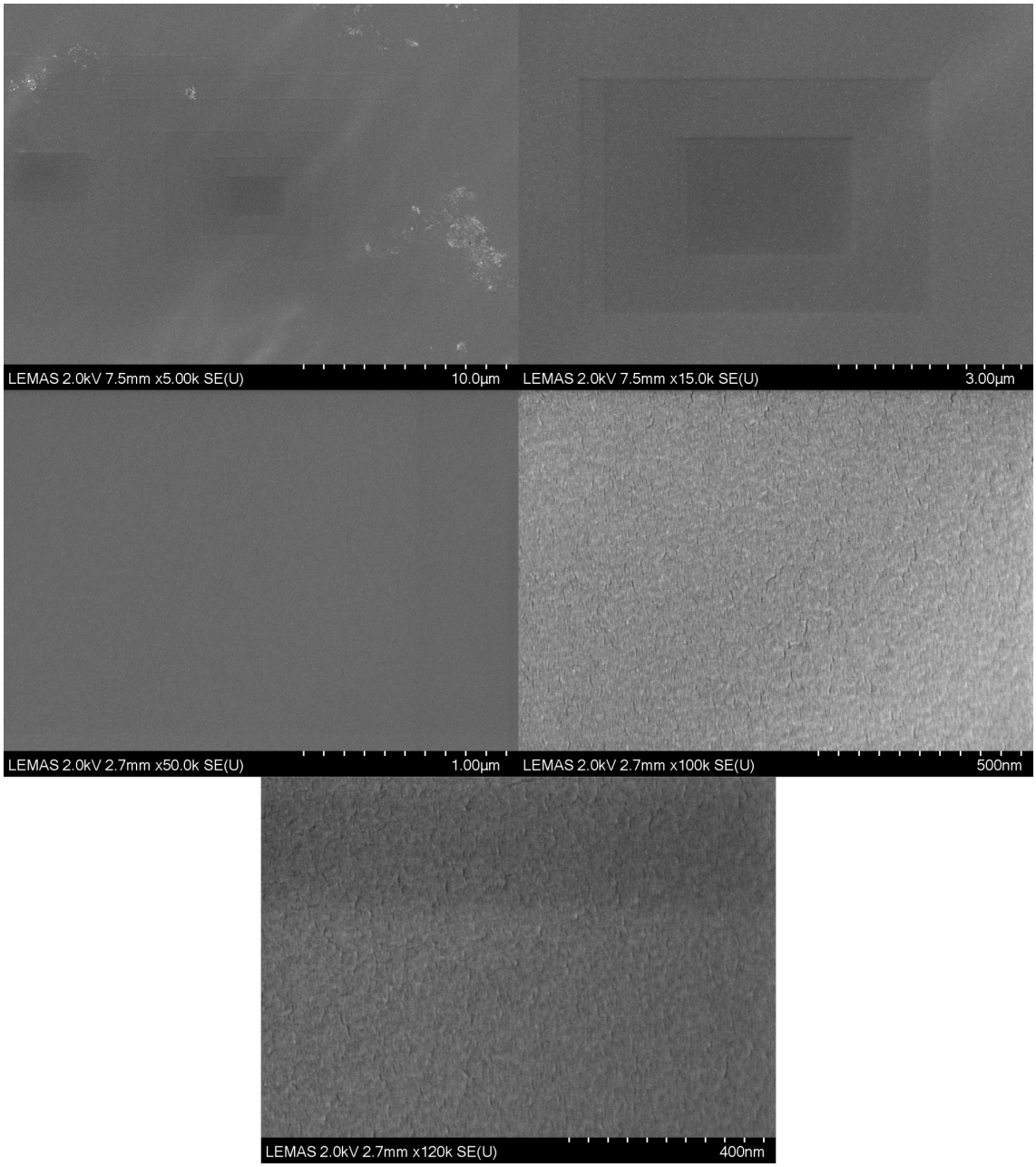

2.5 wt%

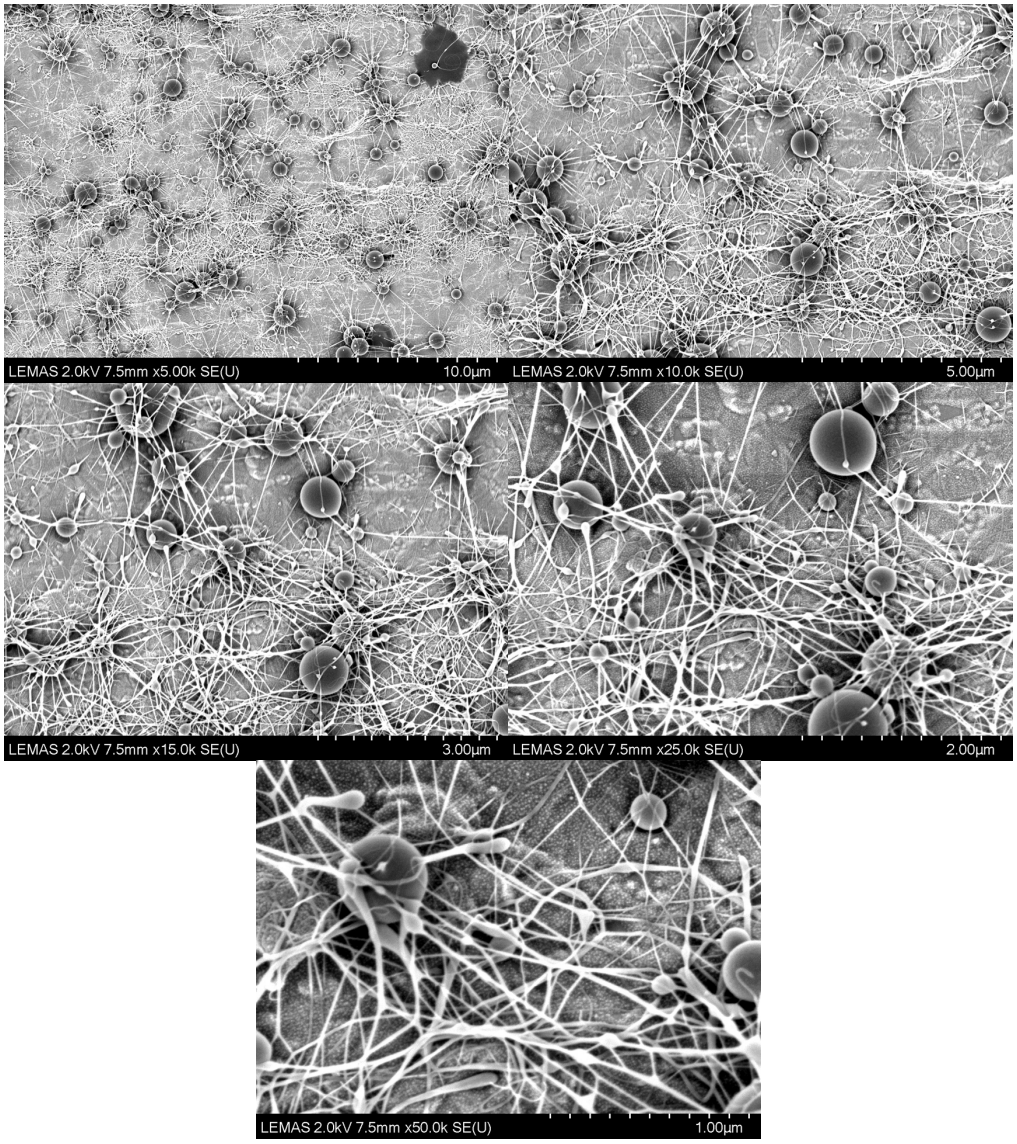
LEMAS 2.0kV 7.5mm x5.00k SE(U)
10.0µm
LEMAS 2.0kV 7.5mm x10.0k SE(U)
5.00µm
LEMAS 2.0kV 7.5mm x15.0k SE(U)
3.00µm
LEMAS 2.0kV 7.5mm x25.0k SE(U)
2.00µm
LEMAS 2.0kV 7.5mm x50.0k SE(U)
1.00µm

5wt%

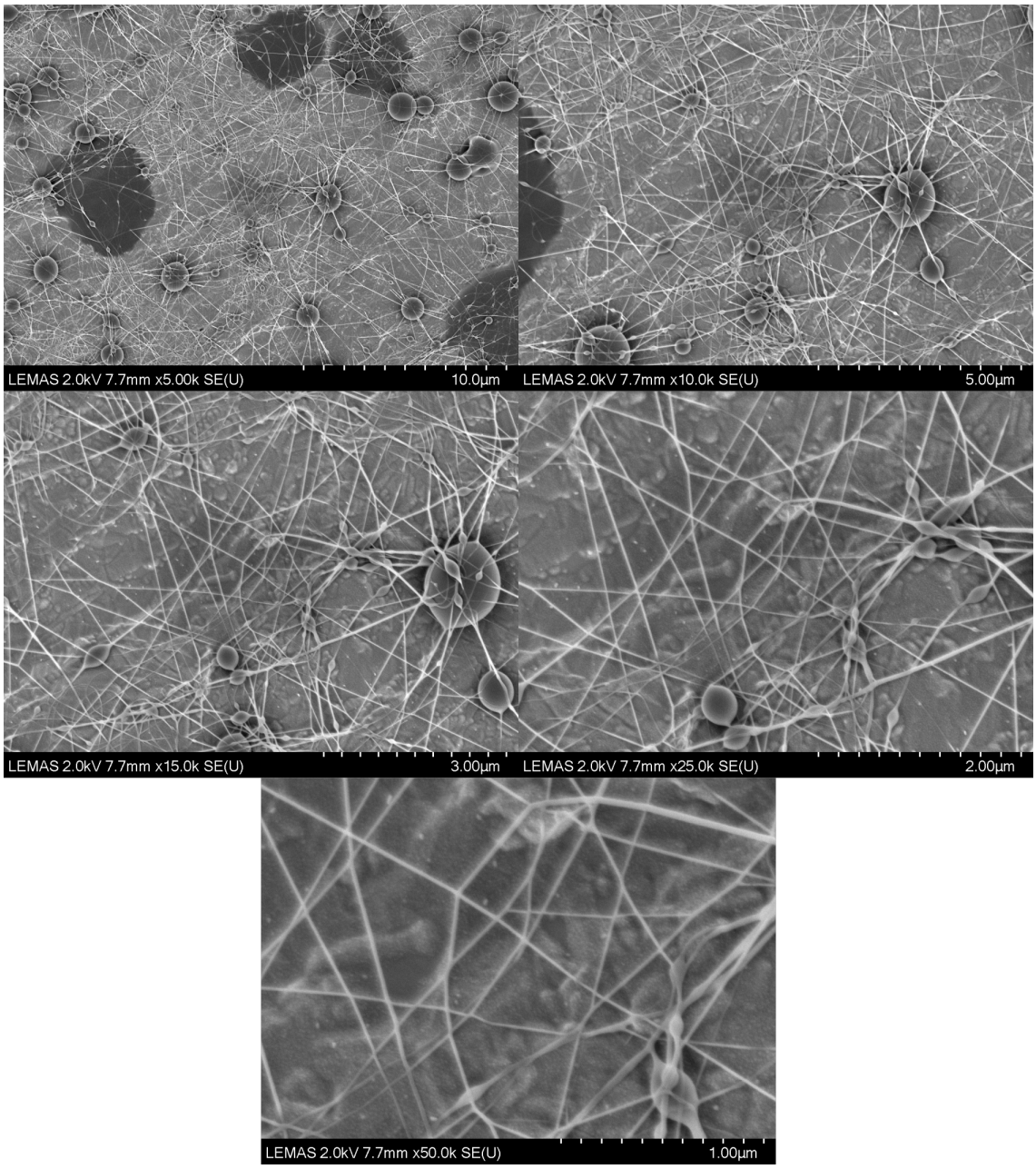
LEMAS 2.0kV 7.7mm x5.00k SE(U)
10.0µm
LEMAS 2.0kV 7.7mm x10.0k SE(U)
5.00µm
LEMAS 2.0kV 7.7mm x15.0k SE(U)
3.00µm
LEMAS 2.0kV 7.7mm x25.0k SE(U)
2.00µm
LEMAS 2.0kV 7.7mm x50.0k SE(U)
1.00µm

7.5wt%

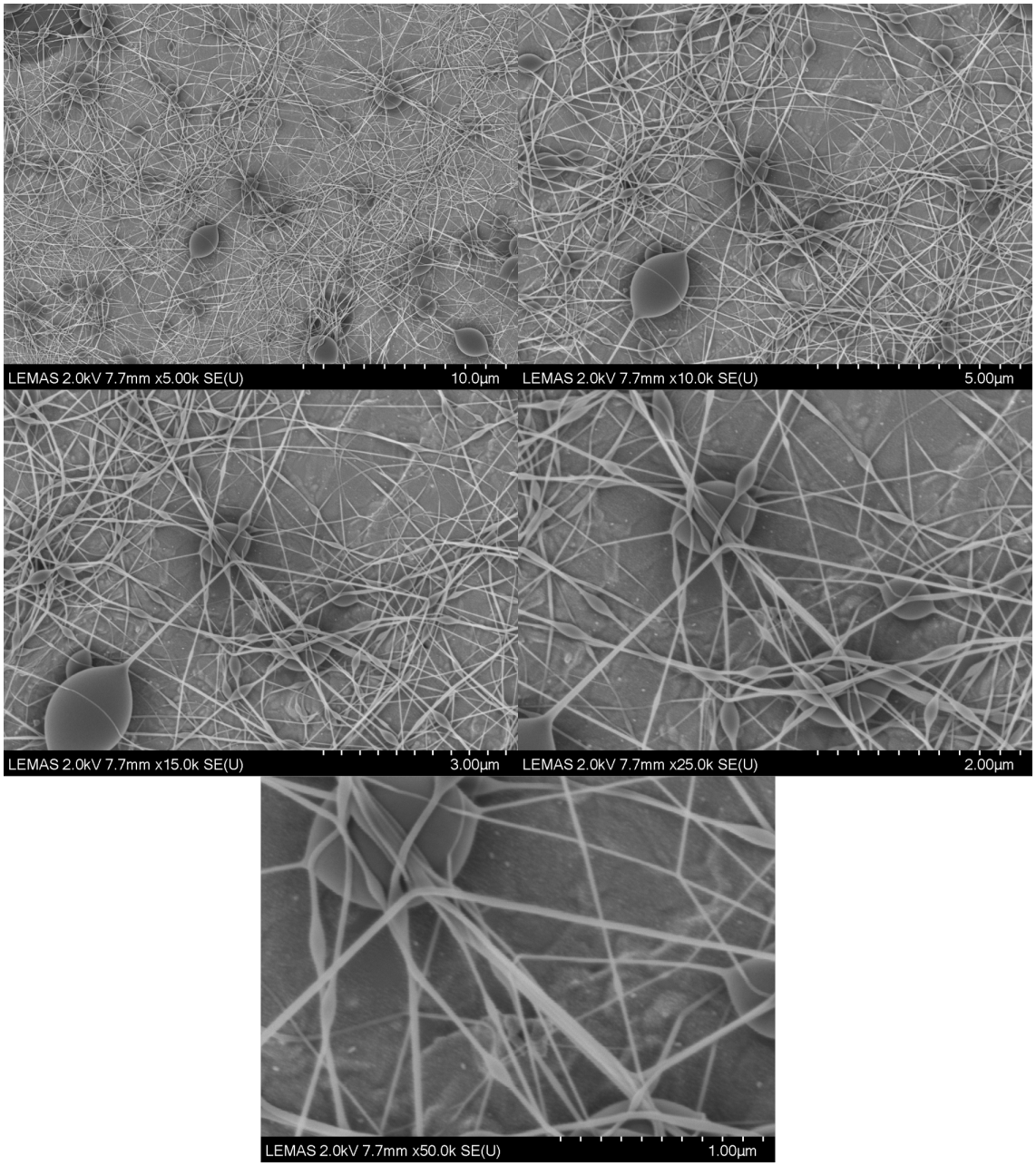
LEMAS 2.0kV 7.7mm x5.00k SE(U)
10.0µm
LEMAS 2.0kV 7.7mm x10.0k SE(U)
5.00µm
LEMAS 2.0kV 7.7mm x15.0k SE(U)
3.00µm
LEMAS 2.0kV 7.7mm x25.0k SE(U)
2.00µm
LEMAS 2.0kV 7.7mm x50.0k SE(U)
1.00µm

10wt%

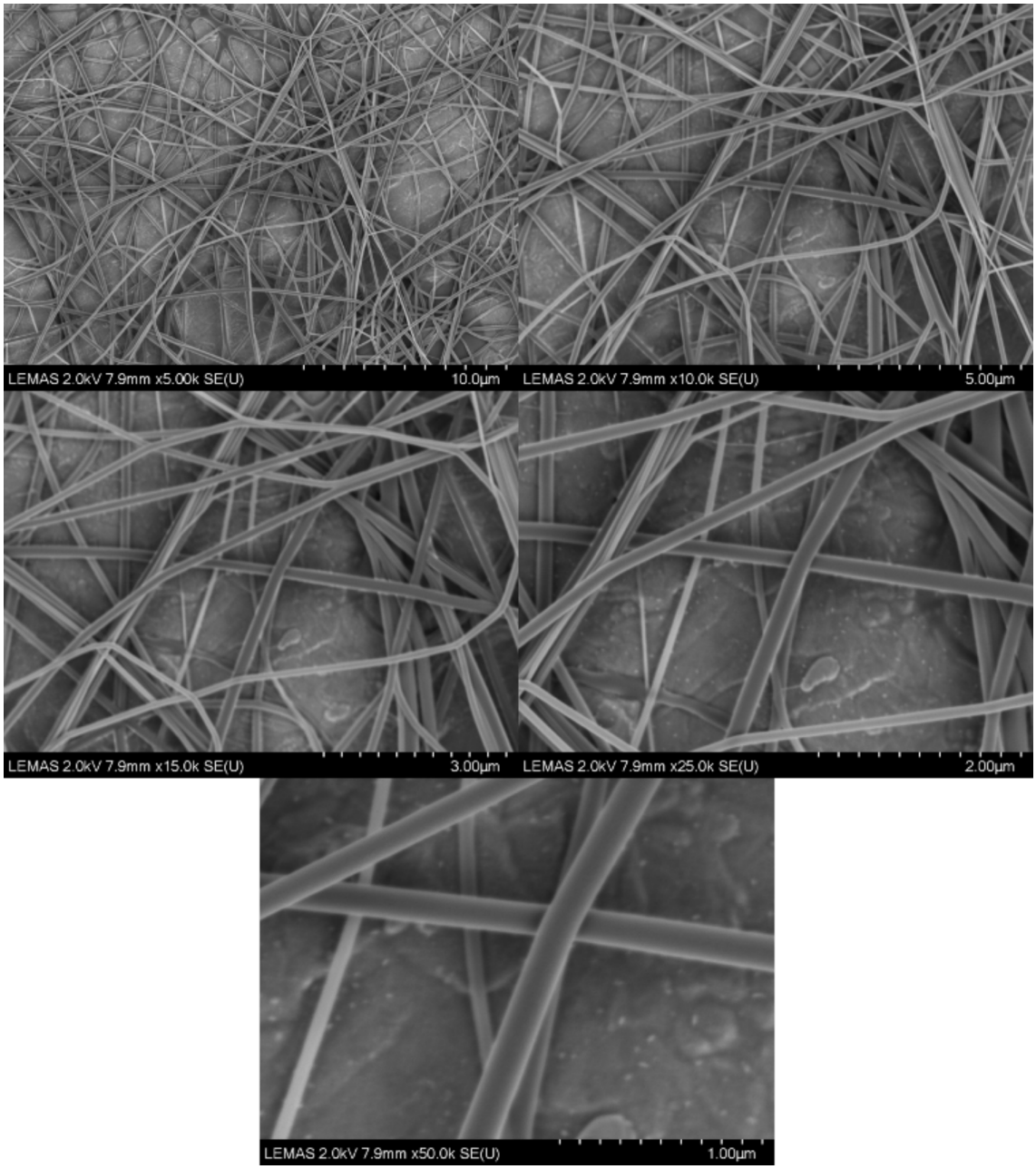
LEMAS 2.0kV 7.9mm x5.00k SE(U)
10.0µm
LEMAS 2.0kV 7.9mm x10.0k SE(U)
5.00µm
LEMAS 2.0kV 7.9mm x15.0k SE(U)
3.00µm
LEMAS 2.0kV 7.9mm x25.0k SE(U)
2.00µm
LEMAS 2.0kV 7.9mm x50.0k SE(U)
1.00µm

12.5wt%

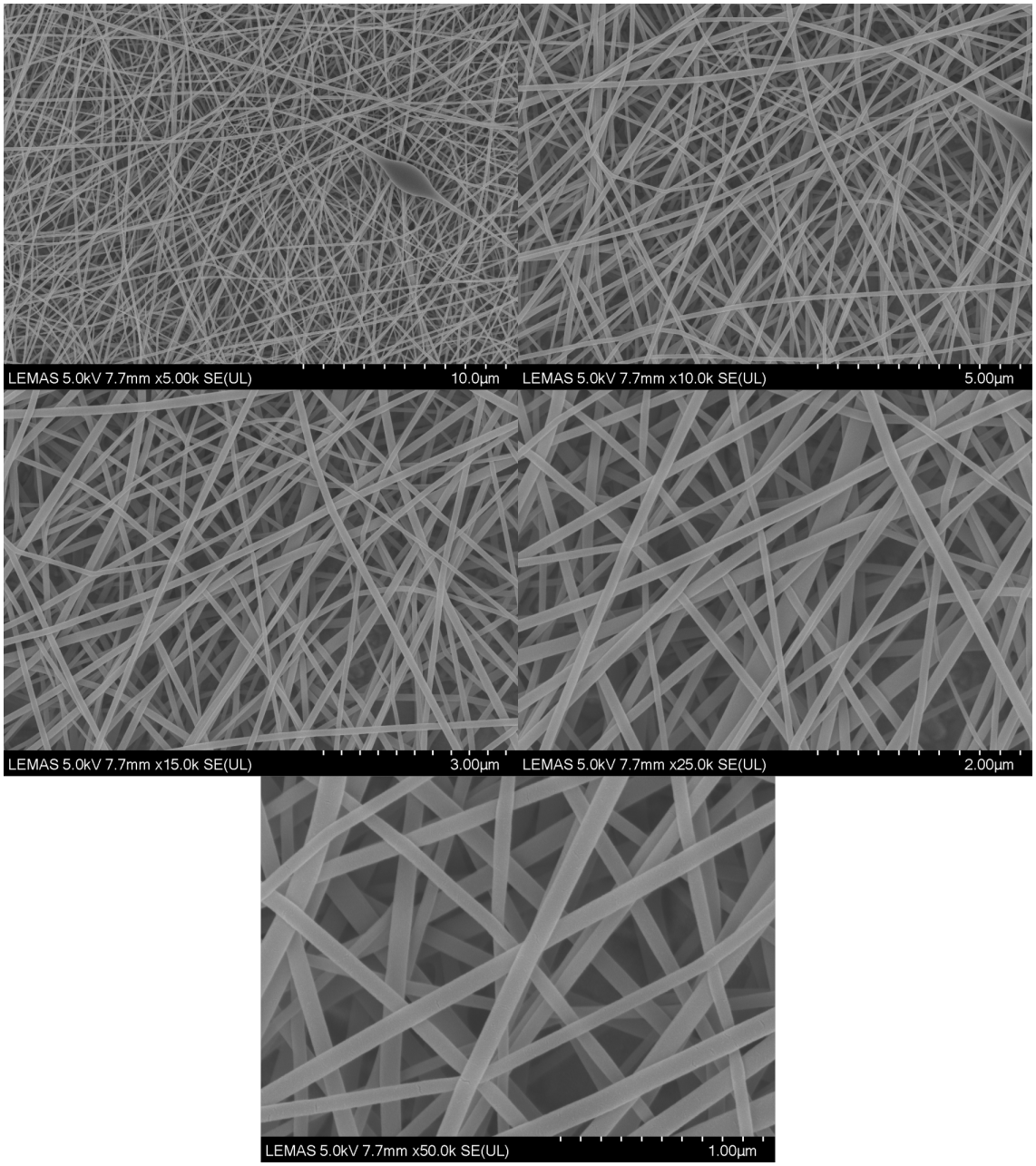
LEMAS 5.0kV 7.7mm x5.00k SE(UL)
10.0µm
LEMAS 5.0kV 7.7mm x10.0k SE(UL)
5.00µm
LEMAS 5.0kV 7.7mm x15.0k SE(UL)
3.00µm
LEMAS 5.0kV 7.7mm x25.0k SE(UL)
2.00µm
LEMAS 5.0kV 7.7mm x50.0k SE(UL)
1.00µm

10 Appendix C

Table 6 - Conductivity of aerosol jet printed samples

Number of passes (Adjacent)	*Resistance (kΩ)*	*Std. Dev.*
1	*33.156*	*7.63734771*
2	*12.814*	*1.48264291*
3	*10.39*	*3.783331187*
4	*7.236*	*1.5214894*
5	*5.588*	*1.32207035*
6	*4.24*	*0.55547277*
7	*3.588*	*0.53382581*
8	*3.372*	*0.68758272*

Table 7 - Conductivity of aerosol jet printed samples (stacked)

Number of passes (stacked)	*Resistance (kΩ)*	*Std. Dev.*
1	*62.38*	*35.4820398*
2	*21.578*	*11.7355856*
3	*11.41*	*4.47071583*
4	*7.638*	*2.59849379*
5	*5.97*	*1.6595632*
6	*4.838*	*0.850541*

7	*4.058*	*0.70605949*
8	*3.5*	*0.76206955*

11 Appendix D

Wilkinson, N.J.; Kay, R.W.; and Harris, R.A. 'Electrohydrodynamic and Aerosol Jet printing for the co-patterning of polydimethylsiloxane and graphene platelet inks'. Adv. Mater. Technol, (2020). DOI: 10.1002/admt.202000148

ADVANCED MATERIALS TECHNOLOGIES
www.advmattechnol.d

Electrohydrodynamic and Aerosol Jet Printing for the Copatterning of Polydimethylsiloxane and Graphene Platelet Inks

*Nathan J. Wilkinson, Robert W. Kay, and Russell A. Harris**

The performance of soft sensing and actuation devices is dependent on their design, the electro-mechanical response of materials, and the ability to copattern structural and functional features. For film based soft structures, such as wearable sensors and artificial muscles, manufacturing challenges exist that prevent the translation of technology from laboratory to practical application. In this work, a hybrid manufacturing technique is presented that integrates electro-hydrodynamic and aerosol jet deposition to print multilayer, multimaterial structures. The combined approach overcomes the respective rheological constraints of the individual processes, while presenting a pathway to higher resolution computer-controlled patterning. Electro-hydrodynamic deposition of a polydimethylsiloxane elastomer is demonstrated and characterized, before being combined with aerosol jet deposition of a graphene platelet ink to produce functional devices. A proof-of-concept, multilayer capacitive sensor is presented as a first demonstration of the manufacturing technology.

Soft robotics presents a unique opportunity to improve the interactions and interfaces between living and computerized systems to drive innovation in healthcare,[1] haptics,[2] and biological sciences.[3] Film-based soft robotics, in the form of actuators and sensors, are of interest due their low-weight, high efficiency, and unobtrusive nature.[4] Innovation in their manufacture, to allow selective patterning of soft and functional materials at improved resolution, will be essential to delivering the potential of soft technologies and will drive their commercial adoption.[5] Specifically, the ability to alternately form thin layers of elastomers with micro-patterned, stretchable circuitry can improve sensor density and fidelity. The automated and repeatable manufacture of low-roughness elastomeric films has importance in actuation technologies as it is the key enabler for dielectric electroactive polymers, commonly known as a type of artificial muscle.[6]

N. J. Wilkinson, Dr. R. W. Kay, Prof. R. A. Harris
Future Manufacturing Processes Research Group
University of Leeds
Leeds LS2 9JT, UK
E-mail: R.Harris@leeds.ac.uk

The ORCID identification number(s) for the author(s) of this article can be found under https://doi.org/10.1002/admt.202000148.

DOI: 10.1002/admt.202000148

Several techniques have been developed for film based soft robotic devices, but they face challenges in processing speed, scalability, and resolution. Common approaches use spin coating,[7,8] blade casting,[9] or pad printing[10] to produce thin layers of elastomer often in combination with masked deposition of electrodes. Despite some success, film thicknesses below 5 µm are challenging and there are limits to the height and area of stacked elastomer structures.[11] Furthermore, these batch processes do not provide opportunity for patterning of elastomer layers and face challenges at larger volumes.

Additive techniques, which selectively deposit elastomeric and functional materials, are removing design constrains and offering new capabilities through improved design. The disparity in rheology between functional and structural inks provides the most prominent hurdle to the development of an effective and integrated manufacturing strategy. Direct ink write (DIW) is growing in popularity for soft robotics,[12] however the process resolution is better suited for large devices over film-based sensors or actuators. Ink jet printing has been the most successful for thin films, with McCoul et al.[13] demonstrating the deposition of thin (2–5 µm) elastomer layers. The authors maintained that nozzle clogging is a significant issue even when using relatively large nozzle orifices with diluted inks. The aforementioned techniques have been most successful in the patterning of functional materials within soft structures. DIW,[14] aerosol jet (AJ),[15] and inkjet printing[16] have all been demonstrated as effective methods for producing stretchable or flexible sensors and actuators.

Electro-hydrodynamic Jet (E-Jet) printing—an additive technique that uses high electric fields to draw material from a nozzle—has been widely investigated for its ability to deposit sub-micron features.[17] Since material is drawn rather than pushed through the application of back-pressure, E-Jet deposition is also able to deposit higher viscosity materials than comparable processes.[18] In this work, we leverage this improved material compatibility through a non-classical deposition regime to selectively pattern unmodified, commercially available polydimethylsiloxane (PDMS). Pulsating jet and pulse-on-demand droplet deposition is investigated before being combined with oxygen plasma surface treatment and AJ printing to demonstrate a digitally driven process route for the

hybrid manufacture of a functional multilayer, multimaterial structure.

When a volume of liquid is ejected from a nozzle, a spheroidal meniscus forms as the surface tension of the fluid is the principle force dictating its shape. Under a high electric field, stresses driven by charge interactions become the predominant factor and, beyond a critical value, the electric field will pull the meniscus in to a conical structure that emits a jet from its apex.[19] If the substrate is sufficiently close to the nozzle, the jet can be used for direct write (E-Jet) before whipping[20] or spraying[21] instabilities arise.

Establishing classical electro-hydrodynamic deposition requires the fluid's electrical relaxation time to be shorter than the hydrodynamic relaxation time[22] (Equation (1)), where ε' is the permittivity of the fluid, ε_0 is the permittivity of free space, K is the conductivity of the ink, L is the distance between the nozzle and electrode, D is the nozzle diameter, and Q_s is the supplied flow rate

$$\frac{\varepsilon' \varepsilon_0}{K} \ll \frac{LD^2}{Q_s} \tag{1}$$

Deposition of silicone elastomers, or silicone oils,[23] through the classical regime can be a challenge due to their low-conductivity. Existing work targeting electro-hydrodynamic deposition of PDMS has modified the ink through simplification of the precursor solution;[24] using carrier materials within the solution;[25] or some combination of the two.[11] These methods aim to increase the conductivity and reduce the permittivity of the fluid to increase the material's affinity to classical deposition.

When the material's electrical relaxation time exceeds the hydrodynamic time, an alternate deposition mechanism known as electrically forced jets arises.[22] In practice, this leads to a loss of resolution compared to classical E-Jet due to the establishment of a ball-cone rather than the traditional Taylor cone. For many soft film applications, increased lateral resolution may present a suitable compromise for increased material compatibility, especially if axial resolution can be preserved. In this study, we investigate the production of droplets through electrically forced jets and the effect of processing parameters on the shape and size of the deposits.

Droplet production can be triggered through the pulsating jet or drop-on-demand techniques. In the pulsating mode, ejection is a result of cyclic imbalances between the surface tension and electrostatic stresses within the meniscus under the application of a static DC field. Once the electrostatic stresses overcome the surface tension, a droplet is ejected and the cone recoils. The process then repeats at high frequencies to produce a steady stream of droplets. The frequency of droplet emission is driven by the properties of the ink, such as viscosity and conductivity, in combination with the applied voltage, nozzle-substrate distance, and material flowrate (**Figure 1**a).

Increasing the magnitude of the DC electric field, through either an increase in the applied voltage or reduction of the nozzle-substrate offset, increases the frequency of the droplet emission and reduces the size of the droplets. Increasing the flow rate led to increased droplet size and a reduction in droplet frequency. The close coupling between process control, droplet size, and frequency provided limited spatial control and resulted in the spacing between consecutive droplets being driven by the translational velocity of the deposition head. This approach requires significant empirical work to understand the interdependencies and derive a reliable process.

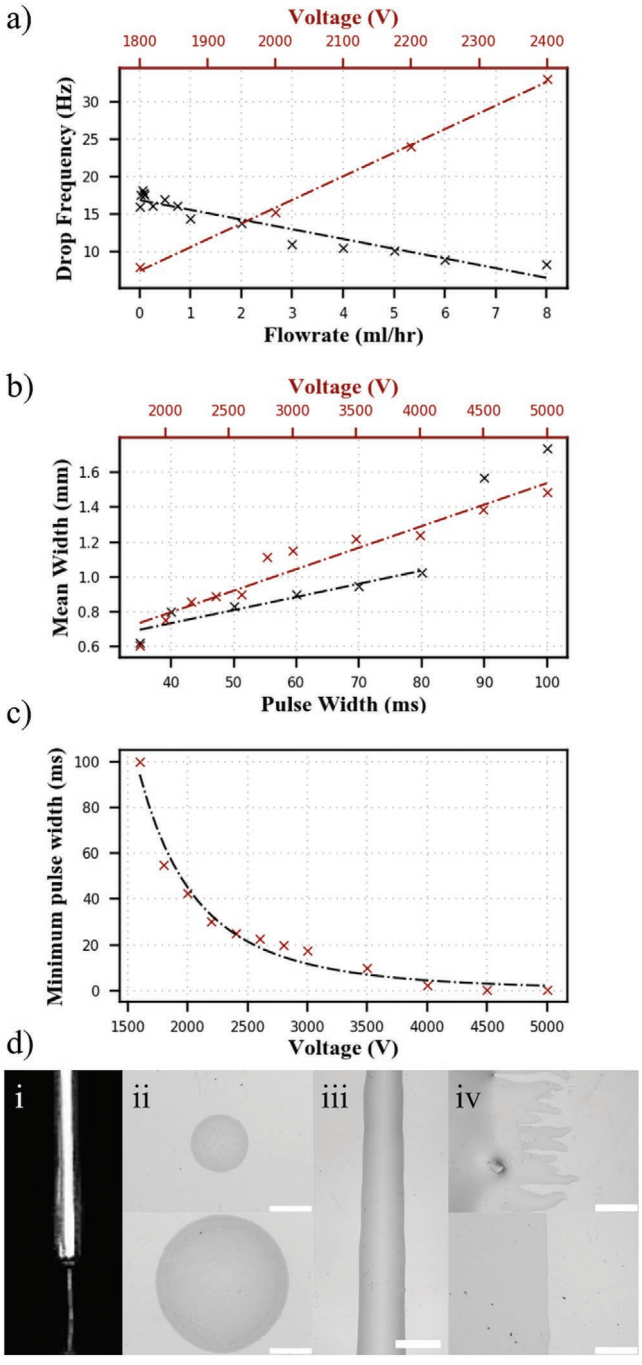

Figure 1. a) Effect of flowrate and applied voltage on droplet frequency in the pulsating jet mode, b) the effect of increasing high voltage pulse width and magnitude on the droplet width, c) Minimum pulse width required to trigger deposition at increasing voltages, d) Micrographs of i) droplet ejection, ii) droplets at the minimum and maximum pulse widths, iii) a confluent line, iv) effects of DC versus AC pulses during pulse-on-demand deposition. All scale bars are 500 µm)

Pulse-on-demand differs as it selectively applies a high voltage pulse to trigger droplet ejection. This provides simplified, independent control of droplet volume and positioning. Decreasing the magnitude and duration of the applied pulse allows a reduction in deposit diameter (Figure 1b), while spatial control can be achieved through coordination of the deposition head with the application of the pulse. For the materials used in this work, high magnitude pulses in combination with short pulse durations were found to be an effective method to increase droplet throughput (Figure 1c), even at voltages that were found to produce unstable jetting in a static field.

In contrast to pulsating E-Jet, increasing the magnitude of the applied voltage pulse was found to increase the diameter of the deposit (Figure 1b). When observed using stroboscopic microscopy, ejection of multiple droplets were identified during the application of a 100 ms square-wave pulse. As shown in Figure 1b, the discontinuity in the pulse width represents the pulse duration required to trigger multiple droplets under a 2 kV electric field.

Deposit geometry was controlled through modulation of the applied voltage and pulse-width. Adjustment of the nozzle-substrate distance allows similar control, however reducing the nozzle offset was found to increase the variation in droplet size. This behaviour is likely due to reduced variation in the magnitude of the electric field caused by misalignments in the motion platform. Deposition at offsets of 3 mm allowed consistent deposition without excessive voltage requirements.

The limited spatial resolution (minimum deposit diameter ≈500 μm) can be attributed to both the nozzle size (160 μm ID) and spreading of the elastomer when it impacts the surface. The contact angle between the elastomer drop and the substrate was found to be 1.2° degrees (Figure S1, Supporting Information). The minimum volume of the droplets presented here are estimated to be ≈800 pL by assuming constant volume during deposition and curing. Although larger than traditional inkjet printing processes, this represents a significant increase over minimum volume when compared to DIW.[26] Furthermore, since no significant instances of nozzle blocking occurred, this could likely be reduced with smaller nozzles in subsequent studies; however, for the film-based devices targeted in this work, the trade-off between manufacturing speed and resolution needs to be considered.

Reducing the spacing between consecutive droplets allows the production of confluent features. A droplet overlap of approximately 40% (Figure S2, Supporting Information) represented a suitable balance when trying to maintain line width and height, while minimizing the gaps within the films. Ejecting droplets in close proximity under a DC field led to charge repulsion in the deposit when attempting to produce films. This manifested itself in the production of dendrites or fingers that reduced edge resolution (Figure 1div). By switching the polarity of consecutive pulses, charge accumulation was avoided and edge definition improved. The polarity of the applied pulse was found to have minimal effect on droplet volume (Figure S3, Supporting Information) when compared to the magnitude.

Patterning multiple inks to produce more functional devices can introduce challenges caused by the interactions of materials. The low porosity and surface energy of PDMS, coupled with the relatively high surface tension of aqueous inks, often leads to limited material wetting and adhesion. These hurdles are more apparent for conductive inks where additives to promote adhesion can have a detrimental effect on the functionality of the deposit.

To encourage adhesion, spreading, and the production of confluent features, PDMS was exposed to an oxygen plasma surface treatment to increase the surface energy of the substrate. The sessile drop imaging technique was used to provide an indication of the efficacy of the plasma treatment and to understand the effect of exposure time on material wetting. An exposure time of six seconds was used to treat the PDMS samples since further exposure had minimal effect on the contact angle and excessive exposure can lead to surface oxidation.

AJ printing is a contactless deposition technique originally developed for the deposition of high-resolution conductive circuitry. Recent reviews of the technique have focused on the underlying deposition mechanism[27] and applications of the process.[28] In this work the process is used to provide reliable, selective patterning of a commercially available graphene ink on to the surface of the e-jet printed elastomers, which builds on previous work in printed sensors for soft robotics through greater conductivity.[15]

In AJ, a functional ink is atomized, suspended within a carrier gas, and directed at a substrate that can then be articulated with respect to the deposition head to achieve spatial patterning. By combining an effective focusing mechanism with the production of uniform aerosol, AJ can produce deposits with resolutions approaching 20 μm.

For AJ, a Collison atomizer was used to produce the aerosol from the bulk ink. Residual pressure drives the aerosol from the atomization chamber, through a virtual impactor, and towards the deposition head. The virtual impactor refines the aerosol by removing droplets with insufficient inertia to be impacted on the substrate. At the deposition head, the aerosol is focused by introducing and annular sheath gas in combination with a physical nozzle (**Figure 2**a). As such, controlling the geometry of AJ printed features requires consideration of the nozzle speed and geometry, relative gas flow rates (focusing ratio), and the evaporation characteristics of the ink.

Deposition from nozzle heights of 1–3 mm produced consistent features with a moderate focal point at ≈2 mm (Figure 2b). From distances of 3–8 mm, the maximum height of printed traces decreased from 0.25 to 0.05 μm and the FWHM increased from ≈100 μm to over 450 μm; therefore, showing a loss of aerosol jet collimation at elevated print heights. The quality ratio, a comparison between the subjective maximum width of the line and the FWHM (Figure S4–S6, Supporting Information), supports this since deposition at 1 mm reliably produced the highest quality features.

Increasing nozzle velocity led to small changes to the width and height (Figure 2c) that can be attributed to the normal distribution of droplets in the aerosol stream leading to increased height growth at the center of the line when compared to the edges. At high print speeds, the maximum height of the line is comparable to the magnitude of overspray, therefore the line quality appears higher as the FWHM approaches the maximum line width.

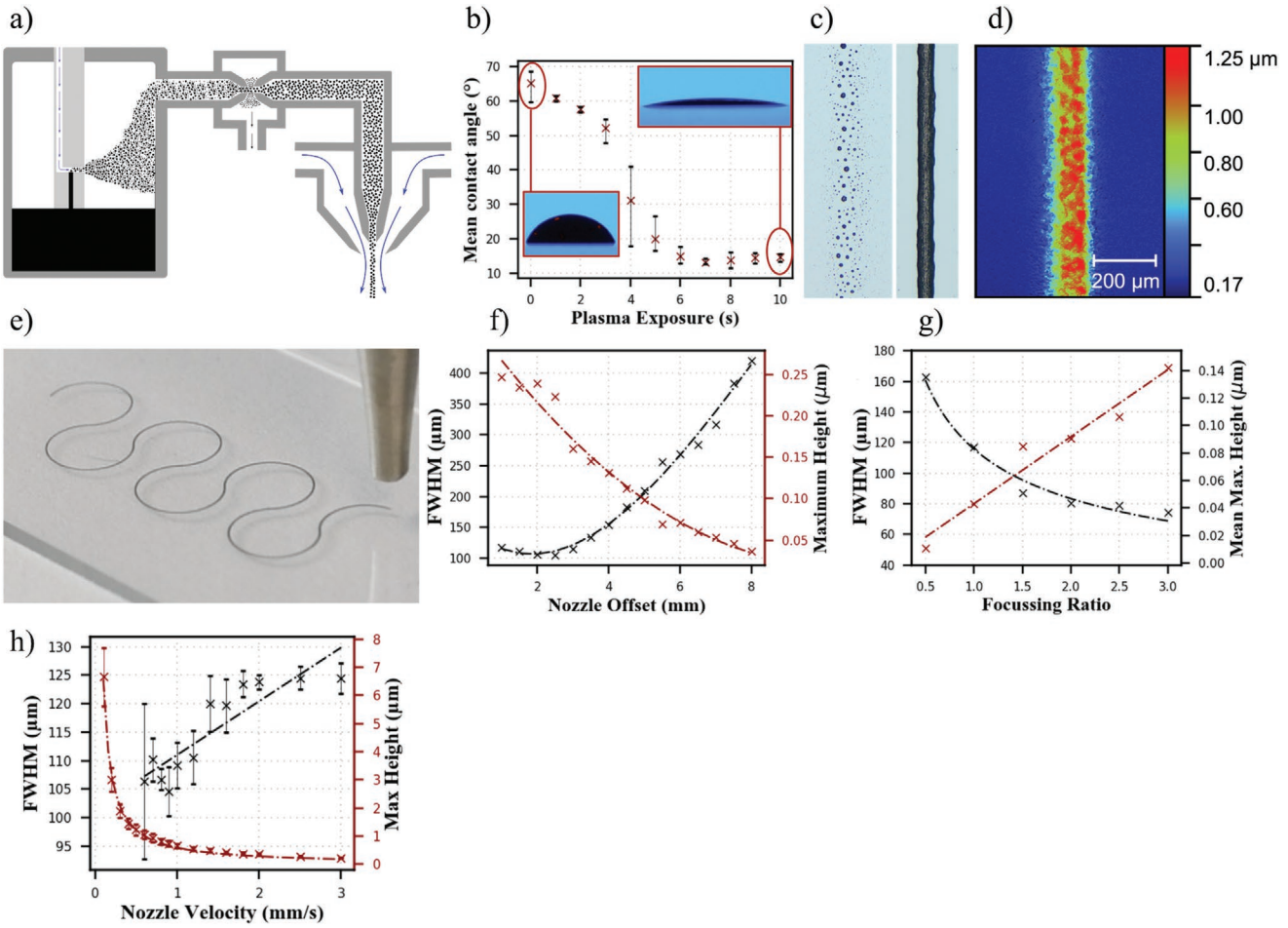

Figure 2. a) Schematic of the aerosol jet process, b) effect of oxygen plasma exposure time on the contact angle between graphene ink and PDMS, c) printed feature on PDMS before and after plasma treatment, d) surface profile of a AJ printed trace, e) image of AJ deposition on glass, f–h) the effect of nozzle offset, focussing ratio, and nozzle velocity on the full width at half maximum height (FWHM) and peak feature height, respectively.

The focusing ratio, defined as the ratio of the sheath gas flow to the atomizer flow, was found to have the inverse relationship to the nozzle height and velocity (Figure 2f). Through manipulation of the focusing ratio, the FWHM and line height could be varied from 50–160 µm and 0.01–0.14 µm, respectively.

For conductive traces, high aspect ratio features are typically targeted as they allow low resistivity at greater trace densities. This is more evident in stretchable conductive sensors as the aspect ratio has a direct effect on the stress present in serpentine, patterned stretchable features. As can be seen in **Figure 3**, the print process should target low-velocity, high focusing ratio, and moderate-to-low stand-off heights within a processing window that produces sufficient line quality (Figure S4–S6, Supporting Information).

Our previous work has shown how high-strain could be achieved at the expense of conductivity.[15] The use of a graphene nanoplatelet ink provides significantly greater conductivity (62.6 Ω sq^{-1}) at the expense of strain tolerance. Through considered design, stress can be minimized to enable moderate strains from relatively stiff electrode material.

The production of free-standing soft films required separation of the PDMS-graphene structure from the underlying substrate. This introduced additional challenges due to tearing or deformation of the films. For soft films, this is particularly challenging as they have low tensile strength when compared to rigid polymer or metallic materials. Simple mechanical removal was found to tear films, especially when separating thin devices that consisted of a low number of layers. To overcome this, a thin sacrificial layer (<1 µm) of polyvinyl-alcohol was spin coated on to the substrates prior to deposition. This layer could then be dissolved in a heated ultrasonic bath following printing to release the film.

Combining the sacrificial support with E-Jet printing, plasma treatment, and aerosol jet printing to produce a single devices creates opportunities for soft films with integrated functionality. A proof-of-concept, five-layer structure consisting of three layers of PDMS with two electrode layers was produced (Figure 3). With electrode and PDMS layers of 3 and 65 µm, respectively, the final thickness of the device was approximately 200 µm and had a surface roughness of ≈0.26 µm (Sa) measured over a 2 mm^2 surface area. In this particular early demonstrator, the surface roughness was impacted by atmospheric dust ingress during manufacture, while higher film thicknesses were targeted for improved process reliability at this experimental

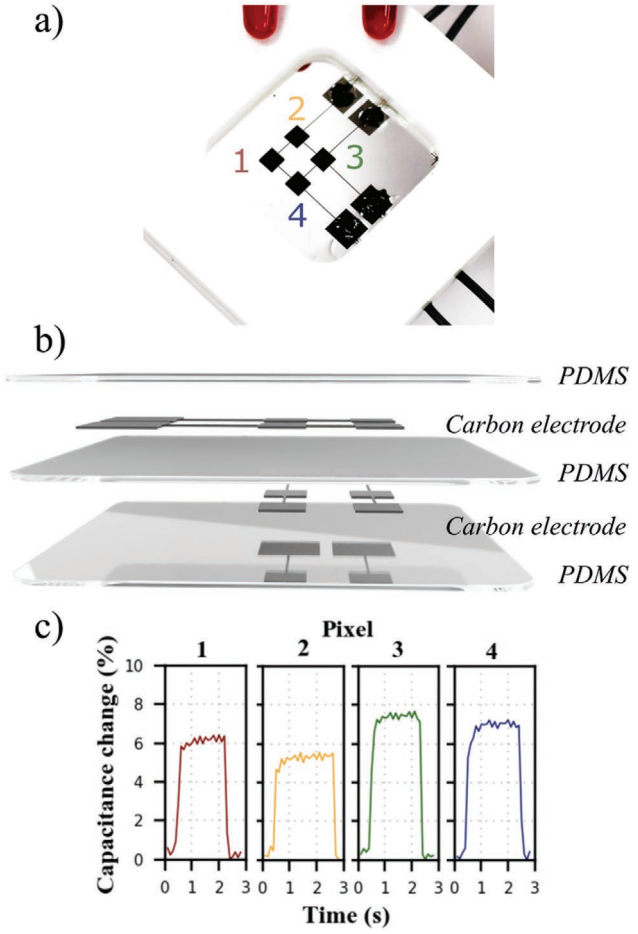

Figure 3. a) Five-layer, four-pixel printed sensor mounted within an acrylic frame, b) CAD explosion of the sensor design, and c) response of each pixel in response to touch.

stage. Electrical connection was made using a carbon grease in combination with cyanoacrylate for strain relief. This resulted in a four-pixel capacitive senor that exhibited a 5–8% change in response upon touch. Subjectively, limited strain tolerance was observed in these early devices, however on-going research to quantify the response, improve materials, and evaluate application specific performance is being enabled by the process and will form the basis of future communications. Although conceptually simple, this first demonstrator shows the value in an integrated, hybrid, and digitally driven approach that is tolerant of inks with disparate rheology for the manufacture of functional soft devices.

We present a new approach that combines alternating current electro-hydrodynamic deposition of high viscosity, low-conductivity elastomer films with aerosol direct write of conductive traces to overcome rheological constraints of the respective processes. Using electrically forced jets, this approach overcomes challenges in nozzle blocking usually associated with the direct write of thin elastomeric films. Droplet sizes of approximately 800 pL were achieved during this work resulting in feature thicknesses of 5 µm using a 160 µm ID nozzle. Reduction of the nozzle diameter, and improved control of the material flow, presents a pathway to higher resolution patterning. By integrating a complimentary direct write technique with EHD, we demonstrate a digitally driven, hybrid manufacturing process that enables the automated manufacture of soft, functional film-based devices.

Experimental Section

Substrate Preparation: Square substrates (50 × 50 mm) were prepared from 300 × 300 sheets of 125 µm polyethylene terephthalate (PET) (Goodfellow, UK). Polyvinyl alcohol (PVA, MP Biomedicals) mixed with deionised water at 3 wt% and left to stir for at least 48 h. A layer was then spin coated on to the PVA sheets at 500 RPM for 60 s. Dissolution was achieved by leaving the printed structures in an ultrasonic bath at 80 °C.

Electrohydrodynamic Printing: The silicone elastomer, Sylgard 1-4128 (Dow Corning, USA), was prepared by mixing part A and B in a ratio of 10:1 in a planetary mixer degasser (Thinky ARE-310, Intertronics, UK). This variant of Sylgard was selected for its long pot life and rapid curing at elevated temperatures. Once prepared, the material was loaded in to a ten milliliter syringe and secured in to a syringe pump (Harvard Precision Instruments, USA). Using luer-lock connections, the syringe was attached to a 30-gauge (OD: 310 µm, ID: 160 µm) stainless steel blunt nozzle by a length of Tygon tubing. The nozzle was then mounted to the deposition head before deposition. Voltage was applied to the nozzle using a high voltage amplifier (20/20C-HS, Trek, USA) in combination with a function generator (AFG2021, Tektronix, USA). PDMS was cured using a hot plate at 105 °C for 5 min. All deposition was conducted on bespoke apparatus designed and constructed for this work. Post-print, nozzles were flushed using ethyl acetate and deionized water to remove any remaining material. Blocked nozzles were cleared through mechanical removal with fine gauge needles.

Aerosol Jet Printing: Samples were exposed to a bulk oxygen plasma treatment for six seconds to increase wettability (Plasma Etch, USA). They were then mounted to a deposition stage (Thorlabs, USA) heated to 120 °C to encourage solvent evaporation. 50 mL of a commercially available graphene nanoplatelet ink (500 nm platelets in an aqueous suspension with ≈1% PEDOT:PSS, viscosity: 10 cP) (CAMINK IJ3, Cambridge Nanosystems, UK) was loaded in to the pneumatic atomizer, held at 30 °C, and stirred continuously at 200 rpm. Three layers were aerosol jet printed (Optomec, USA) for each electrode to improve conductivity. Flow rates of 400 and 200 sccm were used for the atomizer and sheath, respectively. Substrate actuation was conducted on bespoke apparatus.

Metrology: 3D measurements of elastomer droplets and printed electrodes were acquired using white light interferometry (NP Flex, Bruker, USA). This data was used to determine the volume and contact angle of deposits. Four cross sections were taken and an average used to determine the contact angle (Figure S1, Supporting Information). Since no solvents were used, and PDMS had a low shrinkage (≈1%), the droplets were assumed to have approximately equal values to the deposit. For AJ printed traces, the full width at half maximum was used as an objective measure of track width. Optical microscopy (Olympus BX53M) was used for 2D measurements. Conductivity of samples was measured using four-point probing (Jandel, UK). Contact angle measurements of the conductive graphene platelet ink on PDMS substrates were taken using a goniometer (Ossila, UK) through the sessile drop technique. This approach was used over white light since the contact angles were much larger and more prone to variance over time due to solvent evaporation.

Capacitive Sensing: Connections to the sensor were achieved using carbon grease (MG Chemicals, USA), in combination with an acrylic frame and cyanoacrylate (3M, UK) for strain relief. A thicker layer of PDMS was cast before removal from the PET film to protect the sensor an increase mechanical robustness. Measurements were taken using a capacitance-to-digital converter development board (AD7746, Analog Devices, USA) and verified using a calibrated multimeter (Keithley

2110, USA). Since the development board had a single input, pixel selection and cycling was achieved by combining an Arduino Mega with a multiplexer (CD74HC4067, Sparkfun, USA). This approach allowed readings to be taken with a frequency ≈100 Hz.

Supporting Information

Supporting Information is available from the Wiley Online Library or from the author.

Acknowledgements

The authors kindly acknowledge the support of the Engineering and Physical Sciences Research Council (EPSRC) through grants EP/M026388/1, EP/L02067X/2, and EP/P027687/1.

Conflict of Interest

The authors declare no conflict of interest.

Keywords

aerosol jet, fabrication, hybrid manufacturing, soft robotics

Received: February 21, 2020
Revised: March 19, 2020
Published online:

[1] M. Cianchetti, C. Laschi, A. Menciassi, P. Dario, *Nat. Rev. Mater.* **2018**, *3*, 143.
[2] H. Zhao, A. M. Hussain, A. Israr, D. M. Vogt, M. Duduta, D. R. Clarke, R. J. Wood, *Soft Robot.* **2020**, https://doi.org/10.1089/soro.2019.0113.
[3] M. Imboden, E. de Coulon, A. Poulin, C. Dellenbach, S. Rosset, H. Shea, S. Rohr, *Nat. Commun.* **2019**, *10*, 834.
[4] A. Atalay, V. Sanchez, O. Atalay, D. M. Vogt, F. Haufe, R. J. Wood, C. J. Walsh, *Adv. Mater. Technol.* **2017**, *2*, 1700136.
[5] K. Xu, Y. Lu, K. Takei, *Adv. Mater. Technol.* **2019**, *4*, 1800628.
[6] S. Rosset, H. R. Shea, *Appl. Phys. Rev.* **2016**, *3*, 031105
[7] P. Lotz, M. Matysek, H. F. Schlaak, *IEEE/ASME Trans. Mechatronics* **2011**, *16*, 58.
[8] H. Zhao, A. M. Hussain, M. Duduta, D. M. Vogt, R. J. Wood, D. R. Clarke, *Adv. Funct. Mater.* **2018**, *28*, 1804328.
[9] S. Rosset, O. A. Ararom, S. Schlatter, H. R. Shea, *J. Visualized Exp.* **2016**, *108*, 53423.
[10] A. Poulin, S. Rosset, H. R. Shea, *Appl. Phys. Lett.* **2015**, *107*, 244104.
[11] F. M. Weiss, T. Töpper, B. Osmani, S. Peters, G. Kovacs, B. Müller, *Adv. Electron. Mater.* **2016**, *2*, 1500476.
[12] R. L. Truby, M. Wehner, A. K. Grosskopf, D. M. Vogt, S. G. M. Uzel, R. J. Wood, J. A. Lewis, *Adv. Mater.* **2018**, *30*, 1706383.
[13] D. McCoul, S. Rosset, S. Schlatter, H. Shea, *Smart Mater. Struct.* **2017**, *26*, 125022.
[14] A. D. Valentine, T. A. Busbee, J. W. Boley, J. R. Raney, A. Chortos, A. Kotikian, J. D. Berrigan, M. F. Durstock, J. A. Lewis, *Adv. Mater.* **2017**, *29*, 1703817.
[15] N. J. Wilkinson, M. Lukic-Mann, M. P. Shuttleworth, R. W. Kay, R. A. Harris, in *2019 2nd IEEE Int. Conf. on Soft Robotics (RoboSoft)*, IEEE, Seoul, Korea (South) **2019**, pp. 496–501.
[16] E. Bihar, T. Roberts, E. Ismailova, M. Saadaoui, M. Isik, A. Sanchez-Sanchez, D. Mecerreyes, T. Hervé, J. B. De Graaf, G. G. Malliaras, *Adv. Mater. Technol.* **2017**, *2*, 1600251.
[17] M. S. Onses, E. Sutanto, P. M. Ferreira, A. G. Alleyne, J. A. Rogers, *Small* **2015**, *11*, 4237.
[18] J.-U. Park, M. Hardy, S. J. Kang, K. Barton, K. Adair, D. K. Mukhopadhyay, C. Y. Lee, M. S. Strano, A. G. Alleyne, J. G. Georgiadis, P. M. Ferreira, J. A. Rogers, *Nat. Mater.* **2007**, *6*, 782.
[19] A. Lee, H. Jin, H. W. Dang, K. H. Choi, K. H. Ahn, *Langmuir* **2013**, *29*, 13630.
[20] J. Xue, J. Xie, W. Liu, Y. Xia, *Acc. Chem. Res.* **2017**, *50*, 1976.
[21] A. Jaworek, A. T. Sobczyk, A. Krupa, A. Marchewicz, A. K. Krella, T. Czech, *Int. J. Plasma Environ. Sci. Technol.* **2016**, *10*, 29.
[22] S. N. Jayasinghe, M. J. Edirisinghe, *J. Aerosol Sci.* **2004**, *35*, 233.
[23] S. N. Jayasinghe, M. J. Edirisinghe, *Appl. Phys. Lett.* **2004**, *85*, 4243.
[24] F. M. Weiss, T. Töpper, B. Osmani, H. Deyhle, G. Kovacs, B. Müller, *Langmuir* **2016**, *32*, 3276.
[25] L.-F. Ren, F. Xia, J. Shao, X. Zhang, J. Li, *Desalination* **2017**, *404*, 155.
[26] Y.-L. Sung, J. Jeang, C.-H. Lee, W.-C. Shih, *J. Biomed. Opt.* **2015**, *20*, 047005.
[27] E. B. Secor, *Flexible Printed Electron.* **2018**, *3*, 035002.
[28] N. J. Wilkinson, M. A. A. Smith, R. W. Kay, R. A. Harris, *Int. J. Adv. Manuf. Technol.* **2019**, *105*, 4599.

12 Appendix E

N. J. Wilkinson, M. Lukic-Mann, M. P. Shuttleworth, R. W. Kay and R. A. Harris, "Aerosol Jet Printing for the Manufacture of Soft Robotic Devices," 2019 2nd IEEE International Conference on Soft Robotics (RoboSoft), Seoul, Korea (South), 2019, pp. 496-501. DOI: 10.1109/ROBOSOFT.2019.8722766

2019 2nd IEEE International Conference on Soft Robotics (RoboSoft)
COEX, Seoul, Korea, April 14-18, 2019

Aerosol Jet Printing for the Manufacture of Soft Robotic Devices

Nathan J. Wilkinson, *Student Member, IEEE*, Maria Lukic-Mann, Matthew P. Shuttleworth, Robert W. Kay, and Russell A. Harris

Abstract— **Soft robotics is a fast growing field of engineering where there are significant opportunities to realize new forms of actuation and sensing. However, there is also a challenge to translate some of the lab-based developments into a robust industrial manufacturing process. Linked to this is also the opportunity to create new forms of functionality in soft robotic devices by employing a flexible, digital manufacturing process for their creation. Overcoming these hurdles, and unlocking the possibilities for greater functionality, is likely to be a key enabler for wider applications and adoption of soft robotics in practical applications. We present a system of computer-controlled Aerosol Jet Printing that will enable complex soft robotic structures to be manufactured. The process is demonstrated through the deposition of a carbon-based conductive ink on to elastomeric substrates for high resolution, conformal and multi-layer patterning. Functional demonstrators, in the form of a dielectric elastomer actuator and strain sensor, are produced to showcase the potential of the technique.**

I. Introduction

The translation of soft robotic devices from laboratory demonstrators to real world applications will require significant innovation in design, control and materials science [1]. One of the key drivers in addressing these will be the development of manufacturing processes that enable freeform manufacture and improved functionality[2]. Techniques that remove the geometric limitations of the casting, molding and soft lithographic techniques often used in soft robotics will allow promising design approaches, such as algorithmic design, to be applied without restriction [3]. Improvements in control can be realized through in-situ manufacture of sensors that allow a greater degree of proprioception and environmental awareness for closed-loop operation [4]. Furthermore, we are able to extend the range of materials to create soft robotic structures through manufacturing processes which do not have inherent rheological constraints.

Much of the pioneering work within soft robotics was conducted with manual fabrication and assembly techniques. While they may not hamper low-volume experimental work, it is appreciable that these have restrictions when considering translation towards effective manufacture. These methods would prove to be prohibitively expensive and lack the repeatability required for commercialization at greater scales. Consequently, research groups have begun investigating digitally-driven, automated fabrication techniques to address these problems while also presenting opportunities for increased geometric freedom, mass customization, tool-less manufacture, and decreasing the size scales at which soft robots can be produced.

Early examples used commercially available additive manufacturing equipment to produce soft robotics [5], [6] and, despite material limitations, illustrated the potential of the approach. Techniques capable of depositing the materials usually associated with soft robotics, such as silicone rubbers, soon followed [7], [8]. However, methods that can functionalize soft structures through the printing of sensors, electronics or even catalysts are significantly less prevalent.

Some techniques have begun to illustrate the value that resides in different process approaches [9]. For example, the EMB3D technique, which prints both fugitive and functional inks within an uncured elastomer, was recently used to produce a pneumatic actuator capable of sensing inflation, curvature, contact and even temperature [10].

The development of hybrid manufacturing approaches that combine the material and geometric capabilities of different processes show the most promise [11], [12]. The technique demonstrated here uses Aerosol Jet Printing (AJP) to deposit a functional ink on to the surface of pre-cured elastomer substrates. In addition to the aforementioned arguments for translation to effective manufacturing, the use of this jetting technique provides an opportunity for the soft robotics community to explore new possibilities in terms of design and material composition. As a functionalization technique AJP has a number of advantages: it is compatible with ink viscosities of 1-1000cp [13]; can deposit at distances of 1-5mm from the surface of the substrate [14]; and can produce features ranging from microns to millimeters. Furthermore, the relative independence of the deposition mechanism and substrate mean that AJP is compatible with both existing and emerging strategies for the production of soft robotics.

This paper showcases AJP through the deposition of a stretchable conductive ink on to soft structures. High resolution, conformal and multi-layer patterning are demonstrated; as well as functional components in the form of dielectric elastomer actuators (DEA) and strain sensors. This first application lays the ground work for future manufacturing processes that combine AJP surface

* This research is funded by the Engineering and Physical Sciences Research Council (EPSRC) through grants EP/M026388/1 and EP/L02067X/2

N. J. Wilkinson, M. Lukic-Mann, M. P. Shuttleworth, R. W. Kay and R. A. Harris are members of the Future Manufacturing Process Research Group, University of Leeds, LS2 9JT, United Kingdom (e-mail: mnnjw@leeds.ac.uk)

functionalization with other additive techniques for the integrated, push-button manufacture of soft robotic devices.

II. Aerosol Jet Printing

AJP emerged from DARPA's Mesoscale Integrated Conformal Electronics program that aimed to develop technologies capable of printing circuitry on almost any surface. The capabilities of AJP printing have been widely documented for printed electronics through the production of conformal antenna [15]; interconnects [14]; and even electrical componentry, such as OLEDs [16] and transistors [17]. Colloids, solutions and multi-part materials with viscosities ranging from 1-1000cp have been proven to be compatible with the AJP process, which has made it a major driver behind printed electronics research.

Fundamentally, the process does not differ significantly from any aerosol-based process: a functional ink is suspended in a carrier gas, which is then directed at a substrate that can be articulated relative to the nozzle to produce the desired geometry. More uniquely, high resolution is achieved through the production of a consistent aerosol in combination with an effective focusing mechanism (Figure 1). Depending on the viscosity of the ink, the aerosol can be produced using either ultrasonic (1-10cp) or pneumatic atomisation (10-1000cp). Ultrasonic atomisation produces a series of standing capillary waves at the ink-gas interface. Once these are of sufficient magnitude, they begin to eject droplets in to the carrier gas flow. This approach to atomisation produces a monodisperse aerosol that is suitable for printing.

In contrast, the pneumatic atomizer produces an aerosol with much higher dispersity by using a high-speed gas flow to draw ink from a reservoir. The liquid ink is then sheared to form discrete droplets that are suspended in the carrier gas to form an aerosol. As a result of this high force approach to atomisation, a refinement step is required to produce a printable aerosol. Virtual impaction, a process that splits aerosol streams based on the inertia of the droplets, is required to remove droplets with insufficient inertia for impaction on the substrate.

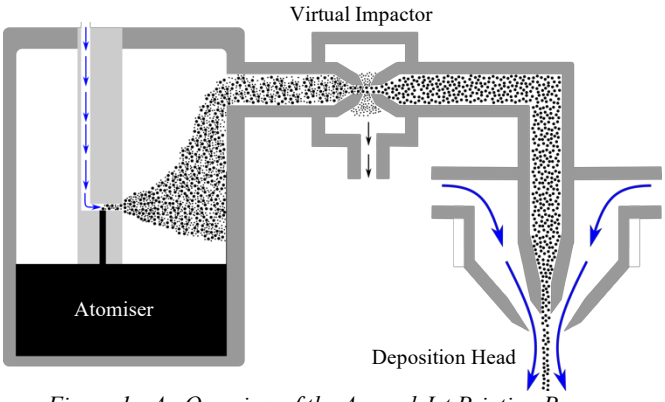

Figure 1 - An Overview of the Aerosol Jet Printing Process

The focusing and deposition of the aerosol is achieved using a combination of a virtual and physical nozzle. The physical nozzle is the predominant factor in determining the scale of the printed feature, with 100μm being the smallest available nozzle. Further focusing can then be accomplished using the virtual nozzle to achieve deposits approaching 10μm [18], [19]. This secondary focusing method works by surrounding the aerosol stream with a sheath gas that both reduces the diameter of the aerosol stream and collimates the aerosol flow. Not only does this improve process resolution, the use of a sheath gas reduces the instances of nozzle clogging as the ink rarely contacts any side walls; enables consistent deposition at stand-off heights of 1-5mm; and allows in-process modification of the effective nozzle diameter by altering the gas flow ratios. These attributes combine to provide a unique opportunity to embed complex actuation, sensing and circuitry within soft robotic devices.

III. Manufacture

This work focusses on the deposition of a carbon-based conductive ink on to three commonly used silicone and acrylic elastomer substrates: Sylgard 184, Elastosil P7670 and 3M VHB 4910. A number of materials were tested to ensure the developed process would be compatible with existing soft robotics materials. The silicone elastomers were processed using both spin coating and casting techniques, while VHB 4910 was purchased as a sheet that was cut and pre-stretched. The strain sensor was manufactured using Elastosil P7670 and the DEA was produced using VHB4910 (3:1 prestrain). All other demonstrators were produced using Sylgard 184 as it has an increased pot life.

All substrate materials were prepared as per the manufacturer's instructions (Sylgard 184, 10:1 & Elastosil P7670, 1:1) and placed in a planetary mixer degasser (Thinky ARE-250) to ensure sufficient mixing and removal of air bubbles. For the cast substrates, the liquid elastomer was then poured in to molds produced using stereolithography (SLA, Formlabs), which were then placed in an oven to ensure the elastomers were sufficiently cured. The final geometry of the strain gauge was achieved by laser cutting the silicone elastomer (Epilog Mini 50W, Epilog Laser, UK)

For spin coating, glass slides were dip-coated in PVA (3%wt aqueous solution) to act as a release layer for the elastomer. The glass slides were then placed in to a spin-coater (SPS, Spin200i, Germany) and a small volume (5ml) of the liquid elastomer was placed on the center of the substrate. Spin coating of elastomeric materials is typically carried out for relatively long times at low speeds, with an initial slow spin to aid in spreading the elastomer. For this process, the elastomer was spun at 1200rpm for 480 seconds. Measurements taken using white-light interferometry (Bruker NPFlex) showed the spin coated elastomer films to have a thickness of approximately 4μm.

Following the manufacture of the base substrates, the silicone elastomers required modification of the surface energy to improve wetting of the printed inks through an oxygen-plasma surface treatment (Plasma Etch, USA). As well as improving wetting characteristics, this approach can enable effective bonding of silicone elastomer structures, as has been recently demonstrated in the field of soft robotics [20].

AJP was achieved through pneumatic atomisation and jetting through a 3mm slotted nozzle for all samples except the high resolution, multilayer device, which was produced using a 300μm circular nozzle. The slotted nozzle allowed increased material flow rates and decreased printing times at the expense of resolution. Toolpaths and G-Code generation for all of the printed deposits was produced from DXF design files using an in-house tool-path generation software designed for continuous printing.

A. Characterization of Printed Lines

AJP is able to produce extremely fine layers, which allows soft robotics to be manufactured at smaller size scales. While this does allow for tunable electrical performance; a consequence of the low layer thickness and the relatively low conductivity of most carbon-based conductive inks is the requirement to build up material through sequential layering or increased throughput.

White light interferometry was used to provide a quantitative assessment of a series of deposits produced using a 3mm slotted nozzle (Figure 3). The thinnest and thickest mean layer height measured during these tests were found to be 345nm and 4.36μm for a single pass and 20 passes, respectively. As predicted, the thickness of the deposit appears to increase linearly with the number of passes of the Aerosol Jet print head.

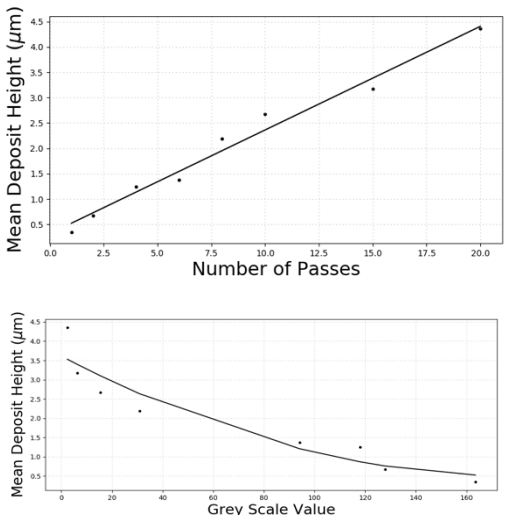

Figure 2 - Mean deposition height of the conductive carbon deposit with an increasing number of passes

Although useful for high resolution quantitative evaluation, interferometry is limited in its use for in-process metrology of the deposit as the time of the scans would severely impact the manufacturing time scales and prohibitively increase machine cost. As a result, assessment using optical microscopy was conducted to investigate its effectiveness at predicting deposition thickness. Image analysis of 80 images showed that mean greyscale was a suitable indicator of both confluency and thickness of the deposit, particularly during the early stages of printing. While limited for highly layered deposits (> 20 layers), this approach shows promise as a relatively simple '*go/no-go*' technique for in-process quality assessment.

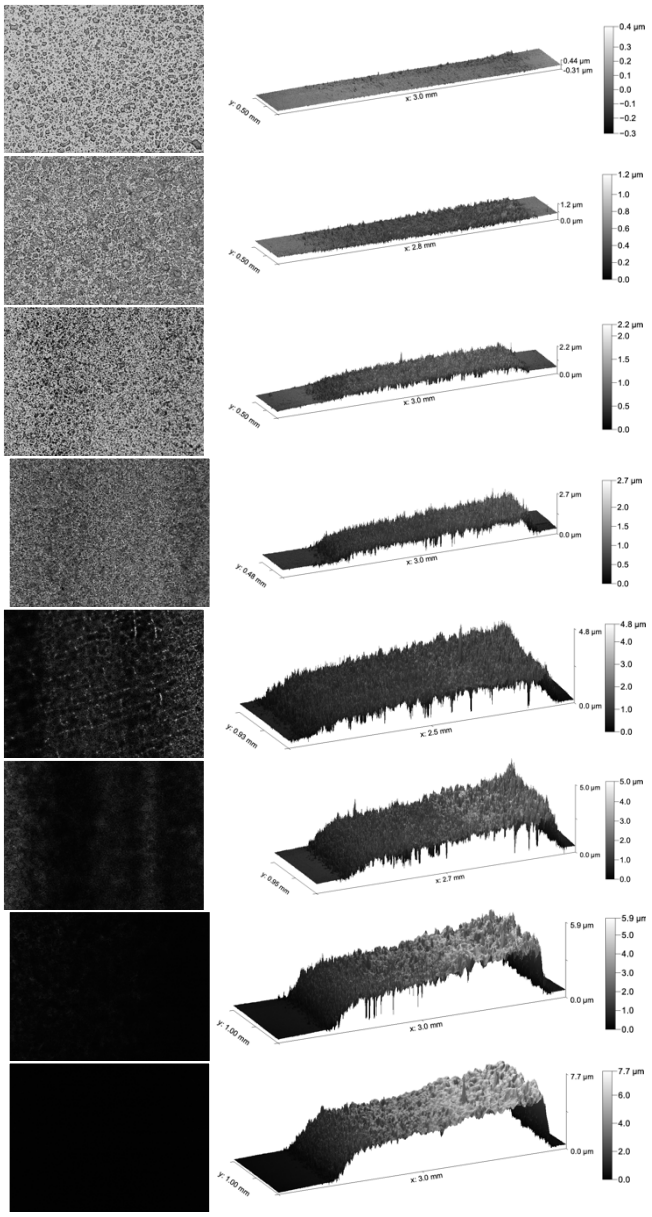

Figure 3 - Optical micrographs and white light interferometry of AJP printed deposits with 3mm slotted nozzle showing changing morphology with increased number of layers

B. High Resolution, Multi-layer Printing

By switching the 3mm slotted nozzle of the Aerosol Jet for a more conventional circular nozzle, it is possible to deposit with high spatial resolution. Using a 300μm nozzle to deposit on to PDMS and glass surfaces, features with an average full width at half maximum (FWHM) height of 25μm where achieved. High variation in line width was observed when printing features on this size, with a 4.3μm standard deviation being observed for the line in Figure 4**.** This has been demonstrated through the production of a 5-layer structure consisting of alternating PDMS and carbon-conductive layers with and overall geometry of 25x75x1mm. The digitally

driven nature of AJP means it is very straightforward to vary the geometry of the printed structure on a layer by layer basis, as compared to template-based techniques. The high spatial resolution presented here presents an opportunity to manufacture intelligent soft robotic systems at smaller size scales. Depositing functional inks at high resolution is attractive for a field that is looking towards miniaturized arrays of imprecise sensors for proprioceptive feedback[11].

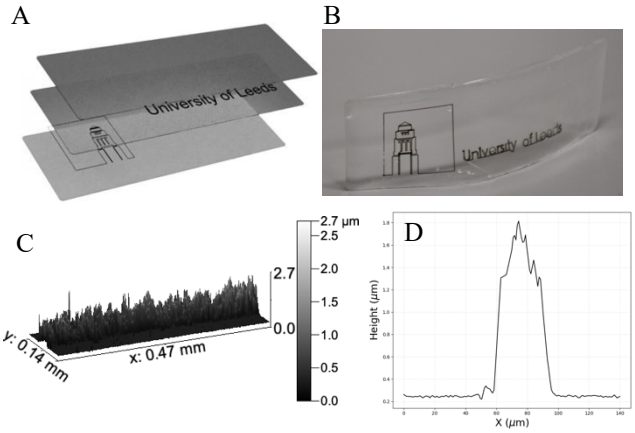

Figure 4 - A) Exploded assembly of multi-layer PDMS and carbon conductive structure, B) Physical part, C) White light interferometry capture of B, D) Typical line profile taken from data in C

C. Conformal Printing

Many direct write, or surface functionalization techniques are reliant on close control of the nozzle substrate distance to achieve consistent deposits. As such, printing on conformal surfaces requires more complex articulation and often imposes geometric limitations when trying to produce toolpaths that track a substrate with non-planar geometry. For example, printing on small concave radii can be difficult owing to bulky deposition heads. However, the ability of AJP to deposit consistently at stand-off heights of 1-5mm presents an opportunity to simplify this by reducing the degree to which the motion of the deposition head needs to replicate the surface. Furthermore, as the nozzle does not need to maintain perpendicularity to the surface, printing on to conformal surfaces can be achieved even with relatively simple 3-axis motion systems (Figure 5). By integrating more complex articulation and toolpath planning it is possible to deposit on to almost any substrate geometry.

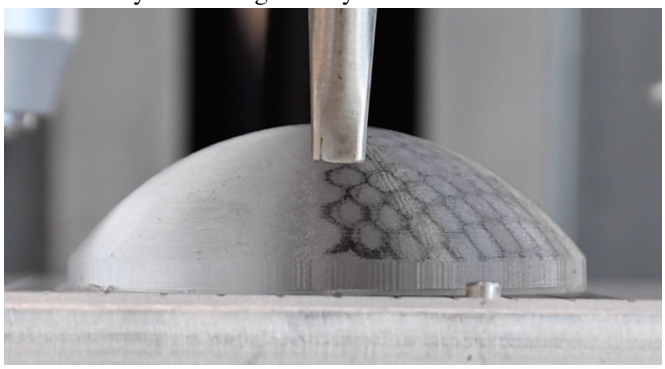

Figure 5 - Aerosol Jet deposit of carbon-based conductive on to a conformal PDMS substrate

IV. Dielectric Elastomer Actuator

Dielectric elastomer actuators were first documented in the late 1990s as an electrically stimulated artificial muscle technology [21], [22]. From this, an entire branch of research has emerged to develop and translate interesting laboratory demonstrators into functional devices. Much of the work in this field has formed around VHB acrylic elastomers owing to their wide availability, relatively low-cost and seemingly high performance. Actuators assembled using this acrylic elastomer have achieved strains exceeding 200% and have been applied to areas as diverse as variable focus lenses [23], audio speakers [24] and haptic feedback devices[25].

A feature of these devices is that the elastomer films require pre-stretch to achieve the highest levels of strains. As a result, the application of electrodes can be challenging as films have a tendency to tear during processing. Furthermore, printing on to the surface of a delicate, suspended film can be challenging for processes that require close control of the nozzle-substrate stand-off. Alternatives to direct write, such as pad printing, have been found to have similar difficulty when depositing on to suspended films[26].

In practice, this means many researchers working with VHB DEAs are still reliant on applying electrodes by hand [27], [28]. AJP provides contactless technique to overcome this challenge as it can provide consistent, high resolution deposits at stand-off heights approaching 5mm. Additionally, as the dielectric elastomer is compressed during actuation, not the conductive itself, the conductive layer should be as thin as possible in order to maximize the overall strain of the device.

To demonstrate this a series of dielectric elastomer actuators were produced (Figure 6) using AJP printing and their strain performance was analyzed using image processing techniques (OpenCV, Nikon D7500, 60fps). The AJP printing process was used to apply electrodes with a diameter of 30mm on the surface of the elastomer film. The DEA was then actuated at voltages ranging from 1kV to 20kV at a frequency of 1Hz using a high-power amplifier (TREK 20/20HS) coupled with a Keithley Function Generator.

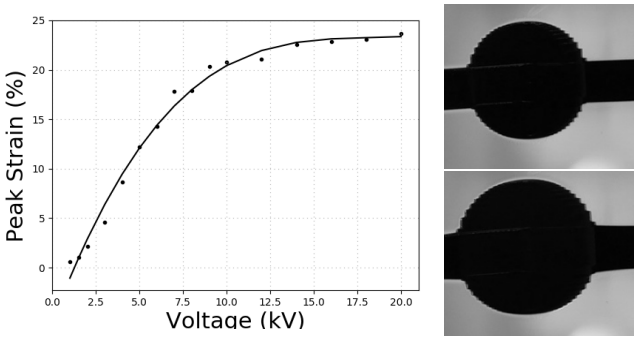

Figure 6 - Strain response of VHB4910 elastomer Actuators with AJP electrodes

As would be expected, strain increased linearly with applied voltage. However, this only occurred up to around 6kV, where the amount of strain began to plateau. At this point, the frequency of actuation was too small relative to the time constant of the actuator. The device was tested up to

audible actuation frequencies of around 6kHz, where it continued to perform successfully.

The performance limitations of the dielectric elastomer actuator can largely be attributed to the relatively high resistance of the electrode material. The charge and discharge time of a dielectric elastomer actuator is dependent on the resistance of the electrodes and capacitance of the device. As such, the performance of the device can be improved by increasing the number of printed conductive layers or transitioning to an ink with higher conductivity. Despite this, the DEA presented here performs comparably to those found in the literature, showing that AJP is a viable and promising technique for printing electrodes in dielectric elastomer actuators.

V. Strain Sensor

Effective techniques for manufacturing soft robots with embedded sensing are appealing to achieve more widespread adoption. Positional feedback is typically centered around resistive [29], capacitive [30], or optical sensing. Optical methods have been developed using both wave guides [31] and vision based tracking techniques [32]. Resistive and capacitive techniques generally rely on geometric deformation to alter the electrical performance.

The simple device presented here (Figure 7A) relies on resistance changes to indicate the degree of strain. During testing the device was strained between 0-140% in 10% increments. The sensor was cycled through each set point 100 times and the strain response plotted in Figure 7B. This test was extended to include 150% strain, however at this point continuity errors begin to present within the sensor. A secondary test was carried out that tested the performance of a sensor over 1000 cycles at a 70% strain set point to evaluate any performance drift over time (Figure 7C). The strain sensor presented here is relatively small in size, with a total length of 20mm and an unstrained thickness of 2mm.

The normalized resistance response was found to be stable for any given value of strain and exhibited near linear performance, particularly for strain values below 60%. However, some challenges remain in both the manufacture and characterization of the strain sensing devices. Firstly, the starting resistance (R_0) of different gauges was found to vary significantly (5-30MOhm). Although the reason for this is yet to be quantified, it is possibly a result of inconsistencies in both the printing and assembly process. Connection between the rigid electrodes and soft elastomer was guaranteed through the manual placement of a small amount of conductive carbon grease, which likely had an impact. It is also expected that the resistance of these devices can be decreased by increasing the volume of deposited material. The data collected above was produced by actuating to a set point, taking a series of measurements, and then returning to the unstrained position. This was then repeated for 100 cycles for each value of strain. As such, hysteresis effects have not yet been characterized.

Future work expects to address some of these challenges through optimization and improvements to the manufacturing methodology. A better transition from the rigid and soft components will likely help overcome some of the challenges with inconsistent values for resistance. Additive approaches present an opportunity for this by printing structures with spatially variable and graded stiffness.

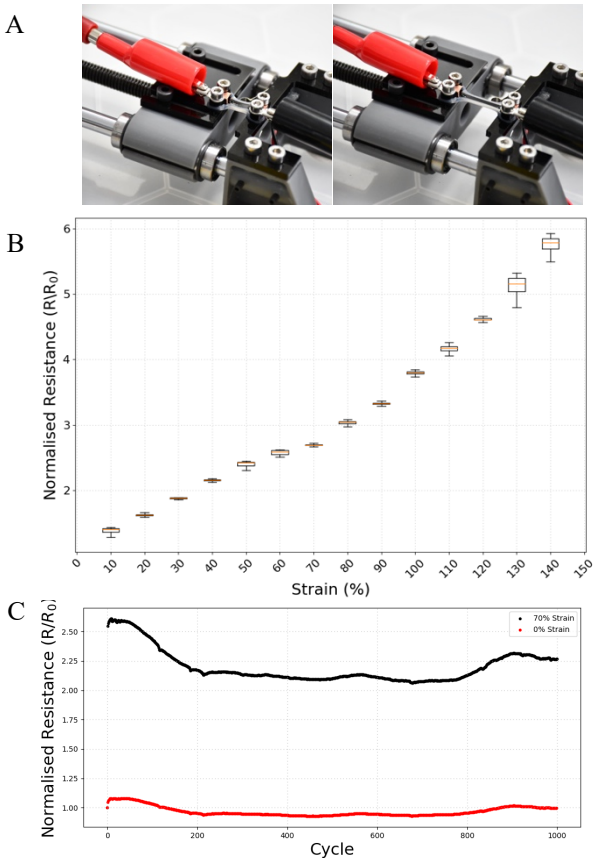

Figure 7 – a) Strain sensor held at 0% and 140% strain b) normalized resistance for 100 readings at various strain set points c) Normalized strain over 1000 cycles at 0% and 70% strain

VI. Conclusion

Aerosol Jet Printing of a carbon-based conductive ink has been demonstrated for embedding functionality within soft robotic devices. This has been illustrated through the creation of a number of devices that highlight the potential impact of AJP in the field of soft robotics.

Inherently digitally driven, the process allows for rapid design changes and layer-by-layer customization of deposit geometry in a way that is difficult or impossible to achieve with conventional template and/or manual processing. This can be realized at resolutions ranging from microns to millimeters, helping to drive the application of soft robotics to challenges at small size scales.

The devices in this research have been produced through the combination of conventional processing (casting, spin coating) and AJP. It demonstrates an opportunity for a hybrid manufacturing approach, in this case by combining surface patterning with additive techniques for the bulk structural geometry. These approaches will enable reliable and repeatable automated manufacture of soft robotics while opening up the possibility for mass customization and

condition monitoring. This has significant appeal across a number of new and high-value applications for soft robotics.

ACKNOWLEDGMENT

This research is funded by the Engineering and Physical Sciences Research Council (EPSRC) through grants EP/M026388/1 and EP/L02067X/2.

REFERENCES

[1] D. Rus and M. T. Tolley, "Design, fabrication and control of soft robots," *Nature*, vol. 521, p. 467, May 2015.

[2] R. L. Truby and J. A. Lewis, "Printing soft matter in three dimensions," *Nature*. 2016.

[3] J. Hiller and H. Lipson, "Automatic design and manufacture of soft robots," *IEEE Trans. Robot.*, 2012.

[4] H. Wang, M. Totaro, and L. Beccai, "Towards Perceptive Soft Robots: Progress and Challenges," *Advanced Science*. 2018.

[5] N. W. Bartlett *et al.*, "A 3D-printed, functionally graded soft robot powered by combustion," *Science (80-.).*, 2015.

[6] T. Umedachi, V. Vikas, and B. A. Trimmer, "Highly deformable 3-D printed soft robot generating inching and crawling locomotions with variable friction legs," in *IEEE International Conference on Intelligent Robots and Systems*, 2013.

[7] T. J. Ober, D. Foresti, and J. A. Lewis, "Active mixing of complex fluids at the microscale," *Proc. Natl. Acad. Sci.*, 2015.

[8] B. N. Peele, T. J. Wallin, H. Zhao, and R. F. Shepherd, "3D printing antagonistic systems of artificial muscle using projection stereolithography," *Bioinspiration and Biomimetics*, 2015.

[9] Y. Yang and Y. Chen, "Innovative Design of Embedded Pressure and Position Sensors for Soft Actuators," *IEEE Robot. Autom. Lett.*, vol. 3, no. 2, pp. 656–663, 2018.

[10] R. L. Truby *et al.*, "Soft Somatosensitive Actuators via Embedded 3D Printing," *Adv. Mater.*, 2018.

[11] T. J. Wallin, J. Pikul, and R. F. Shepherd, "3D printing of soft robotic systems," *Nature Reviews Materials*. 2018.

[12] G.-Z. Yang *et al.*, "The grand challenges of *Science Robotics*," *Sci. Robot.*, 2018.

[13] K. K. B. Hon, L. Li, and I. M. Hutchings, "Direct writing technology-Advances and developments," *CIRP Ann. - Manuf. Technol.*, 2008.

[14] J. A. Paulsen, M. Renn, K. Christenson, and R. Plourde, "Printing conformal electronics on 3D structures with aerosol jet technology," in *FIIW 2012 - 2012 Future of Instrumentation International Workshop Proceedings*, 2012, pp. 47–50.

[15] T. Rahman, L. Renaud, D. Heo, M. Renn, and R. Panat, "Aerosol based direct-write micro-additive fabrication method for sub-mm 3D metal-dielectric structures," *J. Micromechanics Microengineering*, vol. 25, no. 10, p. 107002, Oct. 2015.

[16] J. G. Tait *et al.*, "Uniform Aerosol Jet printed polymer lines with 30 ??m width for 140 ppi resolution RGB organic light emitting diodes," *Org. Electron. physics, Mater. Appl.*, vol. 22, pp. 40–43, 2015.

[17] C. S. Jones, X. Lu, M. Renn, M. Stroder, and W.-S. Shih, "Aerosol-jet-printed, high-speed, flexible thin-film transistor made using single-walled carbon nanotube solution," *Microelectron. Eng.*, vol. 87, no. 3, pp. 434–437, Mar. 2010.

[18] F. Cai, Y.-H. Chang, K. Wang, C. Zhang, B. Wang, and J. Papapolymerou, "Low-Loss 3-D Multilayer Transmission Lines and Interconnects Fabricated by Additive Manufacturing Technologies," *IEEE Trans. Microw. Theory Tech.*, vol. PP, no. 99, 2016.

[19] A. Mahajan, C. D. Frisbie, and L. F. Francis, "Optimization of Aerosol Jet Printing for High-Resolution, High-Aspect Ratio Silver Lines," *ACS Appl. Mater. Interfaces*, vol. 5, no. 11, pp. 4856–4864, Jun. 2013.

[20] T. Ranzani, S. Russo, N. W. Bartlett, M. Wehner, and R. J. Wood, "Increasing the Dimensionality of Soft Microstructures through Injection-Induced Self-Folding," *Adv. Mater.*, 2018.

[21] R. E. Pelrine, R. D. Kornbluh, and J. P. Joseph, "Electrostriction of polymer dielectrics with compliant electrodes as a means of actuation," *Sensors Actuators A Phys.*, vol. 64, no. 1, pp. 77–85, 1998.

[22] R. Pelrine, "High-Speed Electrically Actuated Elastomers with Strain Greater Than 100%," *Science (80-.).*, vol. 287, no. 5454, pp. 836–839, Feb. 2000.

[23] L. Maffli, S. Rosset, M. Ghilardi, F. Carpi, and H. Shea, "Ultrafast all-polymer electrically tunable silicone lenses," *Adv. Funct. Mater.*, vol. 25, no. 11, pp. 1656–1665, 2015.

[24] C. Keplinger, J.-Y. Sun, C. C. Foo, P. Rothemund, G. M. Whitesides, and Z. Suo, "Stretchable, Transparent, Ionic Conductors," *Science (80-.).*, vol. 341, no. 6149, pp. 984–987, 2013.

[25] H. Phung *et al.*, "Interactive haptic display based on soft actuator and soft sensor," in *IEEE International Conference on Intelligent Robots and Systems*, 2017.

[26] S. Rosset and H. Shea, "Towards fast, reliable, and manufacturable DEAs: Miniaturized motor and Rupert the rolling robot," in *Proceedings of SPIE - The International Society for Optical Engineering*, 2015, vol. 9430, no. January.

[27] K. M. Digumarti, C. Cao, J. Guo, A. T. Conn, and J. Rossiter, "Multi-directional crawling robot with soft actuators and electroadhesive grippers," in *2018 IEEE International Conference on Soft Robotics, RoboSoft 2018*, 2018.

[28] A. Fishman, S. Catsis, M. Homer, and J. Rossiter, "Touch and see: Physical interactions stimulating patterns in artificial cephalopod skin," in *2018 IEEE International Conference on Soft Robotics, RoboSoft 2018*, 2018.

[29] J. T. Muth *et al.*, "Embedded 3D printing of strain sensors within highly stretchable elastomers," *Adv. Mater.*, 2014.

[30] M. C. Yuen, R. Kramer-Bottiglio, and J. Paik, "Strain sensor-embedded soft pneumatic actuators for extension and bending feedback," in *2018 IEEE International Conference on Soft Robotics, RoboSoft 2018*, 2018.

[31] H. Zhao, K. O'Brien, S. Li, and R. F. Shepherd, "Optoelectronically innervated soft prosthetic hand via stretchable optical waveguides," *Sci. Robot.*, 2016.

[32] C. Chorley, C. Melhuish, T. Pipe, and J. Rossiter, "Development of a Tactile Sensor Based on Biologically Inspired Edge Encoding," in *International Conference on Advanced Robotics*, 2009.

13 Appendix F

da Veiga, T.; Chandler, J.; Lloyd, P.; Pittiglio, G.; **Wilkinson, N.J.**; Hoshiar, A.; Harris, R.A.; Valdastri, P. 'Challenges of continuum robots in clinical context: a review.' Progress in Biomedical Engineering. DOI: 10.1088/2516-1091/ab9f41

Progress in Biomedical Engineering

Challenges of continuum robots in clinical context: a review

Tomas da Veiga[1], James H Chandler[1], Peter Lloyd[1], Giovanni Pittiglio[1], Nathan J Wilkinson[2], Ali K Hoshiar[3], Russell A Harris[2] and Pietro Valdastri[1]

[1] STORM Lab, School of Electronic and Electrical Engineering, University of Leeds, United Kingdom
[2] School of Mechanical Engineering, University of Leeds, United Kingdom
[3] School of Computer Science and Electronic Engineering, University of Essex, United Kingdom

E-mail: eltgdv@leeds.ac.uk

Keywords: continuum manipulators, soft robots, surgical robots, medical robots, fabrication, magnetic navigation

OPEN ACCESS

RECEIVED
21 January 2020

REVISED
22 May 2020

ACCEPTED FOR PUBLICATION
23 June 2020

PUBLISHED
29 July 2020

Abstract

With the maturity of surgical robotic systems based on traditional rigid-link principles, the rate of progress slowed as limits of size and controllable degrees of freedom were reached. Continuum robots came with the potential to deliver a step change in the next generation of medical devices, by providing better access, safer interactions and making new procedures possible. Over the last few years, several continuum robotic systems have been launched commercially and have been increasingly adopted in hospitals. Despite the clear progress achieved, continuum robots still suffer from design complexity hindering their dexterity and scalability. Recent advances in actuation methods have looked to address this issue, offering alternatives to commonly employed approaches. Additionally, continuum structures introduce significant complexity in modelling, sensing, control and fabrication; topics which are of particular focus in the robotics community. It is, therefore, the aim of the presented work to highlight the pertinent areas of active research and to discuss the challenges to be addressed before the potential of continuum robots as medical devices may be fully realised.

1. Introduction

In the last two centuries, healthcare procedures have changed dramatically. This has been possible due to technological breakthroughs that have enabled the development of new medical devices and techniques [1]. One of the most successful examples is the endoscope. This device allowed surgeons, for the first time in the 19 century, to look into their patients' bodies through natural orifices and wounds as opposed to making fresh incisions [2, 3]. This has impacted screening and intervention, which has also shifted towards less invasive methods and given rise to minimally invasive surgeries (MIS) such as laparoscopy or natural orifice trans-luminal endoscopic surgery (NOTES) [4]. These present several benefits to the patient when it comes to blood loss, recovery time, post-operative trauma, scarring and wound site infection [5]. However, they can be challenging from the surgeons' point of view due to differences in ergonomic control, sensory feedback, dexterity and intuitiveness [6–8].

These limitations and the need for better and improved medical procedures have paved the way to robotically-assisted medical interventions. This has in turn allowed clinicians to perform procedures with more precision, flexibility and control while decreasing procedural times and complications to the patient [9]. Medical robots have come a long way since their inception in the 80 s when a standard industrial robot was used to secure a fixture in place for neurosurgery [10]. The release of the da Vinci Surgical System (Intuitive Surgical, Inc. Sunnyvale, CA, USA) in the early 2000's further heightened the interest in this field. In 2018 more than 1 million procedures worldwide were carried out with the da Vinci system alone [11].

The majority of medical robotic systems in use today rely on rigid instruments with dexterous wrists at the tip. This restricts their movements due to the low number of degrees of freedom (DOF) exhibited [12, 13], hindering the robot's adaptability and safe patient interaction [14]. More recently, continuum robots (CRs) have emerged and are gaining major interest as an alternative to standard rigid-link robots. CRs are able to generate smooth curvilinear motions exhibiting infinite DOFs and, as such, have the potential to reach further into the body with reduced tissue trauma through MIS and NOTES (figure 1) [13]. The use of CRs in medical robotic platforms consequently allows for improvements in existing procedures and the

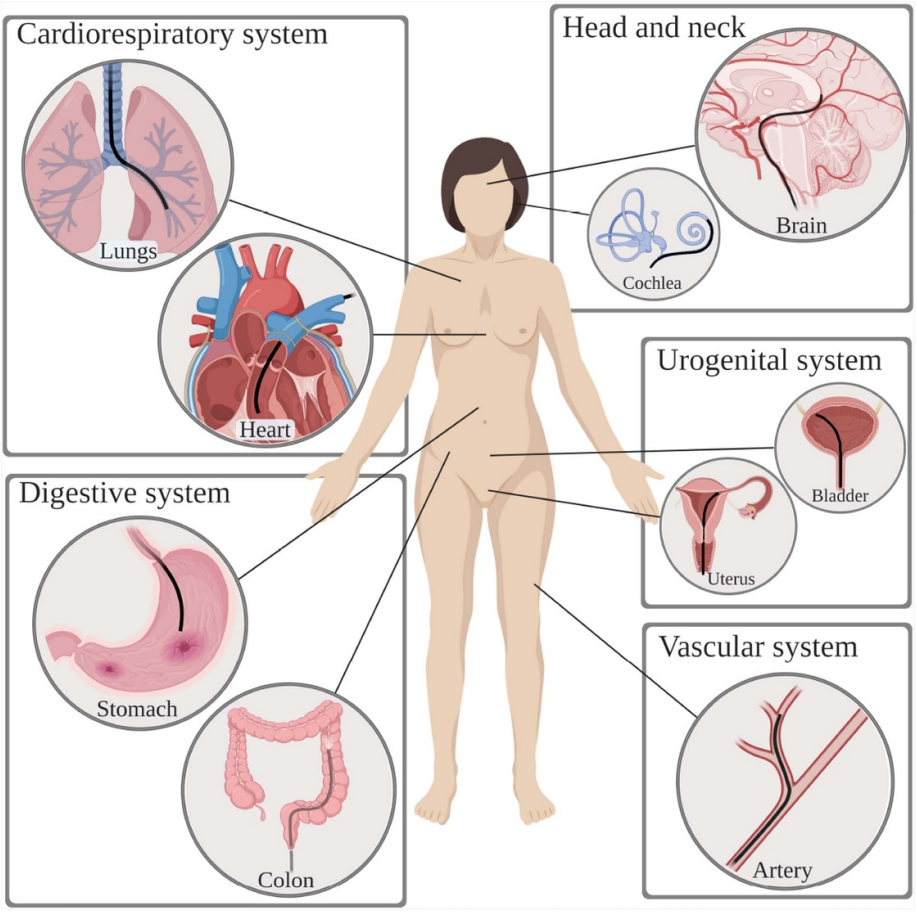

Figure 1. Applications of medical continuum robots to access hard-to-reach areas in a minimally invasive manner. These include the cardiorespiratory system, the digestive system, head and neck, the urogenital system and the vascular system.

development of new and better techniques. This has recently been illustrated by the launch of several continuum platforms such as Monarch™ (Auris Health, Inc. Redwood City, CA, USA) and Ion (Intuitive Surgical, Inc. Sunnyvale, CA, USA).

Despite previous reviews on the topic of medical CRs [15–18], the abundance of attention and development on the topic warrants an updated review. Therefore, in this article we provide an overview of the current challenges that this class of robots face which currently inhibit the realisation of their full potential. We begin the review by presenting the main application areas for medical continuum robots given the current state of the art. We then provide an introduction to the field of CRs followed by an overview of the current actuation methods. We then describe the challenges that these robots face according to their fabrication, modelling, control and sensing; and conclude by providing a comparison between methods and recommendation for future research.

2. Applications of medical continuum robots

2.1. Brain interventions

Open brain surgery is still a common procedure, especially in emergency situations, however MIS has been gaining popularity such as in electrode implantation and endovascular coiling for intracranial aneurysm [19–21]. Since 2010, the robotic system ROSA® Brain (MEDTECH, Inc. Montpelier, France) has been used to perform a variety of these procedures. Lower procedural times and higher accuracy and precision are among its benefits, proving the effectiveness of robot-assisted brain interventions over conventional methods [22].

Most brain procedures (manual or robotic) still employ rigid, straight instruments, limiting the possible paths between the entry point and the target [19]. The use of continuum robotic systems that are able to conform to curvilinear paths will enhance brain MIS; delivering wider freedom to suitable procedures. To this end, some flexible devices, such as magnetic needles [23], have been emerging but remain too stiff to provide increased path freedom.

2.2. Lung interventions

Effective trans-oral bronchoscopy for lung biopsy is a key element in early diagnosis of lung cancer [24, 25]. However, traditional bronchoscopes are restricted to movements only along the lung's bronchial tree limiting procedural efficacy [26]. Continuum robotic systems for a deeper, more consistent and stable bronchoscopy have long been an area of interest. The commercial release of the Monarch™ (Auris Health, Inc. Redwood City, CA, USA) and Ion (Intuitive Surgical, Inc. Sunnyvale, CA, USA) platforms, in 2018 and 2019 respectively, are great examples of systems targeting this need. By using ultra-thin bronchoscopes and catheters, these robotic devices are able to reach further into the lung when compared to conventional bronchoscopes [27–29]. The use of CRs for lung biopsy has resulted in improved control, dexterity and freedom of movement through the airways.

Beyond diagnosis, robotics for treatment of pathologies of the respiratory system has also been emerging; including standard medical robotic platforms alongside newer continuum systems, such as the cable-driven Flex® Robotic System (Medrobotics, Raynham, MA, USA) [30, 31]. However, due to their lack of dexterity and increased size, these systems have thus so far been limited to head and neck interventions [32]. As such, there have been considerable efforts to allow robotic surgery deeper into the trachea and bronchial tree. Indeed, the Virtuoso Surgical (Virtuoso Surgical Inc. Nashville, TN, USA) system recently demonstrated treatment of a central airway obstruction [33] and is an example of progress in this direction

2.3. Endovascular interventions

Continuum structures have long been manually inserted into blood vessels and manipulated to the desired location to treat endovascular and heart conditions in a minimally invasive manner [15]. As can be expected, precise manual catheter navigation and placement is challenging, requiring the surgeon to undergo extensive training. Aligning these existing devices and procedures with robotic navigation and steering is a potential solution to overcome this limitation.

Over the last decade, several robotic navigation and steering systems for guide-wires, stents and catheters have been released, such as Magellan and Sensei (Hansen Medical, Mountain View, CA, USA) and CorPath GRX (Corindus, Inc. Waltham, MA, USA). These systems have been used in a variety of procedures from peripheral vascular to neurovascular interventions [34–40]. Robotic navigation of magnetic catheters has also seen significant progress with systems such as the Stereoaxis Niobe® Robotic Magnetic Navigation System (Stereotaxis, Inc. St. Louis, MO, USA) [41]. These navigation systems, in addition to enabling higher accuracy and precision, are also capable of reducing exposure to radiation and contrast agent for patients and clinicians by being remotely controlled and cutting procedural times [42]. Building on robotic control, autonomous catheter navigation is also now being investigated, however this is still at an early development stage [43].

2.4. Gastroenterological interventions

Currently early screening of cancers of the gastrointestinal (GI) tract is performed via traditional endoscopy or wireless capsule endoscopy (WCE) and, despite their achievements, both methods have their limitations [24, 44–47]. Endoscopes are known to cause tissue damage and discomfort for the patient, whereas WCE lacks active locomotion, tissue interaction and lumen diameter adaptation [46–49].

To this extent, robotic alternatives to these two methods have been reported. Robotically actuated endoscopes are able to improve comfort and reduce pain for the patient by providing an alternative to manual handling and navigation [31, 50, 51]. Robotic alternatives to WCE have mainly focused on achieving active locomotion [52, 53], but ultimately, the capsules' wireless characteristic limits their application to screening only. Additionally, robot assisted GI surgery is common across several procedures, such as removal of liver tumours or the gallbladder, using systems such as the da Vinci [54–57]. Due to the lack of dexterity exhibited by the instruments, open surgery is still the preferred method in some cases. Emerging treatment procedures using continuum micro-robots have been reported, such as the deployment of patches for stomach ulcers [58] or targeted drug delivery [59, 60]. These technologies, however, are still at a very initial development stage.

2.5. Urogenital interventions

Robotic interventions in the urogenital system have long been common for specific procedures such as prostatectomy or nephroureterectomy [61, 62]. However, single-port systems deployable through natural orifices are required to further reduce invasiveness and to treat alternate pathologies. To this extent, a lot of attention has been given to research on continuum robots for urogenital interventions.

Continuum robots to replace rigid resectoscopes used in bladder cancer diagnosis [63, 64], hand-held manipulators for laser prostate surgery [65], or even flexible fetoscopic instruments addressing twin-to-twin transfusion syndrome [66, 67] are some of the proposed devices in the area. However, currently there are no

commercial platforms available. Given the presence of a natural orifice, such as vagina and urethra, the use of continuum robots in this area may deliver several benefits.

3. The rise of continuum manipulators

3.1. Past and present of continuum robots

Traditional robots are composed of discrete rigid links connected by joints and are able to move with high precision and accuracy, making them highly suitable for tightly controlled and repeatable tasks. However, there are often limitations when operating in small and confined spaces where adaptability, dexterity and safe interactions with the patient are necessary [13, 17]. As previously mentioned, the recent coupling of manually steered continuum structures with robotic actuation and control has provided more intuitive and easier to use systems increasing the benefits to both the surgeon and the patient.

Continuum robotic systems can be the innovation needed across several areas of medicine, where current healthcare practices have limited efficacy due to access and safety. Furthermore, replacing straight rigid devices with continuously deformable structures may allow better navigation inside the body through conformation to the patient's anatomy and provide safer physical interaction. Steering and navigating such devices, however, poses significant challenges.

3.2. Definition and classification of continuum robots

CRs can be defined as actuated structures that form curves with continuous tangent vectors [17]. These robots are considered to have an infinite number of joints and DOF, allowing them to change their shape at any point along their length [14]. These characteristics make them ideal for variable environments where flexibility and adaptability to external conditions are necessary.

Continuum manipulators (CMs), structures that resemble an elephant's trunk or an octopus' tentacle, have been gaining popularity for medical applications. These typically have a small diameter and exhibit high dexterity in order to reach confined spaces, such as the lung's bronchi. The design of such structures is, on its own, a challenge given that higher dexterity normally comes associated with a higher number of actuators. This increases the diameter of the structure, which in turn decreases the range of motion [17].

The demand for safer tissue interactions has led to the development of soft robots. This emerging field comprises robots made of intrinsically soft elastomeric materials, giving the robot the ability to absorb energy and deform to their surroundings and external constraints [68]. They are, therefore, highly compliant and flexible, enabling a vast range of complex motions [69]. Soft robots are by definition CRs as they can deform continuously having infinite DOF [70, 71]. Additionally, they exhibit deformation whereas hard CRs only exhibit flexibility. Medical soft robotics have shown possibilities from targeted drug delivery to minimally invasive procedures [59, 72].

4. Actuation of continuum manipulators

4.1. Mechanical actuation

Mechanical actuation refers to the use of solid elements to directly transmit forces and torques through or within the actuator structure. Driven in part by the requirement of high dexterity at small scales for medical interventions, mechanically driven continuum robots have successfully branched from classical serial designs. Given the variety of approaches taken, an abundance of robot designs have emerged, being broadly categorised into steerable needles, concentric tubes and backbone-based [17, 73, 74]. Generally, the order presented here reflects an increase in design complexity and force output, although specific implementations vary. Figure 2 illustrates example implementations utilising these design principles and table 1 summarises many of the mechanically actuated designs proposed in the literature for specific medical interventions.

4.1.1. Steerable needle designs

Steerable needles form their continuum shape exclusively through interaction with the tissues. Development of robotically controlled needle insertion methods has been driven by the aim of accurately and precisely reaching target locations within tissues through non-linear pathways in order to avoid obstacles or delicate structures. Initial designs typically relied on the uneven forces produced at the bevel tip of the needle to steer along curved trajectories [90]. Rotation of the needle with variable duty cycle enabled path control [91, 92].

Over the years, a number of developments have been proposed in an attempt to minimise tissue damage during insertion and reduce the radius of curvature. Needles with kinked bevel tips [93], or with a concentric sleeve and needle stylet [94] have been reported. Furthermore, needles with flexures [75] and notches [80, 81] to reduce tip stiffness have also been proposed. Different steering methods have also been developed using tendons [95, 96], through magnetic actuation [19, 23] and by using water jets [97]. Steering has also

Table 1. Summary of mechanically actuated medical robots.

Ref	Design principle	Application	Actuation	Diameter (mm)	Controllable DOF	Length (mm)	Min. bending radius (mm)
[79]	Bevel tipped steerable needle	MIS		0.7	3	-	-
[80, 81]	Notched steerable needle	Brachytherapy	Ultrasound guided	3.2	3	-	171
[82, 83]	Concentric tube	MRI guided surgery	3 piezoelectrically actuated tubes	-	6	567	72
[33]	Concentric tube	Central airway obstruction	2 motor driven dexterous arms	<2	3 each	-	-
[84]	Monarch™: Concentric tube	Bronchoscopy	Cable driven	4.2	10	-	-
[77]	Backbone	Neuroendoscope	2 tendon driven bending sections	3.4	1 each	120	-
[85]	Backbone	Single-site partial nephrectomy	2 tendon driven segments	26	2 each	240	76
[86]	Backbone	Laparoscopy	Cable driven with compressible spring backbone	8	-	-	-
[87]	Backbone	Neurosurgery	Tendon driven extensible backbone segments with tendon driven bending	21	-	340	-
[88, 89]	Backbone	Cardiac surgery	50 tendon driven serial links	10	105 in total	300	35
[78]	Backbone	Throat MIS	2 multi-backbone segments with push-pull actuation	4.2	20	35	8.13

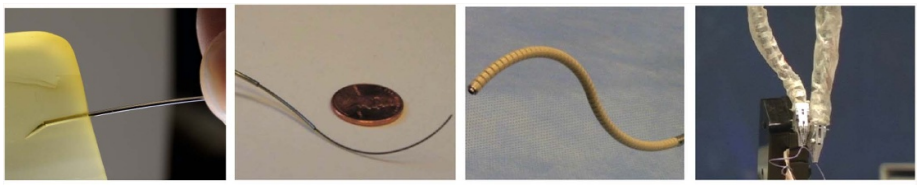

Figure 2. Mechanically actuated continuum robot designs for varied actuation principles; showing: (a) the steerable needle concept [75], (b) a typical concentric tube design [76] and backbone-based designs (c) tendon driven [77] (copyright © 2015, Springer Nature) and (d) multi-backbone [78] (copyright © 2009 by SAGE Publications).

been achieved utilising interlocking translating sections inspired by the wasp [98, 99] and an over tube [100]. Despite their achievements, this type of continuum robots ultimately relies on tissue damage for actuation.

4.1.2. Concentric tube designs

As their name implies concentric tube actuators result from the nesting of pre-curved tubes, typically made from nitinol (NiTi), within one another [76, 101, 102]. With relative rotation and translation, varied sets of curvature are achievable with a further increase in workspace possible through coupled motions. Although first presented for generic needle-steering and surgical applications [76, 101], specific formulations have since been presented for: neurosurgery [103] including endonasal [104, 105]; transurethral prostate surgery [82, 106]; lung access [107] for biopsy [108] and central airway obstruction removal [33]; and needle driving through elastic instability [109].

These applications highlight the immediate benefit of concentric designs as their ability to be realised at small scales, allowing access through the narrow tortuous pathways of the body. However, unlike steerable needles, concentric tubes rely on a change in length to induce varying curvature. Additionally, limitations in pre-curvature of tubes limit their path-following capabilities and require design parameter optimization to match application specific trajectories [110]. Furthermore, the payload that can be supported through concentric tube implementations is an important limitation of their interventional capacity.

4.1.3. Backbone-based designs

A widely adopted approach for realising continuum actuator design is the use of an elastic central backbone. This spine supports the elements required for actuation while its elastic properties produce continuous bending and restoration forces; returning the actuator to a neutral (ordinarily straight) position upon the removal of actuation forces. A number of materials have been employed for this function, such as springs [77, 111, 112], polymers [113–115] and NiTi rods/tubes [78, 116].

With a central elastic structure in place, tendons or rods are routed along the length of the backbone, held to the desired routing pathway through the use of spacing discs and fixed to a specific distal point. Although similar in form tendon driven embodiments produce actuation force only under cable tension, while rod driven (multi backbone) is rigid in tension and compression, resulting in a stiffer overall design. Upon loading, the tendons/rods transmit forces to the termination point resulting in bending-inducing torques. Increased DOF can be achieved by serially stacking actuation segments of this design.

Routing of the actuation element is a key variable in determining the manipulator's performance. Usually, routing configurations per segment are comprised of one or two antagonistic pairs for single or bi-planar bending respectively, or three actuating elements spaced evenly around the central axis of the actuator. A generalised model for tendon routing for single-segment designs [117] and two-segment designs [118] has been proposed. These show that helical tendon routing increases workspace and enhances obstacle avoidance. Radial variation in tendon path routing has also been recently explored [119], illustrating the ability to significantly increase tip stiffness with non-parallel tendons. Although tuning of this nature enables varied actuator design, once implemented the kinematic and dynamic properties are largely invariant. However, features to allow variation in design during operation have also been investigated. Magnetic spacing discs have been used to form extensible segments [116], leading to the possibility of follow-the-leader and path following motions [110, 120]. Alternative designs for achieving extension/contraction include a tendon driven concentric backbone [87] and the use of two interlaced lockable continuum robots [121]. In addition to variable kinematics, designs have also been presented to allow stiffness adjustment through antagonistic tendon-fluid bladder configurations [122–124], pressure/vacuum jamming techniques[85, 125–127], using shape memory alloys [112], or insertable constraints[128].

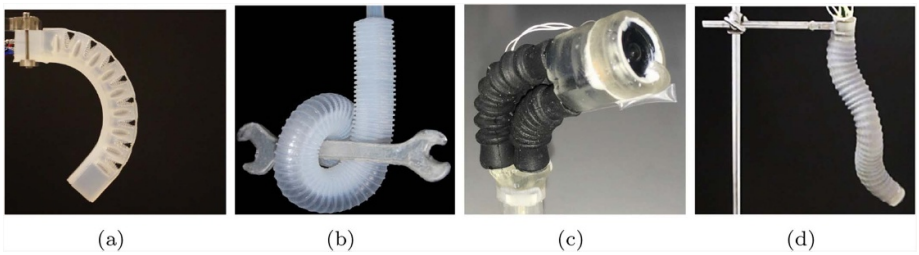

Figure 3. Pneumatically actuated continuum robots; (a) pleated [132, 212] (© 2018 WILEY-VCH Verlag GmbH & Co. KGaA, Weinheim) and (b) corrugated [133] (copyright © 2013 WILEY-VCH Verlag GmbH & Co. KGaA, Weinheim) FEA manipulators, (c) the "Belloscope" tip driven endoscope [134] (copyright © 2018, IEEE) and (d) the STIFF-FLOP multi-modal system [135] (reproduced from [135]. © IOP Publishing Ltd. All rights reserved).

The benefits of backbone designs reside in their large range of motion and configurability. With the addition of multi-segment, variable length designs and tuneable stiffness, they are highly suited to surgical applications. However, scaling down these designs is challenging, in part due to high levels of hysteresis introduced from internal friction and tension loss within actuation cables, which ultimately limits their scope.

4.2. Fluidic actuation

Fluidic actuators operate under the principle that a confined fluid applies any pressure change evenly throughout its volume. Any anisotropic strain limiter included in either the material properties or the material topography will produce correspondingly anisotropic deformation [129]. The fluid employed in these actuators highly influences their performance. In medical applications, the fluids more commonly employed are water and air, hydraulic or pneumatic respectively, given their availability, regulation and disposal and safety to the patient [130]. Pneumatic systems are preferred due to the low viscosity of air which is crucial for miniaturisation. Its compressibility, however, can reduce the system's controllability and introduce lag [131]. Fluidic actuators are able to achieve bending, twisting, extending and contracting through different designs, such as artificial muscles and fluidic elastomer actuators. In table 2, a summary of medical robots utilising fluidic actuation is presented.

4.2.1. Artificial muscles

Artificial muscles are characterised by an axial contraction when pressurised [136, 145]. The McKibben muscle is considered to be the original fluidic actuator and consists of an inner tube enclosed in a flexible double-helix braided sheath responsible for contraction [145]. This actuator is known for providing a high power to weight ratio.

With advances in manufacturing capabilities over the past 25 years, other variants of artificial muscles have emerged, such as pneumatic artificial muscles (PAM) [145]. These employ the same principle as the McKibben muscles but by varying wrap angles and densities of the external sheath, the topology of deformation under pressure can be manipulated [146, 147]. PAMs are able to achieve lighter per unit force than other alternatives, greater compliance and zero static friction, preventing jumps during actuation [145]. These characteristics are of particular interest to the surgical robotics community from a safety perspective and their use has been reported in cardiac compression devices [136].

4.2.2. Fluidic elastomer actuator

Fluidic elastomer actuators (FEA) consist of synthetic elastomer films with embedded channels which expand and/or bend when pressurised[68, 148]. It is a wholly soft structure and its strain limiter is built into the material's geometry. This total absence of rigid material enables a robot with a much greater range of movement and which is, in general, safer in contact with human tissue. FEAs also operate at lower pressures than artificial muscles due to their lack of fibrous support [131]. This enables easier actuation but limits the maximum force the robot can exert.

FEAs come in a range of different topologies offering different solutions to various problems such as cylindrical tubes [135], eccentric tubes [149], pneumatic networks [130, 150], corrugated membranes (ribbed [131] or pleated [151], see figures 3(a) and (b) and helically restricted elastomers [152]. All these options offer variants of anisotropic strain limited geometry, generating highly non-linear deformations which, when incorporated with the natural compliance of the material, produce shapes completely unachievable in traditional hard robots or with artificial muscles. This highly non-linear behaviour is, however, difficult to model and control. Furthermore, large deformations can be viewed as problematic

Table 2. Summary of fluidic actuated medical robots.

Ref	Design principle	Application	Actuation	Diameter (mm)	Controllable DOF	Length (mm)	Maximum bending angle (deg)	Maximum pressure (kPa)	Max. force (N)
[136]	PAM	Direct cardiac compression	Pneumatic	<14	-	140	-	100	50
[66]	McKibben artificial muscles	Fetal surgery	Pneumatic	-	2	-	-	-	-
[135]	FEA	MIS	3 pneumatic modules	25	1	165	240	72	-
[31]	FEA	Colonoscopy	Hydraulic	18	5	60	130	6.1	7.9
[137–140]	FEA	Gastroscopy	Hydraulic waterjet	12	3	-	94	32.8	0.10
[141]	FEA	MIS	2 pneumatic modules	32	-	135	132	65	7.9
[134, 142]	Parallel bellows	Gastroscopy	3 pneumatic bellows at the tip	<14	3	120	65	-	-
[143, 144]	Serial bellows	Endovascular	2 hydraulic segments	3	-	80	-	-	-

when navigating confined spaces such as those within the human body. There is also a risk of rupture due to their unconstrained pneumatic bladders. When operating in sensitive environments and near sharp objects, such as surgical blades, this is rightly considered a real risk.

4.2.3. Emerging actuators

Recently a number of innovative alternative actuators have been developed. One example is actuation via micro-jet propulsion [153]. Despite the potential demonstrated by this method, further safety developments should be addressed such as disposal of actuation fluid in a comfortable manner and ensuring the minimisation of tissue damage by the propulsive jet. Other interesting examples include a robot which is steerable and controllable by growth [154]; and peristaltic motion [155].

In addition to emerging fluidic actuation methods, a large effort has been made to develop safer alternatives from a rupture point of view. One such example is the fibre-reinforced FEA [156] which dopes the elastomer with microfibres turning any potential rupture into a slow puncture. Approaching the same issue from the opposing perspective, series PAM (sPAM) replace the original fibrous sheath with additional pneumatic actuators creating a fully soft actuator with similar power delivery capabilities to the original PAM [157]. Furthermore, self-sealing polymers [151] and vacuum actuated elastomers [158, 159] have also been reported.

4.2.4. Actuator arrangements

Typically one actuator will provide one primitive motion [160]. Continuum robots, especially for medical applications, must be capable of multi-directional deformations [161]. This is most readily achieved via modular actuation [135].

In modular actuation, several actuators are connected with the ramification that each independent actuator must have its own supply line [135]. Actuators may be connected in series to create slender continuum manipulators [147], in a parallel and un-conjoined arrangement to create, for example, grippers [162], or in a parallel and conjoined arrangement for multi-directional manipulators [163]. A common approach is to connect actuators both in parallel and in series as in the STIFF-FLOP project [135] shown in figure 3(d). This robot features ten independently operated actuators each with a 1.5 mm diameter driveline. The robot itself has a diameter of 25 mm illustrating one of the major limiting factors for the application of fluidic actuators to continuum robots' miniaturisation. Obviously, future improvements in manufacturing technology can assist but the trade-off between manipulability and size is a chronic and yet unresolved issue. Some alternatives to address this issue have been reported, such as the use of Band Pass Valves to reduce the number of drivelines [143] but the traditional limitations of miniaturisation still apply with regards to manufacturing technology.

4.3. Magnetic actuation

Magnetic actuation of robots relies on the use of magnetic forces and torques; generated through manipulation of the magnetisation of the robot and the external magnetic field in which the robot is placed. This type of actuation eliminates the need for bulky on-board systems allowing easy miniaturisation and untethered control, both useful for the medical robot applications. Furthermore, magnetic fields are proven safe for clinical applications, having been in use for several decades [164].

Robot designs with time-varying magnetic properties placed under constant fields are challenging to fabricate and present safety concerns due to heat dissipation [165, 166]. For these reasons, magnetic robots for medical applications almost exclusively have constant magnetic properties and are placed inside a varying magnetic field for manipulation [165]. Over the past two decades, advances in the use of magnetism in robotics have led to different ways of incorporating magnetic properties and to the development of novel actuation and navigation systems. Table 3 lists several of the magnetically actuated continuum robots presented in the literature.

4.3.1. Device's magnetism

Embedding magnetic properties in continuum robots has been easily done by inserting permanent magnets in their structures. By optimising the location, number and distance between the magnets, the robot can achieve the desired application [167]. This approach is fairly common with a variety of designs and applications reported, such as the guide-wire for cardiovascular applications shown in figure 4(a) [168–170]. The major advantage of using permanent magnets is that their properties are well known, facilitating the modelling and control of the device. Additionally, the use of components already designed for and used within, clinical settings facilitates the pathway to commercial adoption. In fact, several magnetically steered catheters are already available on the market, such as Polaris X™ Catheter [16, 171]. However, the use of permanent magnets imposes limitations in terms of size and achieving fully soft structures.

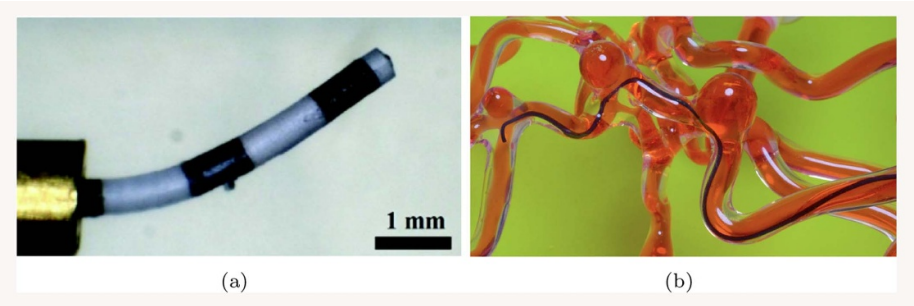

Figure 4. Magnetically actuated continuum robots; (a) embedded permanent magnets [169] (© Sungwoong Jeon *et al* 2019; published by Mary Ann Liebert, Inc.) (b) magnetic composite polymers [174].

Alternatively, one can use magnetic composite polymers. These polymers are characterised by the introduction of magnetic micro or nano particles into a polymer matrix [172]. This results in a magnetisable mixture whose characteristics, such as mechanical properties and suitable manufacturing methods resemble the original ones [172]. By inducing a patterned magnetisation profile into structures made out of these polymers, one can achieve fast transformations into complex 3D shapes and locomotion capabilities [173]. An example of continuum robots that employ such composites can be seen in figure 4(b). Further information about the challenges of fabrication and inducing magnetisation patterns can be found in section 5.1.

4.3.2. Actuation systems

Unlike the previous actuation methods where the limitations were mainly due to the on-board design, magnetic actuation is limited by the external conditions one can generate, in this case, magnetic fields and magnetic field gradients [177–179]. Over the past two decades, a number of actuation systems for magnetic robots have been developed and can be fundamentally classified into either coil-based or permanent magnet-based, depending on the source of the magnetic field.

Coil-based systems

Coil-based systems are able to generate both homogenous and inhomogeneous magnetic fields by controlling the input electric current. Uniform magnetic fields can be generated by Helmholtz coils [180, 181]. These rely solely on magnetic torques for actuation, given the lack of a magnetic gradient. Maxwell coils, alternatively, achieve both force and torque actuation. Due to their design simplicity, these systems achieve low controllable DOF [182–184]. Several systems with a high number of electromagnetic coils have been proposed achieving higher number of controllable DOF [185], such as Minimag [186] and OctoMag illustrated in figure 5(a) [187]. A system capable of fulfilling the theoretical maximum of eight DOF was also recently reported [188]. More recently, emerging systems consisting of moving electromagnetic coils [189] and a magnetic-acoustic hybrid actuation have been reported [190].

Generally, coil-based systems have high controllability and stability [191]. However, they are associated with bulky equipment, small workspace, up-scaling limitations and prohibitively high cost. In fact, adapting these systems to a clinical setting might be a difficult task without loss of the DOF achieved in the research environment.

Permanent magnet-based systems

Permanent magnet-based systems provide a feasible alternative to electromagnetic coils. These do not rely on real time electrical currents to generate a magnetic field, allowing for stronger fields and field gradients while not suffering from overheating problems [50, 192]. Two approaches using permanent magnets have been reported, rotating permanent magnets and robotic manipulation of permanent magnets. Rotating permanent magnets, while providing the advantages of permanent magnets, still suffer from reduced workspace [192, 193]. Alternatively, mounting permanent magnets at the end effectors of robotic manipulators and moving them around the desired workspace can be easily translated into the clinical environment given its much larger workspace [194, 195]. This method has been used for a variety of continuum devices, such as that depicted in figure 5(b) [50, 196].

Despite the advantages of permanent magnets over electromagnetic coils, these systems come with their own limitations. Any changes to the generated fields are performed via mechanical methods, introducing mechanical noise in the system. Furthermore, the non-linear relationship between the magnetic field and induced wrench makes robotic control less straightforward.

Table 3. Summary of magnetically actuated medical robots. Deflection is shown in mm (minimum bending radius) for hard devices and in degrees (deformation angle) for soft devices.

Ref	Design principle	Application	Actuation	Diameter (mm)	Length (mm)	Deflection	Inovation
[168, 170]	Permanent magnet	Heart ablation	Magnetic tip for steering	<2.5	50	7 mm	Variable stiffness segments allowing shape forming
[19, 23]	Permanent magnet	Neurosurgery	Magnetic tip for steering	1.3	-	100 mm	Magnetically guided steerable needle
[49, 50]	Permanent magnet	Colonoscopy	Magnetic tip for steering	20	22 (active tip)	-	Robotic alternative to manual endoscopes
[169]	Permanent magnet	Endovascular	Two magnets along along the body	0.5	3.8	132.7° C	High deformation angles
[175]	Permanent magnet	MIS	Magnetic tip for steering	3	47.5	54° C	Titanium robot with flexures along the body
[171]	Polaris X™ Permanent magnet	Electrophysiology	Tendon drive with magnets for steering	2	1500	-	Commercially available soft magnetic catheter
[174]	Magnetic particles	Cerebrovascular	NdFeB in PDMS tip	0.6	3 (active tip)	<90° C	Fully sub millimeter magnetic robot
[176]	Magnetic particles	Cerebrovascular	Three NdFeB sections along the body	2	42	-	Fully soft shape forming robot

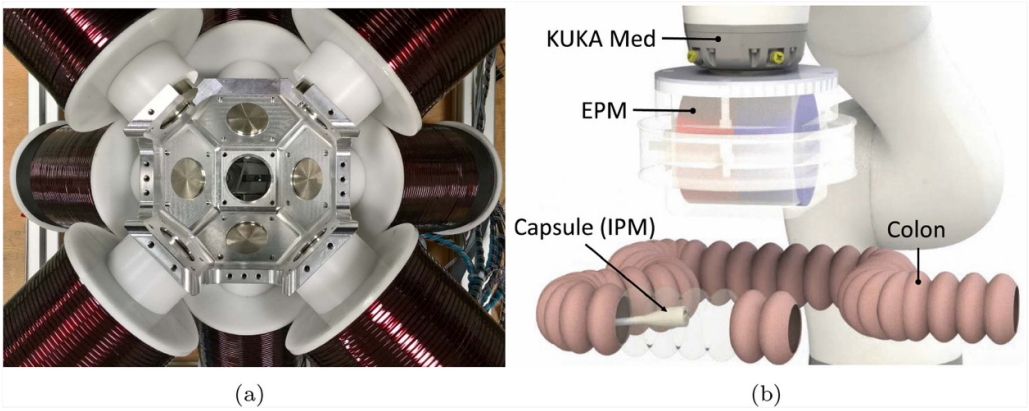

Figure 5. Magnetic actuation systems; (a) coil-based system Octomag (MagnebotiX AG, Zurich, Switzerland) [187] (image used with permission from MagnebotiX) and (b) permanent magnet-based system [50] (copyright © 2019, IEEE).

4.3.3. Magnetic navigation systems

Successful magnetic steering depends not only on reliable magnetic actuation but also on simultaneous monitoring. Magnetic navigation systems based on imaging techniques and electromagnetic tracking have emerged to address this issue.

Imaging

The high quality and real-time nature of x-ray monitoring systems made them the favoured technique for magnetic navigation. Both coil-based and permanent magnet-based systems using x-ray have been reported [41, 167, 170, 197]. Despite the good results achieved, the risks associated with x-ray exposure are a major limiting factor and have encouraged further development of monitoring systems.

Modified magnetic resonance imaging (MRI) machines have emerged as a candidate navigation system [198, 198–201]. In fact, MRI fringe fields have been used for steering continuum magnetic robots [202]. However, the lack of simultaneous monitoring and feedback and the need for more reliable control hinder these systems' use. Ultrasound based monitoring provides a safe, cheap and reliable alternative approach. Their usage in magnetic navigation has been explored [59] and used to provide closed loop navigation in endoscopy [203].

Electromagnetic tracking

Navigation of other actuation methods can be done with the aid of common electromagnetic tracking systems, such as Aurora (Northern Digital Inc. Waterloo, Canada). However, these are incompatible with magnetic actuation due to distortions caused by both the external actuation field and the device's magnetism [49, 204]. This being so, alternative methods have been proposed such as the the incorporation of magnetic field sensors and inertial sensors in the robot to determine its pose [49]. An alternative approach sees the placement of a two-dimensional array of magnetic field sensors in the workspace, facilitating miniaturisation of the device [204].

Despite the promising results shown by tracking approaches these are limited to permanent magnet-based actuation systems. Tracking within magnetic fields generated by coil based systems is not possible due to the high number of singularities present.

4.4. Summary

Mechanical, fluidic and magnetic actuation methods for continuum robots have given rise to a variety of designs. Overall they are well suited for the medical community despite each having its own limitations.

Mechanical and fluidic methods, although abundant, suffer from trade-offs in terms of size, stiffness and controllable DOF. Many designs presented achieve high levels of dexterity, however, to realise the higher number of DOF, larger diameters are typically necessary. Considering mechanical actuation specifically, the relative rigidity and non-compliance can pose a significant safety risk during tissue interaction, necessitating mitigation through complex control strategies. In fact, steerable needles cannot achieve their small bending radii without causing some tissue damage.

Conversely, fluidic robots inherently address this issue given their structural softness and compliance. However, the risk of rupture in these devices during pressurisation still needs to be addressed in an effective and safe way. Furthermore, the relatively low forces they exert opposes progression against device-tissue

friction in tortuous anatomy. Solutions that are able to achieve higher forces at lower operating pressures and with improved patient-specific design may offer safer and more effective options.

Magnetic CRs share many of the inherent benefits with mechanical and fluidic devices, with the addition of being able to achieve much smaller diameters due to the dearth of internal design required, such as cable routes or fluidic channels. Furthermore, the controllable DOF are dependent on the external actuation system, which permits miniaturisation of the device without loss of controllability. This becomes extremely useful when considering endovascular or brain procedures where thin devices are needed. One major drawback when using magnetic composite polymers is biocompatibility. Although solutions are well established for fluidic devices [163], for magnetic CRs the issue persists. Solutions such as coating the devices with biocompatible materials have been reported [174], but further studies in this area are still needed.

A final but crucial consideration for these approaches is the off-board actuation system used. This has been thoroughly explored in the literature for mechanical and fluidic devices, as they rely primarily on well-established and effective robotic methodologies such as cable transmission and pneumatic pumps. Magnetic devices, however, represent a much more recent technology and exhibit less straightforward control strategies. This has hindered a quick and easy implementation of concepts. As such a wide diversity of magnetic actuation strategies have emerged dependent on the requirements of the specific application, however, significant exploration on this topic is still required.

5. Challenges associated with continuum manipulators

5.1. Fabrication

Medical continuum robotics is an emerging field with some examples of devices now breaking into the market. As the technology further matures, the development of effective manufacturing processes that enable greater function and decreased size scales will be essential to growth of the field. This has been shown in soft robots, where innovation in manufacturing processes has illustrated new modalities of actuators, design freedom, sensing and operation.

Fabrication of mechanically actuated robots is well established as they are commonly produced by standard subtractive manufacturing techniques (e.g. milling or electrical discharge machining). However, the use of alternative methods, such as 3D printing, to allow for patient- or procedure- specific customisation has been reported [205], as well as methods to facilitate fabrication of concentric tubes [206]. Given that fabrication for fluidic and magnetic robots is a considerably newer area of research and less explored in the literature, in this paper we first focus on fabrication of polymeric, flexible structures normally employed in soft robotic devices. The focus then shifts to magnetic continuum structures where new fabrication strategies and magnetisation techniques present significant opportunities for increased function within robotic surgical devices.

5.1.1. Soft lithography

Soft lithography is a common technique for producing continuum structures due to its low barrier to entry. The process relies on the accurate replication of features from a master by casting a liquid polymer. Once cured, the polymer can be removed to reveal a negative of the mould. It has been shown that some examples of closed chambers can be produced by assembling components through plasma bonding or using uncured elastomer as an adhesive [131].

This method is suitable for limited life materials often used for experimental continuum devices. Its resolution is also limited by the minimum achievable feature size of the master mould. In practice, this usually requires a compromise between mould expense, production time, material suitability and resolution. Photolithographic techniques can be used to produce high resolution patterns, but production time and cost can be prohibitive. The accessibility of additive techniques/3D printing techniques has increased the use of master moulds due to low lead times and costs. However, resolution restrictions are often higher and several of the mould materials induce a reaction that inhibits curing of silicone elastomers.

Multi-material structures are also a challenge for soft lithography, with each change in material significantly adding to production time. Over-moulding higher stiffness materials is often used to introduce spatially varying mechanical characteristics and induce a bending bias during operation [68]. Selective inclusion of functional elements, such as conductive nano-particles, can only practically be achieved via homogenous distribution throughout the body.

Furthermore, the process is fundamentally 2.5D since the final device needs to be removed from the mould without damage. Lost wax and dissolvable moulds have been used to enhance the complexity of the designs, but their single use increases manufacturing timescales and expense. Creative designs have been important in allowing more complex behaviour in multi-link continuum robots. However limited achievable

complexity using these mould based methods has led to direct additive or even hybrid techniques being increasingly investigated.

5.1.2. Direct addictive manufacture

Direct additive manufacture (AM) has been increasingly used to investigate the fabrication of continuum robots, rather than use as a template for secondary casting processes [207, 208]. This provides enhanced design freedom and geometric complexity, as well as opportunities for true multi-material structures.

Central to all AM processes is the development of materials that are suitable for both the end application and the manufacturing process. Fused deposition modelling (FDM) and selective laser sintering (SLS) greatly limit the material choice, given the need for thermoplastics. In SLS, this is compounded by challenges in multi-material processing. Stereolithography (SLA) faces similar issues being limited to photopolymers. However, materials with properties approaching those of silicone rubber have been demonstrated [209]. Additionally, SLA's optical patterning allows greater feature resolution than competing extrusion processes. Controlled forms of material extrusion and material deposition processes are becoming increasingly popular in continuum robotics due to their ability to deposit high viscosity materials. However, it can be challenging to develop an ink that can flow easily out of the nozzle and maintain its shape once deposited. Currently, this is achieved by inducing a phase change through liquid evaporation, gelation, or temperature change [210]. Recently, rapid material switching has been demonstrated for spatially varying material composition or particle loading [211].

5.1.3. Hybrid approaches

Techniques that combine soft lithography for the production of bulk geometries with direct write for the functional elements have expanded the capabilities of continuum devices. In these types of processes, the bulk material is cast into a mould before a selective deposition technique deposits an ink into the base materials. The secondary deposition process can be completed before or after curing of the bulk structure. The most widely investigated hybrid approach uses DIW to deposit fugitive, strain limiting and conductive sensing elements within an uncured elastomer matrix [212]. Other approaches have used direct write approaches such as inkjet or aerosol jet to deposit onto a cured elastomer [213].

5.1.4. Magnetic composites

Fabrication of magnetic continuum robotics is achieved with specific processes. As discussed in section 4.3, a number of commercial steerable needle products are available in the market that rely on embedding permanent magnets within a soft or flexible structures [16]. These can be manufactured through either mechanical assembly [214] or over-moulding a polymer body around permanent magnets [169, 215]. These approaches illustrated some good applications but also have some limitations of scale of potential devices and their function. These devices have raised questions of robustness in light of a recall of a number of magnetically tipped steerable guide-wires [216].

Alternatively, manufacture of magnetic continuum robots can be based on micro or nano-particles within a polymer matrix. Reducing the size of the particles allows them to be positioned more densely while minimising the impact on the device's mechanical properties. Hard magnetic particles, characterised by high remanence, are limited to the micro-scale [217]. Soft magnetic materials can be synthesised at the nano-scale, however their relatively low remanence leads to a lesser response during actuation. Additionally, the total loading fraction needs to be carefully considered in terms of both the magnetic response and mechanical properties as the higher the concentration the higher the mechanical impact on the polymer [218]. Furthermore, limitations in bio-compatibility of the materials, alignment of the magnetic field and processes that allow selective and spatial patterning within polymer bodies challenge the realisation of the full potential of magnetic continuum robotics. Nonetheless, processes for both types of magnetic particles have been presented that have made progress against these challenges.

Template aided magnetisation

Template aided magnetisation consists of holding a pre-formed magnetic elastomer composite sheet in a template. This is then magnetised through exposure to a large external field [221]. By locally controlling the orientation of the polymer body relative to the magnetising field, it is possible to induce a spatially varying magnetisation profile [59]. Over-moulding and other similar soft-lithographic techniques can be used to spatially vary the particle loading concentration and, therefore, the magnetic response. However, a substitute non-magnetic particle may need to be incorporated to maintain homogenous mechanical properties.

Despite the simple and easy process, this approach is limited to planar actuators and the use of templates prevents discrete changes in the magnetisation profile. More complex structures and magnetisation profiles require secondary assembly stages [222].

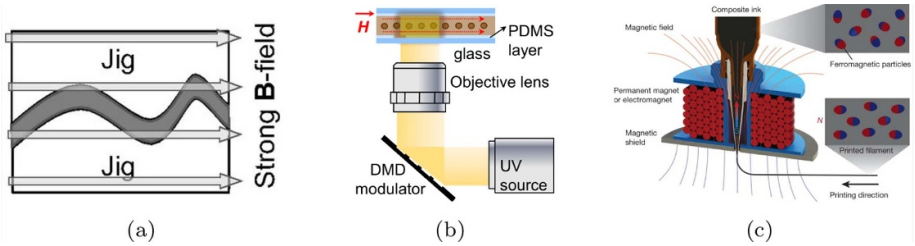

Figure 6. Examples of fabrication processes for magnetic composites. (a) Template aided magnetisation [218]; (b) optical patterning process [219] (copyright © 2011, Springer Nature); (c) extrusion process of magnetic composites [220] (copyright © 2018, Springer Nature).

Optical patterning

Optical patterning utilises lithographic techniques to selectively cure a photopolymer resin loaded with magnetic particles [219]. The uncured resin is exposed to an external magnetic field which induces particle alignment. The resin is then selectively cured, locally fixing the position and orientation of the magnetic particles. The external field can then be adjusted to induce an alternate orientation in the uncured resin. Repetition of this process can pattern both the polymer matrix and the magnetisation profile in one single process.

A number of different techniques have been presented where their primary differences are in the types of particles used, the method of achieving selective light exposure (masked[223] or mask-less [173]) and the incorporation of additional process steps and components to induce further capabilities [223]. Early work used a permanent magnet to align magnetic particles before an ultraviolet light source selectively cured the polymer, achieving 2D magnetisation profiles [219]. More recently, 3D magnetisation profiles were achieved by fixing the permanent magnet to a two DOF rotation axis mounted below the build volume [173]. Furthermore, improved magnetic response was also observed by using higher remanence magnetic materials.

Optical patterning is able to achieve 3D magnetisation profiles, providing greater freedom in magnetic response and device geometry when compared with the template based methods described previously. However, the mechanical properties of photocured polymers are often more restricted than those available to casting or extrusion processing. Additionally, particles in photopolymers can inhibit curing through UV absorbance. This may provide an upper bound to the maximum loading fraction produced by these methods.

Direct inkjet write

Direct inkjet write (DIW) of magnetically loaded materials has been demonstrated by incorporating high remanence microparticles within a polymer matrix [174]. The particles were magnetised to saturation within the suspension prior to extrusion. Additionally, fumed silica particles were added to drive the thixotropic behaviour required to prevent agglomeration during magnetisation and provide the required rheological conditions for DIW [220]. Microparticle alignment can be achieved by using a switchable magnet at the nozzle's exit or by bulk treating post print. Selective alignment during extrusion provides greater control and freedom over the magnetisation profile, however only 63-64% of the magnetic moment density can be achieved when compared to uniform magnetisation.

The addition of microparticles in DIW can often lead to increased instances of nozzle clogging. Robust DIW processes require a high nozzle-particle diameter ratio or a low loading fraction to achieve reliable deposition [210]. Since high remanence particles typically have a minimum diameter of 5μm, compromises between process resolution and magnetic response are currently required. The highest presented loading fraction is 20 wt% significantly lower than the 50 wt% demonstrated using casting techniques [220].

To summarise the state-of-the-art in CR fabrication, we can see that there are several areas of progress but that the processes that have been demonstrated to date typically involve several elements of compromise across their functionality and/or their possible applications. In particular we currently see restrictions to the production of small scale CRs and their dexterity due to fabrication limitations in resolution and material composition. It should also be noted that many of the techniques described are also often not exceptionally scalable for high production rates or high manufacturing standards. There are also particularly significant hurdles for several of the methods with regards repeatability. Advancing beyond these issues is dependant of rationalising multi-step fabrication routes and employing digital-control and automation for their manufacture.

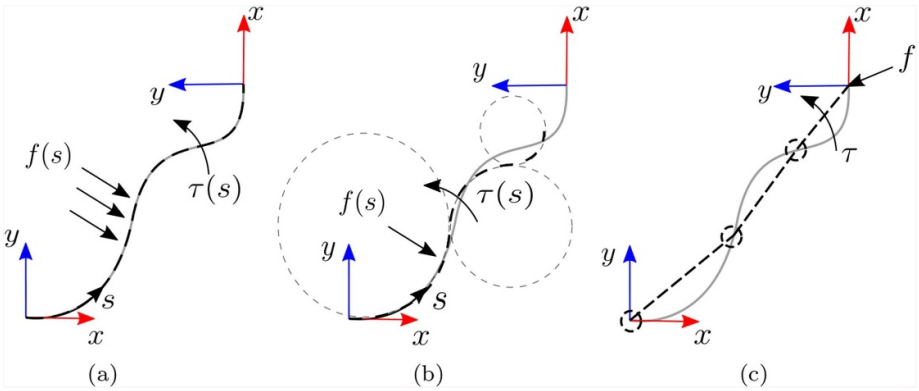

Figure 7. Schematic representation of the three classical modelling approaches of continuum robots (a) Cosserat rod model, (b) piece-wise constant curvature and (c) rigid-link model. $f(s)$ and $\tau(s)$ represent the vector fields force and torque with respect to the robot's length (s), respectively.

5.2. Modelling

In contrast with standard rigid-link manipulators, whose mechanical properties have been fully understood and discussed [224], continuum manipulators are still the subject of much debate within the robotics community in terms of modelling [73, 117] and control [225] (see the following section 5.3).

The lack of generalised approaches makes understanding and usage of these manipulators less straightforward. In fact, continuum robots include a variety of concepts as discussed in previous sections. The non-negligible diversities of these robotic concepts hinder the development of possible unifying and more generalised modelling and control techniques. The differences between proposed actuation methods, as reported in section 4, also make generalisations less trivial and induce extensive dispute. Furthermore, there is an increased difficulty due to the complex mechanical behaviour of these robots. Unlike rigid serial robots, one of the only common concepts among continuum robots is a lack of rigidity, this constitutes their main advantage in terms of application and their main drawback in terms of physical understanding and description. This lack of rigidity also leads to more complex relationships between actuators and End Effector (EE) dynamics. As such, modelling of continuum robots has received significant interest from the robotics community and several concepts have been emerging.

Kinematic modelling is, in general, not particularly effective in continuum robots owing to the redundant design and general lack of rigid coupling between actuators and EE. With the possible exception of concentric tube robots [226] we could describe the physical behaviour of a continuum robot as the outcome of the equilibrium of internal forces (e.g. elasticity, damping, friction, etc) and actuating external wrenches ($(f\ \tau)^T$ in figure 7). As a result of this force balance, the continuum manipulator would shape itself to a minimal energy configuration. Therefore, models that consider static [226–229] and dynamic [117, 230–233] approaches for controller design are particularly effective. Nevertheless, kinematics [73] and differential kinematics [234] approaches have also been investigated and may be of great interest for sensing (see section 5.4).

Modelling techniques for continuum robots can be divided into: classical methods (such as Cosserat rod theory [71], constant curvature [73], rigid link models [229, 234]); combined methods [117, 196, 230, 233, 235]; and emerging techniques [228, 236].

5.2.1. Classical methods

The classical methods applied to modelling of continuum robots can be subdivided in terms of strictness of their assumptions. In particular, Cosserat rod theory aims at solving the static equilibrium of the manipulator fully (figure 7(a)) without simplifying assumptions; (piece-wise) constant curvature modelling assumes the robot shape fits the arc of one or more circles (figure 7(b)); and rigid-link assumption would subdivide the robot into (infinitesimal) rigid links (figure 7(c)). These techniques listed with increasing strictness of assumption and consequent ease in description lead to relative pros and cons, described in the following.

Cosserat rod theory

Cosserat rod theory does not undergo specific assumptions and is, therefore, an exact solution to the statics of the continuum robot (see figure 7(a)). This approach consists of solving a set of equilibrium equations between the position, orientation, internal force and internal torque of the robot [117].

Despite the exact solution given, it suffers from drawbacks that prohibit wide use. There are difficulties in extending to dynamics since it would involve the solution of a system of partial differential equations [237]. Moreover, the solution of this approach is to be computed numerically, leading to high complexity and computational expense and a lack of a closed-form solution.

Constant curvature

Constant curvature models are based on the assumption that the continuum robot deflects as arcs of a circle, as represented in figure 7(b). This constitutes a significant simplification when compared to Cosserat Rod and leads to possible analytical solutions for kinematics [235], statics [232] and dynamics [231]. In figure 7(b), we represent *piece-wise constant curvature* modelling, i.e. the robot is modelled as a series of links that can deflect with constant curvature. Assuming constant curvature only, even if widely used, is more restrictive.

Even if piece-wise constant curvature modelling may constitute a valuable trade-off between the complications of Cosserat rod theory and the assumptions of rigid-link models, most of the literature has focused on the single constant curvature [231, 235] without exploiting the larger generalization provided by combining constant curvature segments [232, 238]. This would be of great value, especially due to the possible extension to dynamic modelling [231] and the reduction of numerical intensity with respect to rigid-link approaches.

As underlined in figure 7(b), one of the drawbacks may be constituted by the lack of compliance to the constant curvature assumption with possible consequent deviation from the real robot's behaviour. Extension to the polynomial curvature case has also been recently proposed [239]. However, further experimental analysis and discussion of its application is needed.

Rigid-link model

Assuming a continuum robot can be divided into (small enough) segments [229, 234], behaving as rigid links (see figure 7(c)), is a significant assumption when dealing with continuum structures. This would either lead to behaviours which are far from reality (few segments) or a very large number of variables (many segments). Employing the rigid-link assumption is a useful simplification since it permits the use of well-established approaches for control and sensing [224].

In the presence of sensing [234] (see section 5.4), the simplifications related to the usage of this model may be mitigated and compensated by the measure of the robot's behaviour. Therefore, the designer may find a balance between model and sensing complexity to find an optimal approach.

5.2.2. Combined methods

Due to the continuously emerging design, fabrication and actuation methods for CMs, single model approaches are of limited use. In fact, depending on the type of actuation, models need to be a combination of the intrinsic robot's behaviour and actuation dynamics. In this case, the wrench we previously defined as extrinsic becomes an integrated module of the robot's model.

Large interest since the early days of continuum robotics has been paid to backbone continuum robots [117, 230, 233, 234, 240] (see section 4.1). Due to the contact between cables and discs, several authors have combined friction models with discs dynamic model [233, 240]; and with the constant curvature model [230].

In the last few years, interest towards magnetically actuated catheters has soared [196, 227, 229]. Here an extrinsic wrench is generated as a consequence of the interaction between internal magnetised agents. In general, the considered models are a combination of the dipole model [50, 241] with rigid-link model [229] or with Cosserat rod model [196, 227]. As far as the authors are aware, combinations with piece-wise constant curvature models have not yet been investigated; although, they may be promising, owing to the possible existence of an analytical solution to the combination of dipole model and constant curvature model.

5.2.3. Emerging techniques

The previously described modelling approaches, given the very novel nature of continuum robots, are not without drawbacks. Therefore, new paradigms for modelling continuum robots have recently been investigated.

In particular, in [236] the authors attempt to overcome the limitations of constant curvature modelling by substituting circular curves with *Euler curves* which proved to be a better fit for a pneumatic continuum robot. In [228], the authors employ a quasi-static approach based on optimal configurations taking inspiration from optimal non-linear control. Despite the promising results, the lack of analytical solution and the difficulties in generalising the dynamic modelling are the main drawbacks of this approach.

Even if, intuitively, research should be driven by the quest for more and more accurate modelling approaches, accuracy is generally paid for with computational burden. This expense, given the interest towards models for real-time control over simulation for design, is a fundamental parameter to consider in the choice and/or investigation of a modelling approach. Moreover, control is generally based on both model and sensors (see section 5.4) and the aim of the designer is the balance between these two components. Therefore, we expect research to evolve towards more affine-to-control modelling approaches [238, 239] with the mindset of complexity mitigation.

5.3. Control

Control is one of the fundamental aspects of any robotic platform since it gives significance to the mechanical properties of any autonomous system. Interestingly though, only 9% of researchers seem to be focused on this topic within soft continuum robots [225]. This could be interpreted both as a consequence of the large interest in other aspects of CRs, such as mechanical design, or equally related to the very limited knowledge in terms of modelling (see section 5.2) and sensing (see section 5.4). In fact, to achieve accurate control, both these aspects are fundamental, even though the presence of a human-in-the-loop - as found in medical robotics - may mitigate some shortcomings [78].

The lack of accurate or appropriate sensing mechanisms in certain situations has led researchers to differentiate between open loop, which is based on model inversion; closed loop based on feedback of the robot's actuator; and feed-forward and feedback combined control [225]. Despite the effectiveness of this partition, the last two classes can be grouped more generally within the closed loop control class [242] with their differences related to being model-based and model-free.

Control in continuum robots can be divided into: kinematic and differential kinematic control [243–246]; adaptive and learning-based approaches [247–254]; and wrench-based controllers [227, 255–260].

5.3.1. Kinematic approaches

Kinematic approaches include any controller that considers the inverse kinematics or inverse differential kinematics, under the clear assumption that any controller needs knowledge of the direct kinematics. The application of inverse kinematics is the most widely used approach to controlling robots and considered straightforward for standard robots [261]. Due to the highly redundant design of continuum robots, inverse kinematics is not particularly effective [243]. In fact, kinematics is generally not bijective for redundant manipulators and infinite solutions exist for the inverse kinematics [224]. Nevertheless, a large amount of research has recently focused on learning inverse kinematics.

Differential kinematics [245], on the other hand, is particularly effective with redundant manipulators, since it allows multi-task control [225]. A good example of such cases is the dual-arm concentric tube coordinated control [244]. Assuming the differential kinematics to be known with sufficient accuracy can be a relatively strong assumption given the modelling approximations designers are forced into. Satisfactory accuracy might not therefore be assured. To overcome this limitation, adaptive approaches have been proved effective in some scenarios.

5.3.2. Adaptive and learning approaches

To deal with partial knowledge of the robots (differential) kinematics, some authors have started investigating adaptive and learning approaches, which are aimed at compensating for modelling approximations with data gathering. These approaches can be subdivided into mechanical adaptation methods and learning-based methods. The former are generally based on some approximated mathematical model for the manipulator and aim at real-time adaptation of the approximations; the latter are data-driven modelling approaches.

Adaptive approach

This approach is generally applied to approximated models, whose inaccuracies can be mitigated by the presence of a feedback loop. The problem is tackled as the estimation of the mechanical parameters is done on-line. In particular, the approach in [253] describes the robot's pose as a Fourier series expansion and a recursive least square approach is applied to update the parameters. More satisfactory results were found by applying a locally weighted projection regression, by approximating the model with a collection of linear models and adaptation performed by means of a stochastic gradient descent approach [254].

A different approach has been recently presented in [252], with the application of a model-free adaptive controller based on visual servoing. Another approach considers the adaptive observer of a Kalman filter [251], designed to estimate the Jacobian matrix of the manipulator. However, the model of state evolution is relatively simple and does not consider the mathematical properties of the Jacobian matrix.

Learning approach

More recently, modelling and control based on machine learning methodologies has gained much interest amongst the robotics community. These methods, as with the previously mentioned adaptive counterpart, have the common aim of avoiding complex and approximated analytical models. In particular, contrived mechanical response models can be replaced with data-driven model-free simulations. Examples of such strategies appear in [247] which uses a multilayer perceptron with a single hidden layer, the multilayer network employed in [176, 248] and a modified Elman neural network and Gaussian mixture model in [250]. Despite some promising results and the recent surge in the application of learning techniques to robotics, a limitation of these methods is the blindness to real mechanical interactions. This lack of physical significance endorses a lack of underlying physical comprehension, this in turn can produce an un-auditable system and may lead to potentially hazardous undetected inaccuracies.

5.3.3. Wrench-based approaches

Since the actuation of a continuum robot can be generally related to the interaction between their flexible structure and actuating (external) wrenches (see section 5.2 for more details), some authors have tackled the control problem by directly controlling the actuating wrench. Some examples are the static approaches in [227, 256, 259] and dynamic approaches in [260].

As an outcome of this vision, due to the redundant nature of continuum robots, compliance/stiffness [255, 259] and task-space force [256] control have been investigated. This is of primary importance for some medical robotics tasks, such as smooth navigation in soft environments and palpation [258]. Nevertheless, the estimation of a robot's force is not trivial without the assistance of sensors. Therefore, [117] and [258] have independently worked on the estimation of the force by applying a probabilistic and deterministic approach, respectively.

Literature on control of CMs shows significant interest in model-based approaches. Given the complex mechanical behaviour of CMs and the need for several diverse and interconnected elements (see section 5.1) in their design, mechanical characterization may lack accuracy and thus induce errors in control. We therefore envisage that other methods, such as adaptive methods or deep learning, will be implemented to compensate for this drawback.

5.4. Sensing

As stated previously, accurately modelling CMs remains a huge challenge, reinforcing the need to further develop techniques to improve controllability, actuation and safety. Real-time shape sensing of CMs allows for more precise and reliable motion control. To date there are three main types of shape sensing employed in CMs: optical sensing, electromagnetic tracking and imaging techniques.

5.4.1. Optical based shape sensing

Optical sensing is based on the use of fibre Bragg grating (FBG) sensors written onto optical fibres. These are able to reflect a narrow range of the full spectrum of input light depending on the fibre's strain and temperature [262]. This way, by incorporating several FBG sensors along an optical fibre it is possible to estimate the shape given the strain measurements at each sensor. Consequently, embedding one or more optical fibres with FBGs in CMs enables shape sensing of the device.

The popularity of this method has been increasing in continuum structures, especially those which undergo small deflections. Needles are one of the most common structures where this sensing method has been employed. Needles are inherently stiff, supporting a nearly perfect strain transfer to the attached FBGs. Three optical fibres with two FBGs each have been reported to give very accurate results for single 2D deflections [263]. However, as the deflection complexity increases to double deflections [264], or 3D deflections [262], the inaccuracy increases significantly. The main sources of errors have been attributed to a low number of sensors and their inaccurate placement during fabrication. Additionally, the location of the FBGs has also been reported to have a fundamental role [263, 264].

This sensing technique has also been used on less stiff structures such as catheters [265–267] and endoscopes [268, 269]. These structures are more challenging due to the lower strain transfers onto the sensors. In fact, preliminary work on the field was not able to achieve accurate results [268] or had to be used in combination with other sensing techniques [266] such as those reviewed here. Recently 3D shape reconstruction of catheters was achieved using multi-core fibres [267].

Overall, using FBGs sensors for shape sensing of CMs is a viable solution, especially for structures that undergo small deflections. Furthermore, its usage on force and torsion sensing has also been demonstrated, allowing higher sensing capabilities without the need of extra equipment [270–273]. Its insensitivity to magnetic fields allows its usage in a variety of medical situations such as MRI or coupled to magnetically actuated devices. Nevertheless, the technology still faces significant challenges that hinder its mainstream

use, especially in high deflection structures. Not only will the sensors give less accurate results due to a lower strain transfer ratio but they will also damage easily when subjected to such strains. This imposes strict limitations to the devices that are suitable for this type of shape sensing. Additionally, the relatively high cost of such technology hinders its application in low cost devices. The number of sensors and their placement are also shown to have a major impact on results [274, 275].

5.4.2. Electromagnetic tracking based shape reconstruction

Electromagnetic (EM) tracking uses mutual induction between a magnetic field generator and a magnetic field sensor for shape reconstruction. Two variations of this method have been proposed based on the location of the magnetic field generator, either external or internal to the robot.

External methods are the most common and use commercially available EM tracking systems, such as the NDI Aurora [276], for shape reconstruction. These systems are able to determine the pose of small sensors on a generated external magnetic field. By placing these sensors along the robot, the system is able to determine the robot's pose. The usage of these systems for shape sensing has been widely demonstrated [277, 278] and methods to estimate contact force have also been reported [279, 280]. Despite its promising results, this method is constrained by the limitations of the localisation method itself, such as limited workspace and variable accuracy within it [278].

Internal methods are able to overcome these limitations by placing the source of the magnetic field inside the robot itself. Two small permanent magnets alternated with two Hall effect sensors along a CM were able to reconstruct 2D shape [281]. By measuring the magnetic field at the location of the Hall effect sensors, it is possible to estimate the relative position and therefore, the deflection of the manipulator. Similar approaches have been reported [282–284] and a common limitation to them all is that with increasing deflections, the errors increase. This is due to cross talk between the sensors and the magnets, posing limitations to minimum bending radii.

Electromagnetic tracking shape sensing methods are able to provide freedom from line-of-sight restrictions and are relatively easy to incorporate into the robot. However, they are highly susceptible to magnetic disturbances from nearby equipment. External methods using commercially available systems cannot be used in conjunction with magnetically actuated robots or MRI applications [285]. Nonetheless, proprietary localisation methods could be developed for the specific application and robot, such as [49]. Internal methods suffer from crosstalk between sensors and magnetic agents during high deformations, hindering the reliability of shape estimation results. Furthermore, the incorporation of an internal magnetic field generator can impose limitations on the robot's size. Nevertheless, assuming these challenges are addressed, this method could potentially achieve much smaller bending radii than FBG, facilitating its use in soft CRs.

5.4.3. Imaging based shape estimation

Imaging methods rely on current medical imaging techniques to track and estimate the shape of CMs. Unlike the previous methods, this approach does not required the integration of any additional sensors onto the surgical instrument which can be beneficial from a design and miniaturisation point of view.

Fluoroscopy [268, 286, 287] and ultrasound [287, 288] are the two main imaging techniques used in shape estimation of CMs and endoscopes. The usage of biplane fluoroscopy for shape estimation of continuum structures has been reported and is known to achieve accurate 3D reconstructions [165, 289]. However, these methods depend on biplane systems that are associated with large radiation dosages and costs. Given the nature of monoplane fluoroscopy, detecting out of plane deflection using imaging alone is not possible [290]. Several works have combined planar imaging techniques with tracking methods [290–292] or kinematic modelling [293, 294] however these systems tend to achieve less accurate results. Shape estimation of CMs using endoscopic cameras has also been reported and is generally performed on a marker-based or markerless approach [295, 296]. Marker-based approaches require additional integration of components into the device, while markerless require large manually labelled training sets [296]. Furthermore, these methods are normally limited by the field of view of the camera.

Imaging based methods can provide reliable results for shape sensing of CMs. There are no limitations to the minimum bending radii these methods can potentially achieve, unlike alternatives methods which, for larger deflections, can become erroneous. They are limited of course by image resolution, noise and processing techniques. Furthermore, due to their dependency on and need for integration with, hospital equipment, they may not be readily implemented.

In summary, recent developments in shape sensing for CMs has improved their efficacy. However, when introducing additional on-board hardware, as in FBG and EM tracking approaches, robot miniaturisation, stiffness, flexibility and durability can be adversely influenced. Off-board sensing methods remove such restrictions and of these, imaging-based methods are most prevalent, offering potentially practicable

solutions to the sensing problem if suitable clinical integration can be realised. A less explored but promising off-board approach employs load cell sensors located at the robots proximal end for estimation of tip force and shape [297, 298]. Ultimately, the limited accuracy of flexible and soft robots, particularly when subject to interaction forces, hinders their reliability in clinical settings. Methods for shape sensing are therefore essential to realise the full potential of medical CRs and future development may engender ever smaller bending radii measurement, while maintaining high accuracy and miniaturisation capabilities.

6. Conclusions and future directions

Medical robotics has seen remarkable innovation over the last decades. Driven by the need for less invasive procedures while maintaining dexterity levels, continuum robots have established themselves as a viable alternative to traditional rigid-link manipulators. The recent commercial releases of continuum platforms for robot-assisted procedures further advocate their future place in advanced healthcare practices.

Despite the progress achieved, further advancements are highly dependent on current challenges across actuation, fabrication, control and sensing. As with traditional surgical robotic systems, continuum robots are commonly intrinsically actuated using tendons or pressurised fluids, limiting the achievable DOF as their size reduces. External actuation via magnetic fields does not suffer from this scaling issue, providing a promising approach for controlling continuum robotic devices, especially at the small scales required for medical applications. Magnetic soft robots may provide an optimal solution as they are able to combine the freedom in scale from magnetism with the safe interaction of soft robots.

Fabrication and control of such devices is currently still a challenge given the materials employed and the magnetisation patterns needed for actuation. However, allied to these challenges is also the possibility for major breakthroughs. Developments in digitally-driven and computer controlled manufacturing processes holds potential to allow an exciting next generation of continuum robots, with greater resolution and dexterity, enabling us to reach and treat areas of the human anatomy that may otherwise be inaccessible.

ORCID iDs

Tomas da Veiga https://orcid.org/0000-0002-4286-4590
James H Chandler https://orcid.org/0000-0001-9232-4966
Giovanni Pittiglio https://orcid.org/0000-0002-0714-5267
Ali K Hoshiar https://orcid.org/0000-0002-0561-5018
Pietro Valdastri https://orcid.org/0000-0002-2280-5438

References

[1] Baura G D 2012 *Medical Device Technologies* (Oxford: Academic)
[2] Doglietto F, Prevedello D M, Jane J A, Han J and Laws E R 2005 A brief history of endoscopic transsphenoidal surgery—from Philipp Bozzini to the first world congress of endoscopic skull base surgery *Neurosurgical Focus FOC* **19** 1–6
[3] Mundy A R, Fitzpatrick J, Neal D E and George N J R 2010 *The Scientific Basis of Urology* (London: CRC Press)
[4] Peters B S, Armijo P R, Krause C, Choudhury S A and Oleynikov D 2018 Review of emerging surgical robotic technology *Surgical Endoscopy* **32** 1636–55
[5] Kim S S and Donahue T R 2018 Laparoscopic Cholecystectomy *JAMA* **319** 1834
[6] Rozeboom E, Ruiter J, Franken M and Broeders I 2014 Intuitive user interfaces increase efficiency in endoscope tip control *Surgical Endoscopy* **28** 2600–5
[7] Simaan N, Yasin R M and Wang L 2018 Medical technologies and challenges of robot-assisted minimally invasive intervention and diagnostics *Annu. Rev. Control Robot. Auton. Sys.* **1** 465–90
[8] Wolfe B M, Gardiner B and Frey C F 2015 Laparoscopic cholecystectomy: a remarkable development *JAMA* **314** 1406
[9] Taylor R H, Menciassi A, Fichtinger G, Fiorini P and Dario P 2016 Medical robotics and computer-integrated surgery *Springer Handbook of Robotics* ed B Siciliano and O Khatib (Berlin: Springer) pp 1657–84
[10] Davies B 2000 A review of robotics in surgery *Proc. Inst. Mech. Eng.* H **214** 129–40
[11] Intuitive Surgical 2018 *Technical report 2018*
[12] Bae S U, Jeong W K and Baek S K 2017 Current status of robotic single-port colonic surgery *Int. J. Med. Robot. Comput. Assist. Surg.* **13** e1735
[13] Singh P K and Krishna C M 2014 Continuum arm robotic manipulator: a review *Universal J. Mech. Eng.* **2** 193–8
[14] Faulkner J and Dirven S 2017 A generalised, modular, approach for the forward kinematics of continuum soft robots with sections of constant curvature *2017 24th Int. Conf. on Mechatronics and Machine Vision in Practice (M2VIP)* pp 1–6
[15] Heunis C, Sikorski J and Misra S 2018 Flexible instruments for endovascular interventions: improved magnetic steering, actuation and image-guided surgical instruments *IEEE Robot. Automation Mag.* **25** 71–82
[16] Hu X, Chen A, Luo Y, Zhang C and Zhang E 2018 Steerable catheters for minimally invasive surgery: a review and future directions *Computer Assisted Surgery* **23** 21–41
[17] Burgner-Kahrs J, Rucker D C and Choset H 2015 Continuum robots for medical applications: a survey *IEEE Trans. Robot.* **31** 1261–80
[18] Shi C, Luo X, Qi P, Li T, Song S, Najdovski Z, Fukuda T and Ren H 2017 Shape sensing techniques for continuum robots in minimally invasive surgery: a survey *IEEE Trans. Biomed. Eng.* **64** 1665–78

[19] Hong A, Boehler Q, Moser R, Zemmar A, Stieglitz L and Nelson B J 2019 3D path planning for flexible needle steering in neurosurgery *Int. J. Medical Robot. Comput. Assist. Surg.* **15** e1998
[20] Calabrese E 2016 Diffusion tractography in deep brain stimulation surgery: a review *Front. Neuroanatomy* **10** 45
[21] Lindgren A, Vergouwen M D I, van der Schaaf I, Algra A, Wermer M, Clarke M J and Rinkel G J E 2018 Endovascular coiling versus neurosurgical clipping for people with aneurysmal subarachnoid haemorrhage *Cochrane Database Systematic Rev.* **8** CD003085
[22] Neudorfer C, Hunsche S, Hellmich M, El Majdoub F and Maarouf M 2018 Comparative study of robot-assisted versus conventional frame-based deep brain stimulation stereotactic neurosurgery *Stereotactic Functional Neurosurgery* **96** 327–34
[23] Petruska A J, Ruetz F, Hong A, Regli L, Surucu O, Zemmar A and Nelson B J 2016 Magnetic needle guidance for neurosurgery: Initial design and proof of concept *2016 IEEE Int. Conf. on Robotics and Automation (ICRA)* (Piscataway, NJ: IEEE) pp 4392–7
[24] Siegel R L, Miller K D and Jemal A 2019 Cancer statistics, 2019 *CA A Cancer J. Clinicians* **69** 7–34
[25] National Institute for Health and Care Excellence 2019 Lung cancer: diagnosis and management *NICE Guideline 122* https://nice.org.uk/guidance/ng122
[26] Swaney P J, Mahoney A W, Hartley B I, Remirez A A, Lamers E, Feins R H, Alterovitz R and Webster III R J 2017 Toward transoral peripheral lung access: combining continuum robots and steerable needles *J. Med. Robot. Res.* **2** 1750001
[27] Hindman A 2019 Robotic bronchoscopy *Oncology Issues* **34** 16–20
[28] Fielding D, Bashirzadeh F, Son J H, Todman M, Tan H, Chin A, Steinke K and Windsor M 2017 First human use of a new robotic-assisted navigation system for small peripheral pulmonary nodules demonstrates good safety profile and high diagnostic yield *Chest* **152** A858
[29] Folch E *et al* 2020 A prospective, multi-center evaluation of the clinical utility of the ion endoluminal system-experience using a robotic-assisted bronchoscope system with shape-sensing technology *A110. Advances In Interventional Pulmonology* (New York: American Thoracic Society) A2719
[30] Chan J Y, Wong E W, Tsang R K, Holsinger F C, Tong M C, Chiu P W and Ng S S 2017 Early results of a safety and feasibility clinical trial of a novel single-port flexible robot for transoral robotic surgery *Eur. Arch. Otorhinolaryngol.* **274** 3993–6
[31] Manfredi L, Capoccia E, Ciuti G and Cuschieri A 2019 A soft pneumatic inchworm double balloon (SPID) for colonoscopy *Sci. Rep.* **9** 1–9
[32] Mattheis S, Hasskamp P, Holtmann L, Schäfer C, Geisthoff U, Dominas N and Lang S 2017 Flex robotic system in transoral robotic surgery: the first 40 patients *Head Neck* **39** 471–5
[33] Gafford J B *et al* 2019 A concentric tube robot system for rigid bronchoscopy: a feasibility study on central airway obstruction removal *Ann. Biomed. Eng.* **48** 181–91
[34] Gong W, Cai J, Wang Z, Chen A, Ye X, Li H and Zhao Q 2016 Robot-assisted coronary artery bypass grafting improves short-term outcomes compared with minimally invasive direct coronary artery bypass grafting *J. Thoracic Disease* **8** 459
[35] Nifong L W, Chitwood W R, Pappas P S, Smith C R, Argenziano M, Starnes V A and Shah P M 2005 Robotic mitral valve surgery: a United States multicenter trial *J. Thoracic Cardiovascular Surgery* **129** 1395–404
[36] Riga C V, Bicknell C D, Rolls A, Cheshire N J and Hamady M S 2013 Robot-assisted fenestrated endovascular aneurysm repair (fevar) using the magellan system *J. Vascular Interventional Radiol.* **24** 191–6
[37] Clements W, Scicchitano M, Koukounaras J, Joseph T and Goh G S 2019 Use of the magellan robotic system for conventional transarterial chemoembolization (ctace): a 6-patient case series showing safety and technical success *J. Clin. Interventional Radiol. ISVIR* **3** 142–6
[38] Thaveau F, Nicolini P, Lucereau B, Georg Y, Lejay A and Chakfe N 2015 Associated da vinci and magellan robotic systems for successful treatment of nutcracker syndrome *J. Laparoendoscopic Adv. Surgical Techniques* **25** 60–3
[39] Pereira V M, Cancelliere N M, Nicholson P, Radovanovic I, Drake K E, Sungur J-M, Krings T and Turk A 2020 First-in-human, robotic-assisted neuroendovascular intervention *J. NeuroInterventional Surgery* **12** 338–40
[40] Lo N, Gutierrez J A and Swaminathan R V 2018 Robotic-assisted percutaneous coronary intervention *Current Treatment Options Cardiovascular Med.* **20** 14
[41] Carpi F and Pappone C 2009 Stereotaxis Niobe® magnetic navigation system for endocardial catheter ablation and gastrointestinal capsule endoscopy *Expert Rev. Med. Devices* **6** 487–98
[42] Bonatti J, Vetrovec G, Riga C, Wazni O and Stadler P 2014 Robotic technology in cardiovascular medicine *Nature Rev. Cardiol.* **11** 266
[43] Fagogenis G *et al* 2019 Autonomous robotic intracardiac catheter navigation using haptic vision *Sci. Robot.* **4** eaaw1977
[44] Smyth E C, Verheij M, Allum W, Cunningham D, Cervantes A and Arnold D 2016 Gastric cancer: ESMO clinical practice guidelines for diagnosis, treatment and follow-up *Ann. Oncol.* **27** v38–v49
[45] Shaheen N J, Falk G W, Iyer P G and Gerson L B 2016 ACG clinical guideline: diagnosis and management of Barrett's esophagus *Am. J. Gastroenterol.* **111** 30
[46] Valdastri P, Simi M and Webster III R J 2012 Advanced technologies for gastrointestinal endoscopy *Annu. Rev. Biomed. Eng.* **14** 397–429
[47] Iddan G, Meron G, Glukhovsky A and Swain P 2000 Wireless capsule endoscopy *Nature* **405** 417
[48] Bynum S A, Davis J L, Green B L and Katz R V 2012 Unwillingness to participate in colorectal cancer screening: examining fears, attitudes and medical mistrust in an ethnically diverse sample of adults 50 years and older *Am. J. Health Promotion* **26** 295–300
[49] Taddese A Z, Slawinski P R, Pirotta M, De Momi E, Obstein K L and Valdastri P 2018 Enhanced real-time pose estimation for closed-loop robotic manipulation of magnetically actuated capsule endoscopes *Int. J. Robot. Res.* **37** 890–911
[50] Pittiglio G, Barducci L, Martin J W, Norton J C, Avizzano C A, Obstein K L and Valdastri P 2019 Magnetic levitation for soft-tethered capsule colonoscopy actuated with a single permanent magnet: a dynamic control approach *IEEE Robot. Automation Lett.* **4** 1224–31
[51] Turiani Hourneaux de Moura D, Aihara H, Jirapinyo P, Farias G, Hathorn K E, Bazarbashi A, Sachdev A and Thompson C C 2019 Robot-assisted endoscopic submucosal dissection versus conventional ESD for colorectal lesions: outcomes of a randomized pilot study in endoscopists without prior ESD experience (with video) *Gastrointestinal Endoscopy* **90** 290–8
[52] Valdastri P, Webster III R J, Quaglia C, Quirini M, Menciassi A and Dario P 2009 A new mechanism for mesoscale legged locomotion in compliant tubular environments *IEEE Trans. Robot.* **25** 1047–57
[53] Son D, Dogan M D and Sitti M 2017 Magnetically actuated soft capsule endoscope for fine-needle aspiration biopsy *2017 IEEE Int. Conf. on Robotics and Automation (ICRA)* pp 1132–9
[54] Rosemurgy A, Ross S, Bourdeau T, Craigg D, Spence J, Alvior J and Sucandy I 2019 Robotic pancreaticoduodenectomy is the future: here and now *J. Am. College Surgeons* **228** 613–24

[55] Giulianotti P C, Bianco F M, Daskalaki D, Gonzalez-Ciccarelli L F, Kim J and Benedetti E 2016 Robotic liver surgery: technical aspects and review of the literature *Hepatobiliary Surgery Nutrition* **5** 311–21
[56] Coccolini F *et al* Open versus laparoscopic cholecystectomy in acute cholecystitis. Systematic review and meta-analysis *Int. J. Surgery* **18** 196–204
[57] Ahmed J, Nasir M, Flashman K, Khan J and Parvaiz A 2016 Totally robotic rectal resection: an experience of the first 100 consecutive cases *Int. J. Colorectal Disease* **31** 869–76
[58] D'Argentré A *et al* 2018 Programmable medicine: autonomous, ingestible, deployable hydrogel patch and plug for stomach ulcer therapy *2018 IEEE Int. Conf. on Robotics and Automation (ICRA)* pp 1511–18
[59] Hu W, Lum G Z, Mastrangeli M and Sitti M 2018 Small-scale soft-bodied robot with multimodal locomotion *Nature* **554** 81
[60] Yim S, Goyal K and Sitti M 2013 Magnetically actuated soft capsule with the multimodal drug release function *IEEE/ASME Trans. Mechatronics* **18** 1413–18
[61] Badani K K, Kaul S and Menon M 2007 Evolution of robotic radical prostatectomy: assessment after 2766 procedures *Cancer* **110** 1951–8
[62] Nanigian D K, Smith W and Ellison L M 2006 Robot-assisted laparoscopic nephroureterectomy *J. Endourol.* **20** 463–6
[63] Sarli N, Marien T, Mitchell C R, Del Giudice G, Dietrich M S, Herrell S D and Simaan N 2017 Kinematic and experimental investigation of manual resection tools for transurethral bladder tumor resection *Int. J. Medical Robot. Computer Assisted Surgery* **13** e1757
[64] Sarli N, Del Giudice G, De S, Dietrich M S, Herrell S D and Simaan N 2018 Preliminary porcine *in vivo* evaluation of a telerobotic system for transurethral bladder tumor resection and surveillance *J. Endourol.* **32** 516–22
[65] Hendrick R J, Mitchell C R, Herrell S D and Webster III R J 2015 Hand-held transendoscopic robotic manipulators: a transurethral laser prostate surgery case study *Int. J. Robot. Res.* **34** 1559–72
[66] Ahmad M A, Ourak M, Gruijthuijsen C, Legrand J, Vercauteren T, Deprest J, Ourselin S and Vander Poorten E 2019 Design and shared control of a flexible endoscope with autonomous distal tip alignment *2019 19th Int. Conf. on Advanced Robotics (ICAR)* IEEE 647–53
[67] Ahmad M A, Ourak M, Gruijthuijsen C, Deprest J, Vercauteren T and Vander Poorten E 2020 Deep learning-based monocular placental pose estimation: towards collaborative robotics in fetoscopy *Int. J. Computer Assisted Radiology Surgery* accepted https://doi.org/10.1007/s11548-020-02166-3
[68] Rus D and Tolley M T 2015 Design, fabrication and control of soft robots *Nature* **521** 467
[69] Drotman D, Jadhav S, Karimi M, DeZonia P and Tolley M T 2017 3D printed soft actuators for a legged robot capable of navigating unstructured terrain *2017 IEEE Int. Conf. on Robotics and Automation (ICRA)* pp 5532–8
[70] Marchese A D and Rus D 2016 Design, kinematics and control of a soft spatial fluidic elastomer manipulator *Int. J. Robot. Res.* **35** 840–69
[71] Trivedi D, Rahn C D, Kier W M and Walker I D 2008 Soft robotics: biological inspiration, state of the art and future research *Appl. Bionics Biomech.* **5** 99–117
[72] Cianchetti M, Ranzani T, Gerboni G, Nanayakkara T, Althoefer K, Dasgupta P and Menciassi A 2014 Soft robotics technologies to address shortcomings in today's minimally invasive surgery: the STIFF-FLOP approach *Soft Robot.* **1** 122–31
[73] Webster III R J and Jones B A 2010 Design and kinematic modeling of constant curvature continuum robots: a review *Int. J. Robot. Res.* **29** 1661–83
[74] Orekhov A L, Abah C and Simaan N 2018 Snake-like robots for minimally invasive, single port and intraluminal surgeries *Encyclopedia Medical Robot.* 203–43
[75] Swaney P J, Burgner J, Gilbert H B and Webster III R J 2013 A flexure-based steerable needle: high curvature with reduced tissue damage *IEEE Trans. Biomed. Eng.* **60** 906–9
[76] Webster III R J, Okamura A M and Cowan N J 2006 Toward active cannulas: miniature snake-like surgical robots *2006 IEEE/RSJ Int. Conf. on Intelligent Robots and Systems* pp 2857–63
[77] Kato T, Okumura I, Kose H, Takagi K and Hata N 2016 Tendon-driven continuum robot for neuroendoscopy: validation of extended kinematic mapping for hysteresis operation *Int. J. Computer Assisted Radiology Surgery* **11** 589–602
[78] Simaan N, Xu K, Wei W, Kapoor A, Kazanzides P, Taylor R and Flint P 2009 Design and integration of a telerobotic system for minimally invasive surgery of the throat *Int. J. Robot. Res.* **28** 1134–53
[79] Webster III R J Kim J S Cowan N J, Chirikjian G S and Okamura A M 2006 Nonholonomic modeling of needle steering *Int. J. Robot. Res.* **25** 509–25
[80] Khadem M, Rossa C, Usmani N, Sloboda R S and Tavakoli M 2016 Introducing notched flexible needles with increased deflection curvature in soft tissue *2016 IEEE Int. Conf. on Advanced Intelligent Mechatronics (AIM)* (Piscataway, NJ: IEEE) pp 1186–91
[81] Khadem M, Rossa C, Usmani N, Sloboda R S and Tavakoli M 2018 Robotic-assisted needle steering around anatomical obstacles using notched steerable needles *IEEE J. Biomedical Health Informatics* **22** 1917–28
[82] Su H, Li G, Rucker D C, Webster III R J and Fischer G S 2016 A Concentric tube continuum robot with piezoelectric actuation for MRI-guided closed-loop targeting *Ann. Biomed. Eng.* **44** 2863–73
[83] Su H, Cardona D C, Shang W, Camilo A, Cole G A, Rucker D C, Webster R J and Fischer G S 2012 A MRI-guided concentric tube continuum robot with piezoelectric actuation: a feasibility study *2012 IEEE Int. Conf. on Robotics and Automation* IEEE 1939–45
[84] Graetzel C F, Sheehy A and Noonan D P 2019 Robotic bronchoscopy drive mode of the auris monarch platform *2019 Int. Conf. on Robotics and Automation (ICRA)* 3895–901
[85] Amanov E, Nguyen T D, Markmann S, Imkamp F and Burgner-Kahrs J 2018 Toward a flexible variable stiffness endoport for single-site partial nephrectomy *Ann. Biomed. Eng.* **46** 1498–1510
[86] Jong Yoon W, Velasquez C A, White L W, Hannaford B, Sang Kim Y and Lendvay T S 2014 Preliminary articulable probe designs with RAVEN and challenges: image-guided robotic surgery multitool system *J. Medical Devices* **8** 1
[87] Zhang Y *et al* 2018 A continuum robot with contractible and extensible length for neurosurgery *2018 IEEE 14th Int. Conf. on Control and Automation (ICCA)* (Los Alamitos, CA: IEEE Computer Society Press) pp 1150–5
[88] Degani A, Choset H, Wolf A and Zenati M A 2006 Highly articulated robotic probe for minimally invasive surgery *Proc. IEEE Int. Conf. Robotics Automation* **2006** 4167–72
[89] Ota T, Degani A, Schwartzman D, Zubiate B, McGarvey J, Choset H and Zenati M A 2009 A highly articulated robotic surgical system for minimally invasive surgery *Ann. Thoracic Surgery* **87** 1253–6
[90] Webster R J, Kim J S, Cowan N J, Chirikjian G S and Okamura A M 2006 Nonholonomic modeling of needle steering *Int. J. Robot. Res.* **25** 509–25

[91] Webster R J, Memisevic J and Okamura A M 2005 Design considerations for robotic needle steering *Proc. of the 2005 IEEE Int. Conf. on Robotics and Automation* pp 3588–94
[92] Reed K B, Majewicz A, Kallem V, Alterovitz R, Goldberg K, Cowan N J and Okamura A M 2011 Robot-assisted needle steering *IEEE Robotics Automation Mag.* **18** 35–46
[93] Minhas D S, Engh J A, Fenske M M and Riviere C N 2007 Modeling of needle steering via duty-cycled spinning *2007 29th Annual Int. Conf. of the IEEE Engineering in Medicine and Biology Society* pp 2756–9
[94] Okazawa S, Ebrahimi R, Chuang J, Salcudean S E and Rohling R 2005 Hand-held steerable needle device *IEEE/ASME Trans. Mechatronics* **10** 285–96
[95] van de Berg N J, Dankelman J and van den Dobbelsteen J J 2015 Design of an actively controlled steerable needle with tendon actuation and FBG-based shape sensing *Medical Eng. Phys.* **37** 617–22
[96] Roesthuis R J, Van De Berg N J, Van Den Dobbelsteen J J and Misra S 2015 Modeling and steering of a novel actuated-tip needle through a soft-tissue simulant using Fiber Bragg Grating sensors *2015 IEEE Int. Conf. on Robotics and Automation (ICRA)* (Piscataway, NJ: IEEE) pp 2283–9
[97] Babaiasl M, Yang F and Swensen J P 2018 Towards water-jet steerable needles *2018 7th IEEE Int. Conf. on Biomedical Robotics and Biomechatronics (Biorob)* (Los Alamitos, CA: IEEE Computer Society Press) pp 601–8
[98] Ko S Y, Frasson L and Baena F R Y 2011 Closed-loop planar motion control of a steerable probe with a programmable bevel inspired by nature *IEEE Trans. Robotics* **27** 970–83
[99] Burrows C, Secoli R and Baena F R Y 2013 Experimental characterisation of a biologically inspired 3D steering needle *Int. Conf. Control, Automation Systems* 1252–7
[100] Yang F, Babaiasl M and Swensen J P 2019 Fracture-directed steerable needles *J. Med. Robotics Res.* **04** 1842002
[101] Sears P and Dupont P 2006 A steerable needle technology using curved concentric tubes *2006 IEEE/RSJ Int. Conf. on Intelligent Robots and Systems* pp 2850–6
[102] Gilbert H B, Rucker C and Webster III R J 2016 Concentric tube robots: the state of the art and future directions *Robotics Research. Springer Tracts in Advance Robotics* vol 114 eds M Inaba and P Corke (Cham: Springer) pp 253–69
[103] Anor T, Madsen J R and Dupont P 2011 Algorithms for design of continuum robots using the concentric tubes approach: a neurosurgical example *2011 IEEE Int. Conf. on Robotics and Automation* pp 667–73
[104] Swaney P J, Gilbert H B, Webster III R J, Russell 3rd P T and Weaver K D 2015 Endonasal skull base tumor removal using concentric tube continuum robots: A phantom study *J. Neurological Surgery* B **76** 145–9
[105] Wirz R, Torres L G, Swaney P J, Gilbert H, Alterovitz R, Webster III R J, Weaver K D and Russell 3rd P T 2015 An experimental feasibility study on robotic endonasal telesurgery *Neurosurgery* **76** 479–84
[106] Mitchell C R, Hendrick R J, Webster III R J and Herrell S D 2016 Toward improving transurethral prostate surgery: development and initial experiments with a prototype concentric tube robotic platform *J. Endourol.* **30** 692–6
[107] Swaney P J, Mahoney A W, Remirez A A, Lamers E, Hartley B I, Feins R H, Alterovitz R and Webster III R J 2015 Tendons, concentric tubes and a bevel tip: three steerable robots in one transoral lung access system *2015 IEEE Int. Conf. on Robotics and Automation (ICRA)* pp 5378–83
[108] Amack S *et al* 2019 Design and control of a compact modular robot for transbronchial lung biopsy *Medical Imaging 2019 Image-Guided Procedures, Robotic Interventions and Modeling* p 10951
[109] Riojas K E, Hendrick R J and Webster R J 2018 Can Elastic Instability Be Beneficial in Concentric Tube Robots? *IEEE Robotics Automation Lett.* **3** 1624–30
[110] Amanov E, Nguyen T-D and Burgner-Kahrs J 2019 Tendon-driven continuum robots with extensible sections—a model-based evaluation of path-following motions *Int. J. Robot. Res.*
[111] Choi D G, Yi B J and Kim W K 2007 Design of a spring backbone micro endoscope *2007 IEEE/RSJ Int. Conf. on Intelligent Robots and Systems* pp 1815–21
[112] Kim Y, Cheng S S and Desai J P 2018 Active stiffness tuning of a spring-based continuum robot for MRI-guided neurosurgery *IEEE Trans. on Robotics* **34** 1–11
[113] Lim G, Minami K, Yamamoto K, Sugihara M, Uchiyama M and Esashi M 1996 Multi-link active catheter snake-like motion *Robotica* **14** 499–506
[114] Yip M C and Camarillo D B 2016 Model-less hybrid position/force control: a minimalist approach for continuum manipulators in unknown, constrained environments *IEEE Robotics Automation Lett.* **1** 844–51
[115] Ataollahi A, Karim R, Fallah A S, Rhode K, Razavi R, Seneviratne L D, Schaeffter T and Althoefer K 2016 Three-degree-of-freedom MR-compatible multisegment cardiac catheter steering mechanism *IEEE Trans. Biomed. Eng.* **63** 2425–35
[116] Nguyen T D and Burgner-Kahrs J 2015 A tendon-driven continuum robot with extensible sections *2015 IEEE/RSJ Int. Conf. on Intelligent Robots and Systems (IROS)* (Piscataway, NJ: IEEE) pp 2130–5
[117] Rucker D C and Webster III R J 2011 Statics and dynamics of continuum robots with general tendon routing and external loading *IEEE Trans. Robotics* **27** 1033–44
[118] Starke J, Amanov E, Chikhaoui M T and Burgner-Kahrs J 2017 On the merits of helical tendon routing in continuum robots *2017 IEEE/RSJ Int. Conf. on Intelligent Robots and Systems (IROS)* (Piscataway, NJ: IEEE) pp 6470–6
[119] Oliver-Butler K, Till J and Rucker C 2019 Continuum robot stiffness under external loads and prescribed tendon displacements *IEEE Trans. on Robotics* **35** 403–19
[120] Neumann M and Burgner-Kahrs J 2016 Considerations for follow-the-leader motion of extensible tendon-driven continuum robots *2016 IEEE Int. Conf. on Robotics and Automation (ICRA)* (Piscataway, NJ: IEEE) pp 917–23
[121] Kang B, Kojcev R and Sinibaldi E 2016 The first interlaced continuum robot, devised to intrinsically follow the leader *PLoS ONE* **11** e0150278
[122] McMahan W, Jones B A and Walker I D 2005 Design and implementation of a multi-section continuum robot: air-octor *2005 IEEE/RSJ Int. Conf. on Intelligent Robots and Systems* pp 2578–85
[123] Maghooa F, Stilli A, Noh Y, Althoefer K and Wurdemann H A 2015 Tendon and pressure actuation for a bio-inspired manipulator based on an antagonistic principle *2015 IEEE Int. Conf. on Robotics and Automation (ICRA)* pp 2556–61
[124] Lee J, Go E, Choi W, Kim W and Cho K 2016 Development of soft continuum manipulator with pneumatic and tendon driven actuations *2016 13th Int. Conf. on Ubiquitous Robots and Ambient Intelligence (URAI)* 377–9
[125] Loeve A J, Plettenburg D H, Breedveld P and Dankelman J 2012 Endoscope shaft-rigidity control mechanism: FORGUIDE *IEEE Trans. Biomed. Eng.* **59** 542–51
[126] Kim Y, Cheng S, Kim S and Iagnemma K 2013 A novel layer jamming mechanism with tunable stiffness capability for minimally invasive surgery *IEEE Trans. on Robotics* **29** 1031–42

[127] Li D C F, Wang Z, Ouyang B and Liu Y 2019 A reconfigurable variable stiffness manipulator by a sliding layer mechanism *2019 Int. Conf. on Robotics and Automation (ICRA)* pp 3976–82
[128] Li Z, Feiling J, Ren H and Yu H 2015 A novel tele-operated flexible robot targeted for minimally invasive robotic surgery *Engineering* **1** 73–8
[129] Fras J, Noh Y, Macias M, Wurdemann H and Althoefer K 2018 Bio-inspired octopus robot based on novel soft fluidic actuator *2018 IEEE Int. Conf. on Robotics and Automation (ICRA)* pp 1583–8
[130] Mosadegh B *et al* 2014 Pneumatic networks for soft robotics that actuate rapidly *Adv. Funct. Mater.* **24** 2163–70
[131] Marchese A D, Katzschmann R K and Rus D 2015 A recipe for soft fluidic elastomer robots *Soft Robotics* **2** 7–25
[132] Truby R L, Katzschmann R K, Lewis J A and Rus D 2019 Soft robotic fingers with embedded ionogel sensors and discrete actuation modes for somatosensitive manipulation *2019 2nd IEEE Int. Conf. on Soft Robotics (RoboSoft)* (Piscataway, NJ: IEEE) pp 322–9
[133] Martinez R V, Branch J L, Fish C R, Jin L, Shepherd R F, Nunes R M D, Suo Z and Whitesides G M 2013 Robotic tentacles with three-dimensional mobility based on flexible elastomers *Adv. Mater.* **25** 205–12
[134] Garbin N, Wang L, Chandler J H, Obstein K L, Simaan N and Valdastri P 2018 A disposable continuum endoscope using piston-driven parallel bellow actuator *2018 Int. Symp. on Medical Robotics (ISMR)* (Piscataway, NJ: IEEE) pp 1–6
[135] De Falco I, Cianchetti M and Menciassi A 2017 A soft multi-module manipulator with variable stiffness for minimally invasive surgery *Bioinsp. Biomim.* **12** 56008
[136] Obiajulu S, Roche E T, Pigula F A and Walsh C J 2013 Soft pneumatic artificial muscles with low threshold pressures for a cardiac compression device *Proc. of the ASME 2013 Int. Design Engineering Technical Conferences and Computers and Information in Conf. IDETC/CIE* (Cambridge, MA: MIT Press) https://doi.org/10.1115/DETC2013-13004
[137] Caprara R, Obstein K L, Scozzarro G, Di Natali C, Beccani M, Morgan D R and Valdastri P 2014 A platform for gastric cancer screening in low-and middle-income countries *IEEE Trans. Biomed. Eng.* **62** 1324–32
[138] Campisano F, Remirez A A, Caló S, Chandler J H, Obstein K L, Webster R J and Valdastri P 2020 Online disturbance estimation for improving kinematic accuracy in continuum manipulators *IEEE Robotics Automation Lett.* **5** 2642–9
[139] Calò S, Chandler J, Campisano F, Obstein K L and Valdastri P 2019 A compression valve for sanitary control of fluid driven actuators *IEEE/ASME Trans. on Mechatronics* https://doi.org/10.1109/TMECH.2019.2960308
[140] Campisano F *et al* 2017 Gastric cancer screening in low-income countries: system design, fabrication and analysis for an ultralow-cost endoscopy procedure *IEEE Robotics Automation Magazine* **24** 73–81
[141] Ranzani T, Gerboni G, Cianchetti M and Menciassi A 2015 A bioinspired soft manipulator for minimally invasive surgery *Bioinsp. Biomim.* **10** 35008
[142] Garbin N, Wang L, Chandler J H, Obstein K L, Simaan N and Valdastri P 2018 Dual-continuum design approach for intuitive and low-cost upper gastrointestinal endoscopy *IEEE Trans. Biomed. Eng.* **66** 1963–74
[143] Ikuta K, Ichikawa H, Suzuki K and Yajima D 2006 Multi-degree of freedom hydraulic pressure driven safety active catheter *Proc. 2006 IEEE Int. Conf. on Robotics and Automation (ICRA)* pp 4161–6
[144] Inoue Y and Ikuta K 2016 Hydraulic driven active catheters with optical bending sensorin *2016 IEEE 29th Int. Conf. on Micro Electro Mechanical Systems (MEMS)* (Piscataway, NJ: IEEE) pp 383–6
[145] Tondu B, Boitier V and Lopez P 1994 Naturally compliant robot-arms actuated by McKibben artificial muscles *of IEEE Int. Conf. on Systems Man and Cybernetics* **3** 2635–40
[146] Daerden F and Lefeber D 2002 Pneumatic artificial muscles: actuators for robotics and automation *European J. Mech. Environ. Eng.* **47** 11–21
[147] Connolly F, Polygerinos P, Walsh C J and Bertoldi K 2015 Mechanical Programming of soft actuators by varying fiber angle *Soft Robotics* **2** 26–32
[148] Hughes J, Culha U, Giardina F, Guenther F, Rosendo A and Iida F 2016 Soft manipulators and grippers: a review *Front. Robotics AI* **3** 69
[149] Gorissen B, Vincentie W, Al-Bender F, Reynaerts D and De Volder M 2013 Modeling and bonding-free fabrication of flexible fluidic microactuators with a bending motion *J. Micromech. Microeng.* **23** 45012
[150] Whitesides G M 2018 Soft robotics *Angew. Chem., Int. Ed. Engl.* **57** 4258–73
[151] Shepherd R F, Stokes A A, Nunes R M D and Whitesides G M 2013 Soft machines that are resistant to puncture and that self seal *Adv. Mater.* **25** 6709–13
[152] Blumenschein L H, Usevitch N S, Do B H, Hawkes E W and Okamura A M 2018 Helical actuation on a soft inflated robot body *2018 IEEE Int. Conf. on Soft Robotics (RoboSoft)* pp 245–52
[153] Yahiaoui R, Zeggari R, Malapert J and Manceau J-F 2012 A MEMS-based pneumatic micro-conveyor for planar micromanipulation *Mechatronics* **22** 515–21
[154] Hawkes E W, Blumenschein L H, Greer J D and Okamura A M 2017 A soft robot that navigates its environment through growth *Science Robotics* **2** eaan3028
[155] Calderón A A, Ugalde J C, Zagal J C and Pérez-Arancibia N O 2016 Design, fabrication and control of a multi-material-multi-actuator soft robot inspired by burrowing worms *2016 IEEE Int. Conf. on Robotics and Biomimetics (ROBIO)* pp 31–8
[156] Sinatra N R, Ranzani T, Vlassak J J, Parker K K and Wood R J 2018 Nanofiber-reinforced soft fluidic micro-actuators *J. Micromech. Microeng.* **28** 84002
[157] Greer J D, Morimoto T K, Okamura A M and Hawkes E W 2017 Series pneumatic artificial muscles (sPAMs) and application to a soft continuum robot *2017 IEEE Int. Conf. on Robotics and Automation (ICRA)* pp 5503–10
[158] Yang D, Mosadegh B, Ainla A, Lee B, Khashai F, Suo Z, Bertoldi K and Whitesides G M 2015 Buckling of elastomeric beams enables actuation of soft machines *Adv. Mater.* **27** 6323–7
[159] Haga Y, Muyari Y, Mineta T, Matsunaga T, Akahori H and Esashi M 2005 Small diameter hydraulic active bending catheter using laser processed super elastic alloy and silicone rubber tube *2005 3rd IEEE/EMBS Special Conf. on Microtechnology in Medicine and Biology* pp 245–8
[160] Ali A, Plettenburg D H and Breedveld P 2016 Steerable catheters in cardiology: classifying steerability and assessing future challenges *IEEE Trans. Biomed. Eng.* **63** 679–93
[161] Gifari M W, Naghibi H, Stramigioli S and Abayazid M 2019 A review on recent advances in soft surgical robots for endoscopic applications *Int. J. Medical Robotics Computer Assisted Surgery* **15** e2010–e2010
[162] Ilievski F, Mazzeo A D, Shepherd R F, Chen X and Whitesides G M 2011 Soft Robotics for Chemists *Angewandte Chemie Int. Edn.* **50** 1890–5

[163] Suzumori K, Iikura S and Tanaka H 1992 Applying a flexible microactuator to robotic mechanisms *IEEE Control Syst. Mag.* **12** 21–7
[164] Huettel S A, Song A W and McCarthy G 2004 *Functional Magnetic Resonance Imaging* vol 1 (Cambridge, MA: Sinauer Associates Sunderland)
[165] Sikorski J, Denasi A, Bucchi G, Scheggi S and Misra S 2019 Vision-based 3-D control of magnetically actuated catheter using BigMag—an array of mobile electromagnetic coils *IEEE/ASME Trans. Mechatronics* **24** 505–16
[166] Petruska A J and Nelson B J 2015 Minimum bounds on the number of electromagnets required for remote magnetic manipulation *IEEE Trans. on Robotics* **31** 714–22
[167] Chautems C, Tonazzini A, Boehler Q, Jeong S H, Floreano D and Nelson B J 2019 Magnetic Continuum device with variable stiffness for minimally invasive surgery *Adv. Intelligent Syst.* **2** 1900086
[168] Chautems C, Tonazzini A, Floreano D and Nelson B J 2017 A variable stiffness catheter controlled with an external magnetic field *2017 IEEE/RSJ Int. Conf. on Intelligent Robots and Systems (IROS)* pp 181–6
[169] Jeon S *et al* 2018 A magnetically controlled soft microrobot steering a guidewire in a three-dimensional phantom vascular network *Soft Robotics* **6** 54–68
[170] Chautems C and Nelson B J 2017 The tethered magnet: Force and 5-DOF pose control for cardiac ablation *2017 IEEE Int. Conf. on Robotics and Automation (ICRA)* (Piscataway, NJ: IEEE) pp 4837–42
[171] Boston Scientific 2015 Polaris X. Steerable Diagnostic Catheter
[172] Gray B L 2014 A review of magnetic composite polymers applied to microfluidic devices *J. Electrochem. Soc.* **161** B3173–B3183
[173] Xu T, Zhang J, Salehizadeh M, Onaizah O and Diller E 2019 Millimeter-scale flexible robots with programmable three-dimensional magnetization and motions *Sci. Robotics* **4** eaav4494
[174] Kim Y, Parada G A, Liu S and Zhao X 2019 Ferromagnetic soft continuum robots *Sci. Robotics* **4** eaax7329
[175] Thomas T, Kalpathy Venkiteswaran V, Ananthasuresh G and Misra S 2020 A monolithic compliant continuum manipulator: a proof-of-concept study *J. Mechanisms Robotics* 1–11
[176] Lloyd P, Hoshiar A K, da Veiga T, Attanasio A, Marahrens N, Chandler J H and Valdastri P 2020 A learnt approach for the design of magnetically actuated shape forming soft tentacle robots *IEEE Robotics Automation Lett.* **5** 3937–44
[177] Liu C 2011 *Foundations of Mems* 2nd edn (Upper Saddle River, NJ: Prentice Hall Press)
[178] Nelson B J, Kaliakatsos I K and Abbott J J 2010 Microrobots for minimally invasive medicine *Annu. Rev. Biomed. Eng.* **12** 55–85
[179] Abbott J J, Peyer K E, Lagomarsino M C, Zhang L, Dong L, Kaliakatsos I K and Nelson B J 2009 How should microrobots swim? *Int. J. Robotics Res.* **28** 1434–47
[180] Kim J, Kim M J, Yoo J and Kim S 2014 Novel motion modes for 2-D locomotion of a microrobot *IEEE Trans. Magn.* **50** 1–5
[181] Xu T, Hwang G, Andreff N and Régnier S 2014 Characterization of three-dimensional steering for helical swimmers *2014 IEEE Int. Conf. on Robotics and Automation (ICRA)* pp 4686–91
[182] Yesin K B, Vollmers K and Nelson B J 2006 Modeling and control of untethered biomicrorobots in a fluidic environment using electromagnetic fields *Int. J. Robotics Res.* **25** 527–36
[183] Hu C, Tercero C, Ikeda S, Fukuda T, Arai F and Negoro M 2011 Modeling and design of magnetic sugar particles manipulation system for fabrication of vascular scaffold *2011 IEEE/RSJ Int. Conf. on Intelligent Robots and Systems* pp 439–44
[184] Go G, Choi H, Jeong S, Lee C, Ko S Y, Park J and Park S 2015 Electromagnetic navigation system using simple coil structure (4 coils) for 3-D locomotive microrobot *IEEE Trans. Magn.* **51** 1–7
[185] Diller E, Giltinan J, Lum G Z, Ye Z and Sitti M 2015 Six-degree-of-freedom magnetic actuation for wireless microrobotics *Int. J. Robotics Res.* **35** 114–28
[186] Kratochvil B E, Kummer M P, Erni S, Borer R, Frutiger D R, Schurle S and Nelson B J 2014 MiniMag: a hemispherical electromagnetic system for 5-DOF wireless micromanipulation *Experiemental Robotics. Springer Tracts in Advanced Robotics* ed O Khatib, V Kumar and G Sukjatme vol 79 (Berlin: Springer) pp 317–29
[187] Kummer M P, Abbott J J, Kratochvil B E, Borer R, Sengul A and Nelson B J 2010 OctoMag: an electromagnetic system for 5-DOF wireless micromanipulation *IEEE Trans. on Robotics* **26** 1006–17
[188] Salmanipour S and Diller E 2018 Eight-degrees-of-freedom remote actuation of small magnetic mechanisms *2018 IEEE Int. Conf. on Robotics and Automation (ICRA)* pp 3608–13
[189] Sikorski J, Dawson I, Denasi A, Hekman E E G and Misra S 2017 Introducing BigMag—a novel system for 3D magnetic actuation of flexible surgical manipulators *2017 IEEE Int. Conf. on Robotics and Automation (ICRA)* pp 3594–9
[190] Youssefi O and Diller E 2019 Contactless robotic micromanipulation in air using a magneto-acoustic system *IEEE Robotics Automation Lett.* **4** 1580–6
[191] Kaya M, Sakthivel U, Khalil I S and Misra S 2019 Development of a coil driver for magnetic manipulation systems *IEEE Magnetics Lett.* **10** 1–5
[192] Ryan P and Diller E 2017 Magnetic actuation for full dexterity microrobotic control using rotating permanent magnets *IEEE Trans. on Robotics* **33** 1398–409
[193] Yim S and Sitti M 2012 Design and rolling locomotion of a magnetically actuated soft capsule endoscope *IEEE Trans. Robotics* **28** 183–94
[194] Valdastri P, Quaglia C, Susilo E, Menciassi A, Dario P, Ho C N, Anhoeck G and Schurr M O 2008 Wireless therapeutic endoscopic capsule: *in vivo* experiment *Endoscopy* **40** 979–82
[195] Valdastri P, Ciuti G, Verbeni A, Menciassi A, Dario P, Arezzo A and Morino M 2012 Magnetic air capsule robotic system: proof of concept of a novel approach for painless colonoscopy *Surgical Endoscopy* **26** 1238–46
[196] Kratchman L B, Bruns T L, Abbott J J and Webster R J 2017 Guiding elastic rods with a robot-manipulated magnet for medical applications *IEEE Trans. on Robotics* **33** 227–33
[197] Filgueiras-Rama D, Estrada A, Shachar J, Castrejón S, Doiny D, Ortega M, Gang E and Merino J L 2013 Remote magnetic navigation for accurate, real-time catheter positioning and ablation in cardiac electrophysiology procedures *J. Visualized Experiments* **74** e3658
[198] Vonthron M, Lalande V, Bringout G, Tremblay C and Martel S 2011 A MRI-based integrated platform for the navigation of micro-devices and microrobots *2011 IEEE/RSJ Int. Conf. on Intelligent Robots and Systems* IEEE 1285–90
[199] Mathieu J-B, Beaudoin G and Martel S 2006 Method of propulsion of a ferromagnetic core in the cardiovascular system through magnetic gradients generated by an MRI system *IEEE Trans. Biomed. Eng.* **53** 292–9
[200] Tamaz S, Gourdeau R, Chanu A, Mathieu J-B and Martel S 2008 Real-time MRI-based control of a ferromagnetic core for endovascular navigation *IEEE Trans. Biomed. Eng.* **55** 1854–63

[201] Martel S, Felfoul O, Mathieu J-B, Chanu A, Tamaz S, Mohammadi M, Mankiewicz M and Tabatabaei N 2009 MRI-based medical nanorobotic platform for the control of magnetic nanoparticles and flagellated bacteria for target interventions in human capillaries *Int. J. Robotics Res.* **28** 1169–82
[202] Azizi A, Tremblay C C, Gagné K and Martel S 2019 Using the fringe field of a clinical MRI scanner enables robotic navigation of tethered instruments in deeper vascular regions *Sci. Robot.* **4** eaax7342
[203] Norton J C *et al* 2019 Intelligent magnetic manipulation for gastrointestinal ultrasound *Sci. Robot.* **4** eaav7725
[204] Son D, Yim S and Sitti M 2015 A 5-D localization method for a magnetically manipulated untethered robot using a 2-D array of Hall-effect sensors *IEEE/ASME Trans. Mechatron.* **21** 708–16
[205] Morimoto T K and Okamura A M 2016 Design of 3-d printed concentric tube robots *IEEE Trans. Robotics* **32** 1419–30
[206] Gilbert H B and Webster R J 2016 Rapid, reliable shape setting of superelastic nitinol for prototyping robots *IEEE Robotics Automation Lett.* **1** 98 III
[207] Wallin T J, Pikul J and Shepherd R F 2018 3D printing of soft robotic systems *Nat. Rev. Mater.* **3** 84–100
[208] Truby R L and Lewis J A 2016 Printing soft matter in three dimensions *Nature* **540** 371
[209] Peele B N, Wallin T J, Zhao H and Shepherd R F 2015 3D printing antagonistic systems of artificial muscle using projection stereolithography *Bioinsp. Biomim.* **10** 55003
[210] Lewis J A 2006 Direct Ink Writing of 3D Functional Materials *Adv. Funct. Mater.* **16** 2193–204
[211] Skylar-Scott M A, Mueller J, Visser C W and Lewis J A 2019 Voxelated soft matter via multimaterial multinozzle 3D printing *Nature* **575** 330–5
[212] Truby R L, Wehner M, Grosskopf A K, Vogt D M, Uzel S G M, Wood R J and Lewis J A 2018 Soft somatosensitive actuators via embedded 3D printing *Adv. Mater.* **30** 1706383
[213] Wilkinson N J, Lukic-Mann M, Shuttleworth M P, Kay R W and Harris R A 2019 Aerosol jet printing for the manufacture of soft robotic devices *2019 2nd IEEE Int. Conf. on Soft Robotics (RoboSoft)* IEEE 496–501
[214] Chautems C, Lyttle S, Boehler Q and Nelson B J 2018 Design and evaluation of a steerable magnetic sheath for cardiac ablations *IEEE Robotics Automation Lett.* **3** 2123–8
[215] Kafash Hoshiar A, Jeon S, Kim K, Lee S, Kim J-Y and Choi H 2018 Steering algorithm for a flexible microrobot to enhance guidewire control in a coronary angioplasty application *Micromachines* **9** 617
[216] U.S. Food and Drug Administration (FDA) 2004 Class 2 medical device recalls: Cronus endovascular guidewires
[217] Zhao R, Kim Y, Chester S A, Sharma P and Zhao X 2019 Mechanics of hard-magnetic soft materials *J. Mech. Phys. Solids* **124** 244–63
[218] Lum G Z, Ye Z, Dong X, Marvi H, Erin O, Hu W and Sitti M 2016 Shape-programmable magnetic soft matter *Proc. Natl Acad. Sci.* **113** E6007–E6015
[219] Kim J, Chung S E, Choi S-E, Lee H, Kim J and Kwon S 2011 Programming magnetic anisotropy in polymeric microactuators *Nat. Mater.* **10** 747–52
[220] Kim Y, Yuk H, Zhao R, Chester S A and Zhao X 2018 Printing ferromagnetic domains for untethered fast-transforming soft materials *Nature* **558** 274–9
[221] Diller E, Zhuang J, Zhan Lum G, Edwards M R and Sitti M 2014 Continuously distributed magnetization profile for millimeter-scale elastomeric undulatory swimming *Appl. Phys. Lett.* **104** 174101
[222] Ren Z, Hu W, Dong X and Sitti M 2019 Multi-functional soft-bodied jellyfish-like swimming *Nat. Commun.* **10** 2703
[223] Huang H-W, Sakar M S, Petruska A J, Pané S and Nelson B J 2016 Soft micromachines with programmable motility and morphology *Nat. Commun.* **7** 12263
[224] Siciliano B, Sciavicco L, Villani L and Oriolo G 2010 *Robotics: Modelling, Planning and Control* (Berlin: Springer)
[225] Chikhaoui M T and Burgner-Kahrs J 2018 Control of continuum robots for medical applications: state of the art *2018 16th Int. Conf. on New Actuators*
[226] Rucker D C, Jones B A and Webster R J 2010 A geometrically exact model for externally loaded concentric-tube continuum robots *IEEE Trans. Robotics* **26** 769–80
[227] Edelmann J, Petruska A J and Nelson B J 2017 Magnetic control of continuum devices *Int. J. Robot. Res.* **36** 68–85
[228] Bretl T and McCarthy Z 2014 Quasi-static manipulation of a Kirchhoff elastic rod based on a geometric analysis of equilibrium configurations *Int. J. Robot. Res.* **33** 48–68
[229] Venkiteswaran V K, Sikorski J and Misra S 2019 Shape and contact force estimation of continuum manipulators using pseudo rigid body models *Mech. Mach. Theory* **139** 34–45
[230] Jung J, Penning R S, Ferrier N J and Zinn M R 2011 A modeling approach for continuum robotic manipulators: Effects of nonlinear internal device friction *IEEE Int. Conf. Intelligent Robots Syst.* 5139–46
[231] Grazioso S, Gironimo Di and Siciliano B 2019 A geometrically exact model for soft continuum robots: the finite element deformation space formulation *Soft Robotics* **6** 790–811
[232] Falkenhahn V, Mahl T, Hildebrandt A, Neumann R and Sawodny O 2015 Dynamic modeling of Bellows-actuated continuum robots using the Euler-lagrange formalism *IEEE Trans. on Robotics* **31** 1483–96
[233] Rone W S and Ben-Tzvi P 2014 Mechanics modeling of multisegment rod-driven continuum robots *J. Mechanisms Robotics* **6** 4
[234] Roesthuis R J and Misra S 2016 Steering of multisegment continuum manipulators using rigid-link modeling and FBG-based shape sensing *IEEE Trans. Robotics* **32** 372–82
[235] Runge G, Wiese M, Gunther L and Raatz A 2017 A framework for the kinematic modeling of soft material robots combining finite element analysis and piecewise constant curvature kinematics *2017 3rd Int. Conf. on Control, Automation and Robotics (ICCAR)* pp 7–14
[236] Gonthina P S, Kapadia A D, Godage I S and Walker I D 2019 Modeling variable curvature parallel continuum robots using Euler curves *2019 Int. Conf. on Robotics and Automation (ICRA)* pp 1679–85
[237] Till J, Aloi V and Rucker C 2019 Real-time dynamics of soft and continuum robots based on cosserat rod models *Int. J. Robotics Res.* **38** 723–46
[238] Della Santina C, Bicchi A and Rus D 2020 On an improved state parametrization for soft robots with piecewise constant curvature and its use in model based control *IEEE Robotics Automation Lett.* **5** 1001–8
[239] Della Santina C and Rus D 2020 Control oriented modeling of soft robots: the polynomial curvature case *IEEE Robotics Automation Lett.* **5** 290–8
[240] Rone W S and Ben-Tzvi P 2014 Continuum robot dynamics utilizing the principle of virtual power *IEEE Trans. Robotics* **30** 275–87
[241] Barducci L, Pittiglio G, Norton J C, Obstein K L and Valdastri P 2019 Adaptive dynamic control for magnetically actuated medical robots *IEEE Robotics Automation Lett.* **4** 3633–40

[242] Isidori A 2013 *Nonlinear Control Systems* (New York: Springer)
[243] Boushaki M N, Liu C and Poignet P 2014 Task-space position control of concentric-tube robot with inaccurate kinematics using approximate Jacobian *2014 IEEE Int. Conf. on Robotics and Automation (ICRA)* (Piscataway, NJ: IEEE) pp 5877–82
[244] Chikhaoui M T, Granna J, Starke J and Burgner-Kahrs J 2018 Toward motion coordination control and design optimization for dual-arm concentric tube continuum robots *IEEE Robotics Automation Lett.* **3** 1793–800
[245] Mahl T, Hildebrandt A and Sawodny O 2014 A variable curvature continuum kinematics for kinematic control of the bionic handling assistant *IEEE Trans. on Robotics* **30** 935–49
[246] Sears P and Dupont P E 2007 Inverse kinematics of concentric tube steerable needles *Proc. 2007 IEEE Int. Conf. on Robotics and Automation* 1887–92
[247] Thuruthel T G, Falotico E, Manti M, Pratesi A, Cianchetti M and Laschi C 2017 Learning closed loop kinematic controllers for continuum manipulators in unstructured environments *Soft Robotics* **4** 285–96
[248] Jiang H, Wang Z, Liu X, Chen X, Jin Y, You X and Chen X 2017 A two-level approach for solving the inverse kinematics of an extensible soft arm considering viscoelastic behavior *2017 IEEE Int. Conf. on Robotics and Automation (ICRA)* (Piscataway, NJ: IEEE) pp 6127–33
[249] Melingui A, Lakhal O, Daachi B, Mbede J B and Merzouki R 2015 Adaptive neural network control of a compact bionic handling arm *IEEE/ASME Trans. Mechatronics* **20** 2862–75
[250] Xu W, Chen J, Lau H Y and Ren H 2017 Data-driven methods towards learning the highly nonlinear inverse kinematics of tendon-driven surgical manipulators *Int. J. Med. Robotics Computer Assisted Surgery* **13** 1–11
[251] Li M, Kang R, Branson D T and Dai J S 2018 Model-free control for continuum robots based on an adaptive Kalman filter *IEEE/ASME Trans. Mechatronics* **23** 286–97
[252] Wang H, Yang B, Liu Y, Chen W, Liang X and Pfeifer R 2017 Visual servoing of soft robot manipulator in constrained environments with an adaptive controller *IEEE/ASME Trans. Mechatronics* **22** 41–50
[253] Kim C, Ryu S C and Dupont P E 2015 Real-time adaptive kinematic model estimation of concentric tube robots *2015 IEEE/RSJ Int. Conf. on Intelligent Robots and Systems (IROS)* (Piscataway, NJ: IEEE) pp 3214–19
[254] Fagogenis G, Bergeles C and Dupont P E 2016 Adaptive nonparametric kinematic modeling of concentric tube robots *2016 IEEE/RSJ Int. Conf. on Intelligent Robots and Systems (IROS)* (Piscataway, NJ: IEEE) pp 4324–9
[255] Mahvash M and Dupont P E 2011 Stiffness control of surgical continuum manipulators *IEEE Trans. on Robotics* **27** 334–45
[256] Bajo A and Simaan N 2016 Hybrid motion/force control of multi-backbone continuum robots *Int. J. Robot. Res.* **35** 422–34
[257] Rucker D C and Webster R J 2011 Deflection-based force sensing for continuum robots: a probabilistic approach *IEEE Int. Conf. Intelligent Robots Systems* 3764–9
[258] Xu K and Simaan N 2010 Intrinsic wrench estimation and its performance index for multisegment continuum robots *IEEE Trans. Robotics* **26** 555–61
[259] Goldman R E, Bajo A and Simaan N 2014 Compliant motion control for multisegment continuum robots with actuation force sensing *IEEE Trans. Robotics* **30** 890–902
[260] Falkenhahn V, Hildebrandt A, Neumann R and Sawodny O 2017 Dynamic control of the bionic handling assistant *IEEE/ASME Trans. Mechatronics* **22** 6–17
[261] George Thuruthel T,Ansari Y, Falotico E and C Laschi 2018 Control strategies for soft robotic manipulators: a survey *Soft Robotics* **5** 149–63
[262] Roesthuis R J, Kemp M, van den Dobbelsteen J J and Misra S 2014 Three-dimensional needle shape reconstruction using an array of fiber Bragg grating sensors *IEEE/ASME Trans. Mechatronics* **19** 1115–26
[263] Park Y-L, Elayaperumal S, Daniel B, Ryu S C, Shin M, Savall J, Black R J, Moslehi B and Cutkosky M R 2010 Real-time estimation of 3D needle shape and deflection for MRI-Guided interventions *IEEE Trans. Mech.* **15** 906–15
[264] Henken K, Van Gerwen D, Dankelman J and Van Den Dobbelsteen J 2012 Accuracy of needle position measurements using fiber Bragg gratings *Minimally Invasive Therapy Allied Technol.* **21** 408–14
[265] Mandal K, Parent F, Martel S, Kashyap R and Kadoury S 2016 Vessel-based registration of an optical shape sensing catheter for MR navigation *Int. J. Computer Assisted Radiol. Surgery* **11** 1025–34
[266] Shi C, Giannarou S, Lee S and Yang G 2014 Simultaneous catheter and environment modeling for trans-catheter aortic valve implantation *2014 IEEE/RSJ Int. Conf. on Intelligent Robots and Systems* pp 2024–9
[267] Khan F, Denasi A, Barrera D, Madrigal J, Sales S and Misra S 2019 Multi-core optical fibers with Bragg gratings as shape sensor for flexible medical instruments *IEEE Sens.* J. **19** 5878–84
[268] Yi X, Qian J, Shen L, Zhang Y and Zhang Z 2007 An innovative 3D colonoscope shape sensing sensor based on FBG sensor array *2007 Int. Conf. on Information Acquisition* pp 227–32
[269] Yi X, Qian J, Zhang Y, Zhang Z and Shen L 2007 3D shape display of intelligent colonoscope based on FBG sensor array and binocular vision *2007 IEEE/ICME Int. Conf. on Complex Medical Engineering* pp 14–19
[270] Li T, Shi C and Ren H 2018 Three-dimensional catheter distal force sensing for cardiac ablation based on fiber Bragg grating *IEEE/ASME Trans. Mechatronics* **23** 2316–27
[271] Xu R, Yurkewich A and Patel R V 2016 Shape sensing for torsionally compliant concentric-tube robots *Proc. SPIE* **9702** 97020V
[272] Xu R, Yurkewich A and Patel R V 2016 Curvature, torsion and force sensing in continuum robots using helically wrapped FBG sensors *IEEE Robotics Automation Lett.* **1** 1052–9
[273] Gao A, Liu N, Shen M, Abdelaziz M E M K, Temelkuran B and Yang G-Z 2020 Laser-profiled continuum robot with integrated tension sensing for simultaneous shape and tip force estimation *Soft Robotics* https://doi.org/10.1089/soro.2019.0051
[274] Mahoney A W, Bruns T L, Swaney P J and Webster R J 2016 On the inseparable nature of sensor selection, sensor placement and state estimation for continuum robots or "where to put your sensors and how to use them" *2016 IEEE Int. Conf. on Robotics and Automation (ICRA)* pp 4472–8
[275] Kim B, Ha J, Park F C and Dupont P E 2014 Optimizing curvature sensor placement for fast, accurate shape sensing of continuum robots *2014 IEEE Int. Conf. on Robotics and Automation (ICRA)* pp 5374–9
[276] Northern Digital Inc NDI Aurora
[277] Wu L, Song S, Wu K, Lim C M and Ren H 2017 Development of a compact continuum tubular robotic system for nasopharyngeal biopsy *Medical Biol. Eng. Computing* **55** 403–17
[278] Dore A, Smoljkic G, Poorten E V, Sette M, Sloten J V and Yang G 2012 Catheter navigation based on probabilistic fusion of electromagnetic tracking and physically-based simulation *2012 IEEE/RSJ Int. Conf. on Intelligent Robots and Systems* pp 3806–11
[279] Ryu H-T, Woo J, So B-R and Yi B-J 2020 Shape and contact force estimation of inserted flexible medical device *Int. J. Control Automation Syst.* **18** 163–74

[280] Rucker D C and Webster R J 2011 Deflection-based force sensing for continuum robots: a probabilistic approach *2011 IEEE/RSJ Int. Conf. on Intelligent Robots and Systems* (Piscataway, NJ: IEEE) 3764–9
[281] Guo H, Ju F, Cao Y, Qi F, Bai D, Wang Y and Chen B 2019 Continuum robot shape estimation using permanent magnets and magnetic sensors *Sensors Actuators* A **285** 519–30
[282] Ozel S, Keskin N A, Khea D and Onal C D 2015 A precise embedded curvature sensor module for soft-bodied robots *Sensors Actuators* A **236** 349–56
[283] Ozel S, Skorina E H, Luo M, Tao W, Chen F, Pan Y and Onal C D 2016 A composite soft bending actuation module with integrated curvature sensing *2016 IEEE Int. Conf. on Robotics and Automation (ICRA)* pp 4963–8
[284] Luo M, Skorina E H, Tao W, Chen F, Ozel S, Sun Y and Onal C D 2017 Toward modular soft robotics: proprioceptive curvature sensing and sliding-mode control of soft bidirectional bending modules *Soft Robotics* **4** 117–25
[285] Franz A M, Haidegger T, Birkfellner W, Cleary K, Peters T M and Maier-Hein L 2014 Electromagnetic tracking in medicine—a review of technology, validation and applications *IEEE Trans. Med. Imaging* **33** 1702–25
[286] Wagner M, Schafer S, Strother C and Mistretta C 2016 4D interventional device reconstruction from biplane fluoroscopy *Med. Phys.* **43** 1324–34
[287] Wu X, Housden J, Ma Y, Razavi B, Rhode K and Rueckert D 2015 Fast catheter segmentation from echocardiographic sequences based on segmentation from corresponding x-ray fluoroscopy for cardiac catheterization interventions *IEEE Trans. Med. Imaging* **34** 861–76
[288] Vrooijink G J, Abayazid M and Misra S 2013 Real-time three-dimensional flexible needle tracking using two-dimensional ultrasound *2013 IEEE Int. Conf. on Robotics and Automation* pp 1688–93
[289] Burgner J, Herrell S D and Webster R J 2011 Toward fluoroscopic shape reconstruction for control of steerable medical devices *ASME 2011 Dynamic Systems and Conf. and Bath/ Symp. on Fluid Power and Motion Control* American Society of Mechanical Engineers pp 791–4
[290] Yang A and Szewczyk J 2019 Marker-assisted image-based 3D monitoring for active catheters *The Symp. on Medical Robotics*
[291] Janjic J, Mastik F, Leistikow M, Bosch J G, van der Steen A F W and van Soest G 2017 Imaging with a single-element forward-looking steerable IVUS catheter using optical shape sensing *Proc. SPIE* **10135** 101350Z
[292] Tran P T, Chang P-L, De Praetere H, Maes J, Reynaerts D, Sloten J V, Stoyanov D and Poorten E V 2017 3D catheter shape reconstruction using electromagnetic and image sensors *J. Medical Robotics Res.* **02** 1740009
[293] Vandini A, Bergeles C, Lin F-Y and Yang G-Z 2015 Vision-based intraoperative shape sensing of concentric tube robots *2015 IEEE/RSJ Int. Conf. on Intelligent Robots and Systems (IROS)* (Piscataway, NJ: IEEE) pp 2603–10
[294] Lobaton E J, Fu J, Torres L G and Alterovitz R 2013 Continuous shape estimation of continuum robots using x-ray images *2013 IEEE Int. Conf. on Robotics and Automation* pp 725–32
[295] Cabras P, Nageotte F, Zanne P and Doignon C 2017 An adaptive and fully automatic method for estimating the 3D position of bendable instruments using endoscopic images *Int. J. Med. Robotics Computer Assisted Surgery* **13** e1812
[296] Rosa B, Bordoux V and Nageotte F 2019 Combining differential kinematics and optical flow for automatic labeling of continuum robots in minimally invasive surgery *Front. Robotics AI* **6** 86
[297] Sadati S H, Shiva A, Herzig N, Rucker C D, Hauser H, Walker I D, Bergeles C, Althoefer K and Nanayakkara T 2020 Stiffness imaging with a continuum appendage: real-time shape and tip force estimation from base load readings *IEEE Robotics Automation Lett.* **5** 2824–31
[298] Xu K and Simaan N 2008 An investigation of the intrinsic force sensing capabilities of continuum robots *IEEE Trans. Robotics* **24** 576–87